

Friction

(Quarterly, Started in 2013)

Volume 6 Number 3 / September 2018

ISSN 2223-7690
CN 10-1237/TH

40544

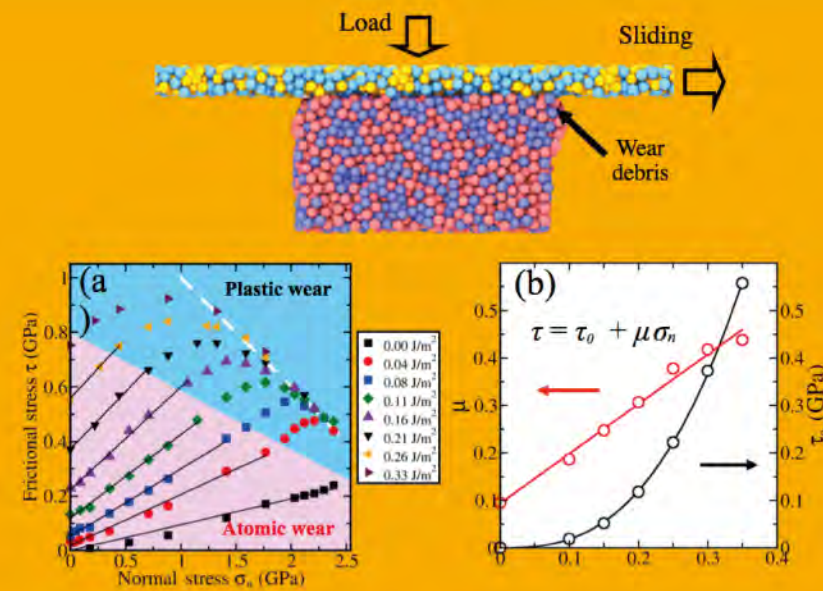
ISSN 2223-7690
CN 10-1237/TH

Friction

Friction

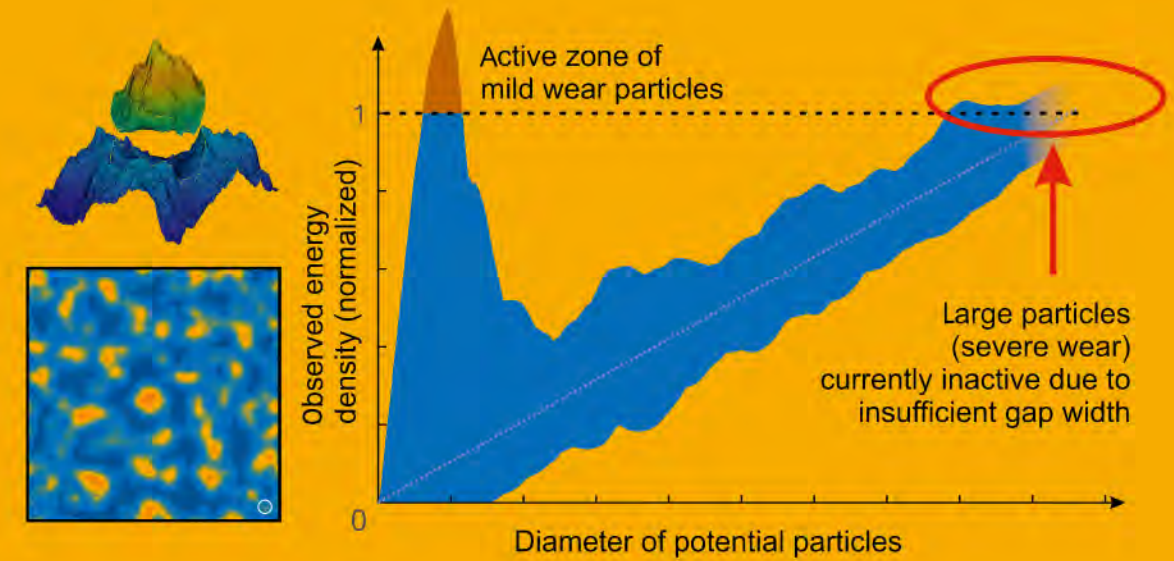
Special Issue on Science of Wear

Volume 6 Number 3 / September 2018



Single asperity friction in the wear regime

Volume 6 Number 3 2018 pp 243–348



Adhesive wear and particle emission: Numerical approach based on asperity-free formulation of Rabinowicz criterion

摩擦 (英文) (季刊, 2013年创刊) 第6卷 第3期 2018年9月出版

Editor-in-Chief Jianbin Luo
Sponsored by Tsinghua University
Supported by Chinese Tribology Institute
Edited by Friction Editorial Office
Published by Tsinghua University Press
Address Xueyan Building, Tsinghua University, Beijing 100084, China

主管单位 教育部
主办单位 清华大学
学术支持 中国机械工程学会摩擦学分会
主 编 雒建斌
编 辑 《摩擦》编辑部
出版发行 清华大学出版社有限公司
印刷单位 北京天成印务有限责任公司

Website <http://www.springer.com/40544> <http://friction.tsinghuajournals.com>
Online Manuscript Submission, Review and Tracking System <http://mc03.manuscriptcentral.com/friction>



Guest editorial: Special Issue on Science of Wear / 243–244

Yonggang MENG, Valentin L. POPOV, Jean-François MOLINARI

Review Article

Adhesive wear mechanisms uncovered by atomistic simulations / 245–259

Jean-François MOLINARI, Ramin AGHABABAEI, Tobias BRINK, Lucas FRÉROT, Enrico MILANESE

Research Articles

Adhesive wear and particle emission: Numerical approach based on asperity-free formulation of Rabinowicz criterion / 260–273

Valentin L. POPOV, Roman POHRT

Combined effect of boundary layer formation and surface smoothing on friction and wear rate of lubricated point contacts during normal running-in processes / 274–288

Yazhao ZHANG, Alexander KOVALEV, Yonggang MENG

Estimating antiwear properties of esters as potential lubricantbased oils using QSTR models with CoMFA and CoMSIA / 289–296

Zhan WANG, Tingting WANG, Guoyan YANG, Xinlei GAO, Kang DAI

Finite element simulation and experimental test of the wear behavior for self-lubricating spherical plain bearings / 297–306

Yahong XUE, Jigang CHEN, Sumin GUO, Qingliang MENG, Junting LUO

Effect of oxide film on nanoscale mechanical removal of pure iron / 307–315

Jinwei LIU, Liang JIANG, Changbang DENG, Wenhao DU, Linmao QIAN

Single asperity friction in the wear regime / 316–322

Yongjian YANG, Yunfeng SHI

Acoustic emission characterization of sliding wear under condition of direct and inverse transformations in low temperature degradation aged Y-TZP and Y-TZP-AL₂O₃ / 323–340

Nikolai L SAVCHENKO, Andrey V FILIPPOV, Sergei Yu TARASOV, Andrey I DMITRIEV, Evgeny V SHILKO, Aleksandr S GRIGORIEV

Short Communication

60 years of Rabinowicz' criterion for adhesive wear / 341–348

Elena POPOVA, Valentin L. POPOV, Dae-Eun KIM

Guest editorial: Special Issue on Science of Wear

Yonggang MENG¹, Valentin L. POPOV², Jean-François MOLINARI³

¹ State Key Laboratory of Tribology, Tsinghua University, Beijing 100084, China

² Technische Universität Berlin, Institute of Mechanics, Berlin 10623, Germany

³ Civil Engineering Department, Materials Science Department, École Polytechnique Fédérale de Lausanne, Lausanne 1015, Switzerland

© The author(s) 2018. This article is published with open access at Springerlink.com

Among the basic tribological phenomena of contact, adhesion, friction, lubrication and wear, wear remains the least scientifically understood. At the same time, wear remains one of the most important tribological phenomena in practice, affecting all aspects of our lives and current technologies. The impact of wear is remarkable in terms of energy losses, environmental impact, component lifetime and economic costs. It may result in catastrophic failures and operational breakdowns that can adversely impact productivity and hence cost. Thus, controlling wear and process optimization play significant roles in sustainable development.

Our understanding of the fundamental processes of wear has been improving recently due to new theoretical approaches, improved experimental techniques and rapidly growing numerical capabilities. It is felt that now it is the right time to revisit the subject of wear intensively, with a special focus on the understanding of physical mechanisms. The Special Issue “Science of Wear” of *Friction* serves to survey the state-of-the-art in the field of wear research and to map out likely developments in the near future. Due to extreme complexity of the wear process, which includes processes from atomic scale up to the scale of the machine as a whole, such a survey cannot be complete. This issue represents exemplary topics which aim to provide a rough general picture of the temporary state of the science of wear and some of its challenges and tendencies.

The Special Issue consists of one review article, seven original research papers and a short communication. It covers a great variety of topics and

methodological approaches in science of wear including adhesive wear, the influence of lubricants on wear, self-lubricating materials, the role of phase transformations and internal damping in the wear process, and the kinetics of the formation and wearing of tribological layers. Methodologically, the papers of the issue cover statistical correlation analysis, numerical simulations on atomic, mesoscopic and macroscopic scales, and experimental investigations on the mechanical system as a whole as well as on individual micro contacts.

The Issue is opened with a review article “Adhesive wear mechanisms uncovered by atomistic simulations”. It is devoted to a review of a recent series of papers on adhesive wear which offers a new paradigm for future wear research. Starting with the breakthrough publication by Aghababaei, Warner and Molinari in *Nature Communications* (Nat Commun 7: 11816, 2016), this series developed a very promising approach for numerical simulations of adhesive wear. A central idea of the approach is the interplay of plasticity and adhesion which introduces a characteristic length scale governing the process of adhesive wear. The review also contains an extensive historical review of the main attempts in simulating wear.

The original research paper “Adhesive wear and particle emission: Numerical approach based on asperity-free formulation of Rabinowicz criterion” is closely related to the ideas described in the opening review paper as well as to an old idea of Ernest Rabinowicz about the criterion of looseness of wear particles. The paper discusses the key problem of those wear criteria which use the concept of “micro

contact” or “asperity”. For real fractal surfaces, this notion is very hard to define. The authors introduce a formulation which allows to completely avoid the notion of “asperity” and illustrate the application of this new approach by a series of wear simulations based on the boundary element method. One of the important conclusions of the paper is a possible breakdown of Archard’s law of wear.

In the paper titled “Combined effect of boundary layer formation and surface smoothing on friction and wear rate of lubricated point contacts during normal running-in processes”, the authors take a closer look at the running-in-process as essential stage of a lifetime of any tribological system. The authors carry out an experimental investigation and use stop-and-go experiments in combination with measurements of surface topography for discriminating the effects of boundary layer of change of surface topography.

In the research paper “Estimating anti wear properties of esters as potential lubricant-based oils using QSTR models with CoMFA and CoMSIA”, the authors apply statistical regression analysis to correlate the structural properties of 57 esters and the wear properties of the oils based on these esters. This method allows considering much more governing parameters than is usually possible in any model based approach, thus producing a rough but complete picture of influence tendencies.

In the paper “Finite element simulation and experimental test of the wear behavior for self-lubricating spherical plain bearings”, the authors numerically and experimentally investigate wear in spherical plain bearings. They identify the stages of rapid initial and stationary wear. Through comparison of experimental findings with finite element simulation, the authors determine parameters of the wear law, which differs from the Archard’s law and is formulated in terms of power dependencies of the wear rate on the normal pressure and sliding velocity.

In the paper “Effect of oxide film on nanoscale mechanical removal of pure iron”, properties of an oxide film formed on a pure iron surface after being polished with an H₂O₂-based acidic slurry were investigated using an atomic force microscope (AFM),

Auger electron spectroscopy (AES), and angle-resolved X-ray photoelectron spectroscopy (AR-XPS) to partly reveal the material removal mechanism of pure iron during chemical mechanical polishing (CMP). The authors come to the conclusion that chemical corrosion-enhanced mechanical wear may dominate the CMP process.

The paper “Single asperity friction in the wear regime” studies wear and friction and their relation by atomic scale simulations. The authors come to the conclusion that depending on adhesion parameters and load, regimes of atomic wear and plastic wear may occur. Interestingly, in the region of atomic wear, the well-known Amontons’ law is valid even at the level of single asperities. It would be interesting to compare these findings with the old ideas of Holm and Rabinowicz about the existence of a very mild wear via atom-by-atom removal.

The research paper “Acoustic emission characterization of sliding wear under condition of direct and inverse transformations in low temperature degradation aged yttria-stabilized tetragonal zirconia polycrystalline (Y-TZP) and Y-TZP-Al₂O₃” is devoted to an experimental characterization of acoustic emission as a powerful *in-situ* tool for investigating the micro-mechanical process going on during the wear process. The paper combines an experimental investigation with corresponding simulations by the method of movable cellular automata.

The Special Issue is closed by a short historical review of the work of Ernest Rabinowicz on adhesive wear. Rabinowicz was one of the first tribologists who recognized the importance of adhesion in tribological contacts and formulated a number of key concepts in tribology. One of his fundamental ideas on the looseness of wear particles, Rabinowicz published in a short paper in 1958. On occasion of the 60th anniversary of this work, the authors carried out a historical research of the subsequent development of the ideas of Rabinowicz and their impact on research in tribology and materials science. The communication is based both on a literature search and personal experience of one of the authors who was fortunate enough to be one of the PhD students of Ernest Rabinowicz at MIT.

Adhesive wear mechanisms uncovered by atomistic simulations

Jean-François MOLINARI^{1,*}, Ramin AGHABABAEI², Tobias BRINK¹, Lucas FRÉROT¹, Enrico MILANESE¹

¹ Civil Engineering Department, Materials Science Department, École Polytechnique Fédérale de Lausanne, Lausanne 1015, Switzerland

² Department of Engineering - Mechanical Engineering, Aarhus Universitet, Aarhus 8000, Denmark

Received: 01 May 2018 / Revised: 14 July 2018 / Accepted: 16 July 2018

© The author(s) 2018. This article is published with open access at Springerlink.com

Abstract: In this review, we discuss our recent advances in modeling adhesive wear mechanisms using coarse-grained atomistic simulations. In particular, we present how a model pair potential reveals the transition from ductile shearing of an asperity to the formation of a debris particle. This transition occurs at a critical junction size, which determines the particle size at its birth. Atomistic simulations also reveal that for nearby asperities, crack shielding mechanisms result in a wear volume proportional to an effective area larger than the real contact area. As the density of microcontacts increases with load, we propose this crack shielding mechanism as a key to understand the transition from mild to severe wear. We conclude with open questions and a road map to incorporate these findings in mesoscale continuum models. Because these mesoscale models allow an accurate statistical representation of rough surfaces, they provide a simple means to interpret classical phenomenological wear models and wear coefficients from physics-based principles.

Keywords: adhesive wear; molecular dynamics; continuum mechanics

1 Introduction

In 1995, when Meng and Ludema [1] reviewed an extensive literature of around 300 equations for friction and wear, times were dire for tribology. Progress had arguably slowed down since the golden age of tribology in the 1950s, and research funding from national science foundations in various countries was being cut for tribology research and reallocated to other scientific fields. This was happening despite the importance of understanding and controlling wear mechanisms for industry and society at large. After a detailed analysis of wear models, including their origin, content and applicability, Meng and Ludema concluded that “No single predictive equation or group of limited equations could be found for general and practical use. The reasons include the perpetuation of erroneous and subjective expressions for the mechanisms of wear, the

slow pace of translation of microscopic observations into macroscopic models of the wearing processes and the paucity of good experiments to verify proposed models”.

Meng and Ludema’s review came after three centuries of scientific investigations on wear mechanisms, which started in 1803 with Hatchett [2]. This had led to the emergence of a myriad of empirical/phenomenological models, often with increasing complexity (Meng and Ludema, for instance, refer to one model with 26 independent material parameters). Amongst them is the ubiquitous Archard wear law [3], which will be discussed at length in this paper. Archard’s law is arguably the simplest existing wear model, and we here briefly recall its proposition: the wear volume (total volume of collected debris) is proportional to the normal load, the sliding distance, and inversely proportional to the hardness of the softer material in contact. Simple theoretical arguments [3]

* Corresponding author: Jean-François MOLINARI, E-mail: jean-francois.molinari@epfl.ch

can be brought forward to explain the mechanistic origins of this model, but the theoretical prediction does not agree with experimental data without using a proportionality constant, the wear coefficient K . This coefficient is essentially an experimental fitting parameter, and it is not a small correction, but a strong adjustment of several orders of magnitude. Typical values for the wear coefficient are between 10^{-2} to 10^{-8} . The origin of K is unclear, but K is usually interpreted as a probability, because only a few contact asperities amongst the many form wear particles. It is telling that even the simplest wear model necessitates an empirical adjustment. As stated by Meng and Ludema, by and large, our macroscopic engineering-scale understanding of wear remains limited [1, 4].

However, this does not come as a surprise to the initiated tribologist, because it is hard to find a more complex and dirty problem than wear. After all, wear processes emerge from a variety of physical and chemical mechanisms at disparate time and length scales. Wear comes in many forms, amongst which adhesive and abrasive wear are the most prominent [5]. Wear processes depend on environmental conditions and vary with time. It is impossible to draw up an exhaustive list here. They depend on the rate of physico-chemical reactions, and also on the evolution of surface roughness that dictates the geometry and pressures at microcontacts. In lubricated contacts the lubricant properties may degrade with time. The wear particles and sheared materials form a tribolayer with complex properties and in turn alter the surface properties. All this complexity resulted in little alternatives to empirical models relying on parameters calibrated for specific materials and applications.

A major advancement came in the 1980s/1990s thanks to nanotribology. Atomic-force microscopy (AFM) provided a means to explore the fundamental mechanisms leading to friction and wear. A turn was taken towards identifying molecular mechanisms experimentally and opening a dialogue with increasingly reliable numerical simulations. Numerical modeling of wear processes is appealing as it opens the possibility to zoom in on an otherwise buried contact interface. However, numerical modeling comes with its own difficulties. These stem from the challenge of scales

of tribological problems and once more from the complex physico-chemical mechanisms taking place at the contact interface. Let us consider the challenge of scales for a moment, and limit ourselves to the question of relevant length scales for wear processes (the question of relevant time scales is equally if not more important but will be left out of the discussion of this paper). One may resort to atomistic simulations, as for instance with classical molecular dynamics (MD). This is a very useful approach in particular because it is relevant in scale to AFM experimental data [6–11]. However, classical MD simulations are limited to sizes below microns, which are disconnected from the vast category of engineering wear scenarios, in which wear particles are of the order of, or above, micrometers, i.e., orders of magnitude larger than the scale at which MD simulations operate. Alternatively, wear modeling approaches can be conducted at a larger scale, at which one would apply efficient continuum mechanics models. This is for instance the approach taken with the finite-element method (FEM) or with the boundary-element method (BEM). Besides computational efficiency, a major advantage of these numerical approaches is that it is fairly straightforward to account for diverse constitutive behaviors. But a major disadvantage is that they do not give insights on molecular mechanisms, and struggle to handle the large deformations, tearing, breaking and mixing of materials resulting from wear processes.

This challenge of scales has motivated us to work at an intermediate scale, denoted here by mesoscale, and to revisit the classical Archard wear law. The present manuscript reviews and discusses the implications of our recent results. It is organized in two steps: we will first describe our efforts at capturing the atomistic mechanisms leading to the formation of wear debris. This will be conducted using classical molecular dynamics. Then we will incorporate our findings in a mesoscale continuum mechanics BEM solver. The focus of the paper is on adhesive wear, i.e., the formation of debris particles when contact junctions form under strong adhesive bonds. We restrict our attention to dry sliding between two identical solid materials. We will consider the adhesive strength between the two bodies to be a constant, thereby

neglecting ageing or oxidation mechanisms. Naturally, the approaches detailed in this paper can be developed further to include the presence of lubricants, ageing, and contrast between material properties as in abrasive wear, but this will be the topic of future work.

Section 2 describes our model atomistic pair potential. We discuss how this potential may be interpreted as a coarse-grained potential or discrete-element potential [12–14], in which case a discrete point should be interpreted as a group of atoms or grains, giving access to larger physical sizes. Section 3 summarizes the main components of our atomistic model for adhesive wear. One may distinguish between three fundamental asperity-level mechanisms behind wear: atom-by-atom attrition in the light load limit [15–17], gradual smoothing by dislocation plasticity [18–21] and amorphization [22], as well as fracture-induced third body formation [23–25]. The chosen geometry imposes a large overlap between opposing asperities and/or large loads, and aims to explore the transition between plastic smoothing of asperities and debris formation. We do not investigate the atom-by-atom attrition mechanism in this paper. In Section 4, we show that our potential is able to reproduce the ductile to brittle transition of contacting asperities [26]. The transition occurs at a critical junction size that depends on material properties. Contact junctions above the critical length scale form a debris particle, while smaller junctions deform plastically, and may form a debris particle at a later stage of the sliding history if the junction size then reaches the critical length scale. This gives a deterministic evaluation at the debris level of the wear coefficient in Archard's wear law. K is either 1 (for large junctions) or 0 (for small junctions). Remarkably, it is not a probability anymore. Section 5 explores the life of a debris particle. We restrict our attention to contact junctions that are large enough to generate a debris particle and examine if Archard's law is recovered at the asperity level. We summarize the findings of a recent paper [27] in which we demonstrate that in the presence of strong adhesive forces, the frictional work is a good predictor of wear volume at the single asperity level, instead of the normal force component as used in Archard's wear law. Section 6 investigates the question of interactions, in the process of debris formation, between contact

asperities. For nearby contact junctions, we show that crack shielding mechanisms occur, resulting in larger debris sizes. We argue that these mechanisms might be key to explain the transition from mild to severe wear [28]. Finally, Section 7 explores the upscaling of these findings in a BEM mesoscale model consisting of an elastic rough surface under normal loading. We examine the microcontact maps and obtain a direct measure of the wear coefficient for Archard's wear law [29].

2 A simple model atomistic potential

Previous atomistic modeling studies of adhesive wear predict a continual smoothing of surface asperities rather than the formation of debris particles [8, 9, 22, 30–33], inconsistent with macroscopic experimental observations. This can be understood in light of the challenge of scales discussed earlier. Simulation sizes amenable to reasonable computation times on modern computers are orders of magnitude smaller than the process zone sizes needed for generating wear particles by nucleation and propagation of subsurface cracks in many materials. These process zone sizes can be estimated by the square of the ratio of fracture toughness to yield strength. For instance, it is of the order of mm or above for metals, orders of magnitude above world-record atomistic simulations.

This long-standing quest for physics-based simulations of wear debris formation has been recently addressed through a coarse-grained atomistic approach [26]. This permits the simultaneous description of plastic deformation and fracture phenomena at a desirable length scale. In this approach, the material is modeled as a set of discrete points. System responses beyond the elastic limit (i.e., plasticity and fracture) are controlled by interactions between those points. For instance, the brittle/ductile response of the system, which is controlled through the competition between surface energy and the energy associated with plastic slip, can be tuned by modifying the potential well, the shape of potential tail and cut-off radius.

Considering a nearest-neighbor pairwise potential, we modified the long range character of the Morse potential [34] without disturbing the short range interactions (elastic properties) as follows:

$$\frac{V(r)}{\varepsilon} = \begin{cases} (1 - e^{-\alpha(r-r_0)})^2 - 1, & r < 1.1r_0; \\ c_1 \frac{r^3}{6} + c_2 \frac{r^2}{2} + c_3 r + c_4, & 1.1r_0 \leq r \leq r_{\text{cut}}; \\ 0, & r_{\text{cut}} \leq r \end{cases} \quad (1)$$

where the r_{cut} parameter defines the potential cut-off radius and controls the interaction length scale and c_1 to c_4 are parameters. A smaller r_{cut} makes the tail of the potential steeper, thereby increasing the yield strength. r_0 is the equilibrium bond distance at $T = 0$ and ε is the bond energy. The 1.1 factor ensures constant elastic properties up to 10% strain. This allows us to study the influence of inelastic properties while keeping the elastic properties fixed. In a coarse-grained interpretation of this potential [26], the distance between discrete points determines the scale at which plasticity and fracture phenomena are simulated. Interpreting this distance as the spacing between atoms gives classical MD results, in which plasticity and fracture are refined to a single dislocation and the rupture of an atomic bond respectively.

Figure 1(a) shows the bond energy versus atomic bond length for six different cut-off radii, with the smallest (P6 potential) corresponding to the most

brittle behavior. In order to obtain the shear strength associated with each potential, we performed 2D indentation simulations. To model non-adhesive contact, we only considered the pure repulsive contribution of the interfacial potential. The indentation responses of all potentials are shown in Fig. 1(b). To extract the hardness value from these curves, we plot the contact pressure as the ratio of the indentation force (P) to the projected contact area (A), versus indentation depth [35]. Surface atoms within the cut-off radius of the interfacial potential are considered to define the atomic area of contact [36–38]. Accordingly, the projected contact area at the atomic scale is computed [39]. Upon continued loading, the stress remains at a relatively constant value, which we take as the hardness. The critical shear strength τ corresponding to each potential is estimated as $\tau = \frac{1}{3\sqrt{3}}H$ [40]. In simulations

with full interfacial adhesion the junction strength σ_j is taken equal to τ . Note that in a 2D setup, plastic deformation occurs on three in-plane dislocation slip planes. We also performed 3D indentation simulations to characterize 3D coarse-grained potentials using a spherical indenter, see Fig. 1.

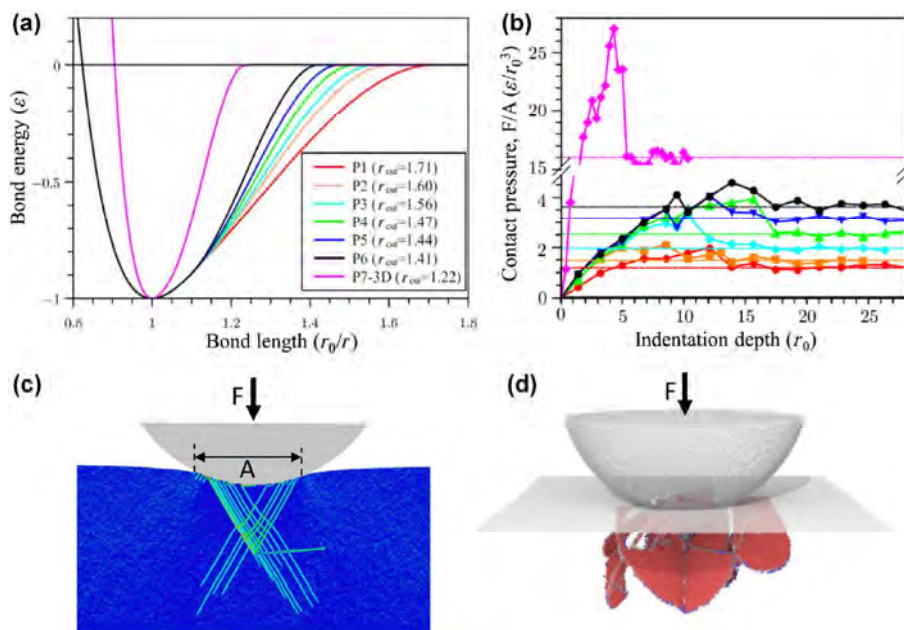


Fig. 1 (a) The bond energy versus atomic bond length is plotted for 2D (P1–P6) and 3D (P7) coarse-grained potentials. Bond energy and length are normalized by the depth of the potential well (ε) and the equilibrium bond length (r_0), respectively. (b) Contact pressure versus indentation depth obtained from 2D and 3D indentation simulations. The contact pressure is computed as the indentation force divided by the projected contact area. The plateau values are considered to be the effective hardness. (c) and (d) show snapshots of indentation simulations, showing plastic activity under the indenter in 2D (with P6 potential) and in 3D (with P7 potential).

3 A simple model for adhesive wear at the asperity level

Besides the different parametrizations described in the previous section, the simulations performed using LAMMPS [41] differ in initial geometry, loading and boundary conditions (Fig. 2). These conditions are described in this section, where all quantities are expressed in reduced units as we model a single atom type with fundamental quantities m , r_0 , ε , and k_B , which are respectively the atom mass, the equilibrium bond length, the equilibrium bond energy, and the Boltzmann constant.

To reduce the computational resources needed, most of the simulations are run in 2D, with some 3D calculations run on high-performance computing platforms. The model consists of two contacting solids with a focus on the atomistic mechanisms at the contacting asperities: to this end, the simulation box size is large enough along the vertical direction to diminish boundary effects, while periodic boundary conditions are applied along the horizontal direction. The top body slides continuously at a constant velocity $v = 0.001 - 0.05\sqrt{\varepsilon m^{-1}}$, which is applied at the top atoms. The bottom atoms of the bottom body are instead fixed horizontally. Both bodies can translate vertically, so that the simulation box can expand or shrink upon asperities collision. To keep the bodies

in contact, a constant vertical force f_y of magnitude up to $0.02\varepsilon r_0^{-1}$ per atom is applied on the top and bottom boundaries. A temperature of $0.1\varepsilon k_B^{-1}$ is enforced by means of Langevin thermostats with a damping parameter of $0.05r_0/\sqrt{\varepsilon m^{-1}}$ applied on two layers of atoms on each body (see Fig. 2). The simulation box has horizontal size $l_x = 200 - 600r_0$ and vertical size $l_y = 400 - 1000r_0$. Surfaces are atomistically flat except for the presence of asperities. Different cases have been analysed including a single asperity (Fig. 2(a)), interlocking asperities leading to one contact junction (Fig. 2(b)), and a pair of contact junctions separated by a distance λ (Fig. 2(c)). Within the set of simulations conducted in Ref. [26], we varied the asperity size ($d = 20 - 140r_0$) and shape (semicircular, half sine, rectangular, triangular). The integration time step for the velocity Verlet algorithm is $0.0025r_0/\sqrt{\varepsilon m^{-1}}$.

4 Critical length scale for ductile to brittle transition

Our simple model potential allows us to examine the asperity-level origins of adhesive wear mechanisms. As detailed in the previous section, a large number of adhesive wear simulations with different geometrical configurations, boundary conditions, and bulk and surface properties were conducted. These simulations demonstrated two adhesive wear mechanisms: gradual

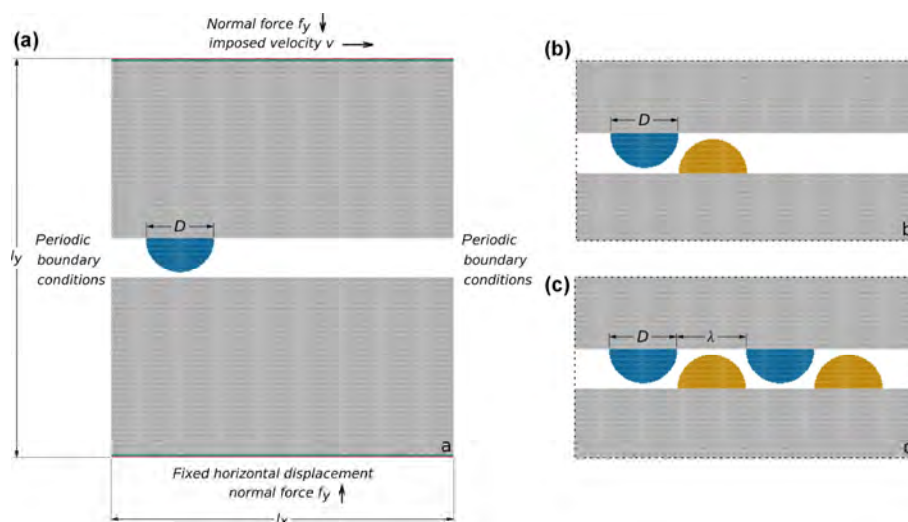


Fig. 2 Schematic for the atomistic simulations. (a) Boundary conditions and single-asperity surface topography. In green and red are the layers of atoms where the thermostats and displacements are applied respectively. (b) Interlocking asperities surface topography, with one asperity on each surface. (c) Interlocking asperities surface topography, with two asperities spaced at a distance λ on each surface.

asperity smoothing by plastic deformation (see Fig. 3(a)) versus fracture-induced debris formation (Fig. 3(b)). Examining a range of simulation parameters, we found that the size of the asperity contact junction and the strength of the adhesive bond dictate the adhesive wear mechanism. Ultimately, hard/brittle materials with large asperities and strong adhesive bonding at the asperity contact junctions favour the debris formation mechanism over the asperity smoothing mechanism.

Inspired by previous theoretical insights [42, 43] and this new understanding [26], we find that the transition between plastic smoothing and fracture-induced debris mechanisms can be predicted with a simple analytic model. The model considers that the transition from plastic deformation to debris formation occurs when the stored elastic energy is large enough to create new wear-debris particle surfaces. The maximum stored elastic energy depends on the junction shear strength and the junction size d , and the surface energy determines the energy cost of creating a debris particle. This yields the existence of a critical length scale d^* . Asperity junctions larger than d^* produce wear debris by fracture while smaller ones smooth out plastically. The analytic model gives

$$d^* = c \cdot \frac{\Delta w}{(\sigma_j^2 / G)} \quad (2)$$

where G is the shear modulus and σ_j is the shear strength of the junction. Δw is the energy associated

to newly created free surfaces (i.e., decohesion energy). c is a shape factor combining contributions of all geometrical factors (e.g., asperities shape and junction configuration). For the removal of an idealized 2D circular and 3D spherical debris, we obtain $c = \frac{8}{\pi}$ and $c = 3$ respectively. This model can be also understood in terms of a crack growth model [44, 45], in which the detailed kinetics of crack growth and other dissipative mechanisms (e.g., plasticity) could be taken into account. Figure 3 illustrates this ductile to brittle transition at a critical junction size in the context of a 3D asperity [27]. In case of a junction size smaller than the critical size, Fig. 3(a), the strong adhesive forces yield a severe plastic deformation of the asperities. This process has been routinely observed in the literature with classical atomistic potentials (see for instance Ref. [30]). With repeated sliding of the simulation box size, one observes a continuous smoothing of the asperity. If the lateral dimension of the simulation box is smaller than d^* , this process will lead eventually to a full contact between the two blocks. However, if the simulation box size and junction size are larger than the critical length scale, as in Fig. 3(b), a debris particle is formed.

The proposed simple analytic model can explain and predict the operative mechanisms in AFM wear experiments, where the AFM tip has been reported to wear due to adhesive forces via both gradual smoothing [17–19, 20, 21, 24, 46, 47] and the creation of fracture induced debris [24, 25, 48].

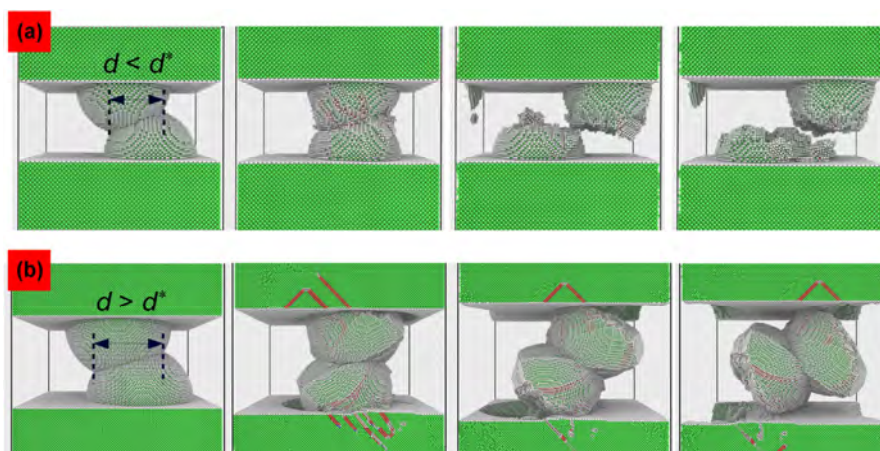


Fig. 3 Numerical simulations distinguish two wear mechanisms at the asperity level. (a) shows the plastic smoothing mechanism in the absence of wear debris particle for a small asperities junction. (b) presents the fracture-induced particle formation mechanism for a large asperity junction. See [26, 27] for detailed information about the simulations.

5 Quantitative prediction of debris size

5.1 Birth of a debris particle

A direct modeling of wear debris formation [27] enables quantifying the amount of detached material at the onset of debris formation and studying the origins of long-standing macroscopic wear observations: (i) the wear volume (i.e., total volume of wear debris) is independent of apparent area of contact [49, 50], (ii) within a certain range of applied load, the wear rate (i.e., wear volume per sliding distance) is linearly proportional to the macroscopic load acting normal to the interface, like in Archard's wear law [49, 3], and (iii) the wear volume is proportional to the frictional work (i.e., the product of frictional force and sliding distance) [5, 51, 52].

A recent systematic set of adhesive wear simulations [27] showed universal features of the process of debris formation despite the variety of parameters and configurations examined. Initially, a strong adhesive bond (junction) forms between contacting asperities. Subsequent sliding leads to the junction growth by localized inelastic deformation, until crack nucleation and growth ensues at the two corners of the junction loaded in tension. These simulations reveal three main observations about the process of single debris particle formation:

- The diameter of the debris particle upon formation is the same as the maximum junction size, independent of the parameters and configurations of a particular simulation. This observation rationalizes the correlation between the *real* contact area and the volume of the debris particle, which is a central tenet of Archard's wear model [3].
- The debris volume does not correlate with the product of applied normal load and sliding distance (i.e., Archard's wear relation). This observation is in fact not surprising for an isolated debris particle considering that two opposing asperities can collide, adhere, and form a debris particle even in the absence of an applied normal force. In this situation, the contact area of a single asperity junction is largely affected by the asperity's geometry [53, 36], shear loading [38, 54] and adhesion [55]. Therefore, the normal applied force does not linearly depend on the junction size and, as a result, cannot predict

debris volume. This finding suggests that the macroscopically observed linear relation between the wear volume and the normal force may be reconstructed via multiasperity contact models, where the contact is a load-controlled process [56].

- Alternatively it is found [27] that the debris volume scales with the work of tangential force that is carried by the junction, with a proportionality constant of 1 over the junction shear strength. This can be explained by the fact that the tangential force transmitted across the asperity junction provides an indication of the maximum asperity junction area. Therefore, as the asperity junction size controls the debris size, the wear debris volume can be quantified via the work done by the tangential component of the load carried by the junction.

These debris-level wear observations [27] together with the concept of the critical junction size [26] confirm that the debris formation is a deterministic process at the asperity level (i.e., wear coefficient of unity at the single debris level if the junction size is above the critical size). It will guide us in proposing a first-level estimation of the wear coefficient in Archard's law. For this, one needs to statistically analyze the junction size probability in a multiasperity contact setting [29], as detailed later in Section 7.

5.2 Life of a debris particle

Once a debris particle has been formed, its following evolution affects both the wear volume and the changes in the surfaces roughness. At the end of an experimental wear test, the shapes of the debris particles can be investigated and are found to be related to the mechanism of wear involved [57]. The particles produced during a wear process where adhesion is relevant are characterized by an elliptic shape [5], and their elongation is small when compared with particles produced in wear processes of the abrasive type [57]. In our 2D simulations of adhesive wear, the debris particle that forms displays a circular shape most of the most of the time, with very little elongation. Of course, 3D simulations would be more relevant to investigate shape evolution.

Preliminary simulations of 2D debris conducted over long time scales reveal that the formed debris particle volume increases with time, although slowly

and at a decreasing rate. Therefore the wear is characterized by first a high wear rate at the onset of debris formation and a transition to a slower wear rate, which is consistent with experimental observations [58]. Future work will present a continuum mechanics model to explain why the asymmetry in the loading favours crack propagation within the bulk at the trailing edge. For circular debris shapes we have observed that the basic mechanism for debris growth is detachment of matter from the substrate, and attachment to the debris. In addition, we have also observed that the debris size tends to saturate with time. More work is needed to understand in details the wear particle growth rate. In particular several mechanisms could break this growth pattern. The debris particle could develop a concave shape with time, leading to stress concentrations within the debris particle. Also the particle could break/fragment upon the action of compressive forces, a process that would be favoured by creating weak layers in the debris particle owing to ageing. We do not currently consider ageing in our simulations, which is an artefact differentiating our results from real wear experiments. Accounting for these mechanisms could eventually lead to the death of the debris particle. Another fate would be its evacuation from the contact interface.

6 Interactions between microcontacts

Until now, we considered the problem of wear on the level of a single debris particle. This is clearly an approximation, which may fail in several common cases: debris particles will come into contact with each other during the wear process, debris particles will interact with asperities, and microcontacts cannot necessarily be separated into individual asperities that behave independently.

Here, we consider the latter case. At low normal load, we expect the contacts to be spaced out. Moreover, many contacts will have sizes $d < d^*$ and will not form debris particles; a model of the macroscopical consequences of this observation will be discussed in the next section. For the moment, we look at the case of high normal load, where more contacts have sizes $d > d^*$ and the average distance between the contact spots shrinks. It is known from literature that

the contact solutions for closely-spaced contact junctions are different from individual junctions [59, 60]. As detailed in Section 4, the detachment of a debris particle is the result of a subsurface crack, which will be influenced by the modified stress field. By extending the simulation setup from Section 4 from a single junction to two junctions, we were able to investigate this in more detail in a recent work [28]. By bringing the contacting asperities close together, the detachment mechanism switches: single asperity mechanisms (either plastic smoothing or debris formation, Figs. 4(a)–4(b)) are replaced by collective deep subsurface cracks that lead to the detachment of a single, large debris particle (Fig. 4(c)). By systematically varying the junction size d and the spacing λ between the junctions, we found that—in this specific case—the transition from individual debris formation to a combined mechanism occurs for $\lambda < d$. Furthermore, the volume of the resulting debris particle is no longer related to the size of the individual junctions.

This latter observation has implications for the “bottom-up” prediction of wear coefficients. When the debris particle size scales with the junction size [27], we should recover a proportionality between the normal load and the wear rate as for example in Archard’s wear law [5, 3, 49, 50]: the actual contact area, i.e., the sum of the junction sizes, is a function of normal load [61] and thus the resulting debris volume is, too. In the case of interacting junctions, on the other hand, the wear rate is no longer related to the actual contact area, but to some effective contact area that is somewhere between the actual contact area and the apparent macroscopic contact area. This mirrors the transition from mild to severe wear, for which a sudden increase of the wear coefficient at a critical load has been observed [62–71]. While the current investigations only treat a simplified model case, they give a first possible explanation for this transition. Further modeling and experiments are needed to quantify the phenomenon.

It remains to be explained why the junctions interact at all instead of being worn off individually. For this, we first look at the initial stages of the wear process for far-spaced junctions in Fig. 5(a). We can see that the asperities come into contact and tensile stress concentrations build up. With increasing sliding distance,

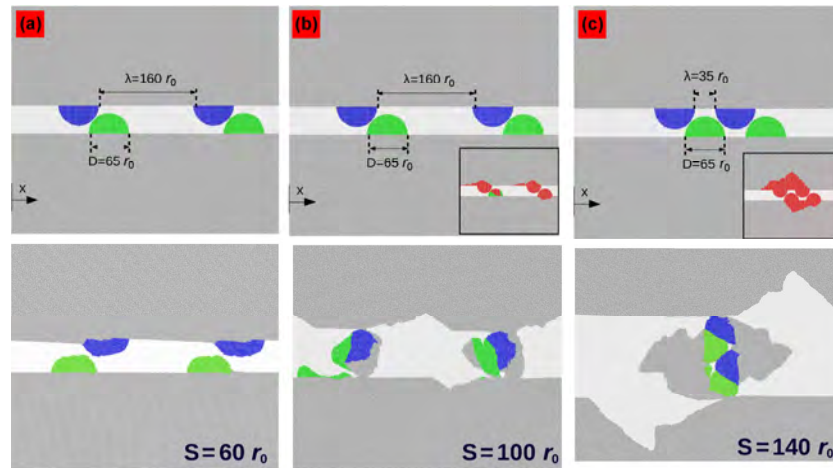


Fig. 4 (a) Asperity smoothing without debris formation, where the asperity junctions are smaller than the critical junction size. This is ensured by reducing the interfacial adhesion, which establishes a weak interfacial junction between interacting asperities and consequently a very large critical junction size [26]. (b) Debris formation at the asperity level in the presence of a high interfacial adhesion, where strong junctions are established. In this case, debris particles of the same size as the asperity junctions are formed individually. (c) Once asperity pairs get close to each other, they interact through their underneath inelastic stress fields, which results in the formation of a large debris particle. In this condition, no correlation between the debris size and junction size is observed. For a better visualization of detached volume, debris atoms are highlighted in the initial configuration in the insets of Figs. 4(b) and 4(c).

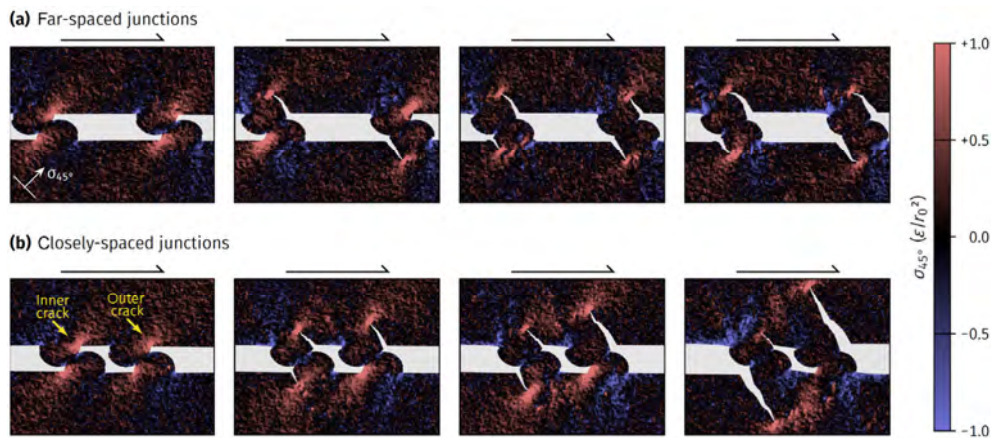


Fig. 5 Mechanisms of debris formation. Sliding simulations are shown, the sliding direction is indicated by the black arrows. The color coding shows the stress component σ_{45° , which acts perpendicular to the crack tips and is responsible for the crack nucleation and propagation.

these stress concentrations lead to the successive formation of cracks that cause the detachment of two debris particles. It is immediately visible that their volume is close to the volume of the asperities. If the asperities are closer, Fig. 5(b), the initial steps are very similar. Stress concentrations build up in the same way and it even seems that cracks occur at the same places. Further sliding, though, changes the picture. The “outer crack” at the leading junction (see label in the figure) grows and starts to unload the “inner crack” at the trailing junction, which then closes. This

mechanism is dictated by the geometry of the problem: due to the imposed sliding direction, a sufficiently propagated outer crack can “envelope” the trailing asperity and completely unload it, as shown in Fig. 5(a), but not vice versa. In the textbook case [72], parallel crack shielding becomes effective roughly when the distance between the two cracks is less than twice their length. Assuming that the depth of a crack at non-interacting junctions is roughly the asperity size d [27], the distance λ must be approximately equal to or smaller than d to reach this distance between the

inner and outer crack. This can justify the observations above. Additionally, the modified subsurface stress field seems to always lead to a deeper propagation of the cracks.

While the model is very simple and a quantitative picture clearly needs to take more realistic 3D geometries into account, it already gives us insight into the complexity of asperity interactions. In fact, given the varied contact geometries that occur when rough surfaces touch, it raises the question of how to exactly define an asperity. Do we need to account for every “internal valley” or should we prefer a more coarse-grained view?

7 A mesoscale model for wear

Finally, we present two mesoscale wear models that up-scale the relations derived at the asperity level from atomistic insights to a multi-asperity setting [29]. These models allow the estimation of the total wear rate as a function of the interface physical properties, the surfaces’ geometrical properties and the normal load applied on the system.

7.1 Archard’s wear model

In his seminal work [3], Archard puts forth a model for macroscopic wear that is composed of two fundamental parts: a single-asperity wear model and a multi-asperity contact model. At the single-asperity level, Archard makes the following considerations:

- given two hemi-spherical asperities in contact in a zone of radius a (which is half the contact junction size d), the resulting wear particle has a volume proportional to a^3 ,
- the sliding distance necessary to produce the particle is $2a$,
- each asperity encounter has a probability K of forming a wear particle.

Archard uses these hypotheses in conjunction with his multi-asperity contact model to derive, in the case of a rigid-plastic material, the well known Archard-Holm equation:

$$R(W) = K \frac{W}{H} \quad (3)$$

where R is the wear rate, W is the applied normal load

and H is the flow stress of the material. This equation has been widely used, but unfortunately Archard does not provide a way to quantify K , so applications of this equation exclusively rely on parameter fitting with experimental data. Archard and Hirst [62] make the claim that “one of the most important problems in an understanding of wear is to explain the magnitude of the probability of the production of a wear particle at an asperity encounter”.

However, the last of Archard’s hypotheses introduces K to account for the fact that not all asperity encounters form wear particles. It is clear from Ref. [26] that the particle formation process follows a Griffith-like criterion and is a deterministic event at the asperity level, so K cannot be introduced at the asperity level. We now present a definition of K at the mesoscale.

Consider a rough surface contact situation (Fig. 6) where the true contact area is composed of a multitude of smaller contacts, here called contact clusters. Since the surface height distribution is random, the distribution of the area of the contact clusters is also random. We denote A the random variable representing the area of a single contact cluster. This variable follows the probability density function $p(A, W)$, which depends on the load.

We suppose that the wear particle formation process is governed by a critical contact area A^* derived from the previously discussed critical length scale d^* . A wear particle is therefore formed if and only if $A > A^*$. Since K is the probability that an asperity encounter forms a debris particle, we obtain the natural definition [29]

$$K \equiv P(A > A^*, W) = \int_{A^*}^{\infty} p(A, W) dA \quad (4)$$

Experimental evidence [62] and our previous simulation results show that the wear rate is proportional to the real contact area in the mild wear regime, with a proportionality constant called the “wear coefficient”. In Archard’s model, the wear coefficient is K , the probability of wear particle formation. However, this interpretation of the wear coefficient is not physically justified by Archard.

An alternative interpretation of the wear coefficient not relying on Archard’s interpretation is possible [29]. Consider a system of finite size, so that there are $N(W)$ contact clusters for a given load. We define the un-normalized cluster size distribution as $n(A, W) =$

$N(W) \cdot p(A, W)$ and the asperity level wear rate $R_1(A) = \omega A$, with ω a shape factor equal to 1/3 in the case of hemi-spherical asperities (the wear rate is the ratio of volume of wear debris over sliding distance, which in the simple case of hemi-spherical asperities gives a 1/3 factor.). These are used in the computation of the total wear rate

$$\begin{aligned} R(W) &= \int_{A^*}^{\infty} R_1(A) n(A, W) dA \\ &= \int_{A^*}^{\infty} \omega A n(A, W) dA = \omega A_c^*(W) \end{aligned} \quad (5)$$

where A_c^* is the cumulative area of contact clusters forming wear particles. If we now introduce $\mathcal{K}(W) = \frac{A_c^*(W)}{A_c(W)}$, we can write the total wear rate as $R(W) = \mathcal{K}(W) \omega A_c(W)$. \mathcal{K} is then the wear coefficient, and naturally arises from the up-scaling process of single asperity wear rate, which was discussed in the previous sections, to a multi-asperity setting. The central difference with Archard's purely probabilistic interpretation is that this second interpretation of the wear coefficient emerges from the sum of volumes of debris particles, which depend on local contact junction areas.

The results of Fig. 6 summarize several BEM calculations in which we have normally loaded elastic self-affine rough surfaces, with λ_s being the shortest wave length in the surface spectrum. Figure 6 shows that the wear coefficient K according to Archard's interpretation reproduces the experimentally [49, 62] observed behavior of mild wear. Specifically, K reaches a plateau implying that there exists a range of loads for which the wear coefficient is independent of load. The wear coefficient introduced in Ref. [29] does not reproduce this behavior, but this is likely due to the constitutive model of the solids in contact, as they are here considered linear elastic, whereas in reality plastic deformations are expected. Another important limitation of this direct interpretation of the wear coefficient is that it does not take into account inelastic interactions between asperities (e.g., crack shielding, third-body contact, plasticity). These were highlighted in a simple 2D context in Section 6. Interactions between contact clusters are certainly even richer in a 3D setting, in which non-convex nearby contact patches may interact through elastic forces and crack shielding

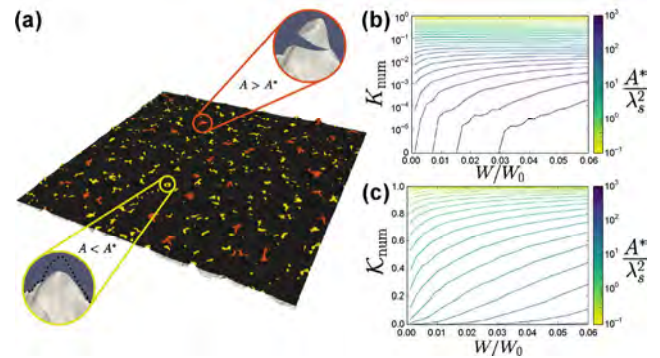


Fig. 6 (a) Multi-asperity contact setting with a fractal rough surface [29]. Yellow clusters are smaller than A^* and deform plastically upon sliding. Red clusters are larger than A^* . (b) shows K , the probability of wear particle formation according to Archard's interpretation. We see that for large values of A^* , K is initially zero, then increases with the load up to a plateau. This is a behavior observed in experiments [49, 62]. (c) shows the wear coefficient according to our model that does not rely on Archard's assumption. In this figure, the wear coefficient also transitions from zero, but increases up to one. This is likely due to the contact model that only considers a purely elastic material.

mechanisms. The question of how to merge these contact patches in an effective contact area A , and in essence of what is an asperity, is far from trivial and is completely neglected in this first attempt. Despite the current limitations of our model, we highlight that mesoscale continuum models provide a remarkably efficient approach to obtain physics-based estimate of wear coefficients. Future models should aim at accounting for plastic deformations, interactions between microcontacts, surface roughness evolution, transport of particles and eventual reattachment or evacuation from the contact interface.

8 Conclusion

We have synthesized our recent theoretical advances towards physics-based modeling of adhesive wear. These advances were made possible by the use of a model atomic potential. Atomic simulations revealed a ductile to brittle transition for large enough contact junction sizes. Small junctions deform plastically, whereas large junctions break to form debris which is transported along the sliding contact interface. The critical length scale at which this transition occurs is a function of the material properties. The junction size also determines the debris particle size at its birth. After

birth, under our idealized condition of full adhesion, the debris particle will continue to grow but at a decreasing rate. We have also shown that interactions between nearby contact junctions are due to crack shielding mechanisms. These interactions become increasingly important at large loads and may explain the change from the mild to the severe wear regime. Finally, we have incorporated some of these findings into a continuum model in order to obtain a deterministic estimation of the wear coefficient used in Archard's wear law.

Clearly, some of the research efforts that were described are still in their infancy. Tribological mechanisms being extremely complex, we make no claims at pretending to present a complete picture of adhesive wear, and in fact we are still a long way from reaching this stage. Perhaps the most pressing efforts should be toward including more materials science in our model. More realistic atomistic potentials should be used. Ageing and alteration of adhesive properties should be accounted for as these are likely to change the long term growth of debris particles. Because these more accurate potentials will come at a larger computational cost than our model potential, the simulations should be conducted on high-performance computing platforms. The influence of sliding velocity and temperature should also be investigated, as well as interactions between contact junctions in a 3D setting. Finally, a lot of room exists for improving the continuum models that we have presented here.

Nonetheless, despite all the current limitations, we emphasize the importance of anchoring tribology research to the fundamentals to make long term progress. Tribology is at a turning point. Current simulation and experimental capabilities give us unprecedented means to revisit empirical wear models with a fresh scientifically-grounded look.

Open Access: The articles published in this journal are distributed under the terms of the Creative Commons Attribution 4.0 International License (<http://creativecommons.org/licenses/by/4.0/>), which permits unrestricted use, distribution, and reproduction in any medium, provided you give appropriate credit to the original author(s) and the source, provide a link to the Creative Commons license, and indicate if changes were made.

References

- [1] Meng H C, Ludema K C. Wear models and predictive equations: their form and content. *Wear* **181–183**: 443–457 (1995)
- [2] Hatchett C, ESQ F R S. IV. Experiments and observations on the various alloys, on the specific gravity, and on the comparative wear of gold. Being the substance of a report made to the Right Honourable the Lords of the Committee of Privy Council, appointed to take into consideration the state of the coins of this Kingdom, and the present establishment and constitution of his Majesty's Mint. *Phil Trans R Soc Lond* **93**: 43–194 (1803)
- [3] Archard J F. Contact and rubbing of flat surfaces. *J Appl Phys* **24**(8): 981–988 (1953)
- [4] Schirmeisen A. Wear: One atom after the other. *Nat Nanotechnol* **8**(2): 81–82 (2013)
- [5] Rabinowicz E. *Friction and Wear of Materials*. New York (USA): Wiley, 1995.
- [6] Ewen J P, Gattinoni C, Thakkar F, Morgan N, Spikes H A, Dini D. Nonequilibrium molecular dynamics investigation of the reduction in friction and wear by carbon nanoparticles between iron surfaces. *Tribol Lett* **63**(3): 38 (2016)
- [7] Onodera T, Martin J M, Minfray C, Dassenoy F, Miyamoto A. Antiwear chemistry of ZDDP: coupling classical md and tight-binding quantum chemical md methods (TB-QCMD). *Tribol Lett* **50**(1): 31–39 (2013)
- [8] Stoyanov P, Romero P A, Merz R, Kopnarski M, Stricker M, Stemmer P, Dienwiebel M, Moseler M. Nanoscale sliding friction phenomena at the interface of diamond-like carbon and tungsten. *Acta Mater* **67**: 395–408 (2014)
- [9] Pastewka L, Moser S, Gumbsch P, Moseler M. Anisotropic mechanical amorphization drives wear in diamond. *Nat Mater* **10**(1): 34–38 (2011)
- [10] Sha Z, Branicio P, Pei Q X, Sorkin V, Zhang Y W. A modified tersoff potential for pure and hydrogenated diamond-like carbon. *Comput Mater Sci* **67**: 146–150 (2013)
- [11] Hu X L, Altoe M V P, Martini A. Amorphization-assisted nanoscale wear during the running-in process. *Wear* **370–371**: 46–50 (2017)
- [12] Cundall P A, Strack O D L. A discrete numerical model for granular assemblies. *Géotechnique* **29**(1): 47–65 (1979)
- [13] Renouf M, Massi F, Fillot N, Saulot A. Numerical tribology of a dry contact. *Tribol Int* **44**(7–8): 834–844 (2011)
- [14] Fillot N, Jordanoff I, Berthier Y. Wear modeling and the third body concept. *Wear* **262**(7–8): 949–957 (2007)
- [15] Jacobs T D B, Gotsmann B, Lantz M A, Carpick R W. On the application of transition state theory to atomic-scale wear. *Tribol Lett* **39**(3): 257–271 (2010)

- [16] Bhaskaran H, Gotsmann B, Sebastian A, Drechsler U, Lantz M A, Despont M, Jaroenapibal P, Carpick R W, Chen Y, Sridharan K. Ultralow nanoscale wear through atom-by-atom attrition in silicon-containing diamond-like carbon. *Nat Nanotechnol* **5**(3): 181–185 (2010)
- [17] Gotsmann B, Lantz M A. Atomistic wear in a single asperity sliding contact. *Phys Rev Lett* **101**(12): 125501 (2008)
- [18] Sato T, Ishida T, Jalabert L, Fujita H. Real-time transmission electron microscope observation of nanofriction at a single asperity. *Nanotechnology* **23**(50): 505701 (2012)
- [19] Merkle A P, Marks L D. Liquid-like tribology of gold studied by *in situ* TEM. *Wear* **265**(11–12): 1864–1869 (2008)
- [20] Vahdat V, Grierson D S, Turner K T, Carpick R W. Mechanics of interaction and atomic-scale wear of amplitude modulation atomic force microscopy probes. *ACS Nano* **7**(4): 3221–3235 (2013)
- [21] Chung K H. Wear characteristics of atomic force microscopy tips: A review. *Int J Precis Eng Manuf* **15**(10): 2219–2230 (2014)
- [22] De Barros Bouchet M I, Matta C, Vacher B, Le-Mogne T, Martin J M, von Lautz J, Ma T, Pastewka L, Otschik J, Gumbsch P, Moseler M. Energy filtering transmission electron microscopy and atomistic simulations of tribo-induced hybridization change of nanocrystalline diamond coating. *Carbon* **87**: 317–329 (2015)
- [23] Stoyanov P, Romero P A, Järvi T T, Pastewka L, Scherge M, Stemmer P, Fischer A, Dienwiebel M, Moseler M. Experimental and numerical atomistic investigation of the third body formation process in dry tungsten/tungsten-carbide tribo couples. *Tribol Lett* **50**(1): 67–80 (2013)
- [24] Liu J J, Notbohm J K, Carpick R W, Turner K T. Method for characterizing nanoscale wear of atomic force microscope tips. *ACS Nano* **4**(7): 3763–3772 (2010)
- [25] Chung K H, Kim D E. Fundamental investigation of micro wear rate using an atomic force microscope. *Tribol Lett* **15**(2): 135–144 (2003)
- [26] Aghababaei R, Warner D H, Molinari J F. Critical length scale controls adhesive wear mechanisms. *Nat Commun* **7**: 11816 (2016)
- [27] Aghababaei R, Warner D H, Molinari J F. On the debris-level origins of adhesive wear. *Proc Natl Acad Sci USA* **114**(30): 7935–7940 (2017)
- [28] Aghababaei R, Brink T, Molinari J F. Asperity-level origins of transition from mild to severe wear. *Phys Rev Lett* **120**(18): 186105 (2018)
- [29] Frérot L, Aghababaei R, Molinari J F. A mechanistic understanding of the wear coefficient: From single to multiple asperities contact. *J Mech Phys Solids* **114**: 172–184 (2018)
- [30] Spijker P, Anciaux G, Molinari J F. Dry sliding contact between rough surfaces at the atomistic scale. *Tribol Lett* **44**(2): 279–285 (2011)
- [31] Sørensen M R, Jacobsen K W, Stoltze P. Simulations of atomic-scale sliding friction. *Phys Rev B* **53**(4): 2101–2113 (1996)
- [32] Zhong J, Shakiba R, Adams J B. Molecular dynamics simulation of severe adhesive wear on a rough aluminum substrate. *J Phys D: Appl Phys* **46**(5): 055307 (2013)
- [33] Sha Z D, Sorkin V, Branicio P S, Pei Q X, Zhang Y W, Srolovitz D J. Large-scale molecular dynamics simulations of wear in diamond-like carbon at the nanoscale. *Appl Phys Lett* **103**(7): 073118 (2013)
- [34] Morse P M. Diatomic molecules according to the wave mechanics. II. vibrational levels. *Phys. Rev.* **34**(1): 57–64 (1929)
- [35] Oliver W C, Pharr G M. An improved technique for determining hardness and elastic modulus using load and displacement sensing indentation experiments. *J Mater Res* **7**(6): 1564–1583 (1992)
- [36] Luan B Q, Robbins M O. The breakdown of continuum models for mechanical contacts. *Nature* **435**(7044): 929–932 (2005)
- [37] Mo Y F, Turner K T, Szlufarska I. Friction laws at the nanoscale. *Nature* **457**(7233): 1116–1119 (2009)
- [38] Mo Y F, Szlufarska I. Roughness picture of friction in dry nanoscale contacts. *Phys Rev B* **81**(3): 035405 (2010)
- [39] Ziegenhain G, Urbassek H M, Hartmaier A. Influence of crystal anisotropy on elastic deformation and onset of plasticity in nanoindentation: A simulational study. *J Appl Phys* **107**(6): 061807 (2010)
- [40] Ashby M F, Jones D R H. *Engineering Materials*. Oxford (UK): Pergamon, 1980.
- [41] Plimpton S. Fast parallel algorithms for short-range molecular dynamics. *J Comput Phys* **117**(1): 1–9 (1995)
- [42] Rabinowicz E. Influence of surface energy on friction and wear phenomena. *J Appl Phys* **32**(8): 1440–1444 (1961)
- [43] Rabinowicz E. The effect of size on the looseness of wear fragments. *Wear* **2**(1): 4–8 (1958)
- [44] Rice J R. Dislocation nucleation from a crack tip: An analysis based on the Peierls concept. *J Mech Phys Solids* **40**(2): 239–271 (1992)
- [45] Griffith A A. VI. The phenomena of rupture and flow in solids. *Philos Trans R Soc A Math Phys Eng Sci* **221**(582–592): 163–198 (1921)
- [46] Tao Z, Bhushan B. Surface modification of AFM silicon probes for adhesion and wear reduction. *Tribol Lett* **21**(1): 1–16 (2006)

- [47] Jacobs T D B, Carpick R W. Nanoscale wear as a stress-assisted chemical reaction. *Nat Nanotechnol* **8**(2): 108–112 (2013)
- [48] Bhushan B, Sundararajan S. Micro/nanoscale friction and wear mechanisms of thin films using atomic force and friction force microscopy. *Acta Mater* **46**(11): 3793–3804 (1998)
- [49] Burwell J T, Strang C D. On the empirical law of adhesive wear. *J Appl Phys* **23**(1): 18–28 (1952)
- [50] Holm R. Frictional wear in metallic contacts without current. In *Electric Contacts*. Holm R, Ed. Berlin, Heidelberg (Germany): Springer, 1946: 232–242.
- [51] Uetz H, Föhl J. Wear as an energy transformation process. *Wear* **49**(2): 253–264 (1978)
- [52] Reye T. Zur theorie der zapfenreibung. *J Der Civilingenieur* **4**: 235–255 (1860)
- [53] Popov V L, Pohrt R, Li Q. Strength of adhesive contacts: Influence of contact geometry and material gradients. *Friction* **5**(3): 308–325 (2017)
- [54] McFarlane J S, Tabor D. Adhesion of solids and the effect of surface films. *Proc R Soc A Math Phys Eng Sci* **202**(1069): 224–243 (1950)
- [55] Pastewka L, Robbins M O. Contact between rough surfaces and a criterion for macroscopic adhesion. *Proc Natl Acad Sci USA* **111**(9): 3298–3303 (2014)
- [56] Persson B N J. Elastoplastic contact between randomly rough surfaces. *Phys Rev Lett* **87**(11): 116101 (2001)
- [57] Stachowiak G P, Stachowiak G W, Podsiadlo P. Automated classification of wear particles based on their surface texture and shape features. *Tribol Int* **41**(1): 34–43 (2008)
- [58] Queener C A, Smith T C, Mitchell W L. Transient wear of machine parts. *Wear* **8**(5): 391–400 (1965)
- [59] Komvopoulos K, Choi D H. Elastic finite element analysis of multi-asperity contacts. *J Tribol* **114**(4): 823–831 (1992)
- [60] Caroli C, Nozières P. Hysteresis and elastic interactions of microasperities in dry friction. *Eur Phys J B* **4**(2): 233–246 (1998)
- [61] Bowden F P, Tabor D. The area of contact between stationary and between moving surfaces. *Proc R Soc A Math Phys Eng Sci* **169**(938): 391–413 (1939)
- [62] Archard J F, Hirst W. The wear of metals under unlubricated conditions. *Proc R Soc A Math Phys Eng Sci* **236**(1206): 397–410 (1956)
- [63] Lim S C, Ashby M F. Overview no. 55 wear-mechanism maps. *Acta Metall* **35**(1): 1–24 (1987)
- [64] Kitsunai H, Kato K, Hokkirigawa K, Inoue H. The transitions between microscopic wear modes during repeated sliding friction observed by a scanning electron microscope tribosystem. *Wear* **135**(2): 237–249 (1990)
- [65] Hokkirigawa K. Wear mode map of ceramics. *Wear* **151**(2): 219–228 (1991)
- [66] Wang Y S, Hsu S M. Wear and wear transition modeling of ceramics. *Wear* **195**(1–2): 35–46 (1996)
- [67] Adachi K, Kato K, Chen N. Wear map of ceramics. *Wear* **203–204**: 291–301 (1997)
- [68] Zhang J, Alpas A. Transition between mild and severe wear in aluminium alloys. *Acta Mater* **45**(2): 513–528 (1997)
- [69] Kato K, Adachi K. Wear of advanced ceramics. *Wear* **253**(11–12): 1097–1104 (2002)
- [70] Hsu S M, Shen M. Wear prediction of ceramics. *Wear* **256**(9–10): 867–878 (2004)
- [71] Wang S Q, Wang L, Zhao Y T, Sun Y, Yang Z R. Mild-to-severe wear transition and transition region of oxidative wear in steels. *Wear* **306**(1–2): 311–320 (2013)
- [72] Murakami Y. *Stress Intensity Factors Handbook*. New York (USA): Pergamon Press, 1987.



Jean-François MOLINARI. He is the director of the Computational Solid Mechanics Laboratory (LSMS) at the École Polytechnique Fédérale de Lausanne (EPFL), Switzerland. He graduated in 1997 with a MS degree in mechanical engineering from the University of Technology of Compiègne,

France. He also obtained a MS degree in aeronautics in 1997 from the California Institute of Technology, USA, and graduated with a PhD degree from Caltech in 2001. He then held professor positions at the Johns Hopkins University, USA, and ENS Cachan, France, before joining EPFL. His research interests cover multiscale modeling with applications to fracture mechanics and tribology.



Ramin AGHABABAEI. He obtained his PhD degree in mechanical engineering from National University of Singapore (NUS) in 2012. He joined the Computational Solid Mechanics Laboratory (LSMS) at École Polytechnique Fédérale of Lausanne (EPFL) as a post-doctoral fellow. In September 2017, he joined the Engineering Department of Aarhus

University in Denmark, as a tenure-track assistant professor, and the principle investigator of the surface mechanics group (SMG). The research interest of his group is to understand the underlying mechanics and physics of failure in materials surfaces at different scales with application to tribology and manufacturing.



Tobias BRINK. He received his doctoral degree in materials science from the Technische Universität Darmstadt, Germany. He is currently working at the Computational Solid Mechanics Laboratory (LSMS) at the École Polytechnique Fédérale

of Lausanne (EPFL) in Switzerland on atomistic simulations of wear at the asperity level. In this context, his research interests include working towards understanding nano-scaled wear mechanisms and how they result in macroscopic wear relations.



Lucas FRÉROT. He holds a bachelor of science and a master of science in civil engineering from the École Polytechnique Fédérale de Lausanne (EPFL), with a focus on computational methods in the modeling

of solids and structures. He joined the Computational Solid Mechanics Laboratory at EPFL in 2015 as a PhD student to conduct research on the elasto-plastic contact of solids with rough surfaces, with application to the study of friction and wear.



Enrico MILANESE. He trained as a civil engineer at the University of Padua, Italy, where he received both his bachelor and master degrees. He later investigated fracture avalanche behaviour in porous media at the

same university. Since 2016 he is pursuing a PhD at the Computational Solid Mechanics Laboratory at the École Polytechnique Fédérale of Lausanne (EPFL), Switzerland. His current research focusses on surface roughness and adhesive wear.

Adhesive wear and particle emission: Numerical approach based on asperity-free formulation of Rabinowicz criterion

Valentin L. POPOV^{1,2,*}, Roman POHRT^{1,*}

¹ Institute of Mechanics, Technische Universität Berlin, Berlin 10623, Germany

² National Research Tomsk State University, Tomsk 634050, Russia

Received: 05 April 2018 / Revised: 02 July 2018 / Accepted: 31 July 2018

© The author(s) 2018. This article is published with open access at Springerlink.com

Abstract: In 1953 Archard formulated his general law of wear stating that the amount of worn material is proportional to the normal force and the sliding distance, and is inversely proportional to the hardness of the material. Five years later in 1958, Rabinowicz suggested a criterion determining the minimum size of wear particles. Both concepts became very popular due to their simplicity and robustness, but did not give thorough explanation of the mechanisms involved. It wasn't until almost 60 years later in 2016 that Aghababaei, Warner and Molinari (AWM) used quasi-molecular simulations to confirm the Rabinowicz criterion. One of the central quantities remained the "asperity size". Because real surfaces have roughness on many length scales, this size is often ill-defined. The present paper is devoted to two main points: First, we generalize the Rabinowicz-AWM criterion by introducing an "asperity-free" wear criterion, applicable even to fractal roughness. Second, we combine our generalized Rabinowicz criterion with the numerical contact mechanics of rough surfaces and formulate on this basis a deterministic wear model. We identify two types of wear: one leading to the formation of a modified topography which does not wear further and one showing continuously proceeding wear. In the latter case we observe regimes of least wear, mild wear and severe wear which have a clear microscopic interpretation. The worn volume in the region of mild wear occurs typically to be a power law of the normal force with an exponent not necessarily equal to one. The method provides the worn surface topography after an initial settling phase as well as the size distribution of wear particles. We analyse different laws of interface interaction and the corresponding wear laws. A comprehensive parameter study remains a task for future research.

Keywords: adhesion; plasticity; wear; Archard's law of wear; Rabinowicz criterion; wear particle emission; surface topography; boundary element method (BEM)

1 Introduction

Wear is one of the most important tribological phenomena in practice, affecting the function and the life time of many mechanical systems. It is a key factor in technical safety and determines maintenance costs of many mechanical parts [1] in motion. Wear affects parts not only in machines and mechanical constructions, but also in medicine: many implants, especially artificial joints, which have to be replaced

after approximately 10 years of service [2] due to wear. The critical issue with wear can be the change of shape and function of a system or the fate and behavior of the material removed in form of wear particles. Indeed, the emission of wear particles into the environment increasingly threatens human health and ecology [3]. When controlled, wear is integral to many methods of manufacturing and material processing such as grinding, polishing or sandblasting [4]. Many areas of technology and medicine are

* Corresponding author: Valentin L. POPOV, E-mail: v.popov@tu-berlin.de; Roman POHRT, E-mail: roman.pohrt@tu-berlin.de

strongly interested in controlling wear by increasing or decreasing it depending on the particular application.

Despite its importance, wear remains one of the least scientifically understood tribological phenomena. This is in part due to the complexity of the processes influencing wear. These include contact, plasticity, crack nucleation and propagation, chemical reactions, material mixing and material transfer between contact partners and lubricants as well as the formation of surface layers. Wear is directly connected to the very broad problem of the tribological “third body”. For most aspects of friction, wear is not only a consequence but also a major influencing factor [5].

For wear calculations, the most common prediction is simply that the wear volume is proportional to the normal force and sliding distance. As an empirical assumption, this law was suggested by Reye as early as 1860 [6] but it took almost a century for wear laws to be based on models of particular conditions and to be experimentally validated. In the 1950s, Kruschov conducted extensive experimental studies on *abrasive* wear of metals [7, 8]. Approximately at the same time, Archard carried out his classical studies of contact mechanics of rough metal surfaces in unlubricated conditions [9, 10] and formulated his famous wear law based on prior works of Holm and Burwell. Today this type of wear would be referred to as *adhesive* wear. Interestingly, both laws of Kruschov and Archard have the same mathematical form and state that the worn volume V is proportional to the normal force F_N and the sliding distance s and inversely proportional to the hardness σ_0 of the softer material:

$$V = k \frac{F_N s}{\sigma_0} \quad (1)$$

The constant k is the so called wear coefficient, whether adhesive or abrasive.

In the case of abrasive wear, the wear coefficient has a relatively clear physical interpretation based on the idea of micro-cutting of the softer material by the asperities of the harder counterpart [11]. The coefficient of abrasive wear is thus relatively well defined and ranges from approximately 10^{-3} to 10^{-2} . It is least when “three-body” wear occurs, e.g., two metallic parts with loose abrasive particles in between

them, and is most severe for “two-body” abrasive wear, like a metal piece in contact with sandpaper [11].

In the case of adhesive wear, no clear physical interpretation of the wear coefficient exists. Archard did only suggest a first idea of the *probability* that two impacting asperities will form a wear particle. In the following 50 years, there was only little progress in formulating physical, model-based criteria for the adhesive wear coefficient. Empirically measured values of the adhesive wear coefficient are known to differ by 5 decimal orders of magnitude and also to depend on the type of materials [11]. This fact makes Eq. (1) a very poor predictor for the wear behavior of a general or unknown tribological system. While the dependencies on the normal force and the sliding distance may be approximately valid for any given system in a limited range of loads, the inverse proportionality of wear volume to hardness loses direct sense. There is a widespread opinion that the higher the hardness, the lower the wear, because the hardness is in the denominator of Archard’s equation. However, Kragelsky [12] formulated the exact opposite principle for minimizing wear—the principle of a positive hardness gradient. According to it, the hardness at surface layers must be less than inside the bulk body in order to avoid catastrophic wear. In Ref. [13], more complicated dependencies of wear rate on hardness are discussed, including inverse dependencies. A very good review of different modes of wear as well as transitions between mild and catastrophic wear is given in Ref. [14] with the conclusion that “no single predictive equation or group of limited equations could be found for general and practical use”. Regrettably, this conclusion, made in 1995, remained mostly valid until today.

In the last few years some ideas emerged which allow a new understanding of the physics of wear. As happens so often in the history of science, recent developments just shed new light on old principles. Aghababaei, Warner and Molinari (AWM) [15] used an artificial model potential to enable simulation in relevant length scale in the frame of quasi-molecular dynamics simulations. Dimaki et al. [16] implemented a mesh-dependent fracture criterion to achieve the same in the discrete element method.

The findings of AWM confirmed an old idea that

was put forward by Rabinowicz in 1958 [17]. In the criterion of Rabinowicz and the AWM simulations, the interplay of plasticity and adhesion leads to the emergence of a characteristic length controlling wear: If a micro contact is smaller than the characteristic length, then it will be plastically deformed; if it is larger than the characteristic length, a wear particle will emerge. The existence of these two scenarios has also been observed in recent molecular dynamics simulations [18]. Combined with advanced numerical simulation methods of contact between rough surfaces [19], this new understanding advances the old idea of Rabinowicz to a new paradigm [19, 20] in the science of wear. Frérot, Aghababaei and Molinari [21] re-interpreted Archard's probability of a given wear particle to actually emerge as the probability to encounter an asperity contact capable of forming a wear particle, according to the deterministic Rabinowicz-AWM criterion [20]. For the first time this concept allowed a microscopic, model-based understanding of the adhesive wear coefficient.

While this concept has enormous attractiveness, it also has an essential shortcoming: just as the original Rabinowicz criterion, it is based on the analysis of a single "asperity". However, it is widely recognized that the notion of asperity is poorly defined for real surfaces having roughness on many length scales. Molecular dynamic simulations of only two neighboring surface peaks show that they can behave as one single asperity if the distance between them is small enough [21, 22]. The authors of Refs. [23, 24] attempted, based on the idea of Rabinowicz, to formulate an asperity-free criterion of forming wear debris. The present paper can be considered a practical numerical implementation of the ideas formulated in Refs. [20, 23, 24]. Based on the asperity-free generalized Rabinowicz criterion, we develop a model describing the formation of wear particles and the evolution of the surface topography.

The paper is organized as follows. In Section 2, we shortly recapitulate the original arguments of Rabinowicz as well as the concept of the asperity free wear criterion formulated in Refs. [23, 24]. In Section 3, we use the asperity-free concept for designing a model of wear processes. Section 4 gives the results of simulations using the formulated wear model. In

Section 5, we discuss the transitions between the stages least wear, mild wear and severe wear which have already been discussed by Rabinowicz and are also found in our simulations. Finally, in Section 6, we present the main conclusions.

2 Generalized Rabinowicz criterion for formation of wear debris

We start with the reproduction of the original Rabinowicz criterion [11, 17, 25]. Consider two micro heterogeneities colliding and forming a welded bridge, as suggested in the well-known generic picture of dry friction suggested by Bowden and Tabor [26] (see Fig. 1).

The maximum stress that can be achieved in the welded contact is of the order of the material hardness σ_0 . The stored elastic energy U_{el} can thus be estimated as the product of characteristic energy density $\sigma_0^2 / (2G)$ and the characteristic stressed volume D^3 :

$$U_{el} \approx \frac{\sigma_0^2}{2G} D^3 \quad (2)$$

where G is the shear modulus and D the characteristic size (diameter) of the joint. If a wear particle was formed, this energy would relax. The process of detaching a wear particle can only occur if the stored elastic energy exceeds the energy needed to create new free surfaces

$$U_{adh} \approx \Delta w \cdot D^2 \quad (3)$$

Here Δw is the work of adhesion per unit area. It follows that only particles larger than some critical size D_{crit} can be detached:

$$D > D_{crit} = \frac{2G \cdot \Delta w}{\sigma_0^2} \quad (4)$$

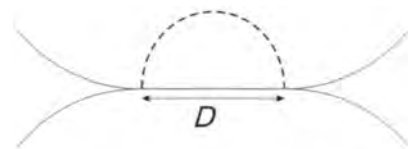


Fig. 1 Welded joint of size D created due to impact and consecutive shear of two asperities.

Note that this equation predicts only the existence of a *lower bound* of the size of wear particles. Possible mechanisms suppressing the appearance of too large particles will be discussed later in this paper (see Sections 3.3 and 5.).

According to Rabinowicz, the key quantity governing the formation of wear particles is D , the “asperity size”, which is poorly defined for real surfaces having fractal character [27]. Looking at a contact configuration of bodies with fractal rough surfaces as shown in Fig. 2, we see loosely connected clusters of contact areas instead of separated asperities. A thoughtful look at the logic behind the Rabinowicz criterion reveals that the notion of a single asperity is in fact not necessary for the application of this logic. Below we describe the basic idea (as first suggested in Refs. [23, 24]) of how an energy based wear criterion can be formulated without it.

In Fig. 2, the contact of an elastic half-space and a rough surface is shown. The topography was generated as described in Ref. [28] with roughness having the Hurst exponent 0.7. Using the BEM implementations as described in Ref. [19] or Ref. [29], the stress distribution at the interface can be calculated according to a particular assumption for the interaction in the contact surface, e.g., a constant coefficient of friction, some given tangential flow stress or adhesive interaction. In Fig. 2(b), the distribution of normal stress is shown but similar distributions can be easily produced for all stress components.

The central idea of the generalized Rabinowicz criterion is the following: Consider a circular region with *arbitrary* diameter D centered at an *arbitrary* point of the contact interface. In Fig. 2(b), several examples

of such regions with different positions and different diameters are shown with white circles. If a wear particle of diameter D is formed at that particular position, then the surface stresses in the chosen region will vanish. This leads to the release of the elastic energy U_{el} which can be estimated with the same BEM program (description of procedure see next section). Following the logic of Rabinowicz, the wear particle can only be formed if

$$U_{el} > \frac{\pi}{4} D^2 \Delta w \quad (5)$$

Thus, probing each surface point with circles of varying diameter, we can always assess whether the formation of a wear particle at the given position and with the given size is possible. Note that this criterion is completely independent on the notion of “asperity”. It can be applied to an arbitrary contact configuration, stress distribution and even to positions which are not part of the actual contact zone. Equation (5) identifies parts of material that *can* detach due to the elastic energy stored in the corresponding zone. Just like the original Rabinowicz criterion, Eq. (5) does not state *whether* the process of detachment will really take place. However, molecular simulations of AWM [15] strongly suggest that it is reasonable to equate the possibility and the actual occurrence of wear debris formation: In the following, we will assume that particles which can be produced energetically will indeed realize this possibility. In this way, we obtain a constructive rule to the formation of wear particles and thereby to the process of surface evolution.

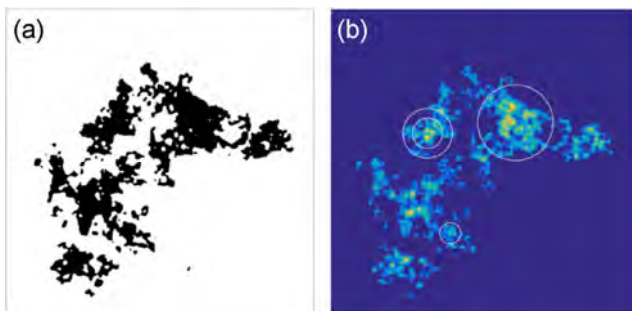


Fig. 2 Numerical simulation of the normal contact between a rough surface and an elastic half-space: (a) contact area at a given indentation depth; (b) pressure distribution in the contact.

3 Minimalistic model of adhesive wear

In this section we describe a simplified, minimalistic model of adhesive wear. Let us start with the contact of a rigid plane surface and an elastic body having a periodic, fractal rough surface characterized by the Hurst Exponent H , lower and upper cut-off wavelengths λ_{long} , λ_{short} and the rms roughness θ . The bodies are first brought into normal contact with average pressure \tilde{p} and then forced into a continuous tangential movement relative to each other. In the present study, we restrict ourselves to purely elastic

normal contact solution—up to the moment of formation of a wear particle. However, the rule for tangential stresses in the interface can be different, for instance it can be based on Coulomb friction or on the assumption of a limiting flow stresses. As was illustrated in Ref. [30], the interface “flow law” can mimic to some extent the material behavior, e.g., plasticity.

The wear model is based on the analysis of the stress distribution in the contact. Only the tangential stress components will be taken into account in this analysis, because pure normal contact does not allow opening cracks—independently of the stress intensity. It is the tangential stress on the surface which is capable of creating conditions for crack nucleation. In the simulations of AWM [15], tangential stress applied to the surface leads to the appearance of tensile stress in a plane inclined approximately 45° to the surface at the trailing end of the contact region; this is what enables crack opening. Of course, the appearance of tensile stress is only one necessary condition for the formation of a wear particle. It is also indispensable that the crack should be able to propagate. This is only the case if enough elastic energy is stored in the material for producing fresh surfaces as described by the Rabinowicz criterion. In the framework of the boundary element method, we do not have the possibility to investigate the process of crack propagation. Following the idea of Rabinowicz-AWM [15], we just assume that if the two above conditions (appearance of tensile stresses and energetic possibility of crack propagation) are fulfilled, then the wear particle will form.

Of course the problem of wear cannot be reduced solely to the formation of wear particles. True wear occurs only when particles have been transported out of the friction zone [31, 32]. During this process they can be integrated again into the surfaces or take part in the process of mass mixing and the formation of surface layers [33]. All these processes are not considered in the present study due to two reasons. First, it is our intention to concentrate in detail on the initial and fundamental sub-process of wear, knowing it is only one part of the series leading to the phenomenon “wear”. Second, there is currently no simple numerical tool available to convincingly simulate the complete chain of wear sub-events. In this study

we thus assume that any formed wear particle will instantly disappear. We are fully aware that in many cases this assumption will be too strong to achieve a correct quantitative prediction of wear but we hope to give a correct qualitative understanding of the main governing parameters of the wear process.

Based on the above explanations, we suggest the following wear model consisting of two main steps.

3.1 Step 1: Determining the location of wear particle initiation and corresponding size

In this first step, the tangential stress distribution is scanned using the criterion (5). Let us discuss this important step in more detail. By dividing (5) by the area $A = \pi/4 D^2$ of a circle with diameter D , we can rewrite this criterion in the form

$$E = \frac{U_{el}}{A} > \Delta w \quad (6)$$

stating that the condition for appearing a wear particle at some position is that the elastic energy density, $E = U_{el} / A$ should exceed the work of adhesion per unit area. We thus start by constructing maps showing the energy density at any position in the contact area. Note that the energy density map should be calculated separately for any diameter D . For the underlying tangential stress, some particular flow law in the interface must be assumed. The following simulations in this section are carried out under the assumption that tangential stress in the contact plane is determined by the Coulomb friction law with a coefficient of friction μ and continuous sliding in all contact points. This translates into the tangential stress distribution τ following the distribution of pressure p :

$$\tau(\vec{x}) = \mu p(\vec{x}) \quad (7)$$

where \vec{x} is a position in the contact plane.

In the framework of the BEM simulation, each calculation step gives the complete distributions for stresses τ and displacements u . The energy which is released by relaxing the stresses inside a circle with diameter D can be readily calculated as

$$U_{el}(\vec{x}) = \frac{1}{2} \int_{A_{\text{Circle}, D}} [u(\vec{x} + \vec{r}) - u^{(0)}(\vec{x} + \vec{r})] \tau(\vec{x} + \vec{r}) d^2 \vec{r} \quad (8)$$

where superscript $^{(0)}$ refers to the stress free state. The integration is carried out over the area of the chosen circle. Scanning point by point the complete computational area, calculating the integral (8) and dividing it by the area A_D , we can produce energy density maps for each position of the circle center as shown in Fig. 3.

The energy density map depends of course on the contact configuration (and thus on the normal load) and on the diameter D of the “probing circle”. Let us first consider the dependency on the diameter. If we take some point in the region of real contact, then increasing D may first lead to increasing the energy density, since the elastic energy stored in a region with homogenous stress is roughly proportional to D^3 . With further increase of the diameter D , the circumference of the circle may leave the region of contact. The stored energy will not increase further, but the denominator A in Eq. (6) still increases, so that the energy density E starts to decrease. We can conclude that when the contact configuration is composed of distinct islands which are not or poorly connected, then the energy density is not a monotonic function of diameter D . This is valid both for each particular point and for the maximum value of the energy density, which is of main interest as it determines the first point of detachment of a wear particle.

To accelerate the construction of the energy density map, we used also an approximate measure. We first determine the average stress in the probe circle $\tilde{\sigma}_D$ which to find is a very simple analytical procedure. The energy density E_D stored due to constant tangential stress in a circle with diameter D is given by

$$E_D = \frac{4D}{3\pi G^*} \tilde{\sigma}_D^2 \quad (9)$$

where $G^* = 4G/(2-\nu)$ is the effective shear modulus.

The results of the evaluation are shown in Fig. 4 in which the normalized energy density $E_D/\Delta w$ is represented as function of D . The shaded area shows the complete interval of energy densities which have been observed in the contact area. Of the main importance is of course the upper boundary of the shaded area showing the maximum energy density for a given D , because it identifies the position where

the condition for forming wear particles is first satisfied. We also show the values of the exact evaluation using Eq. (8) with the black line. When the maximum of the normalized energy density is smaller than 1, formation of wear particle is energetically impossible at any position.

3.2 Step 2: Formation of wear particles

With increasing normal force, the maximum energy density will also increase and the dependency of the normalized energy density on D will touch at some moment the horizontal critical line $E/\Delta w = 1$. The point and the size at which this happens determine unambiguously the position and the size of the wear

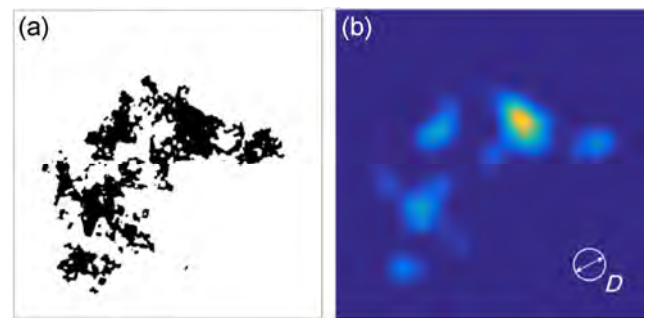


Fig. 3 (a) Contact configuration and (b) the corresponding energy density map for a given diameter D .

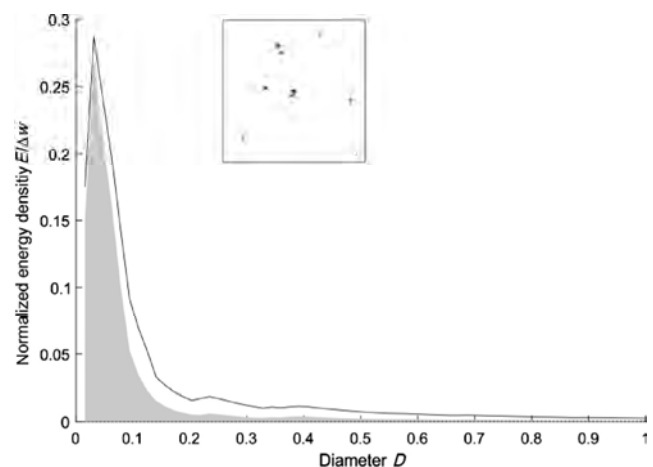


Fig. 4 Dependency of the energy density at the given contact configuration as a function of the diameter D of probing circles. The grey zone is limited by the minimum and maximum values that occur. The contact configuration which has been analyzed is shown in the insert. It was generated using the following parameters: $G^* = 1$, $\nu = 0$, $H = 1$, $L = 1$, $\lambda_{\text{long}} = 1/3$, $\lambda_{\text{short}} = 1/32$, $\tilde{p} = 1/10$, $\Delta w = 1$, $\mu = 0.3$, $\theta = 0.4$.

particle which will be formed. The corresponding wear particle inside the circle with diameter D is then extracted, such that the surface topography is altered from $z_{\bar{x}}$ to $z_{\text{new},\bar{x}}$ according to

$$z_{\text{new},\bar{x}}(\bar{r}) = z_{\bar{x}}(\bar{r}) + \sqrt{1 - 4|\bar{r}|^2} D^{-2} \cdot [\tilde{z}_{\bar{x},D} - z_{\bar{x}}(\bar{r}) - d_D]; \quad (10)$$

$$d_D = 5\theta(0.5D/\lambda_{\text{long}})^H$$

Where $\tilde{z}_{\bar{x},D}$ is the mean height inside the circle region. We chose this particular procedure to ensure that the new surface geometry remains continuous. Figure 5 shows an example of a surface geometry before and after the particle removal. This act closes one cycle of the wear calculation. With the new topography, the stress calculation and energy density evaluation is carried out again and the position and size of the next wear particle is identified, which is detached and extracted again until $E < \Delta w$ in every point.

3.3 The problem of “very large” wear particles and its handling

The described procedure of finding the critical region where a wear particle will be detached following Eq. (6) has a large-particle-paradox. At small normal forces, the contact consists of distinct contact spots as shown in Fig. 4 and the maximum energy density has a pronounced maximum when plotted over D . At higher forces however, the picture changes and resembles Fig. 6.

One can see that when the fraction of area being in contact becomes larger, the energy density in regions with larger D grows. This is an immanent property of any contact of periodic and thus macroscopically flat surfaces. Whatever the particular stress distribution, for large enough probe circles, the surface deformation

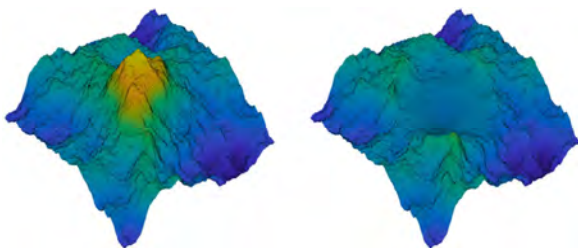


Fig. 5 Topography of a rough surface before and after detachment and disappearance of a wear particle.

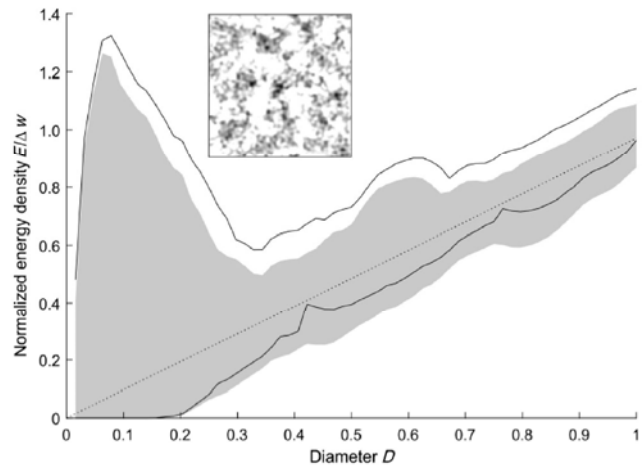


Fig. 6 Illustration of the energy density curve at high forces. Large diameters of probe the circle necessarily lead to large values of E . The mean pressure was chosen as $\bar{p} = 5$, other parameters as in Fig. 4.

and resulting elastic energy inside them resemble the case of homogenous constant stress. The elastic energy scales as D^3 and the corresponding energy density scales as D : it increases linearly with the diameter. Inserting the system’s global average stress $\tilde{\sigma}_{\text{sys}}$ into Eq. (9) we can always find a minimum diameter, where the energy density equals or exceeds the work of adhesion, thus satisfying the detachment criterion. Also one can always find a circle inside the apparent contact area that satisfies $\tilde{\sigma}_D \geq \tilde{\sigma}_{\text{sys}}$. Therefore a catastrophic diameter D_{cat} dependent on the eternal load must exist, which is guaranteed to include enough energy to generate a wear particle.

$$D_{\text{cat}} = \frac{3\pi G^* \Delta w}{4 \tilde{\sigma}_{\text{sys}}^2} \quad (11)$$

This “problem of large particles” is not new; it existed already in the original Rabinowicz criterion, which predicts only the existence of a lower bound of the size of wear particles. A possible mechanism suppressing the appearance of arbitrary large particles was suggested in Ref. [30] and is based on the Rabinowicz criterion itself. If some particle has a size much larger than prescribed by the Rabinowicz criterion (4), then it is energetically favorable for it to disintegrate into smaller ones. This means that particles with the size substantially larger than the Rabinowicz-AWM critical length can never practically

appear. In the present study we enforced this property by formally bounding the particle size by a fixed maximum value.

4 Wear process and development of worn surface topography

Depending on the initial topography, the wear properties of contact partners and the character of interaction in the interface, two basic scenarios of wear are possible. In the first scenario, the wear process alters the surface topography in such way that after an initial phase, no more wear occurs. Instead, the new topography makes the applied load distributed in such a way, that our local wear criterion cannot be satisfied anywhere on the surface. Because of the foregoing wear process leading to new steady-state of no wear, we will refer to this scenario as the “settling” type of wear. The general principle of a surface geometry changing towards a state of no-wear is known from fretting wear. Here small oscillatory tangential displacements wear off material where it is most harshly stressed [34, 35].

On the other hand, one can have continuously proceeding wear. We start with an example of the settling type of wear.

4.1 Wear of “settling” type

We consider the contact between a wear-resistant smooth plane and a rough counterpart where the wear takes place. In the contact interface, we assume Coulomb friction and complete sliding, so that the tangential stress at the surface is proportional to the local normal stress, see Eq. (7). The elastic energy stored in a circle of diameter D with average normal pressure \tilde{p}_D can be estimated with the help of Eq. (9)

$$E_D \approx \frac{4D}{3\pi G^*} (\mu \tilde{p}_D)^2 \tag{12}$$

As one of the counterparts does not change its configuration, a situation is possible that after a number of particle detachment events, the stress will be re-distributed in such a way that no further particles can form. In this case, wear occurs solely during a finite time of “settling”. Afterwards, the surface topography remains stable. Figure 7 shows a sample

surface before and after being subjected to such wear process. Because the opposing flat surface does not wear out, no directional dependence is visible in the wear marks of the worn rough surface in Fig. 7(b).

In every step, we record the sizes of the particles for analysis. With assumed Coulomb law of friction in the interface, the stresses are not bounded by plastic deformation. Thus, arbitrarily small particles can be produced. Simulations show that most of the particles are indeed of the minimal size, given by the grid resolution. Looking at the distribution of the worn volume V , estimated as a spherical particles

$$V = \sum_D n_D \frac{4}{3} \pi D^3 \tag{13}$$

we find a more equal dependency, see Fig. 8. Here n_D is the number of particles with size D .

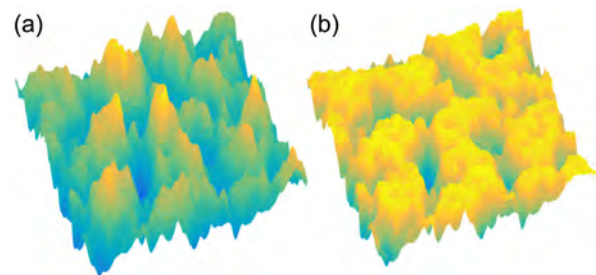


Fig. 7 Illustration of a rough surface (a) and its worn state (b) according to the rules described in Sec. 4.1. It was generated using the following parameters: $G^* = 1$, $\nu = 0$, $H = 1$, $L = 1$, $\lambda_{\text{long}} = 1/3$, $\lambda_{\text{short}} = 1/32$, $\theta = 0.4$, $\tilde{p} = 1/2$, $\Delta w = 1/100$, $\mu = 0.3$.

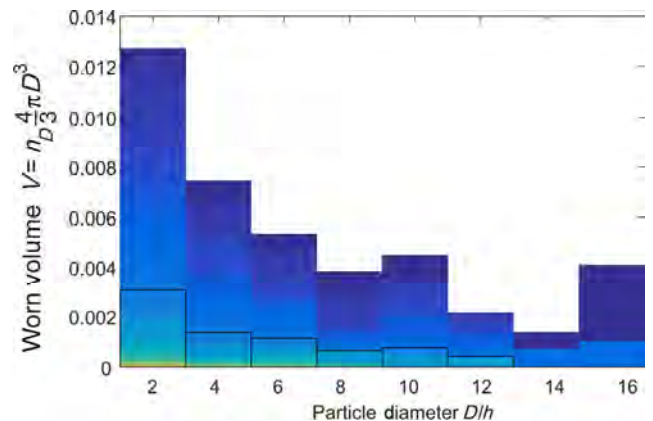


Fig. 8 Histogram of the wear volume of 6986 particles as a function of the particle size (given in terms of the computational grid spacing Δ). No particle larger than $D = 16\Delta$ occurred. Different colors mark different force levels up to $\tilde{p} = 1/2$, see the black boxed series for instance, other parameters as in Fig. 7.

In the final state, both the topography of the worn surface and the overall wear volume depend on the normal loading. In this study we will confine ourselves to the analysis of the total worn volume as a function of the increasing applied load. This is given in Fig. 9. The worn volume can be approximated by a power-law dependency of the average pressure with the exponent 1.4:

$$V \propto \tilde{p}^{1.4}, \tag{5}$$

See the dotted line in Fig. 9.

4.2 Continuous wear in contact of two rough surfaces

As a second example, let us consider the same problem as in the preceding section with the only difference that now the rough body is rigid and the smooth counterpart wears out. As before, we assume the tangential stresses to be proportional to the normal pressure. In numeric experiments a rough rigid surface was moved tangentially over an initially smooth surface.

We investigated the worn volume for the same rough topography for a series of increasing normal pressures. Figure 10 shows resulting topographies of this process for two different average pressures. For each time step corresponding to a certain distance covered, we recorded the worn volume of all particles that were generated. Figure 11 shows a typical evolution of the worn volume. It is practically linear with the

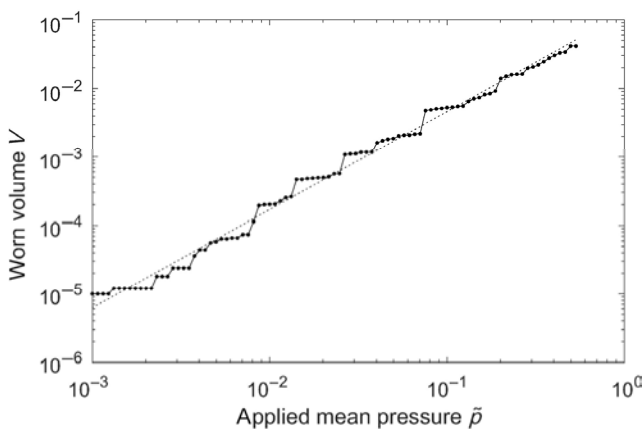


Fig. 9 Dependency of the settled worn volume as a function of the applied external load. In this case, the wear volume does not depend on the distance covered but occurs instantaneously for any given load, parameters as in Fig. 7.

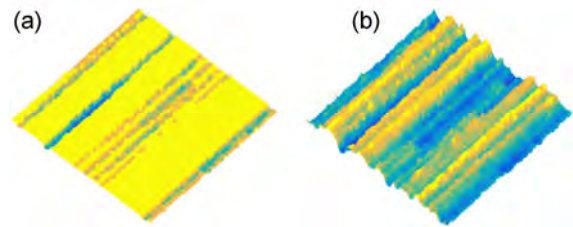


Fig. 10 Two initially smooth surfaces after being subjected to wear as described in Sec. 4.2 with a rough counterpart similar to Fig. 7(a). (a) At light load $\tilde{p} = 0.01$, many contacts slide but do not generate particles and the surface remains undamaged at these spots. (b) With more severe loading at $\tilde{p} = 0.1$, a larger part of the surface is worn. Other parameters as in Fig. 4.

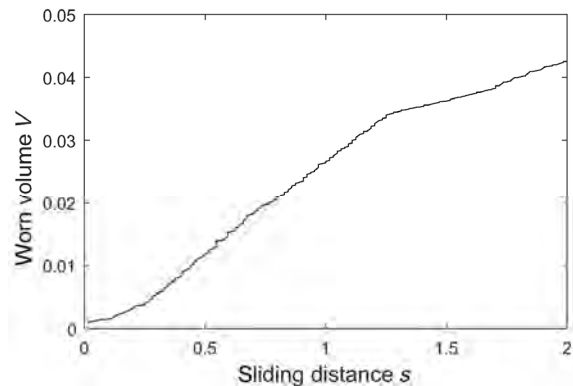


Fig. 11 Dependency of the worn volume as a function of the sliding distance covered. Mean pressure was $\tilde{p} = 1$ (circled value in Fig. 12), other parameters as in Fig. 4.

factor depending on the exact contact configuration in the corresponding instant. We expect the behavior to be more homogenous with smaller λ_{long} , when a greater number of isolated peaks determine the surface topography. Averaging over the complete distance covered ($2L$) one can define a specific worn volume per unit length. Figure 12 displays the corresponding dependency on the applied mean pressure and a power-law fit. We found the wear volume worn by distance to scale as

$$V \propto \tilde{p}^{1.77} \tag{15}$$

which strongly deviates from Archard’s and Krushev’s law.

Note that the worn surface (Fig. 6(b)) has pronounced grooves.

This appearance is usually considered a sign of abrasive wear. However, in the present case we consider pure adhesive wear: there are no processes like micro-cutting or ploughing.

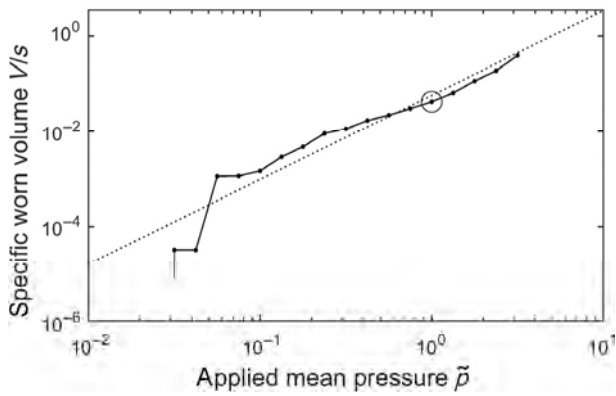


Fig. 12 Dependency of the wear volume per distance as a function of the applied external load. Parameters as in Fig. 4.

4.3 Wear of a rigid rough surface and a rough elastic surface with constant tangential flow stress in the contact region

In this section, we assume that tangential stress in the contact is constant and equal to σ_0 . This case is the most important so far as it mimics most correctly the mechanism of wear of ductile materials like metals. The assumption of a constant flow stress mimics the behavior of elastic-ideally plastic materials [30]. Due to the final flow stress, tangential stresses are now bounded by σ_0 , in much the same way as assumed in the criterion of Rabinowicz. In this case we again have continuous wear. The wear volume, normalized by distance covered is shown in Fig. 13 as a function of the applied load.

After achieving the conditions for wear for the first time, the wear volume increases continually with load. This is the classical region of adhesive mild wear. In this region, the worn volume follows the power-law dependency

$$V \propto \tilde{p}^{1.36} \tag{16}$$

Note that because the wear volume is not proportional to the normal force, Archard’s law is not directly confirmed. However, the exponent 1.36 is close to one and in some finite force intervals the dependency can be considered as approximately linear. Indeed, the non-linear dependencies of worn volume on the normal force in the case of large force interval are well known and have been reported as early as the 1970s [36].

5 Transitions between least wear, mild wear and severe wear

Let us discuss the transitions between the three stages least wear, mild wear and severe wear, as introduced by Rabinowicz [37]. The condition of least wear has a simple physical meaning which basically was already described by Rabinowicz [11]. In the case of a finite flow stress as described in Sec. 4.3, the Rabinowicz characteristic length is directly applicable. If the bodies are pressed against each other at light load, the contacts will typically have under-critical size compared to the Rabinowicz length and will not wear. In our framework, this translates to the normalized energy density being below 1 at any point for any D . In this region, it is very unlikely for a contact of sufficient size to occur and in the numerical model, it might not happen at all. Consequently, only least wear can occur. In Fig. 13, this region of loads is shown on the left side.

At higher loads, the contact configuration becomes dense, and the transition to mild wear (central field in Fig. 13) begins. As we enter the true region of contact of rough surfaces, the statistical properties of the contact start to dominate. For this region, a power-law dependency of the worn volume on the normal load is characteristic.

Finally, at very high normal loads, larger particles form, as elaborated in Sec. 3.3. We interpret this as the

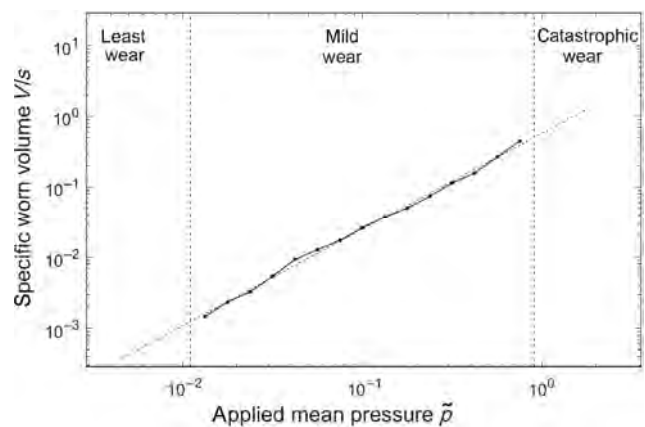


Fig. 13 Dependency of the wear volume per distance as a function of the applied external load for a constant flow stress $\sigma_0 = 10$. Other Parameters as in Fig. 4. For very low loads, no wear occurs in the model (least wear mode). At very high loads, very large particles emerge which the model cannot predict.

beginning of “catastrophic wear” (right field in Fig. 13). Because larger particles are to be expected, the question is rather why they do *not* occur than why they occur. In our simulation we assumed that once a particle of the size comparable to the computation area is possible, wear is catastrophic.

However, this maximum size is set somewhat arbitrarily. The physical understanding of the correct setting of this quantity is still an important future task and will surely be the key to physical understanding of catastrophic wear.

One possible approach follows directly from the concept presented in this paper: the energy density as function of particle diameter. For any wear particle to be formed, it is necessary that the stress distribution generates some tensile stresses and the elastic energy stored must be enough for separating the surfaces. However, there is an additional restriction for the possibility of wear particle formation. In a multi-contact-configuration, a particular wear particle can only be detached if it “fits inside the gap”. No particle can emerge with diameter greater than the current gap between the surfaces, because it would have to increase the global clearing. It is assumed that no single particle can do that. Considering this, the gap itself is comparable to the existing wear particles. In the case of the energy density of the form shown in Fig. 6, our energetic criterion allows the formation of particles corresponding to the first maximum and in principle also those corresponding to the right end of the linear asymptote. In reality, only the particle corresponding to the first maximum will be formed as those corresponding to the linear asymptote are too large and do not fit in the gap. The situation changes at larger normal loads as exemplarily shown in Fig. 14. Now the first maximum has shifted towards the region of larger diameters and finally merges with the linear asymptote which has also risen. This qualitatively changes the situation. Now there is no distinct small-particle-size capable to controlling the gap and thus preventing larger particles from being formed. Starting with smaller particles, wear can now continuously migrate to the formation of larger and larger particles while continuously increasing the gap size at the same time. In the framework of our model, this process is unbounded and indeed catastrophic.

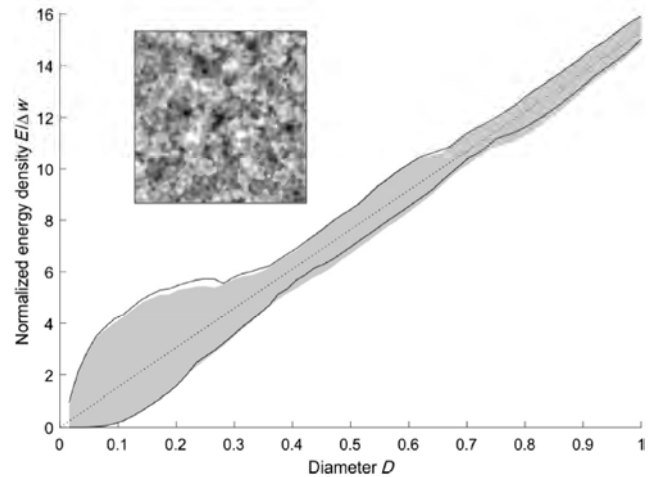


Fig. 14 Transition between bi-modal and uni-modal energy density may be the mechanism of transition to catastrophic wear. The mean pressure was chosen as $\bar{p} = 20$, other parameters as in Fig. 4.

We consider the validation of the above principle an important step for future research. In order for it to be checked and validated, a more extended model, describing both the stages of particle formation and their further transport is required.

6 Discussion and conclusion

This paper is devoted to the generalized applications of principles suggested by Archard and Rabinowicz more than 50 years ago. In this sense, the title of the paper could be: “Archard and Rabinowicz revisited”. Archard emphasized the importance of roughness but at his time he had no possibility to carry out detailed contact mechanics simulations. At present, we can realize his ideas in numerical experiments for particular surface geometries. Similarly, Rabinowicz suggested a very general but also very vague idea about his criterion for the detachment of wear particles. His criterion became a veritable theory only after the recent breakthrough research by AWM. But even in their concept, the central notion of “asperity” remained unclarified. In the present paper, we use the recently suggested concept of an asperity-free wear criterion. As a matter of fact, this criterion generalizes the idea of Rabinowicz by noticing that the notion of asperity is in fact dispensable in the framework of its logic! With the completion of this missing link, all parts of the Archard and Rabinowicz concepts can be

implemented using numerical contact mechanics.

In the present paper we numerically implemented the above ideas, tested the new numerical concept for wear simulation and provided illustrations of how the concept works in various situations. Already these illustrations give an idea of what the main governing parameters of wear may be, but extensive parameter studies and a deeper understanding of the governing parameters will be necessary in the near future, as it was not the intention of the present paper.

Our numerical simulations based on the asperity-free generalized Rabinowicz criterion show that the wear regimes can depend on properties of both materials and on the interactions in the interface. We considered the cases of rigid flat to elastic rough and rigid rough to elastic rough contacts and two interface interaction laws: Coulomb friction and plastic flow. Depending on the conditions, we observe different regimes of wear from settling type to continuous and catastrophic wear. The dependencies of the wear volume on the normal force in the region of mild wear occur to be power-law dependencies. This behavior is congruent with experiments finding wear laws that deviate from Archard's law.

In the present work, we confined ourselves to the elastic behavior of the contacting materials (up to detaching of wear particle). This was mainly due to technical restrictions inherent to BEM. The concept proposed in the paper however, is independent of any underlying numerical procedure determining surface stresses and can equally be applied to other media, such as elastoplastic material.

Acknowledgement

This work has been conducted under partial financial support from the German Ministry for Research and Education BMBF (No. 13NKE011A).

Open Access: The articles published in this journal are distributed under the terms of the Creative Commons Attribution 4.0 International License (<http://creativecommons.org/licenses/by/4.0/>), which permits unrestricted use, distribution, and reproduction in any medium, provided you give appropriate credit to the original author(s) and the source, provide a

link to the Creative Commons license, and indicate if changes were made.

References

- [1] Holmberg K, Erdemir A. Influence of tribology on global energy consumption, costs and emissions. *Friction* 5(3): 263–84 (2017)
- [2] Wilkinson J M. Why do implants fail? In *15th EFORT Congress: A combined programme in partnership with the BOA*, London, 4-6 June, 2014
- [3] Wik A, Dave G. Occurrence and effects of tire wear particles in the environment—A critical review and an initial risk assessment. *Environmental Pollution* 157: 1–11 (2009)
- [4] Cook L M. Chemical processes in glass polishing. *Journal of Non-Crystalline Solids* 120(1–3):152–71 (1990)
- [5] Godet M. Third-bodies in tribology. *Wear* 136(1): 29–45 (1990)
- [6] Reye Th. Zur Theorie der Zapfenreibung. *Der Civilingenieur* 4: 235–255 (1860)
- [7] Kruschov M M. Resistance of metals to wear by abrasion, as related to hardness. *London: Proc. Conf. Lubrication and wear, Institution Mech. Eng.* 655–659 (1957)
- [8] Krushchov M M, Babichev M A. *Investigation of wear of metals*. Moscow: Russian Academy of Sciences, 1960
- [9] Archard J F. Contact and rubbing of flat surfaces. *Journal of Applied Physics* 24: 981–988 (1953)
- [10] Archard J F, Hirst W. The wear of metals under unlubricated conditions. *Proc. R. Soc. London A* 236: 397–410 (1956)
- [11] Rabinowicz E. *Friction and Wear of Materials. Second Edition*. John Wiley & Sons, inc., 1995
- [12] Kragelski I V. *Friction and Wear*. Butter Worth, 1965
- [13] Akbarzadeh S, Khonsari M M. On the applicability of miner's rule to adhesive wear. *Tribology Letters* 63(2): 1–10 (2016)
- [14] Meng H C, Ludema K C. Wear models and predictive equations: their form and content. *Wear* 181: 443–457 (1995)
- [15] Aghababaei R, Warner D H, Molinari J-F. Critical length scale controls adhesive wear mechanisms. *Nature Communications* 7: 11816 (2016)
- [16] Dimaki A, Shilko E, Psakhie S, Popov V L. Simulation of fracture using a mesh-dependent fracture criterion in the discrete element method. *Facta Universitatis, Series: Mechanical Engineering* 16(1): 41–50 (2018)
- [17] Rabinowicz E. The effect of size on the looseness of wear fragments. *Wear* 2: 4–8 (1958)
- [18] Dmitriev A I, Nikonov, A Y, Österle W. MD sliding simulations of amorphous tribofilms consisting of either SiO₂ or carbon. *Lubricants* 4(3): 1–24 (2016)

- [19] Pohrt R, Li Q. Complete Boundary element formulation for normal and tangential contact problems. *Physical Mesomechanics* **17**: 334–340 (2014)
- [20] Aghababaei R, Warner D H, Molinari J-F. On the debris-level origins of adhesive wear. *Proceedings of the National Academy of Sciences* **114**(30): 7935–7940 (2017)
- [21] Frérot L, Aghababaei R, Molinari J-F. A mechanistic understanding of the wear coefficient: From single to multiple asperities contact. *Journal of the Mechanics and Physics of Solids* **114**: 172–84 (2018)
- [22] Aghababaei R, Brink T, Molinari J-F. Asperity-level origins of transition from mild to severe wear, *Physical Review Letters* (2018), accepted paper, <https://journals.aps.org/prl/accepted/af070Y7eUba1b565e38540803364791de29e63f77>.
- [23] Li Q, Popov V L. On the possibility of frictional damping with reduced wear: A note on the applicability of Archard's law of adhesive wear under conditions of fretting. *Physical Mesomechanics* **20** (5): 91–95 (2017)
- [24] Popov V L. Adhesive wear: Generalized Rabinowicz' criteria. *Facta Universitatis, Series: Mechanical Engineering* **16**(1): 29–39 (2018)
- [25] Popov V L. *Contact Mechanics and Friction. Physical Principles and Applications. 2nd Edition*. Berlin: Springer, 2017
- [26] Bowden F P, Tabor D. *The Friction and Lubrication of Solids*. Clarendon Press, 2001
- [27] Ciavarella M, Papangelo A. Discussion of “Measuring and understanding contact area at the nanoscale: A review” (Jacobs T D B, Ashlie Martini A, *ASME Appl. Mech. Rev.* **69**(6): 060802 (2017)). *Applied Mechanics Reviews. ASME International*. **69**(6): 065502 (2017)
- [28] Pohrt R, Popov V L. Contact mechanics of rough spheres: Crossover from fractal to Hertzian behavior. *Advances in Tribology* **2013**:1–4 (2013)
- [29] Popov V L, Pohrt R, Li Q. Strength of adhesive contacts: Influence of contact geometry and material gradients. *Friction* **5**(3):308–25 (2017)
- [30] Popov V L. Generalized Rabinowicz' criterion for adhesive wear for elliptic micro contacts, *AIP Conference Proceedings* **1909**: 020178 (2017)
- [31] Popov V L, Smolin I Yu, Gervé A, Kehrwald B. Simulation of wear in combustion engines. *Computational Materials Science* **19**: 285–291 (2000)
- [32] Popov V L, Psakhie S G. Numerical simulation methods in tribology. *Tribology International* **40**(6): 916–23 (2007)
- [33] Scherge M, Shakhvorostov D, Pöhlmann K. Fundamental wear mechanism of metals. *Wear* **255**: 395–400 (2003)
- [34] Popov V L. Analytic solution for the limiting shape of profiles due to fretting wear. *Scientific Reports* **4**: 3749 (2014).
- [35] Dmitriev A I, Voll L B, Psakhie S G, Popov V L. Universal limiting shape of worn profile under multiple-mode fretting conditions: theory and experimental evidence. *Scientific Reports* **6**: 23231 (2016)
- [36] Rhee S K. Wear equation for polymers sliding against metal surfaces. *Wear* **16**(6):431–45 (1970)
- [37] Rabinowicz E. The least wear. *Wear* **100**: 533–541 (1984).



Valentin L. POPOV. He is full professor at the Berlin University of Technology. He studied physics and obtained his doctorate in 1985 from the Moscow State Lomonosov University. 1985–1998 he worked at the Institute of Strength Physics

and Materials Science of the Russian Academy of Sciences and was a guest professor in the field of theoretical physics at the University of Paderborn (Germany) from 1999 to 2002. Since 2002 he is the head of the Department of System Dynamics and the Physics of Friction at the Berlin University of Technology. He has published over 300 papers in leading international journals and is the author of the book “*Contact Mechanics and Friction: Physical Principles and Applications*” which appeared in three editions in

German, English, Chinese, and Russian. He is the member of editorial boards of many international journals and is organizer of more than 20 international conferences and workshops over diverse tribological themes. Prof. Popov is honorary professor of the Tomsk Polytechnic University, of the East China University of Science and Technology, and of the Changchun University of Science and Technology and Distinguished Guest Professor of the Tsinghua University. His areas of interest include tribology, nanotribology, tribology at low temperatures, biotribology, the influence of friction through ultrasound, numerical simulation of contact and friction, research regarding earthquakes, as well as topics related to materials science such as the mechanics of elastoplastic media with microstructures, strength of metals and alloys, and shape memory alloys.



Roman POHRT. He is researcher at the Berlin University of Technology. He studied physical engineering science with special focus on simulation and optimization of discrete and continuous problems. Since he

joined the group of Prof. V. Popov in 2010, he has been conducting experimental and numerical research on a variety of tribology related industry problems. In his PhD thesis R. Pohrt focussed

on linking scales in the elastic contact of fractal rough surfaces, for which he was awarded by the German Tribological Society in 2013. R. Pohrt has authored a series of influential papers on different tribological problems, applying and extending state-of-the-art numerical methods. His areas of interest include contact mechanics, rail-wheel-interaction of trains, manufacturing technology, lubrication and more generally the influence of surface topography on tribological phenomena.

Combined effect of boundary layer formation and surface smoothing on friction and wear rate of lubricated point contacts during normal running-in processes

Yazhao ZHANG, Alexander KOVALEV, Yonggang MENG*

State Key Laboratory of Tribology, Tsinghua University, Beijing 100084, China

Received: 05 April 2018 / Revised: 26 June 2018 / Accepted: 29 June 2018

© The author(s) 2018. This article is published with open access at Springerlink.com

Abstract: The combined effect of boundary layer formation and surface smoothing on friction and wear rate of metallic surfaces under lubricated point contact condition was investigated. The double trend of friction coefficient variations was revealed during running-in and sub-running-in processes. The evolution of surface topography was measured on-site using white-light interference profilometer and analyzed using bearing area curves. Comprehensive theoretical equations that explicitly express the contributions of boundary friction, adhesive friction and wear have been derived, and results obtained by these equations were compared with experimental observations. It is concluded that the theoretical models are quantitatively adequate to describe the combined effect of surface smoothing due to mechanical wear and formation of boundary films on the changes in friction and wear rate during normal running-in processes.

Keywords: running-in; bearing area curves; friction modeling; wear modeling; mixed lubrication

1 Introduction

Changes in friction and wear during most machine operations typically occur immediately after the onset of sliding in the interface between contacting fresh dry or lubricated solid surfaces. The change is apparently associated with the transitions of microscopic contact and lubrication states arisen during sliding process. The initial transition is known as “running-in” or “break-in” process that occurs under nonzero normal force and relative sliding [1]. So far, very little is known about the running-in phenomenon. Most of the previous studies conducted on the friction and wear behavior of materials overlooked the initial transitional stage in machine operations while focused on the steady phase that follows the running-in process. However, Blau [2] highlighted that owing to ignoring the running-in aspects of sliding, researchers overlooked important clues associated to

the evolution of conjoint process that later affects the long-term machine operation. Thus, better understanding of the running-in process is essential for efficient machine operations.

It is well known that the running-in behavior is induced by wear, and wear prediction is the most significant tribological challenge [3]. The transformation of metallic surface caused by wear is a complex phenomenon that involves the following cyclic changes [4, 5] when the tribopair operates under the appropriate conditions: (1) plastic deformation develops a highly deformed and oriented hardened sub-surface layer; (2) micro-cracks form within the hardened layer; (3) owing to the coalescence of micro-cracks, wear particles are generated and the remaining plateaus bear the normal load; (4) plateau fails leaving a smoother surface that restart the wear cycle. This scenario is suitable for both the running-in and steady wear stages, and it also fits the transitional “sub-stage”

* Corresponding author: Yonggang MENG, E-mail: mengyg@tsinghua.edu.cn

List of symbols

A_h	Fluid film area	\dot{V}_0	Initial value of \dot{V}
h	Oil film thickness	\dot{V}_s	Steady value of \dot{V}
p_h	Hydrodynamic pressure	W	Total load
u	Sliding velocity	W_b	Load fraction supported by boundary layer
F	Total friction force	W_h	Load fraction supported by hydrodynamic lubricant
F_b	Solid-boundary layer-solid friction force	W_s	Load fraction supported by real solid-solid contact areas
F_h	Viscous shear force	α	Hydrodynamic force fraction, W_h/W
F_s	Solid-solid contact adhesive friction force	α_0	Initial value of α
f	Total friction coefficient	α_s	Steady value of α
f_0	Initial value of COF in the continuous test	β	Boundary layer force fraction, $W_b/(W - W_h)$
f'_0	The value of COF at $\alpha = \alpha_0, \beta = \beta_s$	β_0	Initial value of β
f_s	Steady value of COF in the continuous test	β_s	Steady value of β
f'_s	The value of COF at $\alpha = \alpha_s, \beta = \beta_0$	$\bar{\beta}$	Mean value of β for each interval
H	Material hardness	$\dot{\gamma}$	Shear rate
K	Wear coefficient	η	Viscosity of lubricant
k_α	Rate constant relating to the surface smoothing	μ_b	Boundary friction coefficient
k_β	Rate constant relating to the formation of boundary layer	μ_h	Limiting shear stress coefficient
s	Sliding distance	μ_s	Solid-solid contact friction coefficient
V	Wear volume	τ_h	Viscous shear stress
\dot{V}	Wear rate	τ_{lim}	Limiting shear stress

between these phases. The main aim of wear prediction is to estimate the material loss depending on the mechanical properties and surface parameters of rubbing solids as well as the certain schemes of tribotesting devices used. Owing to the multi-scaled physical factors affecting friction and wear, numerous wear models have been proposed [6, 7]. Meng and Ludema [8] were the first to summarize and classify the previously proposed wear models in 1995. They distinguished three main types of wear equations: empirical, phenomenological and those based on selected failure mechanisms. Many of the existing wear models employed to calculate the material loss are based on Archard wear law [9] that is widely used in engineering calculations. It is a quantitatively simple equation expressing the wear volume generated in the sliding process as a linear function of sliding distance and normal load. Archard's law is applicable for the steady wear stage; however, it does not apply to the running-in process, during which the wear rate

is usually not constant.

The prediction of variation in friction coefficient during the running-in process is also challenging. The friction force in lubricated contacts is composed of boundary friction at asperity contacts and viscous shear resistance of fluid lubricant films. According to Bowden and Tabor's theory [10], the boundary friction is further divided into three components, solid-solid contact adhesive friction, solid-boundary layer-solid contact friction and the plowing force caused by the asperity interlocking between the contacting surfaces and indentation of harder asperities into the softer counterparts. During a normal running-in process, contacting asperities could continuously become more or less smoothed with increasing running distance owing to the wear and plastic deformation. Meanwhile, adsorption film and/or tribochemical surface reaction film could form at the asperities [11], leading to variation in friction coefficient even under constant load and sliding speed condition. The interplay and

combined effect of surface smoothing and boundary layer formation complicate the running-in process, leading to more complex model.

The aim of this study is to investigate and to distinguish the combined effect of boundary film formation and surface smoothing on the changes in coefficient of friction (COF) and wear rate during the running-in process. A series of start-stop ball-on-plate experiments were performed to separate the boundary layer effect from the evolution of surface topography, which was measured on-site repeatedly and interruptedly using an optical interference profilometer. The bearing area curve was used to calculate the material losses at different running distances, and the wear rate vs. sliding distance curve was obtained. Comprehensive theoretical equations have been derived based on Bowden and Tabor's boundary lubrication theory and Archard's wear equation. The equations explicitly express the contributions of boundary film and surface smoothing effects to COF and wear rate during the running-in process. The obtained results were compared to experimental observations to verify the accuracy of the developed model.

2 Correlation between wear and friction during running-in processes

Wear has a number of different definitions that describe the progressive damage of surface caused by relative motion with respect to another substance [12]. Two wear processes accompany the surface damage caused by friction. One process involves the loss of materials, the other is the change in the surface topography as a result of plastic deformation, both of which occur in the sliding lubricated surfaces and affect the friction force acting on the interface [13]. Figure 1 shows the typical pattern of variation in wear volume in relation to the sliding distance in tribology tests and the accompanying friction response of the sliding lubricated surfaces. The pattern represents different wear sequences that occur during friction tests [12, 14] and it does not depend on the type of material, test condition and the selected triboscheme.

According to the common theory of wear transition [1], during a normal running-in stage (Region A in

Fig. 1), both wear rate and friction coefficient decrease with the sliding distance. Then the wear process gradually transfers to a steady state (Region B in Fig. 1) as the change in the surface topography is stabilized. When the steady wear characterized by a constant wear rate surpasses a certain period, severe wear occurs at the interface, steadily increasing the wear rate and the friction coefficient during the so-called severe wear stage (Region C in Fig. 1).

In contrast to the uniform wear pattern, the pattern of accompanying friction behavior is multiform during the wear process. Blau has distinguished eight main patterns of friction force that could occur during the running-in process [1]. Several irreversible changes simultaneously take place in the sliding contacting surfaces, sub-surface areas and interfacial regions, resulting in various time-dependent variations in friction coefficient. The pattern of friction coefficient curve shown in Fig. 1 corresponds to the normal situation often taken place under typical lubricated conditions [1, 12], which will be discussed in Section 2.1.

2.1 Estimation of friction force under lubrication condition

As the plowing force is assumed to be negligible in certain circumstances, the total friction force F under lubricated condition can be simply expressed as the sum of three components, F_h , F_b and F_s , as follows,

$$F = F_h + F_b + F_s \quad (1)$$

where F_h denotes the viscous shear force of fluid lubricant films at interface, F_b is the solid-boundary

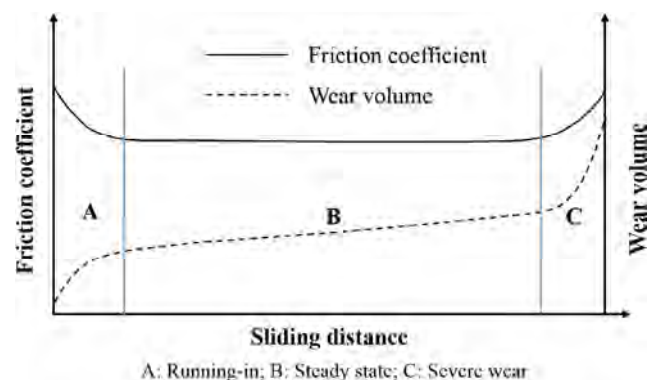


Fig. 1 Sketch of a typical correlation between wear and friction.

layer-solid friction force, and F_s is the solid-solid contact adhesive friction force (see Fig. 2).

The viscous shear force F_h is the integration of the viscous shear stress τ_h over the fluid film area A_h .

$$F_h = \int_{A_h} \tau_h dA = \int_{A_h} \frac{\eta u}{h} dA = \int_{A_h} \eta \dot{\gamma} dA \quad (2)$$

where η is the viscosity of lubricant under contacting pressure and temperature, u is the sliding velocity, h is the oil film thickness, and $\dot{\gamma}$ is the shear rate. It should be noted that Eq. (2) is appropriate for Newtonian fluids, and the shear thinning effect is ignored. In fact, the rheological property of lubricating oils significantly changes at high pressure and shear rate conditions, thus the Newtonian fluids would transform to non-Newtonian fluids with a limiting shear stress τ_{lim} , which is proportional to the hydrodynamic pressure p_h [15].

$$\tau_{lim} = \mu_h p_h \quad (3)$$

where μ_h is the limiting shear stress coefficient that is lubricant specific. Considering the limiting shear stress and shear thinning effect, Eq. (2) can be approximately rewritten by introducing the rheological model proposed by Bair and Winer [16], as follows:

$$F_h = \int_{A_h} \tau_{lim} \left(1 - e^{-\eta \dot{\gamma} / \tau_{lim}}\right) dA \quad (4)$$

For a lubricated point contact, $\eta \dot{\gamma}$ at high hydrodynamic pressure and high shear rate condition is generally far greater than τ_{lim} , thus the value of $e^{-\eta \dot{\gamma} / \tau_{lim}}$ is much smaller than 1. In such a case, Eq. (4)

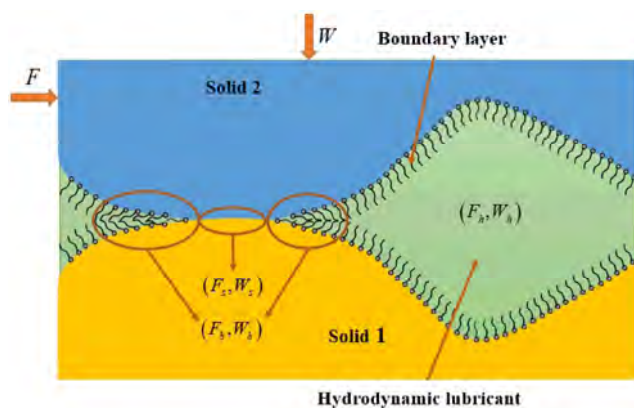


Fig. 2 Schematic of mixed lubrication.

can be written as

$$\begin{aligned} F_h &= \int_{A_h} \tau_{lim} \left(1 - e^{-\eta \dot{\gamma} / \tau_{lim}}\right) dA \approx \int_{A_h} \tau_{lim} dA \\ &= \int_{A_h} \mu_h p_h dA = \mu_h \int_{A_h} p_h dA = \mu_h W_h \end{aligned} \quad (5)$$

where W_h is the hydrodynamic force equated to the integration of hydrodynamic pressure p_h . μ_h can also be regarded as a hydrodynamic friction coefficient.

F_b and F_s are assumed to follow the Amontón's law of friction with a boundary friction coefficient μ_b and a solid-solid contact friction coefficient μ_s , respectively

$$F_b = \mu_b W_b \quad (6)$$

$$F_s = \mu_s W_s \quad (7)$$

where W_b is the load fraction supported by the boundary layer and W_s is the load fraction supported by real solid-solid contact areas. The total applied load W is balanced by the sum of W_h , W_b and W_s [17], as expressed by Eq. (8).

$$W = W_h + W_b + W_s \quad (8)$$

If the two factors, α and β , are introduced to represent W_h as a fraction of the total applied load W and W_b as a fraction of the remaining part of applied load $W - W_h$ respectively, i.e.,

$$W_h = \alpha W \quad (9)$$

$$W_b = \beta (W - W_h) = \beta (1 - \alpha) W \quad (10)$$

$$W_s = (1 - \beta) (W - W_h) = (1 - \beta) (1 - \alpha) W \quad (11)$$

Then, the total friction coefficient can be represented as:

$$f = \frac{F_h + F_b + F_s}{W} = \mu_h \alpha + \mu_b \beta (1 - \alpha) + \mu_s (1 - \beta) (1 - \alpha) \quad (12)$$

In general, the solid-solid contact friction coefficient μ_s is higher than the boundary friction coefficient μ_b and the hydrodynamic friction coefficient μ_h , and they could be assumed as constants during the running-in process. It is worth noting that the separation of solid-solid contact force W_s from other parts

is meaningful for analyzing not only friction but also wear as discussed in Section 2.2.

2.2 Estimation of material wear under lubrication condition

The Archard wear law [9] is a widely used wear equation that has been developed more than 50 years ago. This wear law presumes a linear dependency between the wear volume V of material and total applied normal load W , sliding distance s and material hardness H as follows:

$$V = K \frac{W_s}{H} \quad (13)$$

where K is the wear coefficient.

The wear rate is the derivation of wear volume to time, which can be expressed as:

$$\dot{V} = \frac{dV}{dt} = K \frac{W}{H} \frac{ds}{dt} = K \frac{Wu}{H} \quad (14)$$

where u is sliding velocity. However, the linear dependency is not always observed in experiments especially at the running-in stage. If the material loss in the hydrodynamic lubricated and boundary layer regions is considered negligible compared to the solid-solid contact case, it is reasonable to assume that material loss occurs only at solid-solid interfaces, thus it depends only on the solid-solid contact force W_s rather than the total normal load W .

Therefore, the wear rate function can be modified as follows:

$$\dot{V} = K \frac{W_s u}{H} = (1-\beta)(1-\alpha)K \frac{Wu}{H} \quad (15)$$

Conventionally, the effect of hydrodynamic and boundary lubrication on wear rate used to be implicitly incorporated into the value of wear coefficient K because the solid-solid contact force W_s is difficult to be estimated in experiments under lubricated test conditions. The above modified wear equation explicitly expresses the effect of hydrodynamic lubrication on wear rate via the term $(1-\alpha)$ and the effect of boundary lubrication via the term $(1-\beta)$, hence the interpretation of wear coefficient K here is different from its conventional meaning. When the hydrodynamic force bears the total normal load W (i.e., $\alpha = 1$) or the boundary layer fully supports the load of $W - W_h$ (i.e., $\beta = 1$), no wear will occur even if W and K are nonzero. This equation also shows the relationship between the wear volume and friction coefficient f (Eq. (12)) through factors α and β .

3 Experimental procedure

3.1 Friction measurements

To analyze the frictional behavior during the running-in process, tribology experiments were carried out on a universal tribometer (Rtec Instrument, USA) that is shown in Fig. 3. Both the changes in surface topography and frictional force during the experimental tests were measured. An ordinary set-up of Rtec tribometer was used for testing, where a steel ball was mounted in the stationary upper sample holder and a lower sample holder with a mounted steel disk performed the reciprocating motion driven by a motor. All tests were set with a load of 20 N, corresponding to a maximum Hertzian contact pressure of approximately 1.0 GPa and a contact radius of approximately 93.8 μm ,

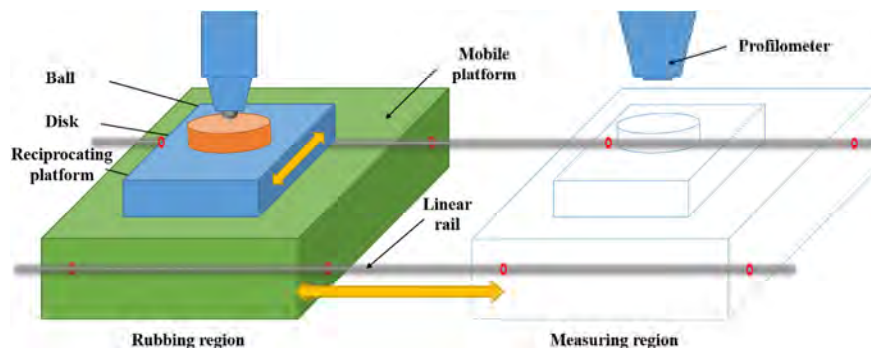


Fig. 3 Schematic of universal tribometer.

and the sliding speed and sliding amplitude were set to be 20 mm/s and 5 mm, respectively.

A start-stop testing scheme was used in order to investigate the evolution of surface topography and distinguish the effect of adsorption boundary layer and surface smoothing caused by mechanical wear on the change in friction during the running-in process. The test is performed according to the following scheme. Every 2 min, the lower holder motor was interrupted and the mobile platform holding the lower specimen was moved from the rubbing region to the measuring region (see Fig. 3) to capture an image of the surface topography, which was measured with a white-light interference profilometer unit attached to the Rtec tribometer. During the interruption period, the lubricant film on the disk specimen was carefully cleaned with acetone before topography measurement. Then the mobile platform was moved back to the rubbing region and the friction test re-started after feeding new lubricant. The start-stop test described above was repeated seven times, and seven images of the worn surface were captured on-site without detaching the test pieces from the holders.

For comparison, a noninterrupted reference experiment with the same load and speed conditions was carried out for a total duration of 14 min. The surfaces of the ball and disk used for all tests were cleaned with acetone in an ultrasonic bath. All tests were performed at 22 ± 2 °C under normal atmospheric conditions.

3.2 Sample preparation

GCr15 bearing steel ball and disk specimens were used owing to material characteristics of GCr15 bearing steel, including uniform-chemical composition, low percentage of harmful elements, high purity, well-distributed carbide and good surface quality. The 40 mm diameter disk specimen was finished by grinding with an average roughness R_a of 65 nm and standard deviation (RMS) of 85 nm, measured over an area of 1.819 mm × 1.137 mm on a white-light interference profilometer. The ball diameter was 12.7 mm with roughness $R_a = 6$ nm. Base oil POE (Polyol Ester) 32# (dynamic viscosity at 40 °C is 0.031 Pa·s) was used as lubricant without additives.

4 Results and discussion

4.1 Comparison of conventional and start-stop friction test results

Frictional force is relatively easy to be measured continuously in-situ in experiments, and curves of COF plotted against sliding time or distance are typically used to analyze the wear transitions occurred during the experiment [18]. The red line in Fig. 4 shows the measured curve of COF vs. the sliding distance in the nonstop reference experiment. The initial COF value of 0.106 gradually decreased to approximately 0.087 after the running-in stage, representing a typical transition pattern of friction for many lubricated rough surfaces.

The blue line in Fig. 4 is the COF values obtained by the seven start-stop tests. All seven segmental curves show similar monotonic decay trend, and the initial peak of each segment is gradually reduced. The initial COF value obtained by the first start-stop test is 0.107, which is very close to that obtained by the reference test. The COF values at the end of each segment are also close to those of the reference test, implying that nearly identical running-in transition of friction behavior occurred throughout the friction tests. Based on the common knowledge regarding the running-in process, such gradual decrease in COF values is attributed to the extensive mechanical wear and/or plastic deformation of asperities that leads to

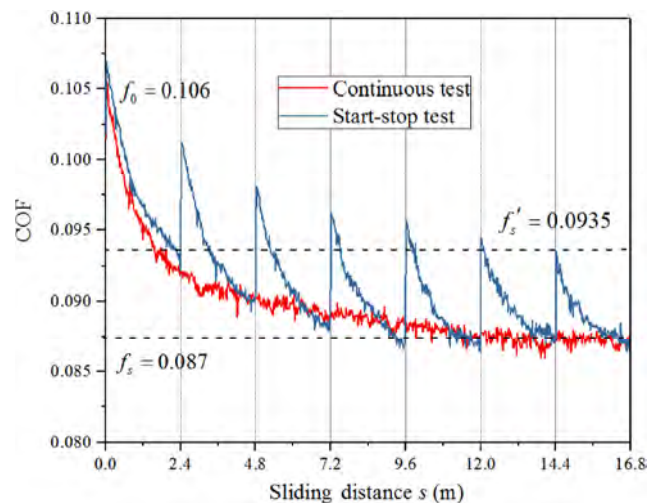


Fig. 4 Comparison of continuous and start-stop friction tests of the same friction pair under lubricated conditions.

a gradual increase of real contact area and decrease of asperity contact pressure to generate adsorbed boundary layer at asperity contact regions. Meanwhile, the decrease in asperity height enhances the hydrodynamic lubrication of oils reserved in the valleys of rough surface. The COF peak values in the start-stop test are caused by the destruction of adsorbed boundary layer owing to the frequent cleaning at every stop between tests, and the sub-running-in leads to re-formation of the adsorption boundary lubrication layer.

If the above friction test results are re-plotted in a semi-logarithmic coordinate (see Fig. 5), a double trend of friction change for the running-in process can be found for the continuous friction test, as illustrated by the red and green straight lines in Fig. 5(a), while the COF curves for the seven start-stop friction tests are all represented by single straight lines with different slopes. The double trend friction change detected in the continuous friction test implies that two independent processes of surface smoothing and boundary layer formation are involved in the running-in process before the intersection point of the two lines (at sliding distance of approximately 3 m). However, the friction change was primarily caused by the surface smoothing due to wear after the intersection point. On the other hand, the start-stop friction tests involved combined effect that was shown only in the first and second tests, while the subsequent five tests predominantly involved single process of boundary layer formation. Fig. 5(a) shows that the red straight line is extended to intersect with the vertical axis at approximately 0.097, denoted as f'_0 ,

which is a characteristic parameter of the running-in phase considered to model friction in Section 4.2.

4.2 Modeling of friction behavior during running-in stage

Based on the experiment results shown in Figs. 4 and 5 analyzed in Section 4.1, it is postulated that the change in COF, f , during the running-in phase is a function of the hydrodynamic force fraction α and boundary layer force fraction β . To derive the function of COF, f , the following assumptions are made:

a) The hydrodynamic force fraction α increases from an initial value α_0 to a steady value α_s , following Eq. (16) as depicted in Fig. 6(a);

b) The boundary layer force fraction β increases from an initial value β_0 to steady value β_s in a similar manner as shown in Fig. 6(b).

It follows that

$$-\frac{d\alpha}{ds} = k_\alpha (\alpha - \alpha_s) \tag{16}$$

where k_α is a rate constant related to the surface smoothing, s is sliding distance.

Then we get

$$\frac{d(\alpha - \alpha_s)}{\alpha - \alpha_s} = -k_\alpha ds \tag{17}$$

Thus,

$$\ln(\alpha - \alpha_s) = -k_\alpha s + c \tag{18}$$

$$\alpha = c'e^{-k_\alpha s} + \alpha_s \tag{19}$$

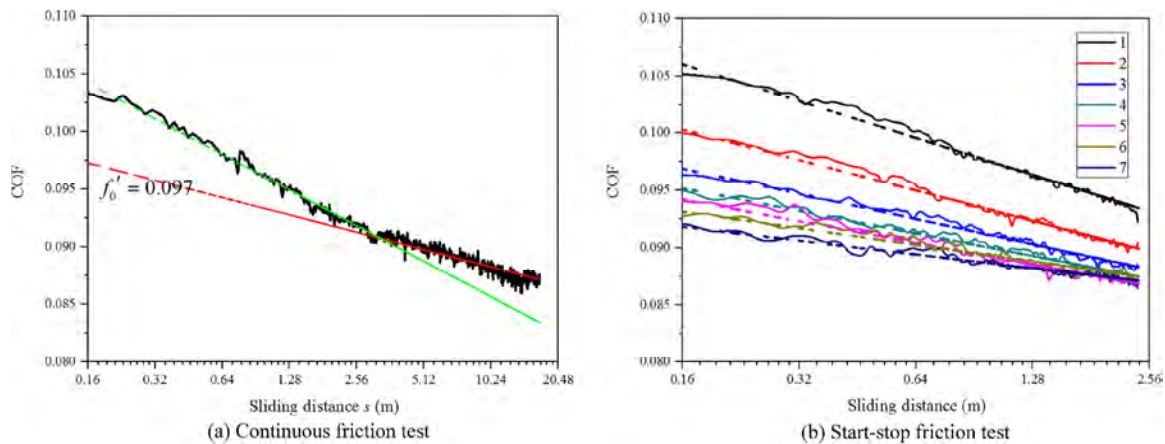


Fig. 5 COF curves of continuous and start-stop friction tests for the same friction pair in semi-logarithmic coordinates.

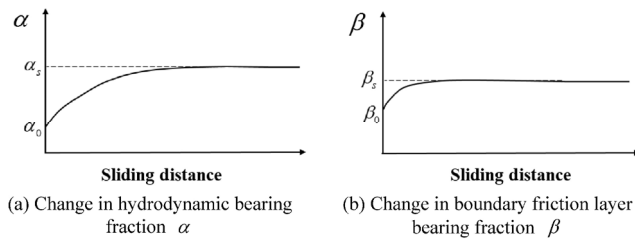


Fig. 6 Change in hydrodynamic bearing fraction α and boundary friction layer bearing fraction β during running-in process.

When $s = 0$, $\alpha = \alpha_0$, therefore, we get $c' = \alpha_0 - \alpha_s$

$$\alpha = (\alpha_0 - \alpha_s)e^{-k_\alpha s} + \alpha_s \tag{20}$$

Similarly, the boundary layer force fraction can be expressed as

$$\beta = (\beta_0 - \beta_s)e^{-k_\beta s} + \beta_s \tag{21}$$

where k_β is a rate constant related to the formation of boundary layer.

Four key values of the COF (f_0 , f'_0 , f_s and f'_s) are plotted in the Figs. 4 and 5(a). When the changes in α and β shown in Fig. 6 are integrated in the model, the four key values of COF can be expressed as follows:

$$f_0 = \mu_h \alpha_0 + \mu_b \beta_0 (1 - \alpha_0) + \mu_s (1 - \beta_0) (1 - \alpha_0) \tag{22}$$

$$f'_0 = \mu_h \alpha_0 + \mu_b \beta_s (1 - \alpha_0) + \mu_s (1 - \beta_s) (1 - \alpha_0) \tag{23}$$

$$f_s = \mu_h \alpha_s + \mu_b \beta_s (1 - \alpha_s) + \mu_s (1 - \beta_s) (1 - \alpha_s) \tag{24}$$

$$f'_s = \mu_h \alpha_s + \mu_b \beta_0 (1 - \alpha_s) + \mu_s (1 - \beta_0) (1 - \alpha_s) \tag{25}$$

or,

$$f_0 - f'_0 = (\mu_b - \mu_s)(1 - \alpha_0)(\beta_0 - \beta_s) \tag{26}$$

$$f'_0 - f_s = \mu_h(\alpha_0 - \alpha_s) - \mu_b \beta_s(\alpha_0 - \alpha_s) - \mu_s(1 - \beta_s)(\alpha_0 - \alpha_s) \tag{27}$$

$$f_0 - f'_s = \mu_h(\alpha_0 - \alpha_s) - \mu_b \beta_0(\alpha_0 - \alpha_s) - \mu_s(1 - \beta_0)(\alpha_0 - \alpha_s) \tag{28}$$

Because the coefficient matrix expressed in Eqs. (22)–(25) is not of full-rank, the values of α_0 , α_s , β_0 and β_s cannot be determined by solving Eqs. (22)–(25). It is reasonable to set the value of β_0 to be zero because of the negligible boundary layer formation at

the beginning of the test. Given that the magnitudes of μ_h , μ_b and μ_s are known, the three unknown parameters, α_0 , α_s and β_s , can be obtained by solving Eqs. (22)–(25).

As shown in Fig. 4, f_0 is the value of COF at the onset of the continuous friction test, at which the initial values of both α and β are expressed by Eq. (22). f_s is the value of COF when the running-in phase is complete with both α and β reaching their saturation values. f'_s is the value of COF when the surface smoothing reached a steady state ($\alpha = \alpha_s$), while the boundary layer was partially removed ($\beta = \beta_0$), corresponding to the peak COF value of the last start-stop friction test. f'_0 shown in Fig. 5(a) represents an imaginary lubrication state where the boundary layer has fully formed ($\beta = \beta_s$) but the surface smoothing did not occur ($\alpha = \alpha_0$). All four characteristic values of COF, f_0 , f_s , f'_0 and f'_s , can be obtained from the experimental results shown in Figs. 4 and 5(a).

Depending on the relative significance of boundary layer formation and surface smoothing to the change in COF during the running-in process, four situations, in which the relationship between COF and sliding distance can be expressed respectively as follows:

Situation A: the formation of adsorbed boundary layer is complete ($\beta = \beta_s$), while the surface smoothing continues. In such a case, COF yields:

$$\begin{aligned} f &= \mu_h \alpha + \mu_b \beta_s (1 - \alpha) + \mu_s (1 - \beta_s) (1 - \alpha) \\ &= \mu_h \alpha_s + \mu_b \beta_s (1 - \alpha_s) + \mu_s (1 - \beta_s) (1 - \alpha_s) + \\ &\quad [\mu_h(\alpha_0 - \alpha_s) - \mu_b \beta_s(\alpha_0 - \alpha_s) - \\ &\quad \mu_s(1 - \beta_s)(\alpha_0 - \alpha_s)]e^{-k_\alpha s} \\ &= f_s + (f'_0 - f_s)e^{-k_\alpha s} \end{aligned} \tag{29}$$

Situation B: the adsorbed boundary layer has not formed ($\beta = \beta_0$), while surface smoothing occurs. In this case, COF becomes:

$$\begin{aligned} f &= \mu_h \alpha + \mu_b \beta_0 (1 - \alpha) + \mu_s (1 - \beta_0) (1 - \alpha) \\ &= \mu_h \alpha_s + \mu_b \beta_0 (1 - \alpha_s) + \mu_s (1 - \beta_0) (1 - \alpha_s) + \\ &\quad [\mu_h(\alpha_0 - \alpha_s) - \mu_b \beta_0(\alpha_0 - \alpha_s) - \\ &\quad \mu_s(1 - \beta_0)(\alpha_0 - \alpha_s)]e^{-k_\alpha s} \\ &= f_0 + (f'_0 - f_0)e^{-k_\alpha s} \end{aligned} \tag{30}$$

Situation C: the formation of boundary layer continues, while no mechanical wear occurs ($\alpha = \alpha_0$) during the running-in process. In this case, the COF changes with the sliding distance as expressed by Eq. (31).

$$\begin{aligned}
 f &= \mu_h \alpha_0 + \mu_b \beta (1 - \alpha_0) + \mu_s (1 - \beta) (1 - \alpha_0) \\
 &= \mu_h \alpha_0 + \mu_b \beta_s (1 - \alpha_0) + \mu_s (1 - \beta_s) (1 - \alpha_0) + \\
 &\quad (\mu_b - \mu_s) (1 - \alpha_0) (\beta_0 - \beta_s) e^{-k_\beta s} \quad (31) \\
 &= f'_0 + (f_0 - f'_0) e^{-k_\beta s}
 \end{aligned}$$

Situation D: the formation of boundary layer and surface smoothing occur simultaneously causing a combined effect on the change in COF. Therefore, f'_0 in Eq. (29) should be replaced by Eq. (31). In this general case, the relationship between COF, f , and sliding distance, s , is an exponential function, the factor of which also includes an exponential function with a different constant rate k_β as expressed by Eq. (32).

$$f = \left[(f_0 - f'_0) e^{-k_\beta s} + f'_0 - f_s \right] e^{-k_\alpha s} + f_s \quad (32)$$

Equation (32) transforms into Eq. (29) when the formation of adsorbed boundary film is complete ($\beta = \beta_s$) and to Eq. (30) when the adsorbed boundary film does not change ($\beta = \beta_0$). If the surface smoothing can be negligible during the running-in ($\alpha = \alpha_0$), Eq. (32) will be simplified as Eq. (31). It worth noting that the derived analytic equations of COF, (Eqs. (29)–(32)), depend only on the parameters $f_0, f_s, f'_0, f'_s, k_\alpha$ and k_β , which can be obtained by friction experiments. Neither the basic properties of μ_h, μ_b and μ_s nor the characteristic fraction parameters, $\alpha_0, \alpha_s, \beta_0$ and β_s are involved in these analytic friction equations derived in this study.

Regression analysis was performed on the experimental data presented by the red line in Fig. 4 together with the function expressed by Eq. (32), and the obtained values of the rate constants, k_α and k_β , for the continuous friction test were 0.24 m^{-1} and 1.75 m^{-1} , respectively. The regression curve plotted as the green line in Fig. 7 agrees well with the measured results obtained from the continuous friction test. Furthermore, substituting $k_\alpha = 0.24 \text{ m}^{-1}$ into Eqs. (29) and (30), which expresses the changes in COF with a constant boundary layer force fraction $\beta = \beta_0$ and $\beta = \beta_s$, respectively, the friction coefficient curves

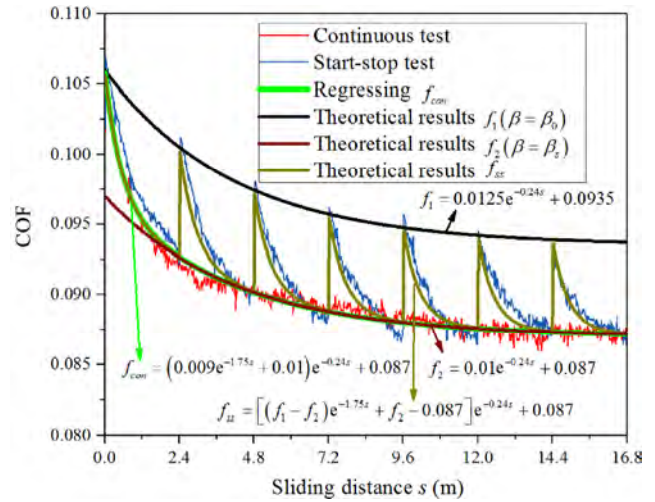


Fig. 7 Comparison of theoretical results and experimental data. Green line is the regression result of continuous test; dark line is the theoretical result of no boundary friction layer.

f_1 and f_2 were calculated and their values were plotted as dark and purple lines in Fig. 7. The functions f_1 and f_2 can be used to express the friction function of the start-stop tests f_{ss} . It can be seen that the calculated COFs accord well with the experimental values of each start-stop test.

4.3 Wear-induced changes in surface topography during running-in process

To explore the evolution of surface roughness under mixed lubrication during the running-in stage, the three-dimensional (3D) topography of wear track formed on the disk specimen was captured at different sliding intervals during the start-stop test series.

Figure 8 shows a set of consequent wear track images. The first image in each column shows the initial (as-manufactured) ground surface. The next seven images represent the grey-scale surface topography captured every two minutes at the same place after each start-stop friction test. When the captured images are compared, it can be seen that the overall grinding marks remain after the running-in stage, implying that the surface was not severely worn; however, wear occurred at the top asperities subjected to direct contact. The change in surface roughness, R_a , during the running-in process shown in Fig. 9, indicates that the value of R_a gradually decreases, which means the surface becomes smoother as the sliding distance increases.

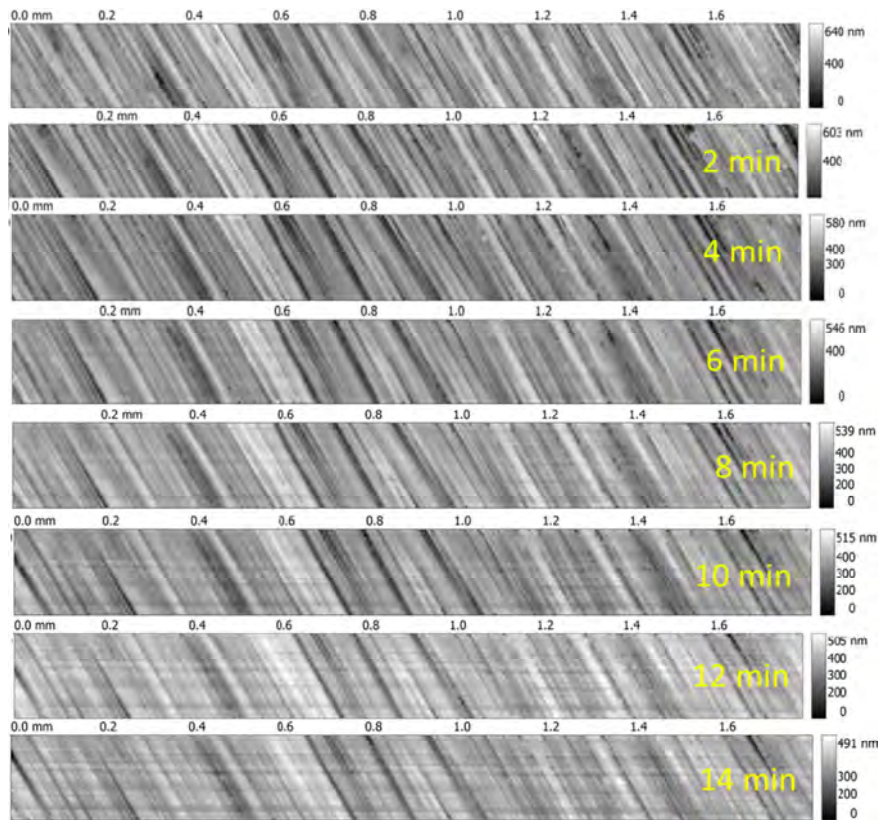


Fig. 8 Change in surface topography with running-in time. Each surface is labeled by corresponding time interval. The rectangular scan size of images corresponds to the wear track size of $1,811 \mu\text{m} \times 195 \mu\text{m}$. The gray scale bar on right side of surface depicts the height range at given time interval.

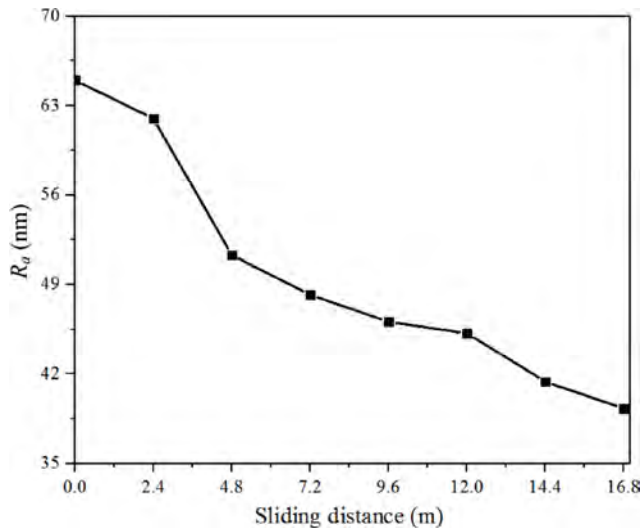


Fig. 9 Change in roughness R_a during running-in process.

Compared to Fig. 8, the change in the surface topography during the continuous test shown in Fig. 10 also indicates that the grinding marks are still clearly preserved on the worn surface.

Better understanding of the initial phase of wear during the running-in stage and the accompanying transition phenomena can be gained by continuously evaluating the asperity wear. Researchers in this field [2, 4, 5] agreed that an equilibrium state between friction surfaces and lubrication is reached after the running-in stage is completed. This balance is characterized by the constant wear rate and constant COF. Based on the friction test result presented in Fig. 4, the steady COF is reached within sliding distance of 12.0 m. This means that the balance between the mechanical response and lubrication condition was reached within this period. The volume loss due to wear will be quantitatively estimated in Section 4.3.1 based on the 3D topography images of subsequent worn surfaces.

4.3.1 Bearing area curves of material volume for running-in surface

Volume is a fundamental measure of wear when

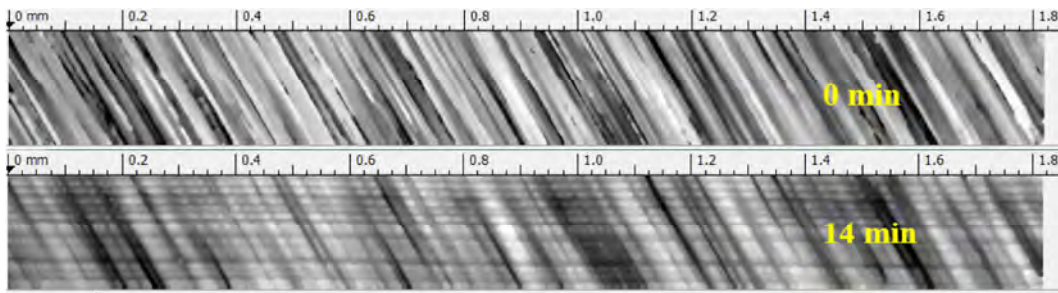


Fig. 10 Change in surface topography during continuous test before and after running-in process.

wear is regarded as the loss of material. Comparative analysis of a surface subjected to wear allows quantitative estimation of material loss in the case where the same location before and after wear on a surface can be identified exactly [19]. However, this approach is limited by the accuracy of image-processing techniques and reallocation procedure. In this study, the surface transformation due to wear was estimated by comparing the bearing area curves (BAC) instead. This method has a statistical origin and does not depend on the accuracy of reallocation.

Similar to the Abbott-Firestone approach, the BAC method is based on analyzing the functional bearing area curves of investigated surface [20]. Sosa et al. [21] employed the BAC method to monitor the steel surface of ground gears and revealed the distinct difference in height between the initial surface and surfaces subjected to running-in after just 44 cycles. The surface roughness parameters from V-parameter set [22] can be successfully implemented in tribological tasks because the splitting of the material ratio curve into three zones, such as “peak zone”, “core zone” and “valley zone”, allows distinguishing the changes in worn surface occurred during wear process. The main idea is that the peak zone corresponds to initial running-in wear, the core zone corresponds to wear throughout the lifetime of components, and the valley zone corresponds to lubricant retention under heavy wear conditions. This approach is based on utilizing the surface parameters such as R_{pk} , R_{vk} , and R_k , which were established in Germanic surface geometrical standard DIN 4776 [23]. Furthermore, the areal S-parameter set was defined in ISO 25178-2 [24] and successfully implemented to characterize worn surfaces [25–27]. Yusof et al. [28] has evaluated the blunted asperity peaks of steel surfaces by means of BAC

and discussed the applicability of volume parameters V_{mp} , V_{mc} , V_{vc} and V_{vv} to distinguish the material wear occurred during running-in.

The BAC of a surface is generated by sorting the original sampled surface data in descending order and plotting the sorted data, from 0 to 100% where 100% = N (number of data points taken). The BAC considered in this study is a cumulative distribution of material volume. The threshold plane was selected at certain height to calculate the material volume curve as a sum of volumes of single truncated right triangular prisms. The bearing volume curve is crucial for estimating the functional parameters of surfaces on the scale of surface roughness as the volume loss of surface due to wear. The set of material volume BACs, calculated using surface data of each worn surface in Fig. 8, are plotted in Fig. 11.

The bearing area curves of material volume for all time intervals have been plotted as normalized volume data. A height value of BAC is stored in metric term to show the real difference in height occurred due to a wear at the top of asperities during the running-in stage. Because of the evident fact that the “valley zone” of BAC is not disturbed due to wear, the minimum height point is set identical for all curves to arrange the curves according to their height loss in the “peak zone”.

Distinct differences between the initial volume (Red line) and all subsequent surfaces can be observed between the peak heights of worn surfaces, as shown in Fig. 11. The Difference in the “core zone” reflects the asperity shape change that caused by plastic deformation. The variance in the curves slope detected in the “core zone” is attributed to the “digitizing error” generated by the light sensor of white-light interferometer device [29].

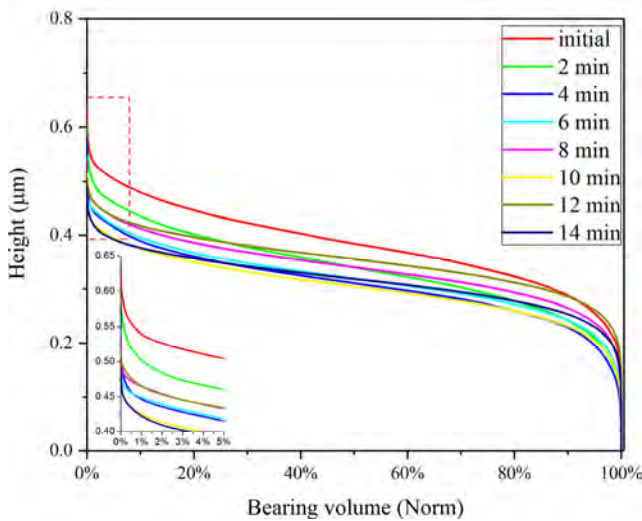


Fig. 11 Bearing curves of material volume calculated based on surface topography data measured every 2 min. Inset–zoomed part (dashed rectangle) of plot shows the overall difference in surface height occurred throughout the test duration time in the short range of 5%.

The surface volume loss at each time interval was estimated as follows: the BAC of initial unworn surface was considered as a reference curve to estimate the volume loss caused by consequent wear. The BAC curve of worn surface has a maximum height lower than the maximum height of the reference curve. This difference is attributed to height loss at asperity peaks. Making the threshold at the maximum height of worn surface regarding to the reference curve, the cutoff part of reference curve, upon the normalized volume axis, is accepted as a plausible material loss due to wear. The obtained values of material loss at each time interval were used in the quantitative analysis of running-in wear discussed in Section 4.3.2.

4.3.2 Wear characteristics of surface subjected to running-in

The estimated wear volumes were plotted against the sliding distance and indicated by square marks in Fig. 12. Unlike the predictions made based on Archard’s wear model [9], the fitted plot of experimental data shows that the wear volume tends to increase nonlinearly as the sliding distance increases. However, these findings are consistent with the common knowledge in this domain.

The wear rate plotted against sliding distance is evaluated in Fig. 13 (Dark scatter and dash line). The

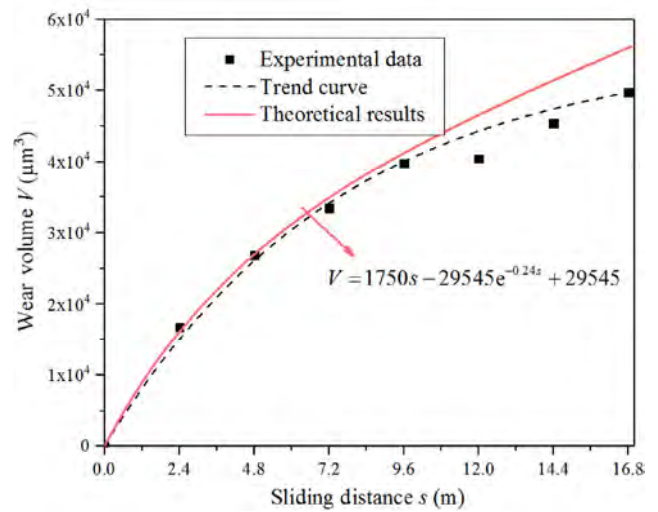


Fig. 12 Evolution of wear volume. Material volume loss at the top of asperities gradually stabilizes with the increase in sliding distance.

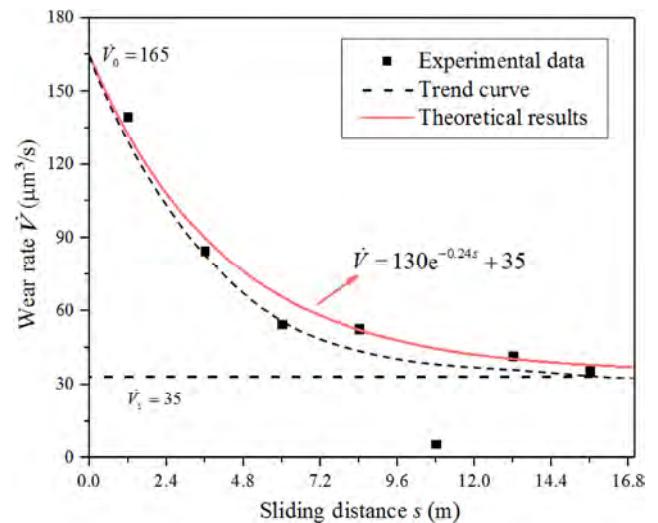


Fig. 13 Evaluation of wear rate against sliding distance. The wear rate was calculated as a ratio of material loss and wear time.

initial wear rate is high because of the small actual contact area and high local pressure. After a certain period of running-in, the surface asperities gradually flatten and the mean pressure of asperity contact decreases, resulting in lower wear rate. Next, an analytical model of wear rate during running-in will be established based on the following assumptions:

- (a) The reduction in wear rate is caused by the surface smoothing effect during running-in, and the formation of boundary friction layer reoccurs in each interval;
- (b) The hydrodynamic force fraction α increases

from α_0 to α_s as shown in Fig. 6(a);

(c) Because the boundary layer is regenerated in each test interval, the boundary layer force fraction β was assumed as a mean value $\bar{\beta}$ for each interval.

Based on Eq. (15), wear rate can be expressed as:

$$\begin{aligned}\dot{V} &= (1-\bar{\beta})(1-\alpha)K\frac{Wu}{H} \\ &= (1-\bar{\beta})\left\{1-\left[(\alpha_0-\alpha_s)e^{-k_\alpha s} + \alpha_s\right]\right\}K\frac{Wu}{H} \\ &= (1-\bar{\beta})(1-\alpha_s)K\frac{Wu}{H} + (1-\bar{\beta})(\alpha_s-\alpha_0)K\frac{Wu}{H}e^{-k_\alpha s}\end{aligned}\quad (33)$$

where u is the sliding speed. The initial wear rate can be written as:

$$\dot{V}_0 = (1-\bar{\beta})(1-\alpha_0)K\frac{Wu}{H}\quad (34)$$

The steady wear rate can be expressed as:

$$\dot{V}_s = (1-\bar{\beta})(1-\alpha_s)K\frac{Wu}{H}\quad (35)$$

Thus, we can obtain:

$$\dot{V}_0 - \dot{V}_s = (1-\bar{\beta})(\alpha_0 - \alpha_s)K\frac{Wu}{H}\quad (36)$$

During the running-in process, the wear rate changes with sliding distance and can be written as:

$$\begin{aligned}\dot{V} &= (1-\bar{\beta})(1-\alpha_s)K\frac{Wu}{H} + (1-\bar{\beta})(\alpha_s-\alpha_0)K\frac{Wu}{H}e^{-k_\alpha s} \\ &= \dot{V}_s + (\dot{V}_0 - \dot{V}_s)e^{-k_\alpha s}\end{aligned}\quad (37)$$

Wear volume is the integral of wear rate to the time, thus it can be expressed as:

$$\begin{aligned}V &= \int_0^t \dot{V} dt = \int_0^t \dot{V}_s + (\dot{V}_0 - \dot{V}_s)e^{-k_\alpha s} dt \\ &= \int_0^t \dot{V}_s + (\dot{V}_0 - \dot{V}_s)e^{-k_\alpha ut} dt \\ &= \frac{\dot{V}_s}{u} s + \frac{(\dot{V}_0 - \dot{V}_s)}{k_\alpha u} - \frac{(\dot{V}_0 - \dot{V}_s)}{k_\alpha u} e^{-k_\alpha s}\end{aligned}\quad (38)$$

Equations (37) and (38) analytically express the changes in wear rate and wear volume with the increase in sliding distance, respectively. The predicted

results obtained based on Eqs. (37) and (38) are indicated by red lines in Figs. 12 and 13, respectively. It is found that reasonably accurate predictions of wear rate and wear volume can be obtained by the analytical models compared to the experimental results. Furthermore, when Eqs. (37) and (32) are compared, a conjunctive relationship between friction and wear rate can be detected during running-in. When $s \rightarrow \infty$, $\dot{V} \rightarrow \dot{V}_s$ and $f \rightarrow f_s$ indicate that COF and wear rate change and attain constant value simultaneously, which is consistent with the universally accepted explanation of friction and wear behaviors during running-in process.

5 Conclusions

Analytical equations of COF and wear rate have been derived considering the combined effect of boundary layer formation and asperity flattening during the running-in process of rough metallic surfaces under lubricated conditions. The findings indicate that the reduction in COF is primarily caused by the combined effect of the adsorbed boundary layer and adaptive surface smoothing due to mechanical wear. This effect could be a combination of dissipative processes at the interface, and it must be analyzed within the context of the given tribosystem and operating conditions.

During the running-in stage, the adsorbed boundary layer generates fast (3.0 m) and surface smoothing can last for longer sliding distance (12.0 m). For the start-stop tests, the adsorbed boundary layer regenerates every time after each stop, thus the running-in occurs in every test. The analytical equations derived to calculate the COF can adequately describe the change in COF during running-in when compared to the experimental results.

The BACs generated from the 3D topography images captured in consequential start-stop test series allow estimating the material loss and wear rate during running-in. The results show that the material loss increases nonlinearly with the increase in sliding distance at a gradually reduced wear rate. Analytical models to describe the material wear volume and wear rate during running-in have been proposed, and the results obtained by these models agree well with the experimental data. The analytical models proposed

in this study to estimate friction and wear rate are conjunctive, which accords with common knowledge in this domain.

Acknowledgements

This work was partially supported by NSFC under grant No. 51635009 and by the State Administration of Foreign Expert Affairs under grant No. DL2017QHDX001.

Open Access: The articles published in this journal are distributed under the terms of the Creative Commons Attribution 4.0 International License (<http://creativecommons.org/licenses/by/4.0/>), which permits unrestricted use, distribution, and reproduction in any medium, provided you give appropriate credit to the original author(s) and the source, provide a link to the Creative Commons license, and indicate if changes were made.

References

- [1] Blau P J. Running-in. In *Encyclopedia of Tribology*. Wang Q J, Chung Y W, Eds. Boston, MA: Springer, 2013: 2967–2969.
- [2] Blau P J. On the nature of running-in. *Tribol Int* **38**(11–12): 1007–1012 (2005)
- [3] Williams J. *Engineering Tribology*. Cambridge (UK): Cambridge University Press, 2005.
- [4] Blau P J. Mechanisms for transitional friction and wear behavior of sliding metals. *Wear* **72**(1): 55–66 (1981)
- [5] Blau P J. How common is the steady-state? The implications of wear transitions for materials selection and design. *Wear* **332–333**: 1120–1128 (2015)
- [6] Blau P J. Embedding wear models into friction models. *Tribol Lett* **34**(1): 75–79 (2009)
- [7] Goryacheva I G. Wear models. In *Contact Mechanics in Tribology*. Goryacheva I G, Ed. Dordrecht: Springer, 1998: 163–190.
- [8] Meng H C, Ludema K C. Wear models and predictive equations: their form and content. *Wear* **181–183**: 443–457 (1995)
- [9] Archard J. Contact and rubbing of flat surfaces. *J Appl Phys* **24**(8): 981–988 (1953)
- [10] Bowden F P, Leben L. The friction of lubricated metals. *Philos Trans R Soc A Math Phys Eng Sci* **239**(799): 1–27 (1940)
- [11] Bai L Q, Meng Y G, Khan Z A, Zhang V. The synergetic effects of surface texturing and MoDDP additive applied to ball-on-disk friction subject to both flooded and starved lubrication conditions. *Tribol Lett* **65**(4): 163 (2017)
- [12] Raymond G B. *Mechanical Wear Fundamentals and Testing*. 2nd ed. New York (USA): Marcel Dekker Inc., 2004.
- [13] Kapoor A, Williams J A, Johnson K L. The steady state sliding of rough surfaces. *Wear* **175**(1–2): 81–92 (1994)
- [14] Straffelini G. Wear processes. In *Friction and Wear: Methodologies for Design and Control*. Straffelini G, Ed. Cham: Springer, 2015: 115–158.
- [15] Bair S S. *High Pressure Rheology for Quantitative Elastohydrodynamics*. Amsterdam (Netherlands), Boston (USA): Elsevier, 2007.
- [16] Bair S, Winer W O. A rheological model for elastohydrodynamic contacts based on primary laboratory data. *J Lubr Technol* **101**(3): 258–264 (1979)
- [17] Hao L C, Meng Y G. Numerical prediction of wear process of an initial line contact in mixed lubrication conditions. *Tribol Lett* **60**(2): 31 (2015)
- [18] Bhushan B, Israelachvili J N, Landman U. Nanotribology: friction, wear and lubrication at the atomic scale. *Nature* **374**(6523): 607–616 (1995)
- [19] Wang W, Wong P L. Wear volume determination during running-in for PEHL contacts. *Tribol Int* **33**(7): 501–506 (2000)
- [20] Abbott E J, Firestone F A. Specifying surface quality. *Mech Eng*, **55**: 569–572 (1933)
- [21] Sosa M, Sellgren U, Björklund S, Olofsson U. In situ running-in analysis of ground gears. *Wear* **352–353**: 122–129 (2016)
- [22] Jiang X, Scott P J, Whitehouse D J, Blunt L. Paradigm shifts in surface metrology. Part II. The current shift. *Proc R Soc A Math Phys Eng Sci*, **463**(2085): 2071–2099 (2007)
- [23] DIN 4776. Kenngrößen Rk, Rpk, Rvk, Mr1, Mr2 zur Beschreibung des Materialanteils im Rauheitsprofil—Meßbedingungen und Auswerteverfahren. In *Deutsche Norm*. Berlin: Beuth Verlag GmbH, 1990.
- [24] ISO. ISO 25178–2: 2012 Geometrical Product Specifications GPS) – Surface texture: Areal – Part 2: Terms, definitions and surface texture parameters. ISO, Geneva, 2012.
- [25] Böhm H J. Parameters for evaluating the wearing behaviour of surfaces. *Int J Mach Tools Manu* **32**(1–2): 109–113 (1992)
- [26] Corral I B, Calvet J V, Salcedo M C. Use of roughness probability parameters to quantify the material removed in plateau-honing. *Int J Mach Tools Manu* **50**(7): 621–629 (2010)

- [27] Franco L A, Sinatora A. 3D surface parameters (ISO 25178–2): Actual meaning of S_{pk} and its relationship to V_{mp} . *Precis Eng* **40**: 106–111 (2015)
- [28] Yusof N F M, Ripin Z M. A technique to measure surface asperities plastic deformation and wear in rolling contact. *Wear* **368–369**: 496–504 (2016)
- [29] Podulka P, Pawlus P, Dobrzański P, Lenart A. Spikes removal in surface measurement. *J Phys Conf Ser* **483**(1): 012025 (2014)



Yazhao ZHANG. He received his bachelor degree in agricultural mechanization and automation in 2014 from Jilin University, Changchun,

China. After then, he was a PhD student in the State Key Laboratory of Tribology at Tsinghua University, Beijing, China. His research interests include mixed lubrication and running-in process.



Alexander KOVALEV. He received his M.S. degree in physics from the Gomel State University, Gomel, Belarus in 1997. He has earned PhD degree in tribology and physics of solids in 2007 from Metal-Polymer

Research Institute, Gomel, Belarus. His current position is a research fellow at State Key Laboratory of Tribology at Tsinghua University, China. His research focuses on micro/nano-tribology, contact mechanics, interfacial phenomena, surface characterization, etc.



Yonggang MENG. He received his M.S. and PhD degrees in mechanical engineering from Kumamoto University, Japan, in 1986 and 1989, respectively. He joined the State Key Laboratory of Tribology at

Tsinghua University from 1990. His current position is a professor and the director of the laboratory. His research areas cover the tribology of MEMS and hard disk drives, active control of friction and interfacial phenomena and nanomanufacturing.

Estimating antiwear properties of esters as potential lubricant-based oils using QSTR models with CoMFA and CoMSIA

Zhan WANG¹, Tingting WANG², Guoyan YANG¹, Xinlei GAO^{2,*}, Kang DAI³

¹ College of Food Science and Engineering, Wuhan Polytechnic University, Wuhan 430023, China

² School of Chemical and Environmental Engineering, Wuhan Polytechnic University, Wuhan 430023, China

³ College of Pharmacy, South-Central University for Nationalities, Wuhan 430074, China

Received: 06 January 2017 / Revised: 03 May 2017 / Accepted: 19 June 2017

© The author(s) 2017. This article is published with open access at Springerlink.com

Abstract: Comparative molecular field analysis and comparative molecular similarity indices analysis were employed to analyze the antiwear properties of a series of 57 esters as potential lubricant-based oils. Predictive 3D-quantitative structure tribo-ability relationship models were established using the SYBYL multifit molecular alignment rule with a training set and a test set. The optimum models were all shown to be statistically significant with cross-validated coefficients $q^2 > 0.5$ and conventional coefficients $r^2 > 0.9$, indicating that the models are sufficiently reliable for activity prediction, and may be useful in the design of novel ester-based oils.

Keywords: quantitative structure tribo-ability relationship; antiwear properties; lubricant-based oils

1 Introduction

As the main component in a lubricant formulation, the basic oil plays an important role in the friction process [1]. Thus far, various lubricant-based oils have been developed, such as mineral-based oils, biodegradable-ester-based oils, halogenated hydrocarbon-based oils, polyethylene (alkylene) glycol-based oil, polyether-based oil, and ionic liquids [2]. Among these, ester-based oils are widely used in environmentally friendly lubricants owing to their biodegradability.

In general, the choice of lubricant depends on conditions such as the operating temperature, rotating speed, load, and the environment. However, for a new specific operating system, a suitable lubricant may not be available, and it may be necessary to design a new one. In practice, the design process takes several design, synthesis, and testing iterations. Because of a lack of effective theoretical guidance, designing a new lubricant is difficult, and we usually need to conduct a large number of experiments.

Theoretically, however, all properties of a chemical

compound are determined by its molecular structure. Clearly, these properties also include friction and antiwear properties. Therefore, in principle, it is feasible to predict the tribological properties of the compound from its structure.

The quantitative structure activity relationship (QSAR) method provides a general framework to predict a specific property of a compound and in past decades, this method has achieved great success in the field of drug design [3–6]. 3D-QSAR methods take advantage of the 3D structures of molecules, and can often achieve a better performance [7–10]. Evidently, the QSAR method can also be applied to the study of a tribology, which we termed the quantitative structure tribo-ability relationship (QSTR) method.

In our previous works, we demonstrated the feasibility of this idea, and showed that the tribological properties can be simply predicted from 2D or 3D structural descriptors of the compound using a regression method or a neural network [11–13]. In our previous research, for poly alpha olefins (PAO) series lubricants, two 3D-QSTR methods, i.e., the comparative molecular

* Corresponding author: Xinlei GAO, E-mail: gaoxl0131@163.com

field analysis (CoMFA) and comparative molecular similarity indices analysis (CoMSIA) models, showed statistically better predictability than a 2D-QSTR method, i.e., the back propagation neural network (BPNN) model. In this work, a series of ester lubricant-based oils were studied, and the relationship between the tribological parameters and molecular conformation was investigated using CoMFA and CoMSIA.

The basic idea of CoMFA is that the difference in the particular properties of a series of molecules is derived from the difference in their shapes of the non-covalent fields, which can be measured using a probe atom. To make the shapes of the non-covalent fields comparable, the first and most important step of the CoMFA analysis is to align the 3D structures of these molecules properly to ensure that they have the same orientation. Starting from a series of superimposed 3D structures, a probe atom is used to measure the molecular interaction field of each structure, which can be represented as the interactions between the molecule and probe atom. The measurements are conducted at the lattice points of a regular Cartesian 3D grid, and the type of interactions can vary [14]. With CoMFA, only van der Waals and electrostatic interactions are considered [15, 16]. With CoMSIA, more physicochemical interactions of the molecule are taken into account, such as the hydrophobicity, hydrogen bond donor, and hydrogen bond acceptor [17].

Once all molecular fields are calculated, a linear correlation between the properties and the fields are expected, and can be obtained through a partial least squares (PLS) analysis. The quality of the QSTR model can be evaluated using the cross-validated coefficient q^2 and conventional coefficient r^2 . Moreover, the relationships can be graphed as contour maps, which provide an intuitive insight regarding the properties and molecular fields. Accordingly, the 3D-QSTR method can not only predict the tribological properties accurately, but can also provide us clear guidance regarding a further molecular design.

In the remainder of this paper, we describe how 3D-QSTR models were constructed using CoMFA and CoMSIA methods to predict the antiwear performance of a series of ester based oils. Furthermore, guided by the 3D-QSTR models, we designed and synthesized two new ester compounds. Experiment results showed that the new compounds achieve a

better antiwear performance, and indicate that 3D-QSTR methods have significant potential application in a lubricant design.

2 Materials and methods

2.1 Dataset

Wear scar diameter data were obtained through a series of ball–disk contact friction tests using a microtribometer (UMT-3, CETR). To determine the antiwear capability of each molecule, the wear scar diameters were related through simple mathematical manipulations.

$$WD = \log_{10} \left(\frac{MW}{D} \right) \quad (1)$$

In Eq. (1), WD represents the wear scar diameter scale, D is the measured size of the wear scar diameter, and MW is the molecular weight of the compound. For a compound, a higher WD value infers a smaller wear scar diameter (D), which means that the compound achieves a better antiwear performance.

A dataset containing 57 esters was used to construct the 3D-QSTR models. The dataset was randomly divided into two subsets: a training set containing 45 compounds (80% of all compounds), and a test set containing 12 compounds (20% of all compounds). The training set was used to develop the CoMFA and CoMSIA models, and the test set was used to validate their accuracy. The compounds with the highest and lowest wear scar diameters were included in the training set.

2.2 Molecular modeling and alignment

The 3D chemical structures of all esters were built using ChemBioDraw Ultra 11.0. Subsequently, all work was conducted using the software TRIPOS SYBYL-X. The partial atomic charges were calculated using the Gasteiger Hückel method, and the geometry optimization was conducted using a MAXIMIN energy minimizer with a Tripos force field. The structures of the compounds are listed in Table S1 in the Electronic Supplementary Material (ESM).

To construct the 3D-QSAR models, all 3D structural structures first need to be properly aligned. This is also the most crucial step in the model development.

In the field of drug design, the compound with the highest biological activity is generally chosen as the template molecule, and the native conformations of all other molecules are aligned into the native conformation of the template molecule, which is also the global minimum-energy conformation of the molecule. Correspondingly, compound A21 (see Table S1 in the ESM) was herein selected as the template molecule, which has the minimum wear scar diameter (D) for all 57 esters.

The native conformation of the template molecule was obtained through a combination of energy minimization and a molecular dynamics (MD) simulation. The MD simulation was carried out under a fixed temperature and pressure in a Tripos force field after energy minimization. The temperature was set to 300 K, the time step was set to 1.0 fs, and the conformations were saved every 5 fs. The pressure was determined using Eq. (2).

$$P = \frac{F}{\pi \left(\frac{D}{2}\right)^2 \times 1.01 \times 10^5} \quad (2)$$

where P is the pressure on the molecule; F is the load under the experimental friction conditions, the value of which is 98 N; and D is the measured wear scar diameter. The simulation was run for 10,000 fs. The energy-time diagram of the template molecule could then be obtained, and the minimum energy conformation was saved as a template. All other geometry-optimized conformations of the molecules were aligned to the template using the ALIGN DATABASE command in SYBYL.

2.3 CoMFA and CoMSIA studies

After the molecular structures were properly aligned, we could conduct CoMFA and CoMSIA analyses. In the CoMFA analysis, molecules were placed in a 3D lattice. The van der Waals and electrostatic interactions between the grid points and the probe atom were then calculated to construct steric and electrostatic fields. In our study, the grid spacing of the 3D lattice was set to 2 Å, and the probe atom was an sp³-hybridized carbon atom with a +1 charge. In the CoMSIA analysis, using the same lattice box and the probe atom, five physicochemical descriptors,

namely, steric (S), electrostatic (E), hydrophobic (H), hydrogen-bond donor (D), and hydrogen-bond acceptor (A), were calculated.

3D-QSTR models could then be derived using a PLS analysis, which is an extension of multiple linear regressions. Concretely, a leave-one-out (LOO) cross-validated method was used to evaluate the predictive capability and robustness of the model [10], and the cross-validation correlation coefficient (q^2) and optimum number of components (N) were reported. Once the optimal number of components was determined, the final model was generated using a non-cross-validated PLS analysis, and the squared correlation coefficient (r^2) values, standard error of the estimate (SEE), and the F-values were calculated. In the PLS analysis, CoMFA and CoMSIA descriptors were used as independent variables, and WD values were used as dependent variables. Additionally, we tried different combinations of the five CoMSIA descriptors. A model with higher q^2 and r^2 values was clearly better. We set $q^2 > 0.5$, $r^2 > 0.6$ as the criteria [18–21], and only the qualified models are summarized in Table 1. CoMFA and CoMSIA contour maps were defined using the StDev × Coeff mapping option contoured based on the contribution, which was set to 80% for the favored region and 20% for the disfavored region during the analysis. The criterion used for the decision was based on an analysis of the relationships between the tribology data and the CoMFA and CoMSIA descriptors.

3 Results and discussions

3.1 CoMFA analysis

The results are summarized in Tables 1 and 2. The optimal number of components N was determined using PLS with a cross-validation. The high q^2 (0.726), r^2 (0.969), and F-values (308.664), along with a low SEE value (0.038), show the good statistical correlation and reasonable predictability of the CoMFA model. The steric and electrostatic field contributions of this model were 0.504 and 0.496, respectively, indicating that the importance of the steric field and that of the electrostatic field were almost the same. The actual and predicted values of WD and D for all compounds are listed in Table 2 and illustrated in Figs. 1(a) and 1(b), which indicate good linear correlations. All the

Table 1 PLS statistics of CoMFA and CoMSIA models using combinations of the five field descriptors.

PLS statistics	CoMFA	CoMSIA							
		SEHDA	SEHA	SHDA	SEH	SHA	SHD	SH	SE
N	4	6	6	3	3	4	5	3	4
q^2	0.727	0.671	0.730	0.732	0.634	0.659	0.649	0.706	0.624
r^2	0.967	0.976	0.979	0.974	0.937	0.966	0.946	0.940	0.957
SEE	0.038	0.034	0.031	0.036	0.053	0.039	0.050	0.052	0.044
F-Value	308.664	257.713	319.397	235.955	204.368	284.529	136.586	212.490	223.082
S	0.504	0.245	0.262	0.308	0.313	0.319	0.440	0.453	0.555
E	0.496	0.222	0.229		0.299				0.445
H		0.320	0.332	0.403	0.388	0.411	0.535	0.547	
D		0.058		0.055			0.025		
A		0.154	0.178	0.234		0.270			

S, E, H, D, and A represent the steric, electrostatic, hydrophobic, hydrogen-bond, and acceptor property fields, respectively.

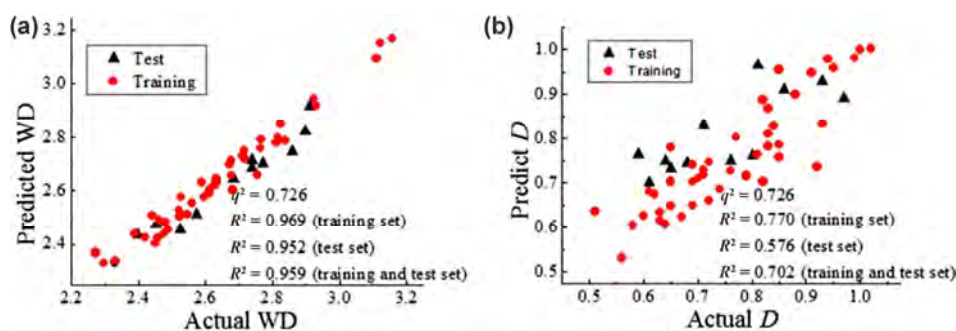


Fig. 1 Plots of the actual versus the predicted values of WD (a) and D (b) obtained by CoMFA model for the training and the test set of compounds.

above results confirm the rationality and predictive capability of our CoMFA model.

The structural characteristics of the compounds and the contribution of the molecular interaction fields can be explained through the contour maps of the CoMFA models.

The steric contour map (Fig. 2) shows three green contours (80% contribution), which indicates that within these regions, bulky groups are favored in molecules with smaller D values. The regions encircling the green regions are the yellow regions (20% contribution), which indicate that the bulky groups near the end of the carbon chain are disfavored.

As shown in Fig. 2, compound A21 has three groups near the green contours, whereas compound A14 has no groups near them. These observations are in accordance with the experimental results: A21 is the compound with the lowest D value, and A14 is the compound with the highest D value. For compounds

A15 and E06, compound A15 has two groups near the green contours, and compound E06 has three groups near the green contours and one group inserting the yellow contours, coinciding with their middle D value.

CoMFA electrostatic contour maps are shown in Fig. 3. In the blue regions (80% contribution), the increased positive charges are in favor of the D values, and in the red regions (20% contribution) the increased negative charges are in favor of them. Two large blue regions are located in the middle of the contour map, which indicates that any positive charge or electron deficient substitute will enhance the D values at these positions. The two small red regions correspond to the positions where the electronegative groups enhance the D values. For the ester-based oils, most of the compounds have relatively low electronegative or electropositive fields, but the electrostatic field has a definite influence on them. For the two compounds,

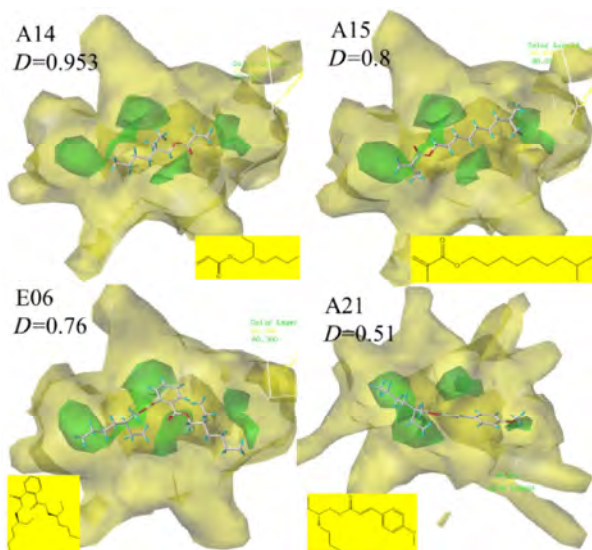


Fig. 2 CoMFA contour diagram for antiwear with embedded A14, A15, E06 and A21 as reference for steric fields, respectively. Green and yellow regions represent the favored and disfavored steric bulk, respectively.

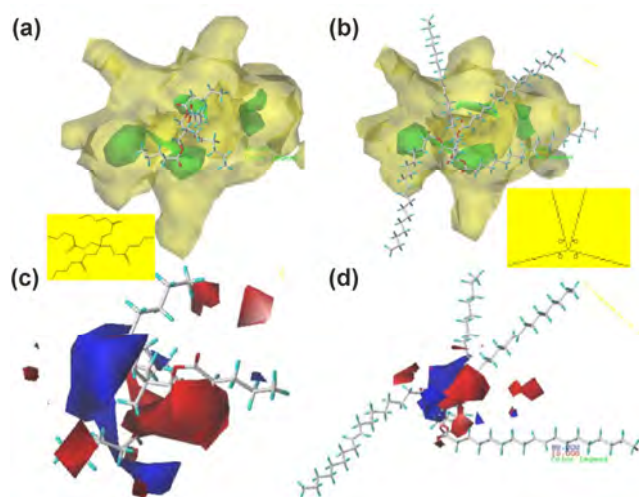


Fig. 3 CoMFA contour diagram for antiwear with embedded D01 and D04 as reference for both steric and electrostatic fields. (a) D01, steric; (b) D04, steric; (c) D01, electrostatic; (d) D04, electrostatic. Green and yellow regions show where steric bulk is favored and disfavored, respectively. Blue region shows that positive charge is favored while red region shows that negative charge is favored.

D01 and D04, which have similar green regions in a steric field, more yellow regions of D04 should result in a poor antiwear performance; in practice, however, compounds D01 and D04 show a similar antiwear performance ($D = 0.81$ and 0.83 , respectively), which can be explained by the electrostatic field having a

greater positive contribution on D04 (Figs. 3(c) and 3(d)). These results demonstrate that both steric and electrostatic fields are important in the CoMFA model.

3.2 CoMSIA analysis

As shown in Table 1, although the CoMFA and CoMSIA SE models are both built based on their steric and electrostatic properties, the calculations of their van der Waals and electrostatic interactions differ. Therefore, q^2 , r^2 , and the contributions of the steric and electrostatic fields are also different. The CoMSIA SE model has smaller q^2 and r^2 values, and the electrostatic field has a smaller contribution to the model. Similarly, the cross-validated q^2 of the SEHA and SHA models is 0.730 and 0.659, respectively, which indicates that the electrostatic field in CoMSIA has a significant influence on the establishment of the model. In general, however, the CoMSIA model can describe the structure-activity relationship more accurately and predictively, which is due to the fact that when CoMSIA descriptors are calculated, some of the inherent deficiencies arising from the functional form of the Lennard–Jones and Coulomb potentials can be avoided using a Gaussian function for the distance dependence between the probe atom and molecule [22].

For the SHDA model, although the cross-validated q^2 is slightly bigger than that of the SHA model, r^2 and the F-value are smaller, and the contribution of the hydrogen-bond donor in this model is only 0.055. Therefore, the hydrogen-bond donor can be considered an irrelevant factor in the establishment of the CoMSIA model.

After comparing the statistical indicators of the predicted results with different models, four descriptors, i.e., steric, electrostatic, hydrophobic, and hydrogen-bond acceptor (SEHA) descriptors, were selected for building the CoMSIA model. The PLS analysis revealed a cross-validated q^2 of 0.730 with an optimum number of components of six, and a conventional r^2 of 0.979 with a standard error of 0.031. The corresponding field contributions of the steric, electrostatic, hydrophobic, and hydrogen-bond acceptor descriptors were 0.262, 0.229, 0.332, and 0.178, respectively. We also used the CoMSIA model to predict the WD and D values of the test set compounds. The predicted and actual WD and D values are presented in Figs. 4(a) and 4(b). The

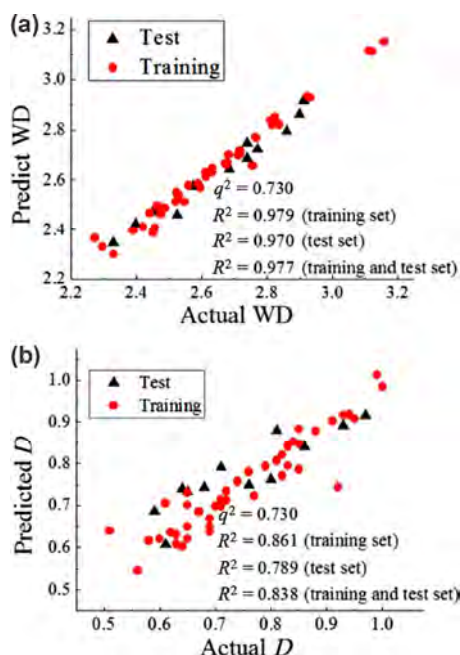


Fig. 4 Plots of the actual versus the predicted values of WD (a) and D (b) obtained by CoMSIA model for the training and the test set of compounds.

results indicate that the proposed CoMSIA model developed using the steric, electrostatic, hydrophobic, and hydrogen-bond acceptor fields can predict the antiwear performance of the ester compounds very well. The results of the SEHA model are slightly better than those of the CoMFA model.

For the steric and electrostatic fields, the CoMFA and CoMSIA models have similar contour diagrams, which further illustrate that the 3D-QSTR models can be constructed using both CoMFA and CoMSIA methods.

In the CoMSIA model, the hydrophobicity and hydrogen-bond acceptor are two other important descriptors. As shown in Table 1, the hydrophobic field makes a considerable contribution to the CoMSIA QSTR model, which means that the hydrophobicity is an important descriptor of the antiwear properties. As shown in Fig. 5, compared with compound B13, compound B12 with a hydrophobic long carbon chain was superimposed on the CoMSIA hydrophobic contour map (white, favored; yellow, disfavored), which clearly shows that a longer carbon chain is disfavored with the D values.

As shown in Fig. 6, compounds A18 and E02 were superimposed on the CoMSIA hydrogen-bond acceptor

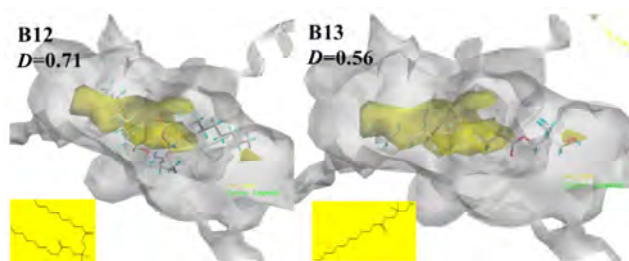


Fig. 5 CoMSIA contour diagram for hydrophobic field with embedded B12 and B13 as reference. White and yellow regions show that hydrophobic substitution is favored and disfavored, respectively.

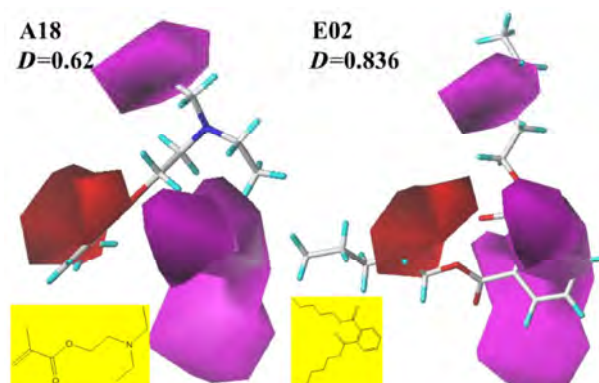


Fig. 6 CoMSIA contour diagram for hydrogen-bond field with embedded A18 and E02 as reference. Magenta and red regions show where hydrogen-bond acceptor is favored and disfavored, respectively.

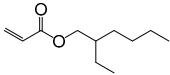
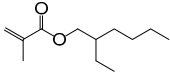
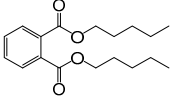
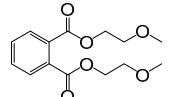
contour map (magenta, favored; red, disfavored). Clearly, the nitrogen atom of A18 is near the two magenta areas, and can accept a proton as a hydrogen-bond acceptor. Therefore, A18 has a better antiwear performance benefitting from the contribution of the hydrogen-bond acceptor field in comparison with E02.

3.3 Design of new potential ester-based oils

According to the detailed contour analyses of both the CoMFA and CoMSIA models, different modifications can be attempted on the potential molecule to enhance the antiwear activity.

For example, two new compounds (2-ethylhexyl methacrylate and bis(methylglycol) phthalate) were introduced to estimate the prediction capability of the models. The structure and D values of the new compounds as compared with their respective reference compounds are presented in Table 2. As the table indicates, the models exhibit a good prediction performance because the relative errors of the actual

Table 2 Comparison of the structure and *D* values of the two new compounds and their reference compounds.

Compounds	Structure formula	Actual <i>D</i> values	Predicted <i>D</i> values	Relative error
2-ethylhexyl acrylate*		0.953	0.932	2.2%
2-ethylhexyl methacrylate#		0.93	0.897	3.5%
Dipentyl phthalate*		0.836	0.851	1.8%
Bis(methylglycol) phthalate#		0.79	0.815	3.2%

*reference compounds, #new compounds

and predicted *D* values are less than 5% for all the introduced compounds. 2-ethylhexyl methacrylate was generated by introducing a steric methyl group into compound A14 (2-ethylhexyl acrylate), and therefore has a better antiwear performance with a smaller wear scar diameter of 0.93 mm. Relative to dipentyl phthalate (compound E02), bis(methylglycol) phthalate was generated by replacing two carbon atoms of the carbon chains with oxygen atoms, which exhibited a better antiwear performance owing to the capability of accepting protons derived from the lone pair of electrons of the oxygen atom.

As future work, more compounds will be designed based on suggestions from the CoMSIA and CoMFA models, and a potential ester-based oil with excellent antiwear performance will be screened and synthesized.

4 Conclusions

The present study dealt with the 3D-QSTR of a series of ester compounds as lubricant-based oils. Robust CoMFA and CoMSIA models with a high predictive performance based on a PLS analysis were constructed. As compared to CoMFA, CoMSIA can provide a better statistical model with more precise contour maps, and possesses more prediction capabilities. Through an analysis of the model parameters and contour maps, the structure-activity relationship was presented in detail, and some useful information regarding a structural modification was provided. These models can also be used to make primary predictions for the antiwear performance of untested compounds.

Acknowledgment

This work was supported by the National Nature Science Foundation of China (NSFC, No. 51675395).

Electronic Supplementary Material: Supplementary Material (Tables S1 and S2) is available in the online version of this article at <https://doi.org/10.1007/s40544-017-0175-5>.

Open Access: The articles published in this journal are distributed under the terms of the Creative Commons Attribution 4.0 International License (<http://creativecommons.org/licenses/by/4.0/>), which permits unrestricted use, distribution, and reproduction in any medium, provided you give appropriate credit to the original author(s) and the source, provide a link to the Creative Commons license, and indicate if changes were made.

References

- [1] Mortier R M, Fox M F, Orszulik S T. *Chemistry and Technology of Lubricants*. The Netherlands: Springer, 2010.
- [2] Mang T, Dresel W. *Lubricants and Lubrication*. Germany: Wiley VCH, Weinheim, 2001.
- [3] Arvind K, Anand Solomon K, Rajan S S. QSAR studies on diclofenac analogues as potent cyclooxygenase inhibitors using CoMFA and CoMSIA. *Medicinal Chemistry Research* **23**: 1789–1796 (2014)
- [4] Pourbasheer E, Amanlou M. 3D-QSAR analysis of anti-cancer agents by CoMFA and CoMSIA. *Medicinal Chemistry Research* **23**: 800–809 (2014)

- [5] Rao G W, Hu C H, Ni J B, Wang J, Wang C, Wang B L. 3D-QSAR study using CoMFA and CoMSIA methods for a series of histone H3 phosphorylation inhibitors. *Medicinal Chemistry Research* **23**: 3244–3254 (2014)
- [6] Wu S F, Qi W, Su R X, Li T H, Lu D, He Z M. CoMFA and CoMSIA analysis of ACE-inhibitory, antimicrobial and bitter-tasting peptides. *European Journal of Medicinal Chemistry* **84**: 100–106 (2014)
- [7] Melo-Filho C C, Braga R C, Andrade C H. 3D-QSAR approaches in drug design: perspectives to generate reliable CoMFA models. *Current Computer-Aided Drug Design* **10**: 148–159 (2014)
- [8] Kumar R, Kumar M. 3D-QSAR CoMFA and CoMSIA studies for design of potent human steroid 5 α -reductase inhibitors. *Medicinal Chemistry Research* **22**: 105–114 (2013)
- [9] Singh S, Supuran T C. 3D-QSAR CoMFA studies on sulfonamide inhibitors of the Rv3588c β - carbonic anhydrase from mycobacterium tuberculosis and design of not yet synthesized new molecules. *Journal of Enzyme Inhibition and Medicinal Chemistry* **29**(3): 449–455 (2014)
- [10] Balasubramanian K P, Balupuri A, Gadhe G C, Cho J S. 3D-QSAR modeling study on 7-aminofuro [2,3-c] pyridine derivatives as TAK1 inhibitors using CoMFA and CoMSIA. *Medicinal Chemistry Research* **24**: 2347–2365 (2015)
- [11] Dai K, Gao X L. Estimating antiwear properties of lubricant additives using a quantitative structure tribo-ability relationship model with back propagation neural network. *Wear* **306**(1–2): 242–247 (2013)
- [12] Gao X L, Wang Z, Zhang H, Dai K, Wang T T. A quantitative structure tribo-ability relationship model for ester lubricant base oils. *Journal of Tribology* **137**(2): 021801-1–021801-7 (2015)
- [13] Gao X L, Wang Z, Zhang H, Dai K. A three dimensional quantitative structure-tribological relationship model. *Journal of Tribology* **137**(2): 021802-1–021802-2(2015)
- [14] Tripos L P. The Tripos Bookshelf for SYBYL-X 1.1.
- [15] Oprea T I, Waller C L, Marshall G R. Three-dimensional quantitative structure-activity relationship of human immunodeficiency virus (I) protease inhibitors. 2. Predictive power using limited exploration of alternate binding modes. *Journal of Medicinal Chemistry* **37**(14): 2206–2215 (1994)
- [16] Temiz-Arpaci O, Tekiner-Gulbas B, Yildiz I, Aki-Sener E, Yalcin I. 3D-QSAR analysis on benzazole derivatives as eukaryotic topoisomerase II inhibitors by using comparative molecular field analysis method. *Bioorganic & Medicinal Chemistry* **13**(23): 6354–6359 (2005)
- [17] Ramasamy T, Raj K, Vem A, Elizabeth MS, Bulusu G, Asit K C. Three-dimensional quantitative structure (3D-QSAR) activity relationship studies on imidazolyl and N-pyrrolylheptenoates as 3-hydroxy-3-methylglutaryl-CoA reductase (HMGR) inhibitors by comparative molecular similarity indices analysis (CoMSIA). *Bioorganic & Medicinal Chemistry Letters* **15**: 1027–1032 (2005)
- [18] Bush B, Nachbar R J. Sample-distance partial least squares: PLS optimized for many variables, with application to CoMFA. *Journal of Computer-Aided Molecular Design* **7**(5): 587–619 (1993)
- [19] Yang Z, Sun P. 3D-QSAR study of potent inhibitors of phosphodiesterase-4 using a CoMFA approach. *International Journal of Molecular Sciences* **8**(7): 714–722 (2007)
- [20] Golbraikh A, Tropsha A. Beware of q²! *Journal of Molecular Graphics and Modelling* **20**: 269–276 (2002)
- [21] Golbraikh A, Tropsha A. Predictive QSAR modeling based on diversity sampling of experimental datasets for the training and test set selection. *Journal of Computer-aided Molecular Design* **16**: 357–369 (2002)
- [22] Klebe G, Abraham U, Mietzner T. Molecular similarity indices in a comparative analysis (CoMSIA) of drug molecules to correlate and predict their biological activity. *Journal of Medicinal Chemistry* **37**: 4130–4146 (1994)



Zhan WANG. She received her M.S. degree in food science and engineering in 2002 from Henan University of Technology, and graduated from Huazhong University



Xinei GAO. She received her M.S. degree in 1996 from Huazhong Normal University in organic chemistry, and graduated from Wuhan Research Institute of Materials Protection in mechanical design

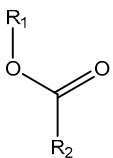
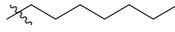
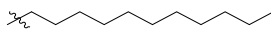
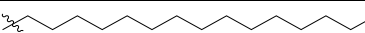
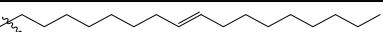
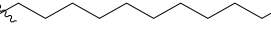
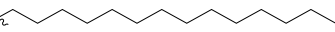
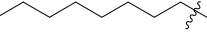
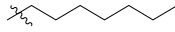
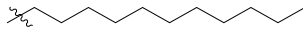
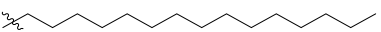
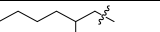
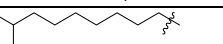
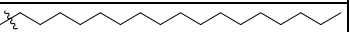
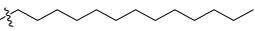
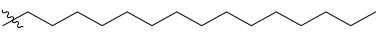
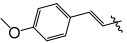
of Science and Technology in biomedical engineering with PhD degree in 2009. Currently she is an associate professor at Wuhan Polytechnic University. Her research interests include organic chemistry and chemical computing.

and theory with PhD degree in 2006. Currently she is a full professor at Wuhan Polytechnic University, member of Chinese Tribology Association. She is interested in tribology chemistry, chemical computing, and designation of lubricant.

Electronic Supplementary Material

Estimating antiwear properties of esters as potential lubricant-based oils using QSTR models with CoMFA and CoMSIA

Zhan WANG¹, Tingting WANG², Guoyan YANG¹, Xinlei GAO^{2,*}, Kang DAI³¹ College of Food Science and Engineering, Wuhan Polytechnic University, Wuhan 430023, China² School of Chemical and Environmental Engineering, Wuhan Polytechnic University, Wuhan 430023, China³ College of Pharmacy, South-Central University for Nationalities, Wuhan 430074, ChinaSupporting information to <https://doi.org/10.1007/s12274-017-0175-5>**Table S1** Esters for the models.

structure	No	D	WD	R ¹	R ²
	A01	0.69	2.4629		
	A02 ^a	0.61	2.5733		
	A03	0.77	2.5225		
	A04	0.69	2.6152		
	A05	0.65	2.682		
	A06	0.83	2.6106		
	A07	0.65	2.4573	-CH ₃	
	A08 ^a	0.64	2.5249		
	A09	0.63	2.6327		
	A10	0.92	2.2724		-CH ₃
	A11	0.61	2.4509	-C ₂ H ₅	
	A12	0.58	2.5952		
	A13	0.6	2.6759		
	A14 ^a	0.953	2.3288		
	A15 ^a	0.8	2.4517		
	A16	0.65	2.7167		
	A17	0.85	2.2965		
	A18	0.62	2.4754		
	A19	0.63	2.6327		
	A20	0.7	2.6299		
	A21	0.51	2.7554		
	A22	0.82	2.4881		

* Corresponding author: Xinlei GAO, E-mail: gaoxl0131@163.com

(Continued)

structure	No	<i>D</i>	WD	R ¹	R ²
	B01	0.85	2.5276		
	B02 ^a	0.59	2.8592		
	B03 ^a	0.76	2.9109		
	B04	0.72	2.6773		
	B05 ^a	0.68	2.68401		
	B06	0.74	2.7158		
	B07	0.71	2.9305		
	B08	0.82	2.4408		
	B09	0.65	2.5455		
	B10 ^a	0.97	2.3975		
	B11 ^a	0.65	2.7392		
	B12	0.71	2.7643		
	B13	0.56	2.9228		
	C01	1.02	2.3303		-CH ₃
	C02	0.99	2.4198		-C ₂ H ₅
	C03	1	2.4805		
	C04	0.95	2.5594		
	C05 ^a	0.86	2.7382		
	C06	0.67	3.1211		
	C07	0.91	2.8169		
	C08	0.72	3.11		
	D01	0.81	2.766		
	D02	0.85	2.8376		
	D03 ^a	0.81	2.8983		
	D04	0.83	3.1579		
	E01	0.64	2.8239		
	E02	0.836	2.5887		
	E03	0.83	2.6726		
	E04 ^a	0.71	2.7706		
	E05	0.84	2.5203		
	E06	0.76	2.7109		
	E07	0.69	2.8111		
	E08	0.93	2.39		
	E09	0.88	2.6124		
	E10	0.94	2.5297	-C ₂ H ₅	

Table S2 Abbreviation.

Abbreviation	Meaning
CoMFA	Comparative molecular field analysis
CoMSIA	Comparative molecular similarity indices analysis
QSAR	Quantitative structure activity relationship
QSTR	Quantitative structure tribo-ability relationship
<i>D</i>	the measured size of the wear scar diameter
WD	wear scar diameter scale
PLS	partial least-squares
LOO	leave-one-out
SEE	standard error of estimate
S	Steric field, CoMSIA descriptor
E	Electrostatic field, CoMSIA descriptor
H	Hydrophobic field, CoMSIA descriptor
D	hydrogen-bond donor field, CoMSIA descriptor
A	hydrogen-bond acceptor field, CoMSIA descriptor
SEHDA	CoMSIA model built by S, E, H, D, A
SEHA	CoMSIA model built by S, E, H, A
SEDA	CoMSIA model built by S, E, D, A
SEH	CoMSIA model built by S, E, H
SHA	CoMSIA model built by S, H, A
SHD	CoMSIA model built by S, H, D
SH	CoMSIA model built by S, H
SE	CoMSIA model built by S, E

Finite element simulation and experimental test of the wear behavior for self-lubricating spherical plain bearings

Yahong XUE^{1,2,3}, Jigang CHEN^{1,2,*}, Sumin GUO^{1,2}, Qingliang MENG^{1,2}, Juntong LUO^{1,3}

¹ School of Mechanical Engineering, Yanshan University, Qinhuangdao 066004, China

² Aviation Key Laboratory of Science and Technology on Generic Technology of Self-Lubricating Spherical Plain Bearing, Yanshan University, Qinhuangdao 066004, China

³ Education Ministry Key Laboratory of Advanced Forging and Stamping Technology and Science, Yanshan University, Qinhuangdao 066004, China

Received: 27 August 2017 / Revised: 04 November 2017 / Accepted: 26 December 2017

© The author(s) 2018. This article is published with open access at Springerlink.com

Abstract: In this study, based on the classical Archard adhesion wear theory, a three-dimensional finite element model was established, with the aim of simulating the failure process of self-lubricating spherical plain bearings in the swinging wear condition. The results show that the self-lubricating spherical plain bearings go through two different stages during the wear process, namely, initial wear stage and stable wear stage. Because the large contact points wear out during the initial wear stage, the maximum contact pressure decreases as the test period increases. The relatively larger wear depth region shows elliptical distribution, and the maximum distribution appears in the central contact area. The wear depth reaches 0.974 mm after swinging 25,000 times. PTFE fibers, which possess a good friction performance but poor abrasion resistance, abundantly exist on the friction surfaces of the fabric liner. Consequently, the friction torque during the initial wear stage is slightly smaller than the friction torque during the stable wear stage; however, the wear rate during the initial wear stage is high. The reliability and effectiveness of the finite element model are verified by experiment. The developed finite element model can be used for the analysis of the wear mechanisms of bearings and the prediction of the service life of bearings.

Keywords: spherical plain bearing; wear mechanisms; wear depth; contact pressure; simulation

1 Introduction

A self-lubricating spherical plain bearing, as a type of spherical sliding bearings, comprises a metal inner ring, outer ring, and self-lubricating fabric liners. Owing to their compact structure, small friction coefficient, and strong impact resistance, self-lubricating spherical plain bearings have been widely used in aircraft landing gears, railway locomotives, brake vibration, and in shock absorption system [1–4].

At present, it is generally believed that the abrasive wear of fabric liners is the main reason for the failure of self-lubricating spherical plain bearings. The wearing

of fabric liners enlarges the clearance between the inner and outer rings of self-lubricating spherical plain bearings, thus resulting in the vibration of bearings, low-working accuracy, and even the failure of the bearings during their service process [5–7].

Experimental exploration is the main method for investigating the friction and wear properties of self-lubricating spherical plain bearings at present [8–10]. In this method, the mechanism of wear failure is investigated by observing macroscopic phenomena such as the morphology and composition change of worn surfaces. However, this experimental exploration is not only time-consuming and costly but also

* Corresponding author: Jigang CHEN, E-mail: 24000082@qq.com

unsatisfactory when it comes to practical problems such as uneven stress distributions or changeable working loads during the wear lifespan of fabric liners [11–15].

Recently, simulation technology based on the finite element method has been widely used to investigate wear problems [16–20]. Bortoleto et al. [21] used finite element software to write user subroutines, and simulated the material removal process of material in pin-on-plate tests based on the Archard wear model. Although establishing the model and writing the subprogram were very complicated, the analysis results indicated that the complex nonlinear wear process could be simulated with a series of discrete quasi static models. Shen et al. [22] established a two-dimensional finite element wear model of self-lubricating spherical plain bearings, which provided an effective way of predicting the wear life of mechanical components. However, the two-dimensional model could not reflect the 3D contact pressure distributions on the whole wear surface. Lu et al. [23] investigated the influences of motion types of the bearings on the distributions of contact pressure by establishing a 3D simplified model. However, this model could not simulate the wear profile and progressive wear process of the bearings.

In this paper, a 3D finite element model of self-lubricating spherical plain bearings was established to simulate the wear behavior of bearings under swing motion. Based on the analysis of the simulation and experimental tests, the wear mechanism of the fabric liner was revealed.

2 Archard wear model of the fabric liner

2.1 Archard adhesive wear theory

The essence of the wear problem is the material loss produced at the contact surface when relative motion occurs. At present, the Archard adhesive wear model is generally used to calculate the wear loss [24]:

$$V = \frac{K}{H} F_n L \quad (1)$$

where V is the wear volume, K is the adhesive wear factor, H is the hardness of the material, F_n is the normal load, and L is the relative sliding distance of

worn surfaces.

Regarding engineering application, the wear depth offers more practical significance. Therefore, a differential form of the Archard wear model can be obtained by dividing both sides of Eq. (1) by a small contact area Δs :

$$\frac{dV}{\Delta s} = \frac{K}{H} \frac{F_n}{\Delta s} dL \quad (2)$$

where $dV/\Delta s$ is the wear depth dh , $F_n/\Delta s$ is the local contact pressure P , and K/H is the linear wear factor K_d . Here, dL can be replaced by the product of the relative sliding velocity v and test time dt . Thus, the local increment of wear depth can be achieved by the following equation:

$$\frac{dh}{dt} = K_d P v \quad (3)$$

The liner wear factor K_d is generally obtained by experimental methods. However, usually the liner wear factor K_d varies with the contact pressure P and relative sliding velocity v . Taking into account the influence of the relative sliding velocity and contact pressure, Eq. (3) can be modified, and the wear rate can be expressed as follows:

$$w = K_d P^m v^n \quad (4)$$

where w is the wear rate, m is the pressure exponent, and n is the velocity exponent.

2.2 Pin-on-plate sliding wear test of the fabric liner

In order to obtain the Archard wear model of fabric liners, the 3-level orthogonal test was carried out on fabric liners under different loads (50 MPa, 75 MPa, and 100 MPa) and sliding velocities (1.896 mm/s, 2.528 mm/s, and 3.160 mm/s). The wear test was carried out on the friction and wear testing machine. The wear form was a pin-on-plate reciprocating sliding wear. The upper sample was a cylindrical pin with a diameter of 4 mm and a length of 12 mm. This testing machine and schematic diagram of pin-on-plate reciprocating sliding wear test are shown in Fig. 1. Before the wear test, the fabric liners were adhered to steel plates with phenolic-acetal resin. The changes of wear depth with time were recorded automatically by

the wear testing machine, and the results are shown in Fig. 2.

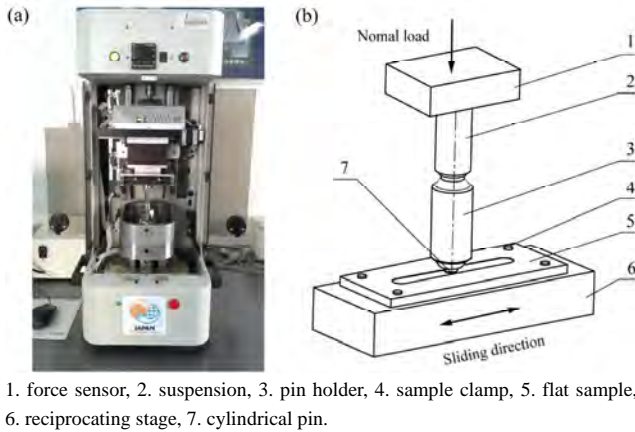


Fig. 1 Physical diagram and schematic diagram of wear test of fabric liners: (a) photograph of the friction and wear tester, and (b) schematic diagram of pin-on-plate reciprocating sliding wear test.

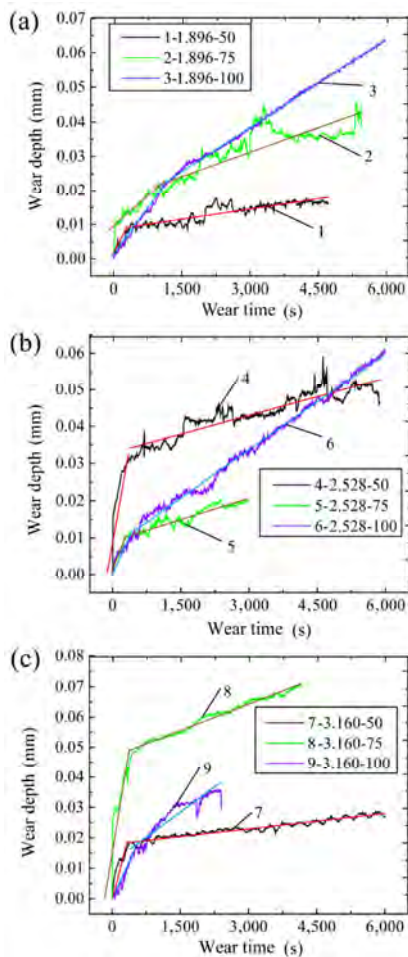


Fig. 2 Variation curves of wear depth of fabric liners under different pressures and velocities: (a) 1.896 mm/s; (b) 2.528 mm/s; and (c) 3.160 mm/s.

It can be seen from Fig. 2 that the wear curves of fabric liners consist of two stages. During the initial wear stage, the wear of fabric liners is fast and the plastic deformation on the wear surface is large. These lead to an increase in the local temperature and affirm adhesion. During the stable wear stage, the elastic-plastic contact conditions are established on wear surfaces, and thus the wear on the surfaces of fabric liners becomes slower. The two slopes on the wear curves are calculated, and the calculated results are taken as the wear rate of the two wear stages of the fabric liner. The wear rate of the initial wear stage and stable wear stage of fabric liners under different pressures and sliding velocities are shown in Tables 1 and 2, respectively.

The wear rates shown in Tables 1 and 2 are fitted using a formula fitting software. The Archard wear models of fabric liners during the initial wear stage and the stable wear stage are obtained as follows:

$$w_1 = K_d \cdot P^m \cdot V^n = 2.415 \times 10^{-8} \cdot P^{1.54} \cdot V^{-0.499} \quad (5)$$

$$w_2 = K_d \cdot P^m \cdot V^n = 5.32 \times 10^{-10} \cdot P^{0.94} \cdot V^{0.98} \quad (6)$$

3 Finite element modeling and simulation

3.1 Basic definition

Taking XRA12 self-lubricating spherical plain bearing as an example, the finite element model of a self-

Table 1 Wear rate (mm/s) of fabric liners in initial wear stage.

Sliding velocity (mm/s)	Pressure (MPa)		
	50	75	100
1.896	18.137E-6	11.307E-6	17.124E-6
2.528	55.214E-6	35.185E-6	25.214E-6
3.160	38.231E-6	61.889E-6	27.384E-6

Table 2 Wear rate (mm/s) of fabric liners in stable wear stage.

Sliding velocity (mm/s)	Pressure (MPa)		
	50	75	100
1.896	1.90262E-6	4.19248E-6	6.44197E-6
2.528	3.58619E-6	3.80271E-6	8.78264E-6
3.160	1.59565E-6	6.18368E-6	9.99676E-6

lubricating spherical plain bearing in swinging wear tests is established. The dimensions, motion type and finite element mesh model of self-lubricating spherical plain bearing are shown in Fig. 3. As displayed in Fig. 3(b), θ_0 indicates the maximum swing motion angle, which is 25° . The numbers 1–4 in Fig. 3(b) as well as the arrow directions indicate the four steps in one swing cycle and swing directions of the pin, respectively. The swing frequency and swing times are, respectively, 0.2 Hz and 25,000 revolutions. To simulate the experimental conditions of the bearing system, a loading plate and a pin are also implemented in the modeling, both of which are considered as flexible bodies. The radial load applied on the loading plate is 18 kN.

3.2 Materials, contacts and wear definition

The inner ring is made of 9Cr18 stainless steel and the outer ring is made of 17-4PH stainless steel. The fabric liner is anisotropic material, which can use spherical coordinates to define its anisotropic material properties. The material properties of the bearing are shown in Table 3.

The bonding contact is set up between the spherical surface of the outer ring and bonding surface of the liner, as well as between the cylinder surface of the outer ring and loading plate. A bonding contact is also defined between the pin and the inner ring. Hence, the inner ring rotates with the pin. Frictional contact between the friction surface of the fabric liner (as contact surface) and the spherical surface of the inner ring (as target surface) is defined. The friction

coefficient is set as 0.08, which was obtained from the pin-on-plat sliding wear test of the fabric liner. The contact elements and target elements are defined as CONTA173 and CONTA174, respectively, because they support modeling wear.

To activate the wear in the contact surface, three wear parameters (liner wear factor K_d , pressure exponent m and velocity exponent n) are defined in the material model via the TB command and assigned to the contact elements of the frictional contact. The parameters of K_d , m and n during the initial wear stage are expressed in Eq. 5, namely $K_d = 2.415 \times 10^{-8}$, $m = 1.54$ and $n = -0.499$. Similarly, the parameters of K_d , m and n during the stable wear stage are expressed in Eq. 6, namely $K_d = 5.32 \times 10^{-10}$, $m = 0.94$ and $n = 0.98$. During the swing process of the spherical bearing, the wear occurs on both the fabric liner and inner ring. Because the wear loss on the spherical surface of the inner ring is very small compared with that of the fabric liner, only mass loss of the fabric liner is considered in the simulation.

3.3 Steps, load, and boundary conditions definition

The analysis type is set as “static, structural”. Owing to the large deformation of the fabric liner, the geometric nonlinear effect is considered.

The swinging wear analysis of self-lubricating spherical plain bearing can be divided into 3 steps. The first step is to establish a stable contact relationship between the contact surfaces of the tested bearing and gradually apply the radial load. Thus, an equivalent radial load of 18 kN is gradually applied to the loading

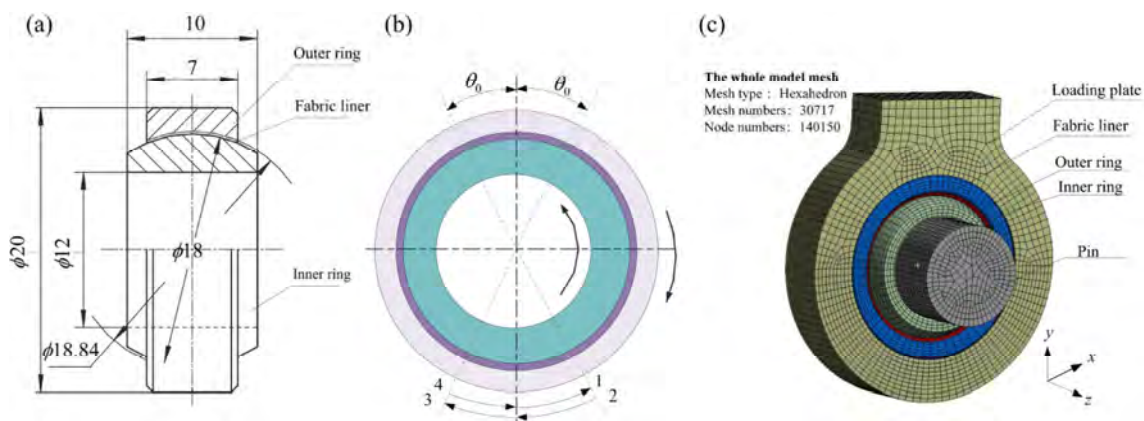


Fig. 3 The schematic diagram of dimensions, motion type and finite element mesh model of the test bearing: (a) dimensions of XRA12 self-lubricating spherical plain bearing, (b) swing motion steps of inner ring, and (c) finite element mesh model.

Table 3 The mechanical properties of self-lubricating spherical plain bearing.

Elastic constants	Outer ring	Inner ring	Fabric liner
E_1 (GPa)	210	203.89	52.04
E_2 (GPa)	—	—	4.71
ν	0.24	0.28	0.37
G_{12} (GPa)	—	—	1.84
G_{23} (GPa)	—	—	3.45

plate in the negative direction of the y -axis. The radial load is kept unchanged during the next two steps.

The second and third steps are mainly to simulate the swinging wear process of the bearing during the initial wear stage and stable wear stage, respectively. A joint rotation is applied on the pin in the z direction, and it is defined as $URZ=25\sin(72\times\text{time})$. To prevent the loading plate from rotating under the friction force, the displacement boundary conditions of the loading plate are defined as $UX=UZ=URZ=0$ (U and UR indicate the line displacement and the rotation displacement, respectively).

3.4 Wear simulation routine

To analyze the dynamical wear problem with finite element method, the entire wear increment is discretized into many wear steps. For each wear step, the contact pressure and relative sliding velocity are calculated according to the contact state of contact nodes. Thereafter, the wear depth in this wear step is obtained by Eqs. (5) and (6). Thus, the wear depth of each node is obtained from the Eq. (7):

$$h_{j,i} = h_{j-1,i} + \Delta h_{j,i} \tag{7}$$

where $\Delta h_{j,i}$ is the wear depth of node i during the wear step j , $h_{j-1,i}$ is the total wear depth of node i in the previous $j-1$ wear steps, and $h_{j,i}$ is the total wear depth of node i in the previous j wear steps.

In the finite element simulation, the material loss in the contact surface is simulated by moving the contact node along the opposite direction of the contact normal. However, the reposition of the contact node results in a loss of equilibrium or a distorted finite element mesh, and thus fails in achieving an optimal solution. Therefore, the mesh is updated when the node moves such that it exceeds a specific proportion of the height of the corresponding element. The boundary displacement method is widely used to update the mesh in finite element analysis [25]. Figure 4 shows the basic procedures for simulating the wear evolution process.

4 Results and discussion

4.1 Contact pressure

Figure 5 shows the contact pressure distribution of fabric liners during both wear stages. During the initial wear stage, the maximum contact pressure appears in the middle contact area, and the contact pressure decreases along both circumferential and width directions. The higher contact pressure zone demonstrates a continuous and elliptic distribution. Owing to the ongoing wearing process, the location of the maximum contact stress does not change. However, the magnitude of the maximum contact pressure drops from 226 MPa to 218 MPa, and the distribution of contact stress is more uniform.

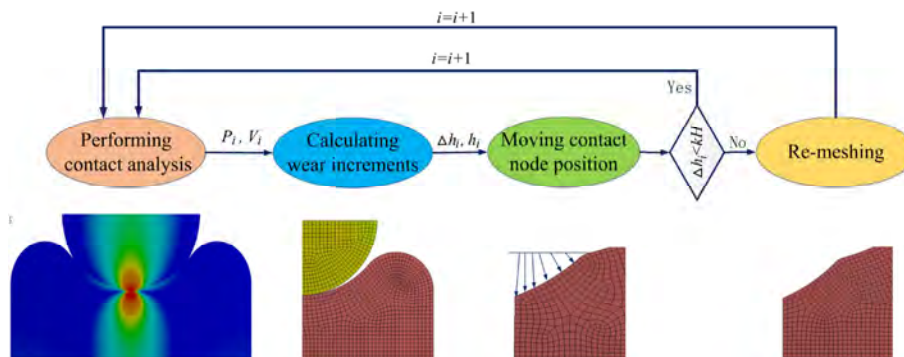


Fig. 4 Basic procedures for simulating the wear evolution process.

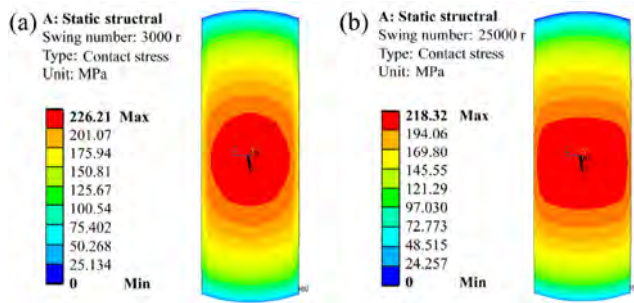


Fig. 5 Contact pressure distribution of fabric liners after different swing numbers: (a) 3,000 times and (b) 25,000 times.

The curve of the change in the maximum contact pressure with swing numbers is shown in Fig. 6. It can be seen from this figure that the maximum contact pressure decreases with increasing swing numbers. It reduces faster during the initial wear stage, and remains almost stable during the stable wear stage. The reason for this phenomenon can be explained as follows: under the action of radial load, the contact pressure at the small contact area of the contact center is large, and thus both the plastic deformation and wear speed here are large during the initial wear stage. As the running-in time extends, the contact point in the contact center is gradually flattened, and

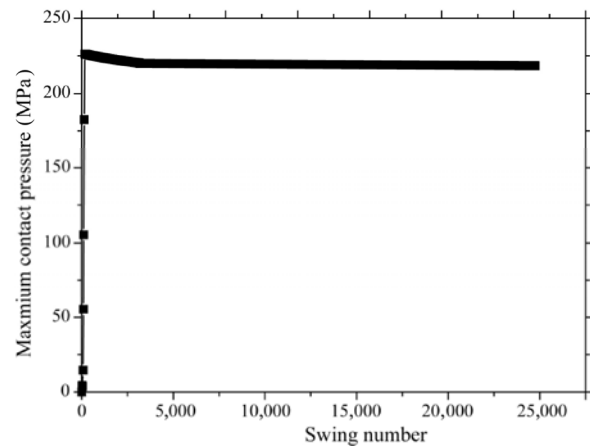


Fig. 6 The curve of maximum contact pressure with swing numbers.

the contact area gradually increases. Thus, the contact stress decreases and tends to be uniform.

4.2 Wear morphology

Figure 7 presents the wear depth distributions on the friction surface of the fabric liner after swinging 25,000 times. It can be seen from Fig. 7 that the wear depth is larger in the middle contact region and it decreases from the middle region in both

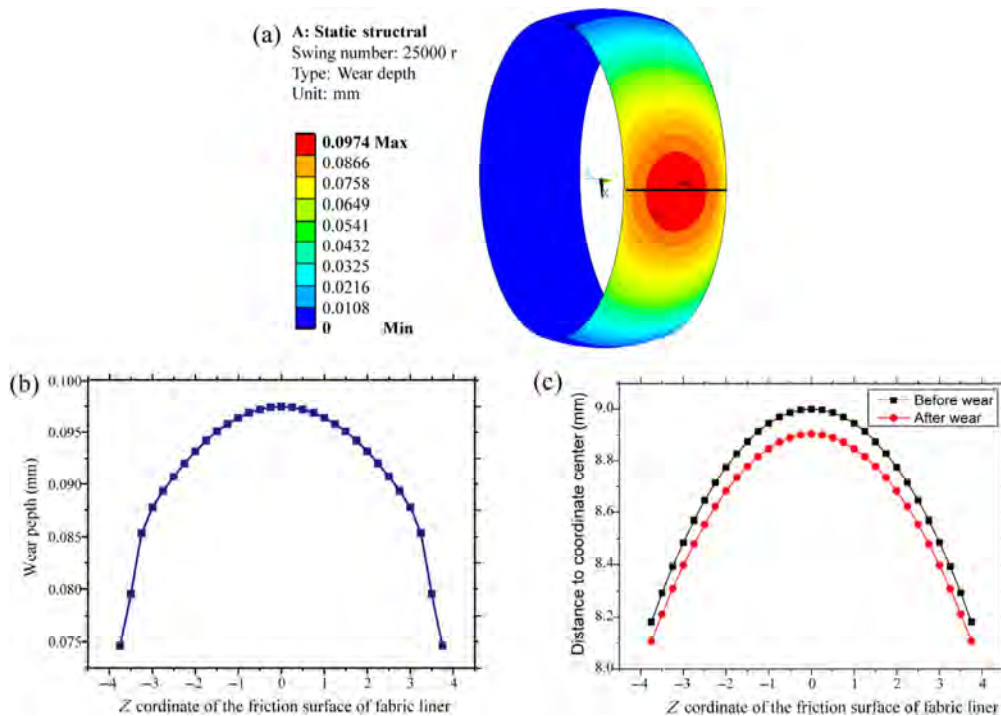


Fig. 7 Wear depth distributions on the friction surface of the fabric liner: (a) wear morphology obtained from simulation, (b) wear depth along the z direction, and (c) comparison of the friction surface of fabric liner before and after wear.

circumferential and width directions. The relatively larger wear depth region also shows elliptic distribution. The maximum wear depth is 0.0974 mm and it occurs at the central contact region. The wear depth of the two border regions is relatively small, which is 0.0746 mm. Therefore, it can be deduced that the wear failure of the fabric liner occurs first in the central contact region.

As indicated by Fig. 8, the wear depth of fabric liners varies with swing numbers. During the initial wear stage, the amount of wear depth presents a sharp increase. This indicates that the self-lubricating spherical plain bearings wear violently at this stage. When the swing number reaches approximately 3000, the wear rate tends to decrease with test period. Additionally, it maintains a relatively steady state over a long period of time. It can be inferred that the self-lubricating spherical plain bearing goes through two different stages during the whole wear process, namely initial wear stage and stable wear stage. As shown in Figs. 6 and 8, the change in contact pressure makes little contribution to the wear depth after the initial wear stage, and the wear rate remains almost constant. Hence, it can be inferred that the cumulative wear of the self-lubricating spherical plain bearing will reach 0.11 mm (the wear depth of bearing failure) after swinging 30,956 times. Therefore, the service life of the self-lubricating spherical plain bearing can be predicted.

5 Wear test and results

5.1 Swinging wear test of self-lubricating spherical plain bearing

The swinging wear test is conducted on a self-made service performance evaluation test machine of self-lubricating spherical plain bearings. The photograph of the swinging wear tester and the schematic diagram of loading devices are shown in Fig. 9. The outer ring is fixed and the inner ring swings continuously along with the pin. The dynamics radial load tests were carried out according to the aeronautical standards (SAE AS 81820 and EN2755). The radial load applied by the loading plate is 18 kN. The swing frequency is 0.2 Hz, and maximum swing angle is 25°. The

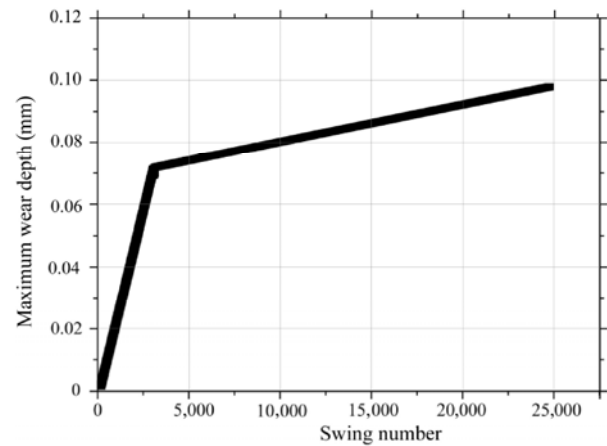


Fig. 8 The curve of the wear depth of fabric liners varies with swing numbers.

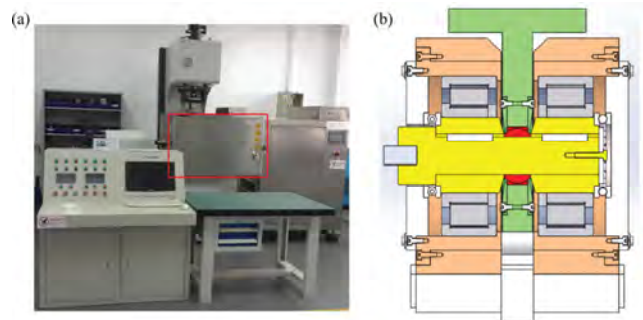


Fig. 9 Physical diagram and schematic diagram of swinging wear test of self-lubricating spherical plain bearing: (a) photograph of the swinging wear tester and (b) schematic diagram of loading devices.

experiments are carried out at room temperature. The friction torque is recorded automatically by a torque sensor in the test machine, and the wear depth of the fabric liner is measured by a displacement sensor installed under the tested bearing. After the wear test, the worn surface morphology of the fabric liner is observed by a confocal laser scanning microscope.

5.2 Wear morphology of the fabric liner

Figure 10 shows the worn surface morphology of the fabric liner. As seen in Fig. 10(a), the friction surface of the fabric liner is relatively smooth before the wear test, and the surface is covered with phenolic resin. The surface of the resin presents the indentation left when the fabric liner solidifies. Figure 10(b) shows that a wear scar exists in the middle contact region of the width direction after 25,000 times of swinging wear. Close to the ends of the bearing, the resin layer

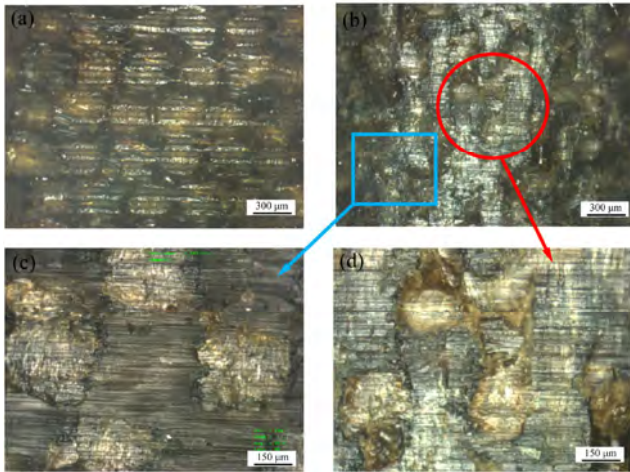


Fig. 10 The worn surface morphology of the fabric liner: (a) before wearing out, (b) after swinging 25,000 times, (c) the region closed to the end of the bearing, and (d) the middle contact region in the width direction.

on the surface of the liner has been worn off. Most of the surface area is covered with the black PTFE, and the yellow aramid fiber is faintly visible. This phenomenon can be explained as follows: PTFE fibers with poor wear resistance are easily worn out and form debris under frictional shearing force. The debris is pressed and filled in the pits of the friction surface. Because of the good tribological properties of PTFE material, a layer of PTFE lubricating film is gradually formed on the friction surface with increasing amount of PTFE fibers, which can prevent the direct contact between the inner ring and the fabric liner. Accordingly, the wear degree here is relatively small. However, because of the high contact pressure and frictional shearing force, the PTFE lubricating film in the middle contact region of the width direction is quickly fractured. A

large number of yellow aramid fibers are exposed on the surface of the fabric liner. Thus, the wear degree here is comparatively serious, which is consistent with the finite element simulation results.

5.3 Wear depth and friction torque

Figure 11 presents the curve of the wear depth and friction torque of fabric liners varies with swing numbers. The wear depth is approximately 0.93 mm after swinging 25,000 times for self-lubricating spherical plain bearing. Compared with the finite element simulation results, the relatively error of the maximum wear depth is approximately 4.50%. The friction torque in the initial wear stage is slightly smaller than that of the stable wear period. However, the wear rate during the initial wear stage is greater. The reason for this can be explained as follows: during the initial wear stage, a large number of PTFE fibers, which possess good friction performance and poor abrasion resistance, exist on the wear surface of the fabric liner. These fibers (mainly PTFE fibers) are extruded and deformed under the frictional shearing force. However, the debris produced in the friction process are filled in the interstices of the fabric liner surface. Therefore, the wear rate is larger at the initial wear stage, whereas the friction torque is smaller.

Owing to the development of the wear process, the proportion of PTFE fibers on the surface of the fabric liner decreases, while the proportion of aramid fibers increases. These aramid fibers possess excellent abrasion resistance. Moreover, the friction surface of the fabric liner is gradually filled up. Thus, the wear comes into a relatively stable stage, and the wear rate becomes small.

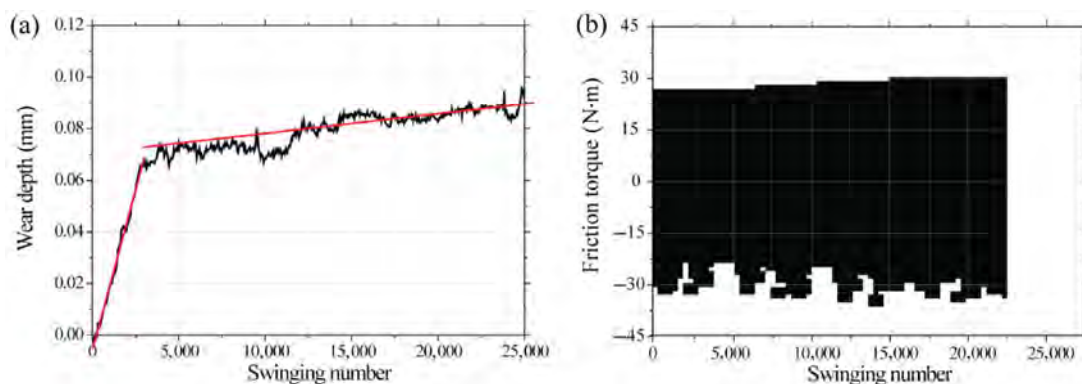


Fig. 11 Variation curves of the wear depth and friction torque with swing numbers: (a) wear depth and (b) friction torque.

6 Conclusions

(1) This paper presented both the procedures and results of the finite element simulation of a 3D swinging wear problem for self-lubricating spherical plain bearings. The proposed methods can be used for analyzing the wear mechanisms and predicting the service life of these bearings. It also provides a good reference for simulating all kinds of 3D wear problems.

(2) The self-lubricating spherical plain bearings went through two different stages during the swinging wear process: namely, initial wear stage and stable wear stage. Owing to the increase of the swing times, there was an increase in the friction torque and a decrease in the wear rate. This phenomenon is attributed to the PTFE fibers existing on the fabric surface. These PTFE fibers with small friction coefficient and large wear rate are worn out owing to the development of swinging wear process.

(3) The magnitude of contact pressure in the central contact region was the biggest, and it decreased along both the circumferential and axial directions. Because of the rapid wear in the central contact zone, the maximum contact pressure decreased with increasing of swing numbers.

(4) The maximum wear depth occurred in the central contact region. This was also the location of the wear failure zone. The value of wear depth reached 0.0974 mm after swinging 25,000 times.

Open Access: The articles published in this journal are distributed under the terms of the Creative Commons Attribution 4.0 International License (<http://creativecommons.org/licenses/by/4.0/>), which permits unrestricted use, distribution, and reproduction in any medium, provided you give appropriate credit to the original author(s) and the source, provide a link to the Creative Commons license, and indicate if changes were made.

References

- [1] Kim B C, Lee D G. Endurance and performance of a composite spherical bearing. *Compos Struct* **87**(1): 71–79 (2009)
- [2] Kim B C, Lee D G. Development of a spherical bearing with uni-directional carbon/epoxy composite. *Compos Struct* **89**(1): 102–109 (2009)
- [3] Barbero E J, Trovillion J, Mayugo J A, Sikkil K K. Finite element modeling of plain weave fabrics from photomicrograph measurements. *Compos Struct* **73**(1): 41–52 (2006)
- [4] Liu Z L, Shen X J. Study on the elastic properties of the woven fabric liner of spherical plain bearing with self-lubricating. *Adv Mater Res* **139–141**: 190–193 (2010)
- [5] Ma J, Yang Y L, Qi X W. Tribological performances of fabric self-lubricating liner with different weft densities under severe working conditions. *Indian J Fib Text Res* **40**(3): 293–300 (2015)
- [6] Qiu M, Duan C C, Chen L, Li Y C, Hu R S. Effect of clearance on thermodynamic characteristics of woven liner spherical plain bearing. *Appl Mech Mater* **668–669**: 164–167 (2014)
- [7] Qiu M, Miao Y W, Li Y C, Lu J J. Influence of ultrasonic modified liners on the adhesive and tribological performances of self-lubricating radial spherical plain bearings. *Tribol Trans* **59**(4): 655–662 (2016)
- [8] Park D C, Kim S S, Kim B C, Lee S M, Lee D G. Wear characteristics of carbon-phenolic woven composites mixed with nano-particles. *Compos Struct* **74**(1): 89–98 (2006)
- [9] Qiu M, Miao Y W, Li Y C, Lu J J. Film-forming mechanisms for self-lubricating radial spherical plain bearings with hybrid PTFE/aramid fabric liners modified by ultrasonic. *Tribol Int* **87**: 132–138 (2015)
- [10] Ren G N, Zhang Z Z, Zhu X T, Men X H, Jiang W, Liu W M. Sliding wear behaviors of Nomex fabric/phenolic composite under dry and water-bathed sliding conditions. *Friction* **2**(3): 264–271 (2014)
- [11] Fan B L, Yang Y L, Feng C, Ma J, Tang Y, Dong Y, Qi X W. Tribological properties of fabric self-lubricating liner based on organic montmorillonite (OMMT) reinforced phenolic (PF) nanocomposites as hybrid matrices. *Tribol Lett* **57**(3): 22 (2015)
- [12] Zhang Y H, Choi J R, Park S J. Thermal conductivity and thermo-physical properties of nanodiamond-attached exfoliated hexagonal boron nitride/epoxy nanocomposites for microelectronics. *Compos Part A* **101**: 227–236 (2017)
- [13] Gu D P, Yang Y L, Qi X W, Deng W, Shi L. Influence of weave structures on the tribological properties of hybrid Kevlar/PTFE fabric composites. *Chin J Mech Eng* **25**(5): 1044–1051 (2012)
- [14] Qiu M, Yang Z P, Lu J J, Li Y C, Zhou D W. Influence of step load on tribological properties of self-lubricating radial spherical plain bearings with PTFE fabric liner. *Tribol Int* **113**: 344–353 (2017)

- [15] Zhang Y H, Rhee K Y, Park S J. Nanodiamond nanocluster-decorated graphene oxide/epoxy nanocomposites with enhanced mechanical behavior and thermal stability. *Compos Part B Eng* **114**: 111–120 (2017)
- [16] McColl I R, Ding J, Leen S B. Finite element simulation and experimental validation of fretting wear. *Wear* **256**(11–12): 1114–1127 (2004)
- [17] Wang Y F, Yang Z G. Finite element model of erosive wear on ductile and brittle materials. *Wear* **265**(5–6): 871–878 (2008)
- [18] Dimaki A V, Dmitriev A I, Menga N, Papangelo A, Ciavarella M, Popov V L. Fast high-resolution simulation of the gross slip wear of axially symmetric contacts. *Tribol Trans* **59**(1): 189–194 (2016)
- [19] Pödra P, Andersson S. Finite element analysis wear simulation of a conical spinning contact considering surface topography. *Wear* **224**(1): 13–21 (1999)
- [20] Bortoleto E M, Prados E F, Seriacopi V, Fukumasu N K, Da S Lima L G D B, Machado I F, Souza R M. Numerical modeling of adhesion and adhesive failure during unidirectional contact between metallic surfaces. *Friction* **4**(3): 217–227 (2016)
- [21] Bortoleto E M, Rovani A C, Seriacopi V, Profito F J, Zachariadis D C, Machado I F, Sinatora A, Souza R M. Experimental and numerical analysis of dry contact in the pin on disc test. *Wear* **301**(1–2): 19–26 (2013)
- [22] Shen X J, Liu Y F, Cao L, Chen X Y. Numerical simulation of sliding wear for self-lubricating spherical plain bearings. *J Mater Res Technol* **1**(1): 8–12 (2012)
- [23] Lu J J, Qiu M, Li Y C. Numerical analysis of self-lubricating radial spherical plain bearings and investigations on fatigue damage mechanisms of the liner. *Tribol Int* **96**: 97–108 (2016)
- [24] Archard J F. Contact and rubbing of flat surfaces. *J Appl Phys* **24**(8): 981–988 (1953)
- [25] Mattei L, Di Puccio F. Influence of the wear partition factor on wear evolution modelling of sliding surfaces. *Int J Mech Sci* **99**: 72–88 (2015)



Jigang CHEN. He received his bachelor degree, master degree and PhD degree from Yanshan University, Qinhuangdao, China, in 1993, 2001 and 2006, respectively. He is a full

professor in the School of Yanshan University. His main research areas are precision forming and manufacturing technology of spherical plain bearings, virtual design and manufacture, and aeronautical self-lubricating material research.



Yahong XUE. She received her master degree in mechanical manufacture and automation in 2015 from Yanshan University, Qinhuangdao,

China. After then, she was a Ph.D. student in material processing engineering at the same university. Her research interests include material forming and friction of composite materials.

Effect of oxide film on nanoscale mechanical removal of pure iron

Jinwei LIU¹, Liang JIANG^{1,*}, Changbang DENG¹, Wenhao DU², Linmao QIAN¹

¹ Tribology Research Institute, State Key Laboratory of Traction Power, Southwest Jiaotong University, Chengdu 610031, China

² Institute of Machinery Manufacturing Technology, China Academy of Engineering Physics, Mianyang 621900, China

Received: 09 May 2018 / Revised: 30 July 2018 / Accepted: 02 August 2018

© The author(s) 2018. This article is published with open access at Springerlink.com

Abstract: In this paper, the properties of an oxide film formed on a pure iron surface after being polished with an H₂O₂-based acidic slurry were investigated using an atomic force microscope (AFM), Auger electron spectroscopy (AES), and angle-resolved X-ray photoelectron spectroscopy (AR-XPS) to partly reveal the material removal mechanism of pure iron during chemical mechanical polishing (CMP). The AFM results show that, when rubbed against a cone-shaped diamond tip in vacuum, the material removal depth of the polished pure iron first slowly increases to 0.45 nm with a relatively small slope of 0.11 nm/μN as the applied load increases from 0 to 4 μN, and then rapidly increases with a large slope of 1.98 nm/μN when the applied load further increases to 10 μN. In combination with the AES and AR-XPS results, a layered oxide film with approximately 2 nm thickness (roughly estimated from the sputtering rate) is formed on the pure iron surface. Moreover, the film can be simply divided into two layers, namely, an outer layer and an inner layer. The outer layer primarily consists of FeOOH (most likely α-FeOOH) and possibly Fe₂O₃ with a film thickness ranging from 0.36 to 0.48 nm (close to the 0.45 nm material removal depth at the 4 μN turning point), while the inner layer primarily consists of Fe₃O₄. The mechanical strength of the outer layer is much higher than that of the inner layer. Moreover, the mechanical strength of the inner layer is quite close to that of the pure iron substrate. However, when a real CMP process is applied to pure iron, pure mechanical wear by silica particles generates almost no material removal due to the extremely high mechanical strength of the oxide film. This indicates that other mechanisms, such as *in-situ* chemical corrosion-enhanced mechanical wear, dominate the CMP process.

Keywords: oxide film; nanoscale mechanical removal; pure iron; chemical mechanical polishing

1 Introduction

Iron is one of the most common elements on earth. Iron-based materials such as steels and pure iron have been widely used in various high technology applications. Pure iron has been intensively used in high energy density physics [1, 2], as a liner material [3], and in some comparative experiments as a reference material [4]. In some occasions, an ultra-smooth surface with excellent surface integrity is required and is even indispensable for satisfactory device performance [5]. However, conventional ultra-precision machining

techniques, such as ultra-precision cutting, may not meet such stringent requirements [1, 2, 6]. It is known that chemical mechanical polishing (CMP), which has been widely used to manufacture ultra-large scale integrated circuits, can yield an ultra-smooth surface with nano and even sub-nano surface roughness and nearly zero subsurface damage by taking advantage of the synergetic effects of chemical corrosion and mechanical wear [7–9]. Li et al. [7] fabricated a near-perfect silicon surface with 0.5 Å surface roughness at the atomic scale by optimizing the CMP process. Jiang et al. [10] reported that an ultra-smooth copper

* Corresponding author: Liang JIANG, E-mail: jiangliang09@gmail.com

surface with nearly 1 nm surface roughness could be obtained with the proper chemistry. Recently, Jiang et al. [11–13] extended the application of CMP to iron-based metals, including AISI 1045 steel, AISI 52100 steel, and 316L stainless steel, yielding ultra-smooth surfaces with nanoscale surface roughness. Therefore, it is feasible to obtain an ultra-smooth pure iron surface with CMP technique.

Normally, when applying CMP to metals, such as copper and iron-based metals, oxidation reactions between the metal substrate and oxidizer (such as H_2O_2) are indispensable to oxidize the metal to its corresponding oxidation states. The oxidized surface can subsequently react with other chemical additives, such as complexing agent, enabling effective and controllable material removal. Therefore, the oxide film formed during the polishing process via oxidation reactions is critical for polishing performance. As for copper, the copper oxide film becomes thick, dense, and passive in the presence of H_2O_2 as pH increases within the range of 2–10 [14]. Therefore, the material removal rate (MRR) of copper decreases. Moreover, the nanoindentation results indicate that, at pH 2, the hardness of the film decreases significantly compared with the virgin copper surface, while no measurable effect is observed at pH 7 or 12. This further confirms that the film formed at low pH is weak enough to be easily removed by mechanical abrasion. As for iron-based metals, it is revealed that the oxide film plays a significant role in material removal [11–13]. For AISI 52100 steel CMP, in the presence of glycine at pH 4.0, the MRR first dramatically increases when H_2O_2 concentration increases from 0 to 0.01 wt%. The result is due to formation of a porous iron oxide layer on the surface. With a further increase in H_2O_2 concentration, the MRR gradually decreases. This outcome is caused by dense growth of the porous iron oxide layer with relatively high mechanical strength via transformation of γ -FeOOH into α -FeOOH and even into α -Fe₂O₃. A similar MRR trend was observed in our preliminary results for CMP of pure iron. However, for pure iron, the properties of the oxide film formed on the top surface and its role in material removal during the CMP process remain unclear. Only a few studies showed that an oxide film with approximately 3–5 nm thickness is formed under different oxidation conditions [15–19]. Lin et al. [17] showed that oxide films

produced by O_2 exposure are predominantly trilayers of FeO, Fe₃O₄, and FeOOH phases, wherein FeOOH phase is in the outermost layer. However, Bhargava et al. [15] suggested that FeO is unstable below 570 °C, and the oxide that can coexist with iron is Fe₃O₄. Therefore, the oxide films reported by Lin et al. [17] are most likely a bilayer consisting of Fe₃O₄ and FeOOH phases. Dong et al. [20] studied the corrosion mechanism of mild steel, which has a similar chemical composition as pure iron, under wet/dry alternate conditions with 0.052 wt% NaHSO₃ solution at pH 4.0. The oxidation process can be divided into two stages. At the initial stage, the oxide film is porous and primarily composed of amorphous iron oxides, and small amounts of α -FeOOH, γ -FeOOH, and Fe₃O₄. At the later stage, the content of α -FeOOH (and even Fe₂O₃ [16, 21]) rapidly increases as γ -FeOOH transforms into α -FeOOH (and even Fe₂O₃ [16, 21]) when γ -FeOOH accumulates to a certain amount, and the oxide layer becomes compact [22]. Meanwhile, crystallization of α -FeOOH can induce polymerization of the amorphous iron oxides, and the iron oxide layer becomes compact as a result [23]. Chao et al. [24] found that the addition of H_2O_2 can efficiently accelerate oxidation without changing the basic mechanism. However, a lack of studies on the oxide film formed on a pure iron surface during CMP might become an obstacle to further improving polishing performance of pure iron.

In this work, nanoscale mechanical removal of a pure iron sample polished with an H_2O_2 -based acidic slurry was investigated using an atomic force microscope (AFM) with a cone-shaped diamond tip and an SiO₂ microsphere tip in vacuum. The chemical composition of the polished pure iron surface was subsequently characterized using Auger electron spectroscopy (AES) and angle-resolved X-ray photoelectron spectroscopy (AR-XPS). Based on the above results, the effect of the oxide film on nanoscale mechanical removal of pure iron was discussed.

2 Material and methods

Experimental samples with a size of 10 mm × 10 mm × 2 mm were first cut from a large piece of polycrystalline pure iron (DT4E) and were polished using a UNIPOL-802 desktop polisher with a designated H_2O_2 -based acidic slurry. The samples were subsequently rinsed

with deionized (DI) water, dried with nitrogen, and then immediately placed into a vacuum chamber to avoid further oxidation and contamination. After applying the above treatments, the arithmetic average surface roughness (R_a) over a $2\ \mu\text{m} \times 2\ \mu\text{m}$ area reduced from its initial value of $122.4 \pm 48.6\ \text{nm}$ to $0.31 \pm 0.07\ \text{nm}$, and an ultra-smooth surface was obtained. The samples were subsequently used for AFM, AES, and AR-XPS tests. The polishing slurry was composed of 4 wt% NexSil 85K colloidal silica (purchased from Nyaacol Nano Technologies, Inc., 50 nm primary particle size), 0.01 wt% H_2O_2 (reagent grade, purchased from Sinopharm Chemical Reagent Co., Ltd) and DI water at pH 4. The polishing conditions were set as follows: 6.4 psi down force, 200 rpm table speed, 25 mL/min slurry flow rate, and 5 min polishing time. An IC1010/Sub-IV composite pad was used. Between each polishing, ex-situ pad conditioning was performed for 2 min to deglaze the pad surface.

To study the nanoscale mechanical removal behavior of pure iron, wear tests of the polished pure iron sample against a cone-shaped diamond tip (NC-LC, Adama, Ireland, 100 N/m spring constant) were carried out using an AFM (SPA-300HV/SPI3800N Probe Station, Seiko, Japan) in vacuum at room temperature under the following experimental conditions: 2–10 μN applied load F_N , 0.5 $\mu\text{m/s}$ relative sliding velocity v , 1 μm relative sliding length L , and 1 number of reciprocating sliding cycles N . All wear tests were repeated at least three times to ensure the results were reproducible. Figure 1 illustrates the nanoscale wear tests conducted within one crystalline grain of pure iron. As shown in the inset of Fig. 1, the radius of the diamond tip is approximately dozens of nanometers, which is consistent with the nominal value. After the wear tests, a silicon nitride AFM probe (MSCT, Bruker, USA) with less than 20 nm nominal radius of curvature was used to scan the 3D surface topography of the experimental area. In order to determine the exact wear area, a microhardness tester was used to indent an L-shape marker on the pure iron surface before conducting the wear tests. The marker has five points in each direction with an interval of 50 μm between each point. All the points can be clearly observed with a light microscope. Based on the relative location in the L-shape coordinate system, the exact wear area can be easily identified.

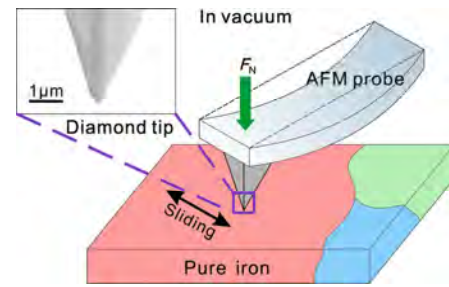


Fig. 1 Schematic of the nanoscale wear tests conducted within one crystalline grain of pure iron. The inset shows a scanning electron microscopy image of the cone-shaped diamond tip.

To comparatively study the effect of the oxide film, a dilute HCl solution was used to obtain an oxide-free pure iron surface by removing the initial oxide film. The polished pure iron sample was first dipped into a dilute HCl solution at pH 1.5 for 30 s and was then washed, dried, and placed into a vacuum chamber for wear tests against a cone-shaped diamond tip under the same experimental conditions as the polished pure iron sample. The R_a value for the HCl-treated pure iron surface over a $2\ \mu\text{m} \times 2\ \mu\text{m}$ area was $4.51 \pm 0.29\ \text{nm}$.

To further reveal the effect of the oxide film on the material removal of pure iron in a real CMP process, similar wear tests of the polished pure iron sample against a chemically active SiO_2 microsphere tip of 2.5 μm diameter (Novascan Technologies, Inc., 16 N/m spring constant) were carried out in vacuum at room temperature under the following experimental conditions: 4 μN applied load F_N , 0.5 $\mu\text{m/s}$ relative sliding velocity v , 1 μm relative sliding length L , and 100, 300, 500, and 1000 numbers of reciprocating sliding cycles N separately.

The chemical composition of the polished pure iron surface was characterized using AES and AR-XPS. The sample was first degaussed before being transferred to the chamber in order to avoid negative measurement effects. AES was used to quantitatively analyze the chemical depth profile at the sample surface. The measurements were performed using a PHI-700 Scanning Auger Nanoprobe (ULVAC-PHI, Japan) with a 5 kV coaxial electron gun and a cylindrical mirror energy analyzer. In addition, the energy resolution was 1%, the incidence angle was 30° , the vacuum chamber pressure was less than 3.9×10^{-9} Torr, and a scanning Ar^+ gun was used to sputter depth profiling. AR-XPS was used to characterize the chemical

composition of the sample surface at different depths. The measurements were carried out using a PHI Quantera SXM (ULVAC-PHI, Japan) with a hemispherical energy analyzer and a monochromatic aluminum target. The X-ray beam spot size was 200 μm , and the analysis chamber pressure was less than 1.0×10^{-7} Torr. By rotating the sample, spectra were obtained at four different photoelectron take-off angles from the surface (5° , 25° , 55° , and 85°). Here, the take-off angle is the angle between the sample surface and the photoelectron emission direction [15]. The XPS detection depth increases as the take-off angle increases, and thereby the chemical composition at different depths can be acquired. High-resolution spectra corresponding to Fe and O were obtained using 55 eV pass energy with 0.1 eV step size. The data was then analyzed with CasaXPS software.

3 Results and discussion

3.1 Nanoscale mechanical removal behavior of pure iron with an oxide film

A thin oxide film inevitably forms on the top surface of pure iron during the polishing process due to oxidation reactions between H_2O_2 and pure iron. Typical AFM surface topographical images and average cross-section profiles of the material removal traces after wear tests against the diamond tip are shown in Fig. 2. Corresponding statistical data showing the amount of removed material, including the material removal depth d and the material removal volume V , are shown in Fig. 3. Assuming that no material removal occurs when the applied load is zero in vacuum, the material removal depth slowly increases linearly with a relatively small slope of $0.11 \text{ nm}/\mu\text{N}$ as the applied load increases from 0 to 4 μN . Specifically, at 2 μN , an extremely shallow groove-like scratch with a depth of 0.2 nm starts to form on the surface. The depth increases to 0.45 nm at 4 μN . A turning point emerges at 4 μN . When the applied load further increases from 4 to 10 μN , unlike the preceding trend, the material removal depth rapidly increases from 0.45 to 11.83 nm with a large slope of $1.98 \text{ nm}/\mu\text{N}$. At 10 μN , an apparent scratch with a depth of 11.83 nm can be observed on the surface. The material removal volume shares a similar trend with the material

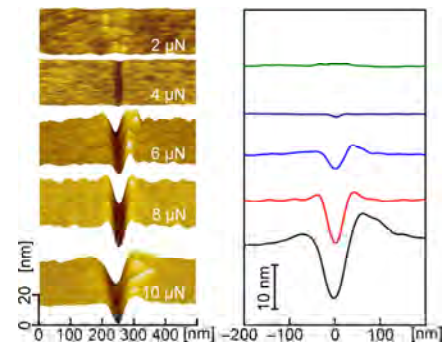


Fig. 2 Typical AFM surface topographical images and average cross-section profiles of the material removal traces after performing wear tests on the polished pure iron surface against a diamond tip in vacuum.

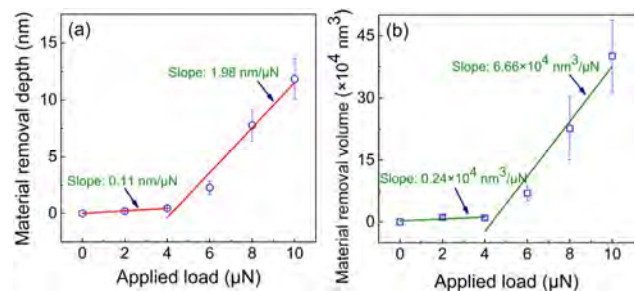


Fig. 3 Corresponding statistical data for the amount of removed material after performing wear tests on the polished pure iron surface against a diamond tip in vacuum. (a) Material removal depth d . (b) Material removal volume V .

removal depth, except for the slope. The difference in the slopes can be attributed to the influence of the nonuniform cross-section area along the depth. Based on the existence of a turning point at 4 μN , one can infer that the polished pure iron surface is layered, probably due to the formation of the oxide film, and the resultant mechanical strength is inhomogeneous along the depth direction. Moreover, the top layer exhibits high mechanical strength since the slope of the amount of removed material versus the applied load is initially small.

3.2 Nanoscale mechanical removal behavior of oxide-free pure iron

To verify the above inference on the oxide film, the polished pure iron sample was etched with a dilute HCl solution to obtain an oxide-free surface and was subsequently rubbed against the diamond tip. Typical AFM surface topographical images and average cross-section profiles of the material removal traces after the wear tests are shown in Fig. 4(a). The correspon-

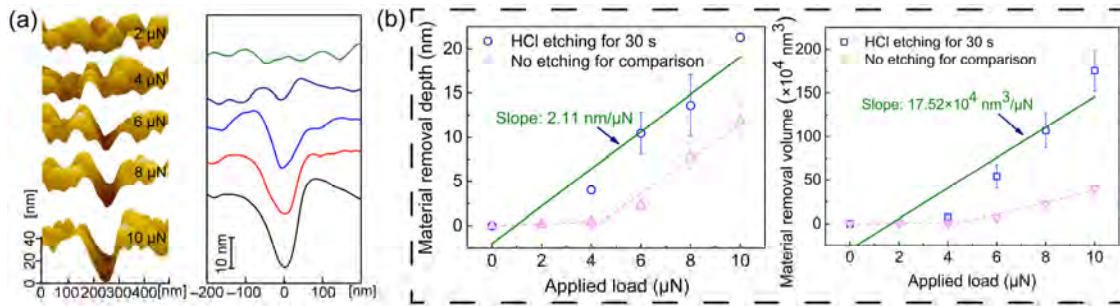


Fig. 4 (a) Typical AFM surface topographical images and average cross-section profiles of the material removal traces after performing wear tests on the oxide-free pure iron surface treated with a dilute HCl solution at pH 1.5 against a diamond tip in vacuum. (b) Corresponding statistical data for the amount of removed material and comparison with the results of the polished pure iron sample as presented in Fig. 3.

ding statistical data showing the amount of removed material are shown and compared with the data from the polished pure iron sample in Fig. 4(b). As shown in Fig. 4(a), the surface treated with the dilute HCl solution becomes much rougher compared with the polished pure iron surface, which is probably due to nonuniform etching by hydrogen ions. As seen from Fig. 4(b), the material removal depth and material removal volume almost linearly increase with slopes of 2.11 nm/μN and $17.52 \times 10^4 \text{ nm}^3/\mu\text{N}$, respectively, based on linear fitting when the applied load increases from 0 to 10 μN. This assumes that no material removal occurs at 0 μN and also the result at 2 μN is excluded since it is almost impossible to identify the scratch due to the relatively rough surface. No turning point emerges throughout the test range, unlike the trend for the polished pure iron sample. This result indicates that the mechanical strength of the oxide-free pure iron surface is quite homogeneous along the depth direction. Moreover, by removing the oxide film, the amount of removed material apparently increases probably due to a much lower mechanical strength of the pure iron substrate compared with the oxide film. Therefore, the oxide film formed on the pure iron surface results in inhomogeneous mechanical strength, which can be roughly divided into two parts. The higher strength portion is near the top of the film, as indicated by the initial relatively small slope for the amount of removed material versus the applied load. However, whether the boundary between the two regions with different mechanical strengths is situated within the oxide film or in between the oxide film and the pure iron substrate remains unclear.

3.3 Characterization of oxide film formed on pure iron surface

To determine the boundary, AES and AR-XPS tests were carried out to characterize the chemical composition and structure of the oxide film formed on the pure iron surface. The AES depth profiles of the oxide film after polishing are shown in Fig. 5(a). The corresponding AES spectra before and after sputtering for 3 min are shown in Fig. 5(b). In general, the typical depth probed by AES is approximately 2 nm [25]. The reference sputtering rate of SiO₂ is 2 nm/min. Baera et al. [26, 27] reported that the average value of relative sputter ratio of Fe₂O₃ to SiO₂ is 0.61 with 0.06 standard deviation. This data is used to roughly estimate the thickness of the pure iron oxide film in our experiment. Based on the criterion where AES depth profiles at a point where the oxygen concentration becomes near zero and stable, the total oxide film thickness can be estimated to be approximately 2 nm. When the sputtering time increases from 0 to 0.3 min/0.4 min, the concentration of iron on the exposed pure iron surface increases from 37.8 at% to 42.4 at%/43.6 at%, and the Fe/O ratio increases from 0.61 to 0.74/0.77, indicating that the remaining oxide film can be primarily composed of Fe₃O₄ since the Fe/O ratio of Fe₃O₄ is 0.75 [15, 17]. Moreover, the sputtered oxide film can be primarily composed of ferric oxides, such as FeOOH and Fe₂O₃ [16, 17, 21] with a film thickness ranging from 0.36 to 0.48 nm. The thickness of ferric oxides film is quite consistent with the observed 0.45 nm material removal depth at the aforementioned 4 μN turning point from the polished pure iron sample. When the sputtering time increases further,

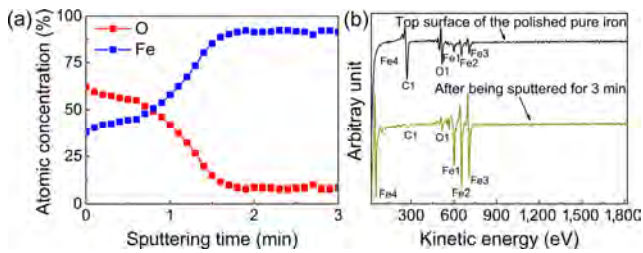


Fig. 5 (a) AES depth profiles of the oxide film formed on the top surface of pure iron after being polished with the H_2O_2 -based acidic slurry. (b) Corresponding AES spectra before and after sputtering for 3 min.

the concentration of iron on the exposed pure iron surface continuously increases and then stabilizes, which suggests that the oxide film gradually transitions to the pure iron substrate underneath. As shown in Fig. 5(b), the atomic concentration of iron becomes much larger after being sputtered for 3 min.

AR-XPS was used to further analyze the chemical composition of the oxide film. The experimental sample was the same as that in the AES measurement. The corresponding O(1s) spectra, which were obtained at four different photoelectron take-off angles (5° , 25° , 55° , and 85°) are shown in Fig. 6. Deconvolution of the O(1s) spectra reveals two peaks at approximately 530.1 eV and 531.5 eV, which correspond to oxygen as forms of O^{2-} and OH^- , respectively [15]. Moreover, the proportion of oxygen as OH^- gradually decreases from 70.1 at% to 47.9 at% as the photoelectron take-off angle increases from 5° to 85° , which indicates that OH^- exists in the outer layer of the oxide film. The

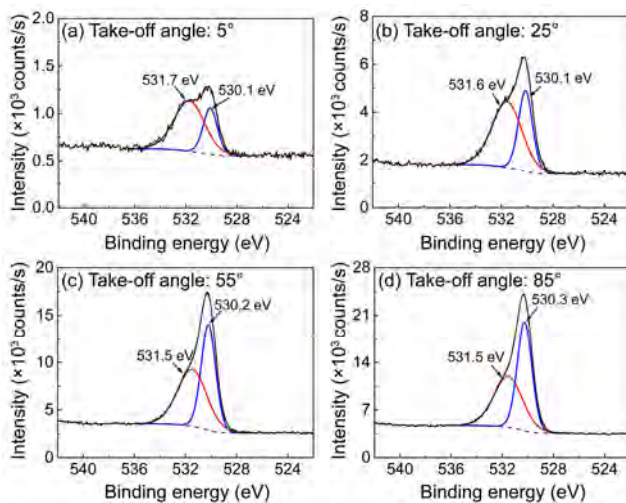


Fig. 6 XPS O(1s) spectra of the polished pure iron surface obtained at four different photoelectron take-off angles.

corresponding Fe(2p) spectra are shown in Fig. 7. Deconvolution of the Fe(2p) spectra reveals two peaks. Specifically, the peak with the low binding energy corresponds to iron as a form of metallic iron, and the peak with the high binding energy corresponds to iron as a form of a mixture of ferric and ferrous oxides [15]. In addition, as the photoelectron take-off angle increases from 5° to 85° , the proportion of iron as metallic iron gradually increases from almost 0 to 16.8 at%. The XPS signal of metallic iron is probably derived from the pure iron substrate underneath the oxide film.

3.4 Effect of oxide film on nanoscale mechanical removal of pure iron

Based on the above results, one can conclude that a thin oxide film with approximately 2 nm thickness (roughly estimated from the sputtering rate) formed on the pure iron surface after being polished with the H_2O_2 -based acidic slurry. According to the AES and AR-XPS results, the oxide film can be roughly divided into an outer layer and an inner layer, as shown in Fig. 8. Any intermediate layer is ignored. The thickness of the outer layer ranges from 0.36 to 0.48 nm (roughly estimated from the sputtering rate) and is primarily composed of FeOOH (most likely $\alpha\text{-FeOOH}$) and possibly Fe_2O_3 , while the inner layer is primarily composed of Fe_3O_4 [15–17]. In accordance with the proposed bilayer oxide film structure, one can find that the boundary between the two regions with

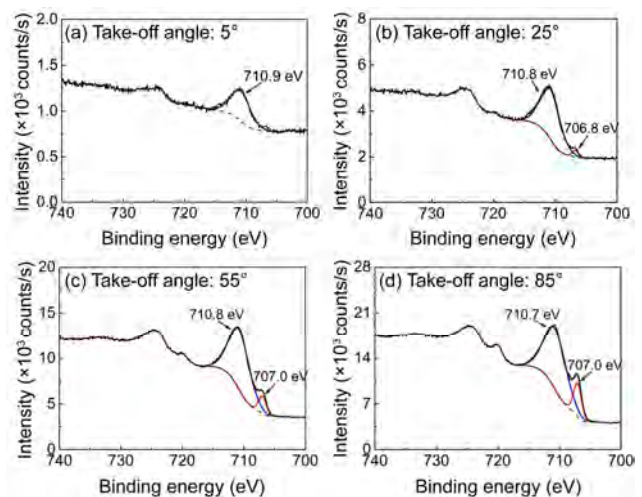


Fig. 7 XPS Fe(2p) spectra of the polished pure iron surface obtained at four different photoelectron take-off angles.

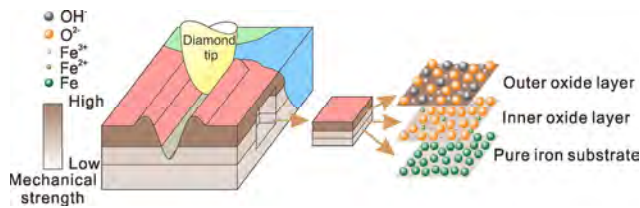


Fig. 8 Schematic illustration demonstrating the effect of the oxide film on nanoscale mechanical removal of pure iron.

different mechanical strengths is situated within the oxide film and in between the outer and inner layers, given the fact that the thickness of the outer layer agrees well with the 0.45 nm material removal depth at the 4 μN turning point from the polished pure iron sample. Moreover, based on the AFM results, the mechanical strength of the outer layer of the oxide film is much larger than those of the inner layer and the pure iron substrate, possibly due to the increased compactness induced by crystallization of $\alpha\text{-FeOOH}$ [20, 22, 23]. In addition, the mechanical strength of the inner layer is quite close to that of the pure iron substrate since the amount of removed material increases linearly without any distinct turning point when the applied load increases from 4 to 10 μN until the material removal depth reaches 11.83 nm at 10 μN , which is far beyond the oxide film thickness [28].

As for real CMP of iron-based metals, colloidal silica is widely used as an abrasive to obtain an ideal ultra-smooth surface without micro scratches [29]. Our preliminary CMP results show that the MRR of pure iron can reach as high as 163 nm/min when being polished with the slurry containing 4 wt% colloidal silica, 0.01 wt% H_2O_2 , and DI water at pH 4 under the aforementioned polishing conditions. However, no material is removed when the polished pure iron surface is rubbed against a SiO_2 microsphere tip at 1.15 GPa contact pressure (according to Hertz contact theory) in vacuum, even after applying 1000 reciprocating sliding cycles, as shown in Fig. 9. This result is due to the extremely high mechanical strength of the oxide film formed on the pure iron surface compared with that of SiO_2 . The wear tests results indicate that other mechanisms, such as *in-situ* chemical corrosion-enhanced mechanical wear, control material removal during CMP. Furthermore, one possible mechanism is that H_2O_2 in the acidic slurry will react with ferric ions near the surface to form ferrous ions.

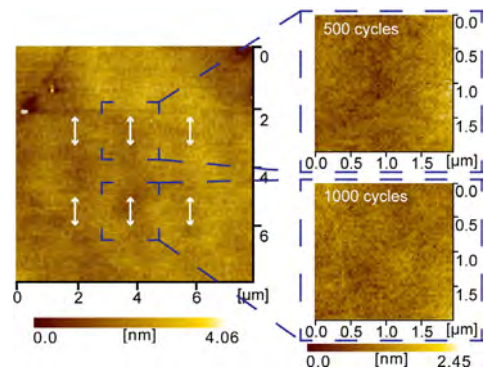


Fig. 9 Typical AFM surface topographical images after performing wear tests on the polished pure iron surface against a SiO_2 microsphere tip in vacuum.

As a result, either the resultant reactivity of the surface will be improved, or the resultant mechanical strength of the surface will be reduced, or both. More investigation is ongoing so that the material removal mechanism during the CMP process can be better understood.

4 Conclusions

The mechanical properties of the oxide film formed on the pure iron surface after being polished with the slurry containing 0.01 wt% H_2O_2 at pH 4.0 were investigated using an AFM against the diamond tip in vacuum. The chemical composition and structure of the oxide film were characterized using AES and AR-XPS. The conclusions are summarized as follows:

(1) A thin oxide film with approximately 2 nm thickness is formed on the pure iron surface after being polished with the H_2O_2 -based acidic slurry. The oxide film is layered and can be roughly divided into an outer layer and an inner layer. The outer layer has a thickness ranging from 0.36 to 0.48 nm (close to the 0.45 nm material removal depth at the 4 μN turning point) is primarily composed of FeOOH (most likely $\alpha\text{-FeOOH}$) and possibly Fe_2O_3 , whereas the inner layer is primarily composed of Fe_3O_4 . Moreover, the mechanical strength of the outer layer is much larger than the strength of the inner layer and the pure iron substrate. The mechanical strength of the inner layer is quite close to that of the pure iron substrate.

(2) With respect to real CMP of pure iron, given the fact that the mechanical strength of the oxide film is extremely high compared with that of colloidal silica,

pure mechanical wear with colloidal silica generates almost no material removal. This phenomenon indicates that, from the view of mechanical removal, the oxide film functions as a handicap. Moreover, other mechanisms, such as *in-situ* chemical corrosion-enhanced mechanical wear, dominate the entire CMP process. The results provide insight into how CMP affects pure iron, suggesting that it is important to select proper chemical additives, such as 0.01 wt% H₂O₂, to promote *in-situ* chemical corrosion and obtain an ultra-smooth surface with high removal efficiency.

Acknowledgements

The authors are grateful for the financial support provided by the National Natural Science Foundation of China (No. 51605396), Young Elite Scientists Sponsorship Program by CAST (No. YESS20160056), Science Challenge Project (No. TZ2018006-0101-04), and Self-developed Project of State Key Laboratory of Traction Power (No. 2017TPL_Z02).

Open Access: The articles published in this journal are distributed under the terms of the Creative Commons Attribution 4.0 International License (<http://creativecommons.org/licenses/by/4.0/>), which permits unrestricted use, distribution, and reproduction in any medium, provided you give appropriate credit to the original author(s) and the source, provide a link to the Creative Commons license, and indicate if changes were made.

References

- [1] Kong J X, Deng F, Zhao W, He N. Effects of cooling/lubrication conditions on surface integrity of pure iron materials during turning. (in Chinese). *Journal of South China University of Technology (Natural Science Edition)* **43**(6): 89–95 (2015)
- [2] Kong J X, Hu K, Xia Z H, Li L. Effects of tool wear on surface integrity of pure iron material under finish turning. (in Chinese). *Journal of South China University of Technology (Natural Science Edition)* **44**(2): 74–80 (2016)
- [3] Li W-B, Wang X-M, Zhou H. Effect of the liner material on the shape of dual mode penetrators. *Combustion, Explosion, and Shock Waves* **51**(3): 387–394 (2015)
- [4] Pérez Escobar D, Miñambres C, Duprez L, Verbeke K, Verhaege M. Internal and surface damage of multiphase steels and pure iron after electrochemical hydrogen charging. *Corros Sci* **53**(10): 3166–3176 (2011)
- [5] Jia W, Zhang Q, Bai Z, Ma S, Yao D, Wang Y. Progress on manufacturing techniques of shaped charge liners. (in Chinese). *Rare Metal Materials and Engineering* **36**(9): 1511–1516 (2007)
- [6] Massarelli L, Marchionni M. Morphology of spark-affected surface layers produced on pure iron and steels by electro-discharge machining. *Metals Technology* **4**(1): 100–105 (1977)
- [7] Li J, Liu Y H, Dai Y J, Yue D C, Lu X C, Luo J B. Achievement of a near-perfect smooth silicon surface. *Science China Technological Sciences* **56**(11): 2847–2853 (2013)
- [8] Li Y. *Microelectronic Applications of Chemical Mechanical Planarization*. Wiley-Interscience, USA, 2007.
- [9] Babu S. *Advances in Chemical Mechanical Planarization (CMP)*. Woodhead Publishing, 2016.
- [10] Jiang L, Lan Y, He Y, Li Y, Luo J. Functions of Trilon® P as a polyamine in copper chemical mechanical polishing. *Appl Surf Sci* **288**: 265–274 (2014)
- [11] Jiang L, He Y, Luo J. Effects of pH and oxidizer on chemical mechanical polishing of AISI 1045 steel. *Tribol Lett* **56**(2): 327–335 (2014)
- [12] Jiang L, He Y, Luo J. Chemical mechanical polishing of steel substrate using colloidal silica-based slurries. *Appl Surf Sci* **330**: 487–495 (2015)
- [13] Jiang L, He Y, Yang Y, Luo J. Chemical mechanical polishing of stainless steel as solar cell substrate. *ECS Journal of Solid State Science and Technology* **4**(5): P162–P170 (2015)
- [14] Du T, Desai V. Chemical mechanical planarization of copper: pH effect. *J Mater Sci Lett* **22**(22): 1623–1625 (2003)
- [15] Bhargava G, Gouzman I, Chun C M, Ramanarayanan T A, Bernasek S L. Characterization of the “native” surface thin film on pure polycrystalline iron: A high resolution XPS and TEM study. *Appl Surf Sci* **253**(9): 4322–4329 (2007)
- [16] Grosvenor A P, Kobe B A, McIntyre N S, Tougaard S, Lennard W N. Use of QUASES™/XPS measurements to determine the oxide composition and thickness on an iron substrate. *Surf Interface Anal* **36**(7): 632–639 (2004)
- [17] Lin T-C, Seshadri G, Kelber J A. A consistent method for quantitative XPS peak analysis of thin oxide films on clean polycrystalline iron surfaces. *Appl Surf Sci* **119**(1): 83–92 (1997)
- [18] Mathieu H J, Datta M, Landolt D. Thickness of natural oxide films determined by AES and XPS with/without sputtering. *Journal of Vacuum Science & Technology A: Vacuum, Surfaces, and Films* **3**(2): 331–335 (1985)
- [19] Stambouli V, Palacio C, Mathieu H J, Landolt D. Comparison of in-situ low-pressure oxidation of pure iron at room

- temperature in O₂ and in O₂/H₂O mixtures using XPS. *Appl Surf Sci* **70–71**: 240–244 (1993)
- [20] Dong J, Dong J, Han E, Liu C, Ke W. Rusting evolvement of mild steel under wet/dry cyclic condition with pH 4.00 NaHSO₃ solution. (in Chinese). *Corrosion Science and Protection Technology* **21**(1): 1–4 (2009)
- [21] Miyazawa T, Terachi T, Uchida S, Satoh T, Tsukada T, Satoh Y, Wada Y, Hosokawa H. Effects of hydrogen peroxide on corrosion of stainless steel, (V) characterization of oxide film with multilateral surface analyses. *J Nucl Sci Technol* **43**(8): 884–895 (2006)
- [22] Wang J J, Guo X D, Zheng W L, Chen J G, Wu J S. Analysis of the corrosion rust on weathering steel and carbon steel exposed in marine atmosphere for three years. (in Chinese). *Corrosion & Protection* **23**(7): 288–291 (2002)
- [23] Junhua D, Wei K. The accelerated test of simulated atmospheric corrosion and the rust evolution of low carbon steel. (in Chinese). *Electrochemistry* **15**(2): 170–178 (2009)
- [24] Chao Y, Huixia Z, Weimin G, Yubin F. Effects of H₂O₂ addition on corrosion behavior of high-strength low-alloy steel in seawater. (in Chinese). *Journal of Chinese Society for Corrosion and Protection* **33**(003): 205–210 (2013)
- [25] Brundle C R, Evans C A, Wilson S. *Encyclopedia of Materials Characterization: Surfaces, Interfaces, Thin Films*. Gulf Professional Publishing, 1992.
- [26] Baer D R, Engelhard M H, Gaspar D J, Matson D W, Pecher K H, Williams J R, Wang C M. Challenges in applying surface analysis methods to nanoparticles and nanostructured materials. *Journal of Surface Analysis* **12**(2): 101–108 (2005)
- [27] Baera D R, Engelhard M H, Lea A S, Nachimuthu P. Comparison of the sputter rates of oxide films relative to the sputter rate of SiO₂. *Journal of Vacuum Science & Technology A* **28**(5): 1060–1072 (2010)
- [28] Chicot D, Mendoza J, Zaoui A, Louis G, Lepingle V, Roudet F, Lesage J. Mechanical properties of magnetite (Fe₃O₄), hematite (α-Fe₂O₃) and goethite (α-FeO-OH) by instrumented indentation and molecular dynamics analysis. *Mater Chem Phys* **129**(3): 862–870 (2011)
- [29] Kao M J, Hsu F C, Peng D X. Synthesis and characterization of SiO₂ nanoparticles and their efficacy in chemical mechanical polishing steel substrate. *Advances in Materials Science and Engineering* **2014**: 1–8 (2014)



Jinwei LIU. He received his bachelor degree in mechanical engineering in 2016 from Southwest Jiaotong University, Chengdu, China. He is

currently a PhD candidate in Tribology Research Institute at the same university. His research interest includes metal materials chemical mechanical polishing.



Liang JIANG. He is an associate professor in mechanical engineering at Southwest Jiaotong University, Chengdu, China. He received his bachelor degree in mechanical engineering in 2009 from Harbin Institute of Technology, Harbin,

China, and his PhD degree in mechanical engineering in 2015 from Tsinghua University, Beijing, China. During the period 2010–2012, he studied as a joint PhD student in Clarkson University, Potsdam, NY, USA. After then, he joined the faculty at Southwest Jiaotong University in 2015. His research interest includes chemical mechanical polishing.

Single asperity friction in the wear regime

Yongjian YANG, Yunfeng SHI*

Department of Materials Science and Engineering, Rensselaer Polytechnic Institute, Troy, NY 12180, USA

Received: 02 May 2018 / Revised: 29 July 2018 / Accepted: 03 August 2018

© The author(s) 2018. This article is published with open access at Springerlink.com

Abstract: We used molecular dynamics simulation to investigate the friction of a single asperity against a rigid substrate, while generating debris. In the low wear regime (i.e., non-linear wear rate dependence on the contact stress, via atom-by-atom attrition), the frictional stress is linearly dependent on the normal stress, without any lubrication effect from the wear debris particles. Both the slope (friction coefficient) and friction at zero normal stress depend strongly on asperity-substrate adhesion. In the high wear regime (i.e., linear wear rate dependence on the contact stress, via plastic flow), the friction-normal stress curves deviate from a linear relation merging toward plastic flow of the single asperity which is independent of the interfacial adhesion. One can further link wear and friction by considering debris generation as chemical reaction, driven by both normal and frictional forces. The coupling between wear and friction can then be quantified by a thermodynamic efficiency of the debris generation. While the efficiency is less than 5% in the low wear regime, indicating poor mechanochemical coupling, it increases with normal stress toward 50% in the high wear regime.

Keywords: single-asperity contact; friction; molecular dynamics; atomic wear; plastic wear

1 Introduction

Friction and wear are two paramount questions in all tribological processes where two surfaces in relative motion are brought in contact. Examples of such contact range from conventional machineries (e.g., gears) [1] to tectonic boundary (e.g., earthquake) [2, 3] and to probe-based instrument for nanotechnology (e.g., atomic force microscopy (AFM)) [4, 5]. With a long history of human tribology practice dating back to at least ancient Egyptians [6], several empirical laws of friction, i.e., Amontons' laws [7–9], have been found and broadly applied: (1) the friction is proportional to the normal force, (2) the friction is independent of the apparent contact area, and (3) the kinetic friction is independent of the velocity. Recently, driven by device miniaturization and the complexity of multi-asperity contact, the focus of tribologists has been partially shifted to the single-asperity contact, well-defined between a slider-tip tribo pair [4,10–12]. Both experi-

mental work and simulation work have provided new insights into the friction and wear mechanisms for single-asperity contact. For example, using molecular dynamics (MD), Mo et al. [8] have demonstrated that the friction force in a single-asperity contact is proportional to the contact area which is defined based on the number of atoms in contact. In our recent MD studies, we have demonstrated a transition from atomic wear to plastic wear in a single-asperity system and showed that the work of adhesion promotes such transition [13–15]. While the atomic wear is comprised of isolated debris and is generated at low load and low adhesion, the plastic wear involves collective debris formation from plastic flow at either high load or high interfacial adhesion. Both atomic wear and plastic wear have been quantified and the results are consistent with the experimental work by others [10, 12, 16]. The conditions for either mechanisms have been mapped out in the domain combining both the contact stress and the work of adhesion.

* Corresponding author: Yunfeng SHI, E-mail: shiy2@rpi.edu

As friction is often investigated in the wearless regime [17–21], appropriate for tribo-systems with negligible debris during sliding [13, 14, 18–20], it is interesting to examine the behavior of friction in the wear regime. Debris particles may affect the contact stress distribution as third bodies. At the same time, the debris generation is an additional energy dissipation mode which may affect friction. Specifically, we will leverage the single-asperity sliding system in our previous study on tip wear exhibiting atom-by-atom attrition to large debris cluster generation, in which the wear rate varies over four orders of magnitude [13, 16]. In this study, we focus on the frictional force (i.e., shear force) in the single-asperity contact system under different normal stress and interfacial adhesion. The effects of velocity, temperature and adhesion, and the mechanical work efficiency will be investigated. It appears that the friction is largely insensitive to the debris generation, following the same trend over wear rate spanning orders of magnitude. This is consistent with the weak chemo-mechanical coupling of the tribo-system, as quantified by the low thermodynamic efficiency of debris generation. Furthermore, friction force varies smoothly from atomic wear regime to plastic wear regime, with the thermodynamic efficiency of debris generation approaching 50%.

2 Simulation methodology

2.1 Simulation model

Two types of simulation setup have been used for the current study. One has been shown in Ref. [13], in which the system consists of an atomically-smooth rigid slider and a truncated-cone-shaped tip. The other setup is schematically shown in Fig. 1 in which a rectangular tip is used. The main advantages of using a rectangular tip include that (1) the contact area can be considered constant provided that the wear rate is small, so that the contact stress can be controlled by keeping the normal contact force at a constant value; and (2) smaller samples can be used for simulating over long period of time. Both the tip and the slider are made of glassy binary alloy interacting with the Wahnstrom potential [22]. The force field and the preparation of the samples are detailed in Ref. [13]. The slider is moving in the x -direction at a constant

speed v varying from 0.01 to 30 m/s. The bottom of the tip is fixed by setting a rigid layer, above which a thermostat layer is set at a constant temperature T (NVT ensemble, Nose-Hoover thermostat) in order to maintain the temperature of the tip. For most sliding conditions used in this study, the interface temperature is close to the thermostat temperature. When the thermostat temperature is very low and the work of adhesion is high, the interface temperature can be 50 K higher than that of the thermostat temperature. The top part of the tip is simulated without pressure control or temperature control. For the rectangular tip, either periodic boundary conditions or non-periodic boundary conditions were used in the x -direction. The difference between these two types of condition is that the former does not allow tip atoms to leave the interface so that the height of the slider is not dropping, while the later allows tip atoms to leave the interface at the trailing end so that the height of the slider is continuously decreasing as a result of wear as seen in Refs. [13, 14]. We note that the friction is not sensitive to the boundary condition. In the z -direction (Fig. 1), periodic boundary conditions are used because we are interested in the friction and wear along the sliding direction (x -direction). We use LAMMPS package [23] to conduct all the MD simulations.

2.2 Tuning the work of adhesion

The work of adhesion between the tip and the slider is controlled by rescaling the bonding energy between the tip atoms and the slider atoms with a factor κ , i.e., $\varepsilon^{\text{Tip-Slider}} = \kappa\varepsilon$ where ε is the bonding energy of the tip or the slider [13]. As κ increases from 0.1 to 0.4, the work of the interface adhesion, W_{adh} increases following a power law form [13] ($W_{\text{adh}} = a\kappa^b$ with $a =$

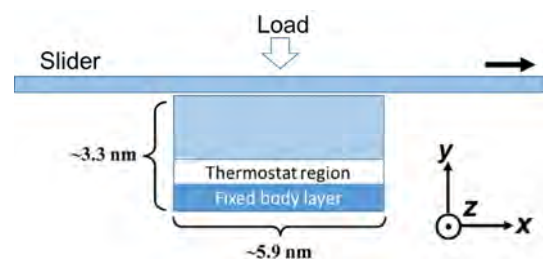


Fig. 1 Schematic of single asperity sliding model using a rectangular tip. The thickness of the sample in z -direction is about 5.0 nm.

1.29 J/m² and $b = 1.5$). Since there will be no interaction (attraction or repulsion) between the tip and the slider if κ is set to 0, to simulate a contact without adhesion, we use the original Lennard-Jones force field but set the potential cutoff at the bottom of the potential well (or $2^{1/6}\sigma$, in which σ is the Lennard-Jones length parameter). Note that when $\kappa=0$, there will still be friction due to the atomistic-level surface roughness between the slider and the tip.

2.3 Calculation of normal stress and shear stress

The normal contact stress and the shear stress are both calculated by dividing the normal force and frictional force with the nominal contact area. Because both stresses fluctuate with time, the average values and the standard deviation are reported where necessary. Under non-periodic boundary conditions in x -direction, debris atoms are generated and accumulate at the trailing end as shown in Fig. 2(a), where the change of the tip is relatively small and can be ignored for atomic wear. In the case of plastic wear, data from short sliding distance is used so that the change of tip shape can be safely ignored. In the current study, we define the wear debris as any tip atoms whose

displacement is beyond a threshold value, following our previous study [13].

2.4 Calculation of the thermodynamic efficiency of debris generation

During the sliding, mechanical work done by sliding/compression is dissipated via both atomic/plastic wear and frictional heat. One can consider debris generation as chemical reaction, driven by mechanical work. Therefore, the conversion of mechanical energy to chemical energy (stored in the debris particles) can be quantified by a thermodynamic efficiency, characterizing the strength of mechanochemical coupling between the friction and wear. As the energy associated with wear is correlated with the potential energy change of the slider-tip system during sliding, the thermodynamic efficiency can be computed from the ratio of the potential energy change over the mechanical work done (including work done by shear force in the sliding direction and work done by normal force in the loading direction).

3 Results and discussion

3.1 Normal/friction stress distribution along the sliding direction x

At the beginning of the sliding, the frictional force increases monotonically due to the elastic deformation of the tip until it reaches a peak value as seen in both experiments and simulations by Refs. [17, 24]. Thereafter, the system reaches a steady state where the frictional force fluctuates around an average value. The steady state can be easily achieved in the binary Lennard-Jones tribo-system as demonstrated in our previous study [13]. Figures 2(b) and 2(c) show the distribution of normal stress and shear stress along the sliding direction. Finite element modeling on similar geometry has shown a singularity of normal stress at the leading edge between a post and rigid surface [25]. However, no stress singularity is observed because of the breakdown of continuum elasticity for our discrete MD model. Along the sliding direction, the values of both normal stress and shear stress are relatively constant.

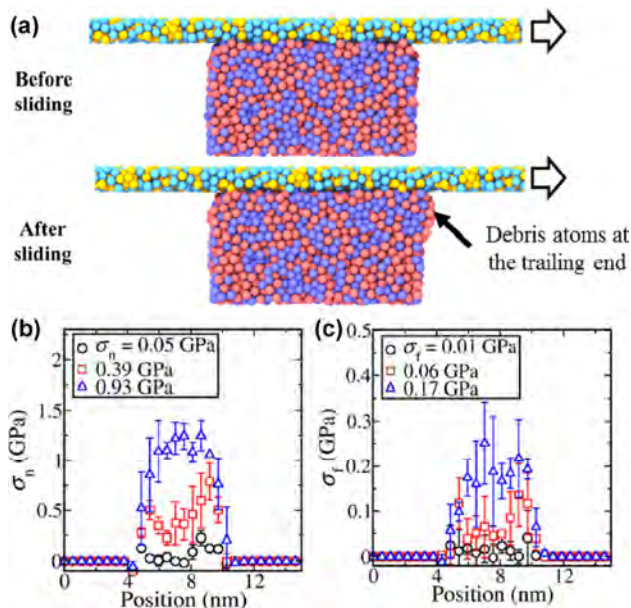


Fig. 2 (a) A side view of the sliding system before and after the sliding. As denoted by the arrow, some debris atoms (defined as atoms whose displacement is beyond a threshold value [13]) can be seen accumulating at the trailing end of the tip. Normal stress (b) and frictional stress (c) distribution along the sliding direction.

3.2 Temperature dependence of the frictional stress

The influence of temperature and velocity on the frictional stress is shown in Fig. 3. We found in most cases the change of the frictional stress with temperature is generally minor. For low adhesion, such as $W_{\text{adh}} = 0.04 \text{ J/m}^2$, there seems to be a small increase of frictional stress with the temperature when the normal stress is smaller than 0.6 GPa. Beyond that, the frictional stress change with temperature can be ignored considering its statistical variation.

For high adhesion, such as $W_{\text{adh}} = 0.16 \text{ J/m}^2$, the situation is different in that the frictional stress is unchanged for normal stress up to 0.4 GPa, and then decreases with the temperature at higher normal stress. For example, the frictional stress for the normal stress of 1.2 GPa decrease from 0.51 GPa at $T = 63 \text{ K}$ to 0.42 GPa at $T = 535 \text{ K}$. The drop of frictional stress with temperature at high work of adhesion has been observed by Spijker et al. [26] and is probably due to the softening of the tip material under high shear stress (the glass transition temperature of the tip has been estimated to be $\sim 1,000 \text{ K}$ [13]). The influence

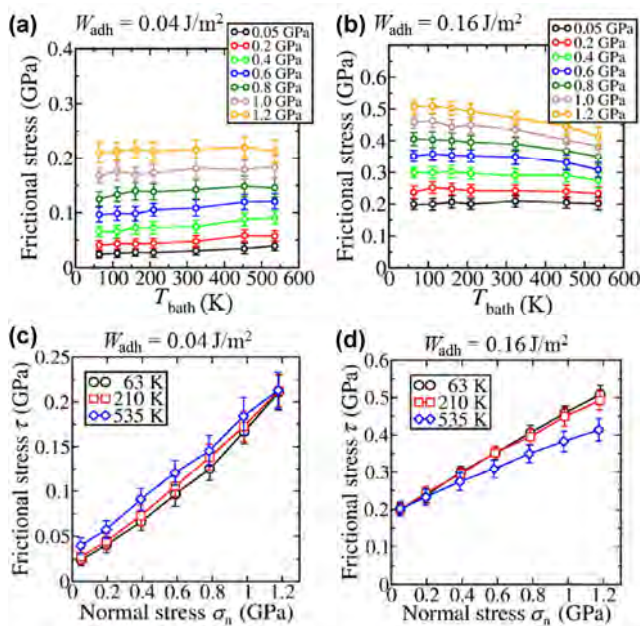


Fig. 3 (a, b) Variation of shear stress with the bath temperature at two levels of work of adhesion using periodic boundary conditions. The normal stress during sliding is shown in the legend. (c, d) Frictional stress as a function of normal stress at two levels of work of adhesion at different temperatures.

of the temperature on the dependence of the shear stress on the normal stress can be ignored in low adhesion case as shown in Fig. 3(c) whereas at high adhesion and high temperature, the slope, i.e., friction coefficient could drop at relatively high temperatures, as seen in Fig. 3(d).

3.3 Velocity dependence of the frictional stress

The dependence of the frictional stress on the velocity is shown in Fig. 4, where the shear stress is independent of the sliding speed spanning almost four orders of magnitude. Because the velocity in our simulation is much larger than the typical scanning speed used in AFM ($< 10^{-5} \text{ m/s}$), it may be possible that the friction decreases at much lower sliding velocity as seen in the experiments predicted from a thermal activation friction model [27]. On the other hand, when the sliding speed is increased to more than 30 m/s, there is a small amount of increase in friction, possibly due to the viscous damping for which the frictional force is proportional to the sliding velocity [28]. We also note that the velocity independence of the friction has also been observed by Zwörner et al. [28] in the range of nm/s to $\mu\text{m/s}$ between a silicon tip and carbon compounds when the sliding velocity is smaller than the velocity of tip slip.

3.4 Relation between the frictional stress and the normal stress

With increasing normal stress, the single asperity sliding experiences a transition from the atomic wear mechanism to the plastic wear mechanism as seen in

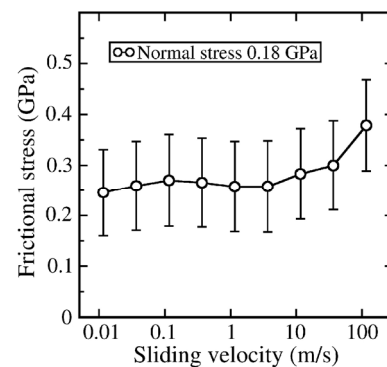


Fig. 4 Variation of shear stress with sliding velocity at the normal stress of 0.18 GPa. $W_{\text{adh}} = 0.16 \text{ J/m}^2$ and $T = 63 \text{ K}$. The sliding velocity is varied from 0.01 to 116 m/s.

Ref. [13]. Due to geometrical limitation, the simulation setup (Fig. 1) does not allow the plastic wear to occur via shear deformation in an angle declining along the sliding direction if the slip line touches the bottom of the tip. Therefore, sliding simulation using a truncated cone tip is more appropriate in this case [10]. The frictional stress as a function of normal stress is shown in Fig. 5(a). It can be found in the atomic wear region and under different work of adhesions that, the frictional stress increases linearly with the normal stress, which can be well fitted with a linear function: $\tau = \tau_0 + \mu\sigma_n$. Both τ_0 and μ depend sensitively on interfacial adhesion. From the linear fitting in Fig. 5(a), τ_0 and μ are plotted against the adhesion factor κ in Fig. 5(b). In the plastic wear region, the frictional stress-normal stress curves start to deviate and merge into a master curve, see the white dash line in Fig. 5(a) (a yield surface that can be described by Mohr-Coulomb yield criterion [29, 30]), which corresponds to plastic yielding of the single-asperity, independent of interfacial adhesion.

It is important to note that, in the atomic wear region, there are atomic wear debris constantly generated at the interface. Intuitively, one may expect that the atomic wear particles could serve to lubricate the interface and therefore reduce the friction [31]. However, as shown in Fig. 5(a), the friction coefficient stays constant for the entire range of normal stress, spanning wear rate (see Ref. [13]) over three orders of magnitude. It appears that debris particles generated at the tribo-interface, without chemical alteration such as oxidation, may not be considered as third bodies.

3.5 Efficiency of the mechanical work

The efficiency for sliding simulation with a truncated cone at different work of adhesion is shown in Fig. 6. There exists a transition of the thermodynamic efficiency of debris generation from low normal stress (atomic wear) to high normal stress (plastic wear) which is in correspondence with the wear rate transition between the atomic wear regime and the plastic wear regime [13]. In the low wear regime, less than 5% mechanical energy is dissipated through wear and most of the mechanical energy is converted to frictional heat. Debris generation can be considered as chemical reaction, driven by the mechanical agitation of the slider [12]. Thus, the low mechanical efficiency in the low wear regime indicates a poor mechanochemical coupling between friction and wear. For high normal stress, the thermodynamic efficiency increases with the normal stress, in a manner similar to the wear rate in the plastic wear region [13]. It can be also seen in Fig. 6 that, at very high normal stress, all three curves saturate to an efficiency of roughly 50%, where the normal stress is very close to the tip crushing stress ~ 2.5 GPa [13]. That is, the mechanical work is equally dissipated by wear, i.e., plastic flow, and frictional heat, which is somewhat similar to the equipartition of kinetic energy and potential energy in a harmonic oscillator in equilibrium. Recently, Aghababaei et al. [32] have discovered a linear dependence of the wear debris volume on the frictional work in single-asperity wear via fracture-induced debris, which is a clear evidence that part of the

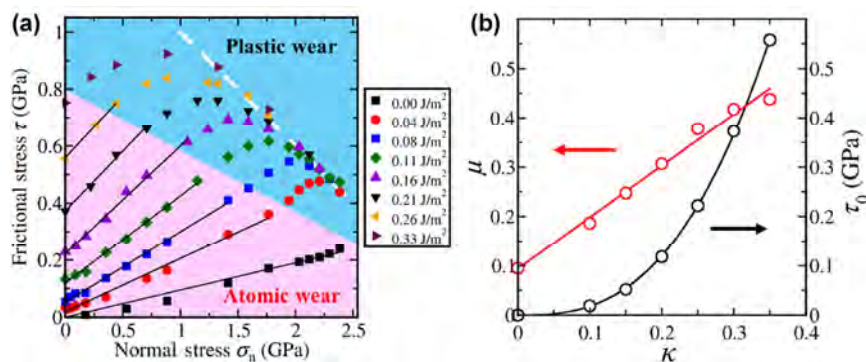


Fig. 5 (a) Frictional stress as a function of normal stress and work of adhesion. The boundary between atomic wear (purple region) and plastic wear (blue region) is schematically drawn according to Ref. [13]. The largest normal stress, ca. 2.52 GPa corresponds to tip crash stress and the largest shear stress, ca. 1.05 GPa corresponds to $\kappa = 100\%$. The yield surface is denoted by the white dash line in the plastic wear regime. (b) τ_0 and μ from linear fitting in (a) at different κ (the linear fitting for $W_{\text{adh}} = 0.00$ J/m² is forced to pass the origin).

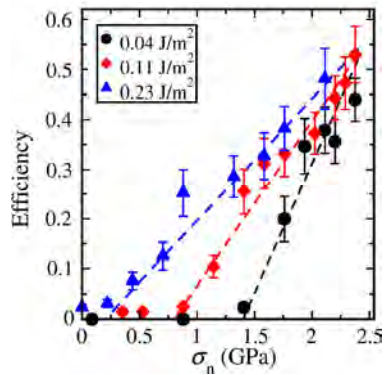


Fig. 6 Variation of the efficiency of the mechanical work with normal stress at three levels of adhesion. The dash lines are guides for eyes to show the linear dependence of the efficiency on normal stress in the plastic wear regime.

mechanical work is spent on wear debris generation. Since the authors have not reported any data on the frictional heat during the sliding, it will be very interesting to measure the efficiency of the mechanical work in this type of wear.

4 Conclusions

For single-asperity sliding system, we have found the friction is generally independent of temperature or sliding velocity within our simulation range. In the atomic wear region, Amontons' first law is observed from the linear dependence of the frictional stress on the normal stress. No lubrication effect from wear debris particles is observed. The frictional stress deviates from the linear trend in the plastic wear regime until the tip crashes. The low efficiency (<5%) of the mechanical work in the atomic wear regime indicates a poor coupling between wear and friction. In the plastic wear regime, the mechanical efficiency increases linearly with normal stress toward 50%.

Acknowledgement

We thank Professors Liping Huang (Rensselaer Polytechnic Institute), Thierry Blanchet (Rensselaer Polytechnic Institute), Izabela Szlufarska (Univ. of Wisconsin), Rob Carpick (Univ. Pennsylvania), Mark Robbins (Johns Hopkins) and Michael Falk (Johns Hopkins) for useful discussions. We are grateful to the support from the National Science Foundation (Grant No. CMMI-1031408). Molecular dynamics

simulations were carried out in LAMMPS using supercomputers in the Computational Center for Innovations (CCI) at RPI.

Open Access: The articles published in this journal are distributed under the terms of the Creative Commons Attribution 4.0 International License (<http://creativecommons.org/licenses/by/4.0/>), which permits unrestricted use, distribution, and reproduction in any medium, provided you give appropriate credit to the original author(s) and the source, provide a link to the Creative Commons license, and indicate if changes were made.

References

- [1] Bowden F P, Tabor D. *The Friction and Lubrication of Solids*. Oxford (UK): Oxford University Press, 2001.
- [2] Scholz C H. Earthquakes and friction laws. *Nature* **391**(6662): 37–42 (1998)
- [3] Brace W F, Byerlee J D. Stick-slip as a mechanism for earthquakes. *Science* **153**(3739): 990–992 (1966)
- [4] Szlufarska I, Chandross M, Carpick R W. Recent advances in single-asperity nanotribology. *J Phys D Appl Phys* **41**(12): 123001 (2008)
- [5] Carpick R W, Salmeron M. Scratching the surface: Fundamental investigations of tribology with atomic force microscopy. *Chem Rev* **97**(4): 1163–1194 (1997)
- [6] Dowson D. *History of Tribology*. London (UK): Longman Group Limited, 1979.
- [7] Gao J P, Luedtke W D, Gourdon D, Ruths M, Israelachvili J N, Landman U. Frictional forces and amontons' law: From the molecular to the macroscopic scale. *J Phys Chem B* **108**(11): 3410–3425 (2004)
- [8] Mo Y F, Turner K T, Szlufarska I. Friction laws at the nanoscale. *Nature* **457**(7233): 1116–1119 (2009)
- [9] Archard J F. Elastic deformation and the laws of friction. *Proc Roy Soc A* **243**(1233): 190–205 (1957)
- [10] Gotsmann B, Lantz M A. Atomistic wear in a single asperity sliding contact. *Phys Rev Lett* **101**(12): 125501 (2008)
- [11] Jacobs T D B, Gotsmann B, Lantz M A, Carpick R W. On the application of transition state theory to atomic-scale wear. *Tribol Lett* **39**(3): 257–271 (2010)
- [12] Jacobs T D B, Carpick R W. Nanoscale Wear as a stress-assisted chemical reaction. *Nat Nanotechnol* **8**(2): 108–112 (2013)
- [13] Yang Y J, Huang L P, Shi Y F. Adhesion suppresses atomic Wear in single-asperity sliding. *Wear* **352–353**: 31–41 (2016)

- [14] Vargonen M, Yang Y J, Huang L P, Shi Y F. Molecular simulation of tip Wear in a single asperity sliding contact. *Wear* **307**(1–2): 150–154 (2013)
- [15] Yang Y. Quantitative understanding of single-asperity contact via molecular simulations. Ph.D Thesis. Rensselaer Polytechnic Institute, 2017.
- [16] Sha Z D, Sorkin V, Branicio P S, Pei Q X, Zhang Y W, Srolovitz D J. Large-scale molecular dynamics simulations of wear in diamond-like carbon at the nanoscale. *Appl Phys Lett* **103**(7): 073118 (2013)
- [17] Li Q Y, Dong Y L, Perez D, Martini A, Carpick R W. Speed dependence of atomic stick-slip friction in optimally matched experiments and molecular dynamics simulations. *Phys Rev Lett* **106**(12): 126101 (2011)
- [18] Gnecco E, Bennewitz R, Gyalog T, Loppacher C, Bammerlin M, Meyer E, Güntherodt H J. Velocity dependence of atomic friction. *Phys Rev Lett* **84**(6): 1172–1175 (2000)
- [19] Riedo E, Gnecco E, Bennewitz R, Meyer E, Brune H. Interaction potential and hopping dynamics governing sliding friction. *Phys Rev Lett* **91**(8): 084502 (2003)
- [20] Sang Y, Dubé M, Grant M. Thermal effects on atomic friction. *Phys Rev Lett* **87**(17): 174301 (2001)
- [21] Jansen L, Hölscher H, Fuchs H, Schirmeisen A. Temperature dependence of atomic-scale stick-slip friction. *Phys Rev Lett* **104**(25): 256101 (2010)
- [22] Wahnström G. Molecular-dynamics study of a supercooled two-component Lennard-Jones system. *Phys Rev A* **44**(6): 3752–3764 (1991)
- [23] Plimpton S. Fast parallel algorithms for short-range molecular dynamics. *J Comput Phys* **117**(1): 1–19 (1995)
- [24] Luan B Q, Robbins M O. Effect of inertia and elasticity on stick-slip motion. *Phys Rev Lett* **93**(3): 036105 (2004)
- [25] Minsky H K, Turner K T. Achieving enhanced and tunable adhesion via composite posts. *Appl Phys Lett* **106**(20): 201604 (2015)
- [26] Spijker P, Anciaux G, Molinari J F. Relations between roughness, temperature and dry sliding friction at the atomic scale. *Tribol Int* **59**: 222–229 (2013)
- [27] Liu X Z, Ye Z J, Dong Y L, Egberts P, Carpick R W, Martini A. Dynamics of atomic stick-slip friction examined with atomic force microscopy and atomistic simulations at overlapping speeds. *Phys Rev Lett* **114**(14): 146102 (2015)
- [28] Zwörner O, Hölscher H, Schwarz U D, Wiesendanger R. The velocity dependence of frictional forces in point-contact friction. *Appl Phys A* **66**(S1): S263–S267 (1998)
- [29] Vargonen M, Huang L P, Shi Y F. Evaluating Mohr–Coulomb yield criterion for plastic flow in model metallic glasses. *J Non Cryst Solids* **358**(24): 3488–3494 (2012)
- [30] Lund A C, Schuh C A. Yield surface of a simulated metallic glass. *Acta Mater* **51**(18): 5399–5411 (2003)
- [31] Berman D, Deshmukh S A, Sankaranarayanan S K R S, Erdemir A, Sumant A V. Macroscale superlubricity enabled by graphene nanoscroll formation. *Science* **348**(6239): 1118–1122 (2015)
- [32] Aghababaei R, Warner D H, Molinari J F. On the debris-level origins of adhesive wear. *Proc Natl Acad Sci USA* **114**(30): 7935–7940 (2017)



Yunfeng SHI. He received his Ph.D. degree in materials science from the University of Michigan, Ann Arbor, in 2006. He then spent two years in North Carolina State University as a postdoctoral research associate. Dr. Shi joins the Department of Materials Science and

Engineering at Rensselaer Polytechnic Institute in Fall 2008 as an assistant professor and was promoted to associate professor in 2014. His research focuses on simulation and modeling of advanced materials systems. His recent interests include nanoporous carbon, molecular motors, energetic materials, nanotribology and metallic glasses.



Yongjian YANG. He received his Ph.D. degree in materials engineering from Rensselaer Polytechnic Institute in Troy, New York in 2017. Now he

is a postdoctoral scholar at the Penn State University in State College. His research interests include nanotribology, glass science, metal-organic framework, etc., using molecular simulation.

Acoustic emission characterization of sliding wear under condition of direct and inverse transformations in low-temperature degradation aged Y-TZP and Y-TZP- Al_2O_3

Nikolai L SAVCHENKO^{1,*}, Andrey V FILIPPOV^{1,2}, Sergei Yu TARASOV^{1,2}, Andrey I DMITRIEV^{1,3}, Evgeny V SHILKO^{1,3}, Aleksandr S GRIGORIEV¹

¹ Institute of Strength Physics and Materials Science SB RAS, Tomsk 634055, Russian Federation

² National Research Tomsk Polytechnic University, Tomsk 634050, Russian Federation

³ National Research Tomsk State University, Tomsk 634050, Russian Federation

Received: 05 April 2018 / Revised: 24 May 2018 / Accepted: 14 June 2018

© The author(s) 2018. This article is published with open access at Springerlink.com

Abstract: In this research, results of the investigation of the sliding friction and wear of yttria-stabilized tetragonal zirconia polycrystalline (Y-TZP) and Y-TZP- Al_2O_3 samples preliminarily subjected to low-temperature degradation are reported. The investigation was carried out using a pin-on-disk tribometer with simultaneous recording of acoustic emission (AE) and vibration acceleration. The sliding wear process was found to be determined by dynamic direct and inverse Y-TZP transformations detected by monoclinic and tetragonal X-ray diffraction peak ratios. The AE signals generated under direct and inverse transformations can be used to characterize wear and friction mechanisms as well as direct and inversed sliding-induced phase transformations. The AE signal energy grows with the friction coefficient and the inverse transformation degree. Reduction of the AE signal energy indicates establishing the mild wear stage caused by effective stress-induced direct martensitic transformation. The AE signal median frequency increases in the case of lower friction. Numerical studies of wear subsurface fracture under conditions of stress-induced martensitic transformation were used to elucidate the role played by the phase transformation in Y-TZP and Y-TZP- Al_2O_3 . Martensitic transformation in Y-TZP was described with use of the non-associated dilatant plasticity model. Simulation results particularly show that increase in the value of dilatancy coefficient from 0 to 0.2 is accompanied by 25%–30% reduce in characteristic length and penetration depth of sliding-induced subsurface cracks. As shown the AE may be an effective tool for *in-situ* monitoring the subsurface wear of materials experiencing both direct and inverse transformations.

Keywords: zirconia; transformation toughening; low-temperature degradation; friction; acoustic emission; numerical modeling; movable cellular automata method

1 Introduction

Tetragonal zirconia polycrystalline ceramics (TZP) partially stabilized by 3 mol% of yttria (3Y-TZP) are a well-known material that makes it possible to combine high strength, fracture toughness, ion conductance, and low thermal conduction. Therefore, they have been evaluated for numerous applications, ranging from

thermal barrier coatings to biomedical materials. However, 3Y-TZP is prone to low-temperature degradation (LTD) in a humid atmosphere [1]. The LTD may occur in the 20–400 °C range when polycrystalline 100% tetragonal-phase material slowly transforms into a monoclinic zirconia with corresponding fast degradation of strength and fracture toughness. Phase transformation in LTD starts locally and results

* Corresponding author: Nikolai L SAVCHENKO, E-mail: savnick@ispms.ru

in surface fissuring by means of micro and macro cracks [2]. The LTD may be inhibited by introducing various hard particles, such as alumina, and thus results in a ceramic material composite [3].

The effect of transformation-induced plasticity on Y-TZP wear has been extensively studied. Thus, Fischer et al. [4] investigated the effect of transformation-induced fracture toughness of this ceramic on the wear resistance depending on the dissolved Y_2O_3 content. The improved fracture toughness corresponded to high Y-TZP wear resistance. The sliding speed was very low (0.001 m/s) to avoid heating the sample.

Sliding tests on Y-TZP should be stopped on reaching the sliding speed value 1 m/s to avoid further catastrophic deterioration on the Y-TZP worn surface [5]. The rationale is that the transformation toughening contribution to wear resistance is reduced as the worn surface temperature grows with the sliding speed and becomes closer to the tetragonal-phase stability boundary of 900 °C.

Grinding texture formation for tetragonal and monoclinic peaks in Ce-TZP and Y-TZP materials was explained by friction heating the worn surface layers, which promoted reversible martensite transformation and, thus, caused the crystalline lattice reorientation [6, 7].

It is common to discuss the 100% tetragonal Y-TZP wear against a steel counter body in a sliding speed range of 0.2–0.9 m/s in terms of microcutting by ceramic wear particles detached from the sample under the action of the stress exerted by the volume expansion effect of strain-induced martensitic transformation [8, 9]. Such a wear process may be referred to as mild wearing contrast to the brittle fracture that occurs at higher speeds when strain-induced plasticity is not effective. The LTD-aged samples are less prone to the direct martensite transformation and, therefore, studying wear and friction on them is of interest for the research community.

Deville et al. [2] analyzed in a critical manner the applicability of different analytical methods for characterization of the LTD aging, including X-ray diffraction (XRD), scanning electron microscopy (SEM), optical interferometry (OI), and atomic-force microscopy (AFM). It was shown that both XRD and SEM have limited spatial resolution, which does not allow

observing subsurface and superficial structural changes at the first LTD stage, respectively. However, both OI and AFM allow observing the LTD onset stage on the surface of a sample, but no information about subsurface structural changes can be obtained. Also, the AFM observation is confined by small surface areas of interest. Therefore, the above-named methods do not allow obtaining adequately full information about the LTD, and new methods should be applied. One of these methods used for studying LTD in 3Y-TZP is acoustic emission (AE) [10]. It was shown that both the AE count rate and amplitude correlate with LTD evolution and, therefore, may be used for real-time monitoring of the 3Y-TZP structural condition.

There is a lack of studies on the behavior of the LTD-aged 3Y-ZP ceramics in mechanically mated couples, i.e., when the 3Y-TZP subsurface already contains some amount of monoclinic phase, while the mechanical behavior of 3Y-TZP ceramics subjected to LTD is an interesting issue concerning the wide application of these ceramics.

Most of the investigations in the field of AE monitoring focused on AE monitoring of metallic sliding contacts, and little research was devoted to the AE monitoring of ceramic ones [11–13]. It was established that the AE signal root mean square (RMS) amplitude is linearly dependent on the friction force work given that the sliding speed is kept constant.

There is another approach to AE signal studies that looks for correlations between the AE signal time–frequency domain values and mechanical loading parameters. The AE signal's most informative parameters are median frequency and power spectral dependencies on time [14–17].

The AE signal sources in sliding wear on zirconia-base ceramics depend on the martensitic transformation. McBride et al. suggested [18] that wear debris removal from the unlubricated sliding contact was characterized by high-amplitude short-rise-time AE signals, while running-in wear and plastic flow resulted in low-amplitude long-rise-time AE signals.

Deformation and fracture processes in zirconia-based materials have been studied using the AE by many researchers [19–22]. Lankford [20] used AE for controlling the deformation and fracture on magnesia partially stabilized zirconia (Mg-PSZ) ceramics in a

compression test. The AE events occurred only on reaching the yield offset stress, so that the acoustic emission was related to the nonlinear stress-strain curve portion, i.e., the portion whose nonlinearity was determined by martensitic transformation. There was no such nonlinear behavior at elevated temperatures (700 °C) when martensitic transformation became hardly feasible. Further mechanical loading resulted in registering the AE signals from a final catastrophic failure. These observations allowed Lankford to suggest that AE signals have been generated only by a microfracture dissipation mechanism and not by the transformation itself.

Droz dov et al. [21] established that AE signals during a transformation-induced plastic deformation stage on zirconia-base materials have been generated by microcracking under tensile loading. The AE count rate was in good correlation to the crack size and propagation velocity. Therefore, AE signals in sliding friction are generated by the subsurface cracks that are responsible for the wear particle formation. It was found earlier that crack propagation caused by sliding might be detected by median frequency drops [14–16].

Another fast-developing trend in studying the integral martensitic transformation as well as the LTD phenomenon is computer-aided modeling. Numerical approaches in the field of modeling the wear and friction processes occurring in Y-TZP-base ceramics face the necessity of modeling the martensitic transformation effects; therefore, a continuous theoretical description of integral martensitic transformation manifestations in materials (including 3Y-TZP) is traditionally performed using associated plastic flow models based on different yield criteria [23–27]. Experimental investigations show that both first and second stress tensor invariants (or equivalent stress and mean/hydrostatic stress, respectively) should be included with these yield criteria [23]. The necessity of considering the hydrostatic stress is determined by the high value of volume change, 4% to 5%, that occurs during direct or inverse martensitic phase transformation and by a significant contribution of localized dilatancy/compaction to toughening/embrittlement.

The well-known examples of the above-described models are various versions of the two-parameter micromechanical Hwang-Lagoudas model, which

makes allowance for the hydrostatic stress contribution into the yield criteria in the form of linear approximation [23–27]. Characteristic 3Y-TZP values of a volume expansion strain of 4% to 5% and a lattice shear of 7% to 16% are used as the two-parameter model yield criterion parameters. Despite giving noticeable advantages, the use of these “localized” models for description of inelastic deformation in volumes that partially experienced martensitic transformation is complicated by the necessity of introducing extra new phase growth kinetic models. Furthermore, the generation of transformation-induced shear bands gives highly distorted localized stress fields, which serve to nucleate microcracks and, thus, further contribute to inelastic volume expansion (dilatancy) [28]. The latter fact is, as a rule, not considered within the frameworks of the above-described plastic flow models. At the same time, the key integral manifestations of such a combined transformation/microcrack-induced plasticity mechanism could be adequately described using general mathematical models based on the nonassociated plastic flow rule.

A key feature of those models is introducing an extra integral parameter, such as a dilation rate, as well as a specific ratio that makes it possible to determine the dilation rate dynamics in the course of inelastic deformation. The well-known example of such a model is the Nikolaevsky nonassociated plastic flow model based on the von Mises-Schleicher yield criterion [29–30]. Note that structural form of this criterion is a full analogue of the Hwang-Lagoudas micromechanical criterion as well as the Nikolaevsky model parameters can be estimated, among others, from those of micromechanical model. The Nikolaevsky model has originally been formulated for description of a microcrack-induced dilatant inelastic behavior of brittle rocks and ceramics. However, its generality and independence of the localized stress relaxation mechanisms allowed using it for modeling the mechanical behavior of Y-TZP (as well as Y-TZP- Al_2O_3 ceramics) under pressure/temperature (PT) conditions favorable for direct phase transformation accompanied by material dilation [31].

Wear in ceramics is mainly by subsurface fracture. Therefore, this model is used here for a numerical study of the subsurface damages accumulated in Y-TZP and Y-TZP- Al_2O_3 ceramic materials during sliding.

This research combines the results of experimental and numerical studies of the effect of transformation-induced plasticity on the subsurface fracture. The objective of this research is to understand how direct and inverse transformations occur during the wear and friction in LTD-aged Y-TZP/steel and Y-TZP-Al₂O₃/steel and establish correlations with the AE and vibration acceleration signal parameters.

2 Material and methods

The ceramic samples had a chemical composition as follows: 97 mol% ZrO₂ + 3 mol% Y₂O₃ (Y-TZP) and 80 wt% ZrO₂ (3 mol% Y₂O₃) + 20 wt% Al₂O₃ (Y-TZP-Al₂O₃). Freshly sintered Y-TZP and Y-TZP-Al₂O₃ samples had 5% porosity and contained 100% tetragonal-phase zirconia. These samples were stored for more than 20 years at the room temperatures and humidity. The resulting LTD-aged samples contained both tetragonal/monoclinic phases at ratios of 64/36 and 75/25, for Y-TZP and Y-TZP-Al₂O₃, respectively. The LTD-aged samples revealed multiple instances of spalling and microcracking on their surfaces formed as a result of tetragonal-to-monoclinic transformation.

The tribological behavior of the samples was studied using a pin-on-disk scheme and TRIBO technic tribometer. The ceramic samples were 3 mm × 3 mm in cross-section area and 10-mm-high pins. The disk's surfaces were mechanically ground to roughness Ra = 0.32 μm. The sliding speed and path were 0.5 m/s and 1 m/s, respectively. Normal loads were 13 N and 26 N. After testing, the worn surfaces of the ceramic samples were examined using an optical microscope Altami MET 1C. XRD studies of the polished surfaces were performed using an XRD instrument DRON 3.0, 40 kV, 22 μA, and Cu-K_α radiation in the 2θ range 26°–38°.

An EYa-2 setup (Togliatti State University) attached with a MSAE-L230-1000kHz bandpass 20-mm-diameter sensor was used to receive and analyze the acoustic emission signals. Parasite signals generated by the mechanical system were removed by means of a 50 kHz highpass LC-filter. The AE signal sampling rate was 1 kHz. Therefore, an AE signal envelope characterized the slowly occurring processes. The quickly occurring processes were characterized by the AE 0.021 s duration frames recorded at sampling rate 6.25 MHz. The AE

frames were analyzed together with the simultaneously obtained vibration acceleration signal. Special software was developed for determining median frequency values for each frame using the short-time Fourier transformation (STFT) with a rectangle 1000-data-point window size and 300-point length shift. Doing so enabled the time dependencies of these characteristics to be reconstructed for the full signal duration.

The vibration acceleration signals were registered by an IMI industrial accelerometer and USB data logger NI-9234 (National Instruments) at a sampling rate 25.6 kHz. The running root mean square (run RMS) of acceleration was calculated for 1-s signal acquisition periods.

3 Results

Experimental time dependencies characterizing the friction coefficient, AE median frequency, AE signal energy, and RMS vibrational accelerations in two perpendicular planes are shown in Fig. 1, Fig. 2, Fig. 4, and Fig. 5 for different sliding-speed and normal-load values as obtained on LTD-aged Y-TZP/steel and Y-TZP-Al₂O₃/steel couples.

3.1 Y-TZP/steel

3.1.1 Friction coefficient

Sliding at 0.5 m/s and 13 N load (Fig. 1(a)) was characterized by high-frequency and low-frequency friction coefficient oscillations in the range ~0.05–0.64. The low-frequency oscillation period was approximately 1,000 s. Increasing the normal load to 26 N resulted in increasing the friction coefficient range to ~0.05–0.92 (Fig. 1(b)).

Sliding at 1 m/s and 13 N load (Fig. 2(a)) was in steady friction mode with an almost constant friction coefficient 0.2 until approximately the 1800th s, which then changed for high-amplitude oscillation mode in the range ~0.07–0.42. Sliding at 1 m/s and 26 N was characterized by a short running-in period and then high-amplitude oscillations in the range ~0.09–0.6 (Fig. 2(b)).

3.1.2 AE signal median frequency

Y-TZP/steel, 0.5 m/s. The AE signal median frequency

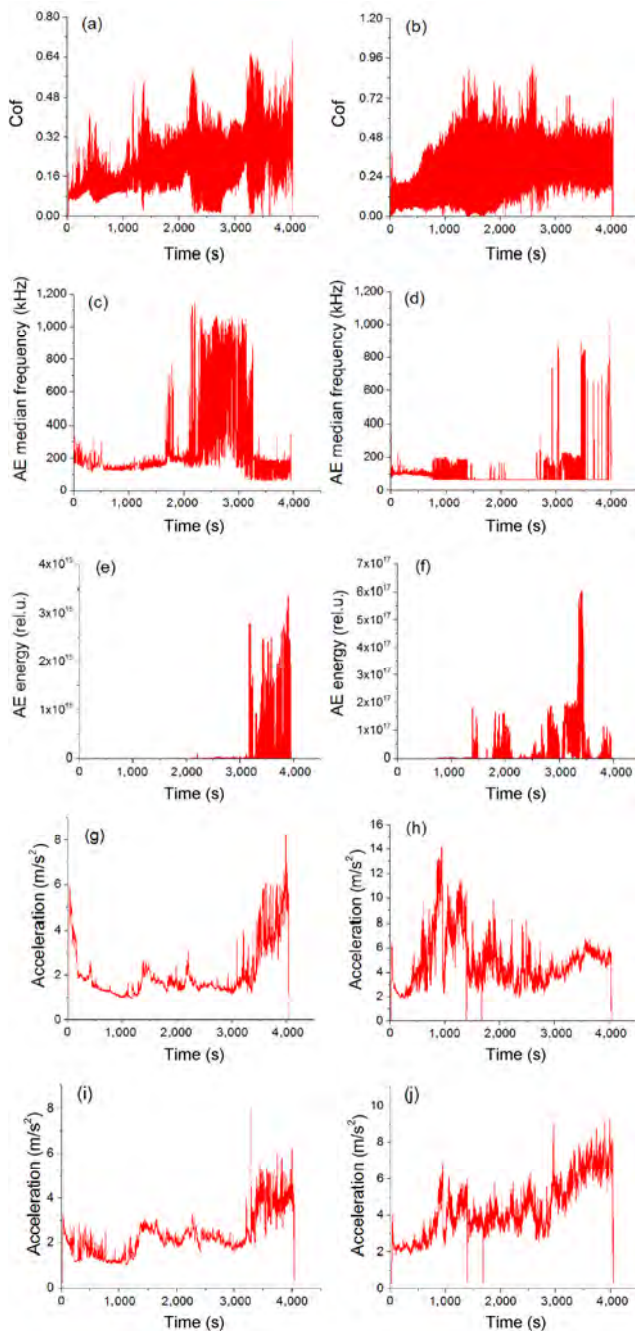


Fig. 1 Time dependencies of friction coefficient ((a), (b)), AE median frequency ((c), (d)), AE energy ((e), (f)), and vertical ((g), (h)) and horizontal ((i), (j)) vibration acceleration RMS for Y-TZP ceramics obtained in sliding at 0.5 m/s, 13 N ((a), (c), (e), (g), (i)) and 26 N ((b), (d), (f), (h), (j)) normal load.

(MF) stays almost constant until approximately the 1700th s, when it shows first a narrow high-frequency burst and then a set of bursts of even higher frequency (Fig. 1(c)). Increasing the normal load to 26 N gives a row of 75–215 kHz frequency peaks, which then

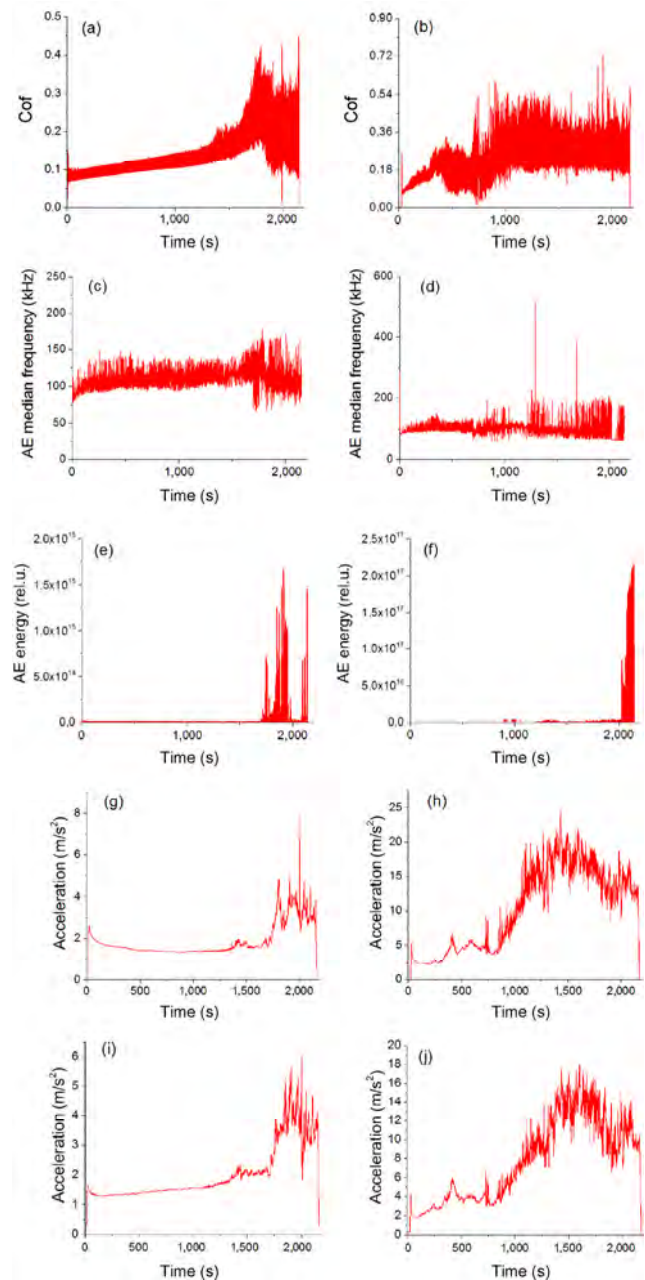


Fig. 2 Time dependencies of friction coefficient ((a), (b)), AE median frequency ((c), (d)), AE energy ((e), (f)), and vertical ((g), (h)) and horizontal ((i), (j)) vibration acceleration RMS for Y-TZP ceramics obtained in sliding at 1 m/s, 13 N ((a), (c), (e), (g), (i)) and 26 N ((b), (d), (f), (h), (j)) normal load.

disappear (Fig. 1(d)). High-frequency 1 MHz narrow bursts arise again from 2600th s (Fig. 1(d)).

MF histograms in Figs. 3(a) and 3(c) show that the values are predominantly in the frequency range of 55–300 kHz for sliding at a normal load of 13 N. For a 0.5 m/s sliding speed, there is a high-frequency 300–1,050 kHz tail (Fig. 3(a)). Sliding at a higher normal

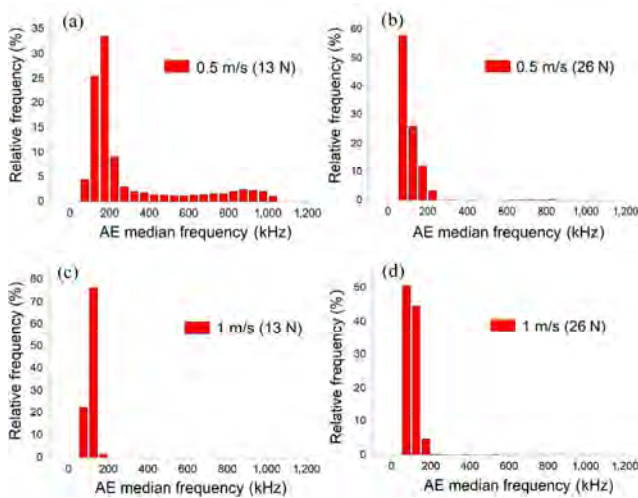


Fig. 3 Median frequency distribution histograms for Y-TZP in sliding at 0.5 m/s 13 N (a) and 26 N (b) and at 1 m/s 13 N (c) and 26 N (d).

load of 26 N shifts the distribution to the lower frequency end (i.e., 55–225 kHz) leaving a small amount of high-frequency 600–1,060 kHz peaks (Figs. 3(b) and 3(d)).

Y-TZP/steel, 1 m/s. The median frequency changes in the range 75 to 175 kHz at a normal load of 13 N (Fig. 2(c)). The 26 N sliding is accompanied by non-steady MF growth in the 70–225 kHz range (Fig. 2(d)). MF histograms (Figs. 3(c) and 3(d)) show a narrow MF distribution within 55–175 kHz for samples tested at 1 m/s 13 N (c) and 1 m/s 26 N (d).

3.1.3 AE energy

Y-TZP/steel, 0.5 m/s. The AE energy plot shows almost no changes during the first 3,200 s period of sliding at a 13 N load (Fig. 1(e)). High peaks appear starting from the 3200th s. Sliding at a higher load of 26 N gives a set of medium-amplitude peak groups as well as one high-amplitude one (Fig. 1(f)) starting from 1300th s.

Y-TZP/steel, 1 m/s. The first high-energy peaks appear after sliding for 1,600 s and 2,000 s at a 13 N and 26 N load, respectively (Figs. 2(e) and 2(f)).

3.1.4 Vibration acceleration in vertical and horizontal planes

Y-TZP/steel, 0.5 m/s. Vertical and horizontal plane vibration acceleration RMS values stay below the 4 m/s² range during sliding at a 13 N load until reaching a 3,200 s time at which they start sharply

growing to 8 and 6 m/s², respectively (Figs. 1(g) and 1(i)). The vertical and horizontal vibration acceleration RMS values show sequences of peaks whose heights decay and grow, respectively, depending on the 26 N sliding test time (Figs. 1(h) and 1(j)).

Y-TZP/steel, 1 m/s. The vertical and horizontal vibro-accelerations are low and in a steady mode from the beginning of the sliding under a 13 N load (Figs. 2(g) and 2(i)). The first high-amplitude vibrations in sliding at 13 N and 26 N appear starting from 1500th s and 1000th s, respectively (Figs. 2(g)–2(j)).

3.2 Y-TZP-Al₂O₃/steel

3.2.1 Friction coefficient

Sliding composite ceramics Y-TZP-Al₂O₃ against steel is accompanied by high-amplitude friction force oscillations for 13 N and 26 N loads at 0.5 m/s (Figs. 4(a) and 4(b)). The same type of behavior is exhibited at a 1 m/s sliding speed (Figs. 5(a) and 5(b)).

A diagram in Fig. 6(a) shows that increasing the normal load resulted in increasing the mean friction coefficient while increasing the sliding speed to reduce it. The mean friction coefficient values of Y-TZP/steel were higher than those of the Y-TZP-Al₂O₃/steel couple.

3.2.2 AE signal median frequency

Y-TZP-Al₂O₃/steel, 0.5 m/s. MF starts increasing from the beginning of the sliding at 13 N, thus reaching a maximum value of 250 kHz (Fig. 4(c)) at the 3250th s and then diminishing to 70 kHz. A higher load of 26 N gives a background MF level of approximately 100 kHz with a 500 s duration group of bursts starting at the 750th s (Fig. 5(c)). The MF histograms demonstrate (Figs. 7(a) and 7(b)) that sliding at 13 N provides an uneven MF distribution with a predominating low-frequency and fewer AE high-frequency events. The distribution becomes greater even in sliding at 26 N with the peak value in the range of 75–125 kHz as well as a smaller group of 125–275 kHz signals.

Y-TZP-Al₂O₃/steel, 1 m/s. Increasing the sliding velocity had only a minor effect of MF for normal load values of 13 N and 26 N (Figs. 4(c) and 4(d) and Figs. 5(c) and 5(d)). According to the diagrams in Fig. 3 and Figs. 7(c) and 7(d), mean MF values for both Y-TZP/steel and Y-TZP-Al₂O₃/steel couples fall into the

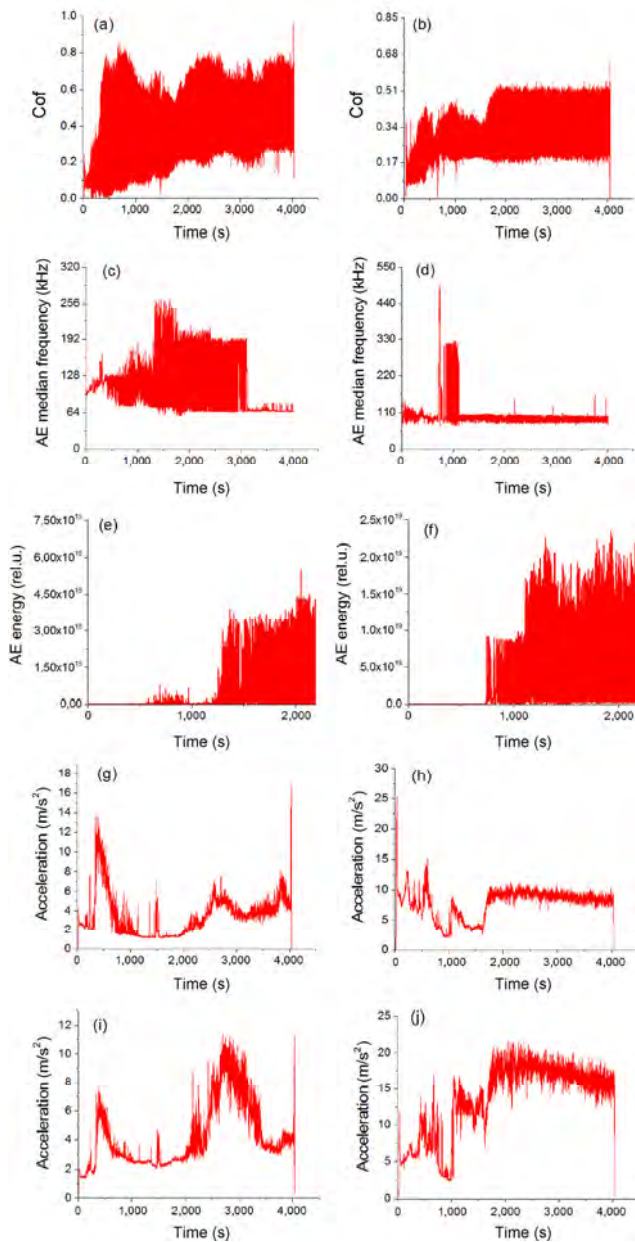


Fig. 4 Time dependencies of friction coefficient ((a), (b)), AE median frequency ((c), (d)), AE energy ((e), (f)), and vertical ((g), (h)) and horizontal ((i), (j)) vibration acceleration RMS for Y-TZP- Al_2O_3 ceramics obtained in sliding at 0.5 m/s, 13 N ((a), (c), (e), (g), (i)), and 26 N ((b), (d), (f), (h), (j)) normal load.

75–200 kHz range. Maximal MF was found for Y-TZP/steel at 0.5 m/s and 13 N. All other speed and load combinations provide MF values higher than those obtained from the Y-TZP/steel couple.

3.2.3 AE energy

Y-TZP- Al_2O_3 /steel, 0.5 m/s. A medium-energy peak group formed after sliding for 2,400 s at 13 N and then

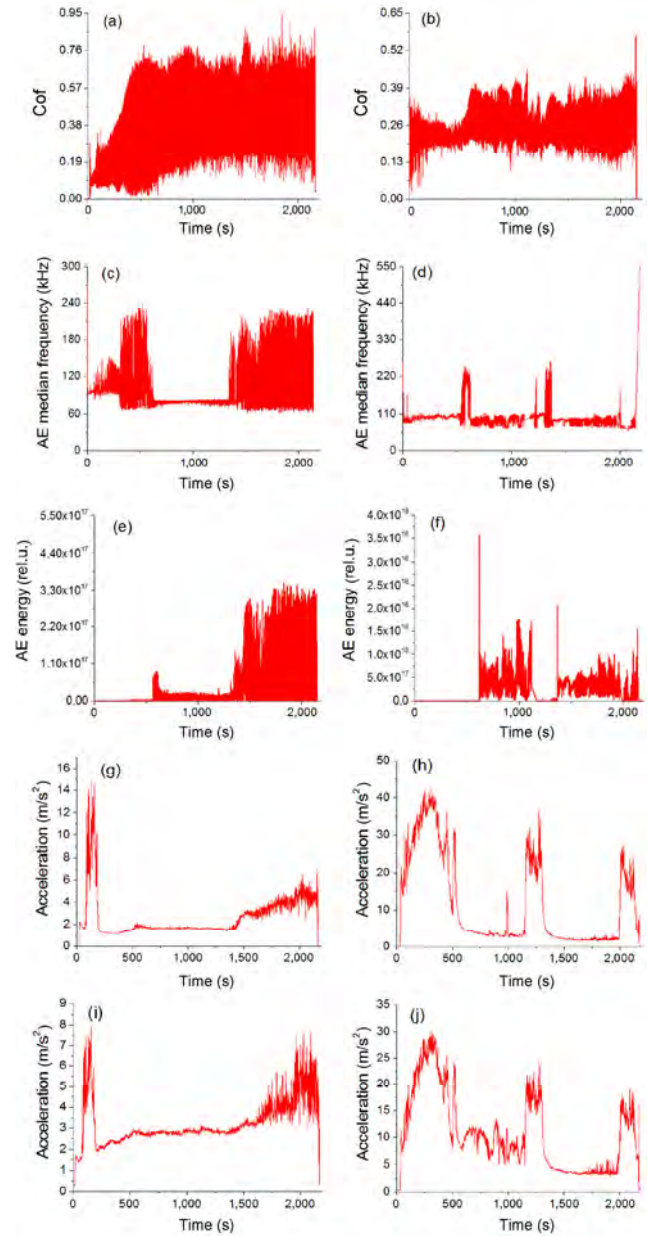


Fig. 5 Time dependencies of friction coefficient ((a), (b)), AE median frequency ((c), (d)), AE energy ((e), (f)), and vertical ((g), (h)) and horizontal ((i), (j)) vibration acceleration RMS for Y-TZP- Al_2O_3 ceramics obtained in sliding at 1 m/s, 13 N ((a), (c), (e), (g), (i)), and 26 N ((b), (d), (f), (h), (j)) normal load.

changed for a high-energy peak group, thus forming a steplike diagram in Fig. 4(e). Analogous AE energy behavior was observed for sliding at a 26 N load (Fig. 4(f)). The first medium energy peak group formed after sliding for 750 s and then quickly changed for almost-constant-height high-energy peaks (Fig. 4(f)).

Y-TZP- Al_2O_3 /steel, 1 m/s. Medium energy peaks were observed after 13 N load sliding for 550 s (Fig. 5(e))

and then changed for the high-energy peaks according to the above-described two-step plot pattern. Another type of behavior was observed for sliding at a 26 N load when two almost-equal height peak groups appear (Fig. 5(f)). The minimum AE energy value was observed in the case of Y-TZP-Al₂O₃/steel sliding (Fig. 6(c)).

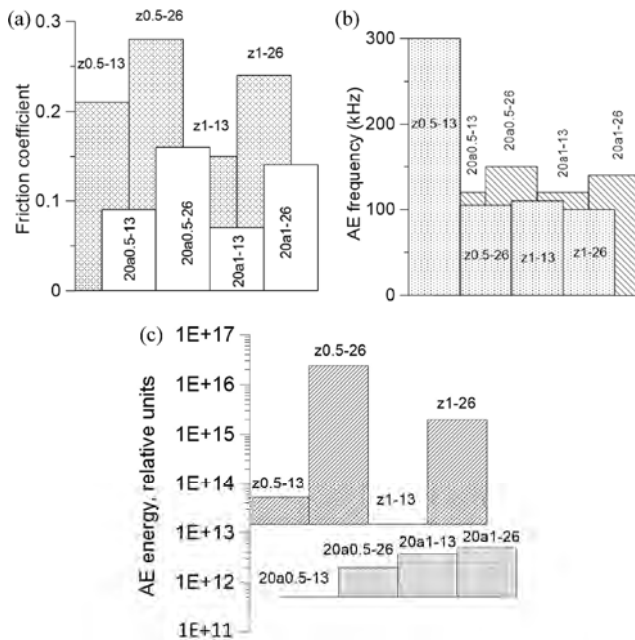


Fig. 6 Diagrams showing (a) mean friction coefficient values, (b) mean AE median frequency values, and (c) mean AE energy values for Y-TZP (z) and Y-TZP-Al₂O₃ (20a) samples. The first number after the material index (“z” or “20a”) denotes the sliding velocity (0.5 m/s or 1 m/s), while the second index corresponds to the normal load value (13 N or 26 N).

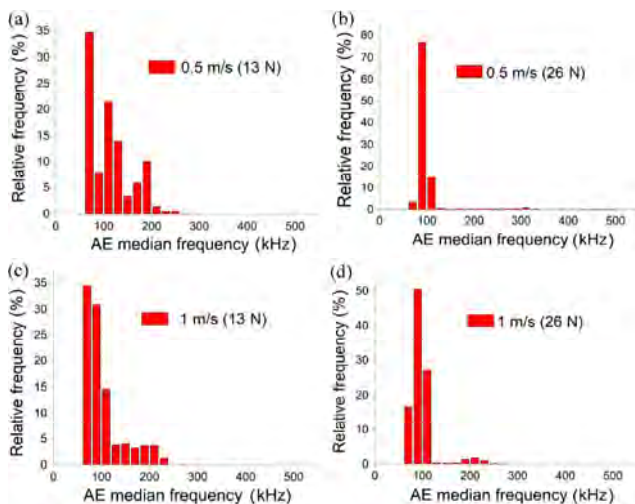


Fig. 7 Median frequency distribution histograms for Y-TZP-Al₂O₃.

3.2.4 Vibration acceleration in vertical and horizontal planes

Y-TZP-Al₂O₃/steel, 0.5 m/s. Vertical and horizontal vibro-acceleration RMS values showed their first 14 m/s² and 7.8 m/s² peaks in the range 0 to 1,000 s for sliding at a 13 N load (Figs. 4(g) and 4(i)). Gradual reducing vibro-acceleration RMS values were observed until the 2000th s, when high peaks appeared. The horizontal RMS's second peak was higher than that of vertical one. Sliding at 26 N provided another RMS dependence pattern when medium-height irregular peaks existed from the beginning of the process, and then it changed for low-amplitude ones, thus revealing steady-mode load-sliding stages for vertical and horizontal vibro-accelerations (Figs. 4(h) and 4(j)). Again, horizontal vibro-acceleration RMS values are higher than those of vertical.

Y-TZP-Al₂O₃/steel, 1 m/s. For 13 N sliding, two RMS peaks were observed when the first sharp and high peak arose close to the sliding onset point, and the second irregular and wide one appeared starting at the 1500th s (Figs. 5(g) and 5(i)). A more complicated pattern was observed in the case of sliding at a 26 N load. There were three peaks followed by reducing RMS amplitudes (Figs. 5(h) and 5(j)). The vertical and horizontal vibro-accelerations were low and in a steady mode from the beginning of the sliding under a 13 N load. The first high-amplitude vibrations in sliding at 13 N and 26 N appear starting from the 1500th s and 1000th s, respectively (Figs. 5(g)–5(j)).

3.3 Structural and phase evolution of worn surfaces

Y-TZP worn surfaces were more rough with the presence of cracks and spalling than those on Y-TZP-Al₂O₃ (Fig. 8).

The worn surfaces of all samples contained both monoclinic and tetragonal phases. The amount of

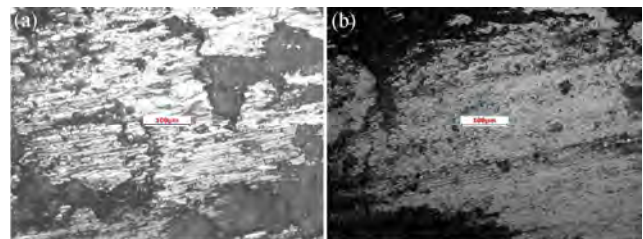


Fig. 8 Optical microscopy images of Y-TZP (a) and Y-TZP-Al₂O₃ (b) worn surfaces on sliding at 1 m/s 26 N.

monoclinic phase on the worn surface reduced by 10% compared with that of as-received LTD samples, resulting in 55% in Y-TZP monoclinic and 65% in Y-TZP- Al_2O_3 .

Another finding was that the worn surfaces revealed some XRD texturing, which is determined as the ZrO_2 tetragonal-phase XRD peak intensity ratio $I_{(002)}/I_{(200)}$. This ratio is increased by sliding and becomes higher than the 0.5 value inherent in the random crystalline lattice orientation as determined from XRD on the freshly polished ceramics surface. This ratio becomes higher than 0.8 and is applicable to the ZrO_2 monoclinic-phase XRD peak ratio $I_{(11-1)}/I_{(111)}$.

In the case of Y-TZP- Al_2O_3 , the tetragonal $I_{(002)}/I_{(200)}$ and monoclinic $I_{(11-1)}/I_{(111)}$ ratios were higher than those of Y-TZP for all sliding speed and load combinations (Fig. 9). This may tell much about sliding-induced transformation in the LTD-aged ceramics. This was investigated from the standpoint of AE parameters, which may denote the effect of the transformation on sliding.

Possible correlations among the friction coefficient, XRD, and AE parameters are shown in Fig. 10 and Fig. 11. The AE energy/friction coefficient and friction coefficient/XRD peak ratios are also shown in Fig. 10 and Fig. 11. There is a correlation between the AE energy and friction coefficient (Fig. 10). Furthermore, the minimal AE energy and friction coefficient values correspond to those of Y-TZP and Y-TZP- Al_2O_3 ceramic samples, demonstrating high ZrO_2 tetragonal $I_{(002)}/I_{(200)}$ and monoclinic $I_{(11-1)}/I_{(111)}$ ratios.

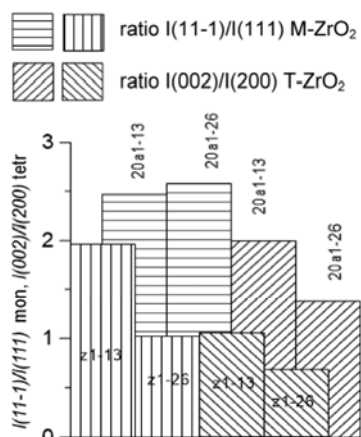


Fig. 9 Monoclinic and tetragonal-phase peak intensity ratios I_{11-1}/I_{111} and I_{002}/I_{200} , respectively, for Y-TZP (z) and Y-TZP- Al_2O_3 (20a) after sliding at 1 m/s 13 N (1–13) and 1 m/s 26 N (1–26).

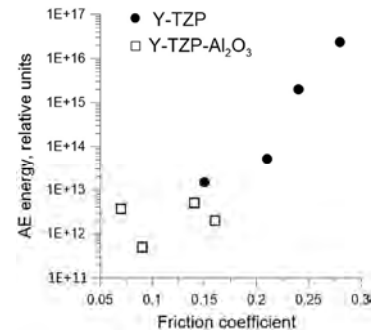


Fig. 10 AE energy vs. friction coefficient.

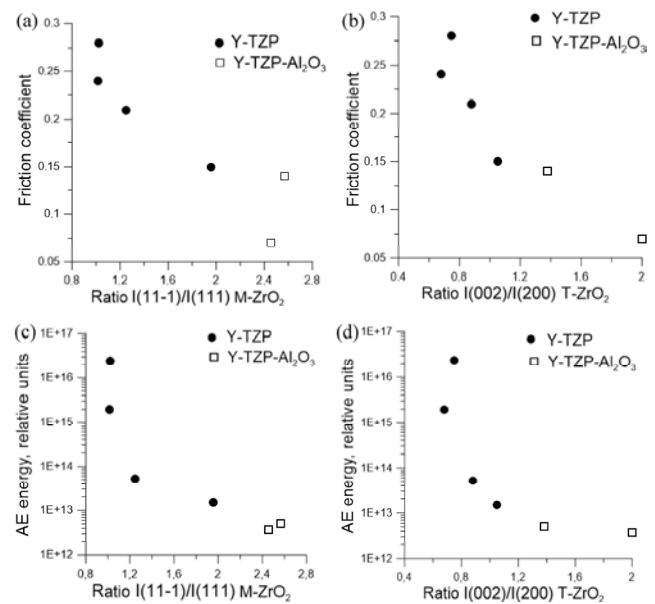


Fig. 11 Monoclinic-phase peak I_{002}/I_{200} (a) and tetragonal I_{11-1}/I_{111} (b) peak intensity dependencies of friction coefficient and AE energy ((c) and (d)).

4 MCA modeling

A numerical 2D movable cellular automata (MCA) method was used to gain more understanding of the subsurface tribological behavior of both composites. The MCA method is one of the so-called “explicit” discrete-elements methods (DEMs) when the evolution of an ensemble of discrete elements is defined by a numerical solution of the system of classical equations of motion using an explicit numerical scheme. Specific features of this method of 2D implementation are as follows: (1) approximation of equivalent disks for interpreting the element shape when numerically solving equations of motion (this makes it possible to use simplified Newton–Euler equations of motion); (2) approximation of homogeneous distribution of strain

and stresses in the volume of discrete elements (the stress-strain state of a discrete element is determined by the average stress tensor $\sigma_{\alpha\beta}$ and average strain tensor $\varepsilon_{\alpha\beta}$); (3) element-element interaction forces are formulated in the framework of the original many-body form with the use of average stresses and strains [32–35]. To describe the elastic behavior of the Y-TZP and Y-TZP- Al_2O_3 ceramic materials within the MCA framework, a model of locally isotropic linear Hook’s law materials is used. The inelastic behavior of discrete elements used for Y-TZP simulation have been described using the pressure-dependent Nikolaevsky’s plastic flow model [34]. This model is based on the nonassociated plastic flow rule and Mises–Schleicher criterion $\Phi = \omega J_1 + \sqrt{J_2} = 3\omega\sigma_{mean} + \sigma_{eq}/\sqrt{3}$, where J_1 and J_2 are the first stress tensor invariant and second stress tensor deviator, respectively; ω is the dimensionless parameter proportional to the internal friction coefficient α ($\alpha = 3\omega$); σ_{mean} is the mean stress; and σ_{eq} is the stress intensity. A limiting state condition for the discrete-element volume is defined by breaking the equality as follows [30]:

$$\Phi = Y \tag{1}$$

where Y is the value of yield stress under the condition of pure shear (cohesion). An important feature of Nikolaevsky’s model is a postulated linear relation between the rates of shear and bulk plastic strains with the dilatancy factor A [29]:

$$\dot{I}_1^p = 2A\sqrt{\dot{I}_2^p} \tag{2}$$

where \dot{I}_1^p is the first invariant of plastic deformation rate tensor, and \dot{I}_2^p is the second invariant of the plastic deformation rate tensor. The necessity for using the nonassociated plastic flow rule for describing the transformation-induced inelastic behavior of Y-TZP is dictated by the rather high value of dilatancy achieved as a result of this transformation. An extra contribution is given by microcracks formed near the localized transformation shear bands because of high local distortion of the stress fields.

This localized fracture within the MCA method is modeled by an unlinked state of two automata, which is opposed to the normally linked (bonded) state. The automata state is changed on achieving

either the strength limit for ductile materials or a multiparameter criterion in the case of brittle materials. The Drucker-Prager [36] pressure-dependent criterion is used in this work as a fracture criterion:

$$\sigma_{eq} 0.5(a+1) + \sigma_{mean} 1.5(a-1) \geq \sigma_c \tag{3}$$

where σ_c is the strength limit, σ_t is the tensile strength, and σ_{mean} and σ_{eq} are the mean stress and stress intensity on the interaction surface of this pair, respectively.

Detailed description of numerical implementations of Nikolaevsky’s model as well as the fracture model within the formalism of the MCA method can be found elsewhere [34]. A numerical study was carried out with the use of the 2D sample, which models the microscale real contact area between two bodies of the same phase composition brought in sliding adhesionless contact (Fig. 12). The samples’ surfaces had a roughness mean period of $0.06 \mu\text{m}$ and mean asperity height of $0.03 \mu\text{m}$. Periodic boundary conditions were established along the horizontal x -axis.

The contacting bodies were simulated by close-packed ensembles of equal-sized discrete $5 \times 10^{-4} \text{ m}$ elements. Initially, all neighboring elements in each body were in an as-linked state. The subsurface layers were free of any defects. The top sample was fixed against displacement along the x -axis. A normal load F_y was applied to the top sample along the y -axis, thus giving a contact stress of 200 MPa. The bottom of sample moved at $V_x = 5 \text{ m/s}$ with respect to the fixed top one. Given that the bottom sample was fixed against displacement along the y -axis, the whole

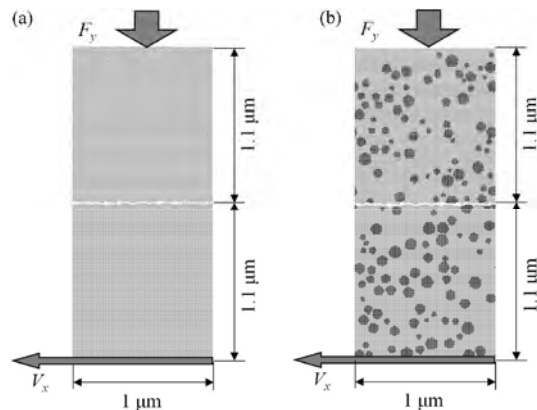


Fig. 12 Schematics of Y-TZP (a) and Y-TZP-20% Al_2O_3 (b) for the model samples and loading.

system represented the sliding experiment when the fixed top sample slides over the surface of the moving bottom one.

Two types of friction couple were modeled: Y-TZP/Y-TZP and Y-TZP-20%Al₂O₃/Y-TZP-20%Al₂O₃. Their mechanical characteristics are shown in Table 1. Y-TZP and alumina were represented as elastic–plastic and elastic–brittle materials, respectively (Fig. 13).

The volume expansion effect of tetragonal-to-monoclinic transformation in Y-TZP was modeled using a dilatancy effect, as described above. The dilatancy coefficient was varied to reveal its effect on subsurface structure evolution in the numerical MCA experiment. The first stage was using zero dilatancy and internal friction coefficients, i.e., this was a no-dilatancy associated plastic flow von Mises criterion model implying that the shear strength does not depend on the pressure and the inelastic volume does not change during inelastic deformation. All other material characteristics corresponded to those shown in Table 1. The results obtained at this stage show that the effective toughness of the Y-TZP ceramics was reduced, because numerous and deep cracks were

generated during sliding. These subsurface cracks could facilitate wear by fracture (Fig. 14(a)).

The results of the experiments with $\lambda = 0.1$ and $\lambda = 0.2$ show that the number of cracks, as well as their in-depth penetration, is reduced with λ (Figs. 14(b) and 14(c)). The integral parameters of submicron-sized sliding-induced cracks formed in the Y-TZP subsurface (Table 2) show that the crack characteristic length and penetration depth reduce by 25%–30% when the dilatancy coefficient grows from 0 to 0.2. The rationale here is that the dilatancy of the material ahead of the crack tip might have created the constraint conditions for the crack growth and thus improved the fracture toughness by analogy with the effect of transformation plasticity in real Y-TZP. These crack parameters depend nonlinearly on the dilatancy coefficient λ with

Table 1 Mechanical characteristics of the materials modeled.

Characteristic	ZrO ₂	Al ₂ O ₃
Density ρ (kg/m ³)	5,700	3,984
Young modulus E (GPa)	172	416
Poisson ratio, ν	0.3	0.3
Elasticity limit σ_y (MPa)	980	–
Internal friction coefficient, α	0.57	–
Dilatancy coefficient, λ	0.1	–
Compression strength σ_c (MPa)	1,400	1,400
Tensile strength σ_t (MPa)	700	300

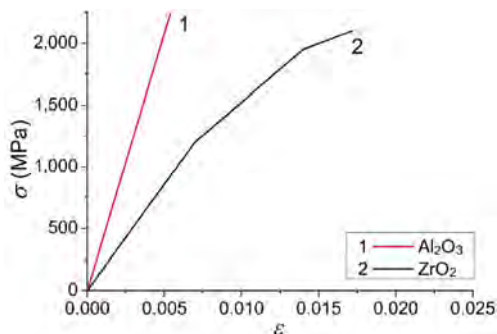


Fig. 13 Stress-strain diagrams for alumina (1) and Y-TZP (2).

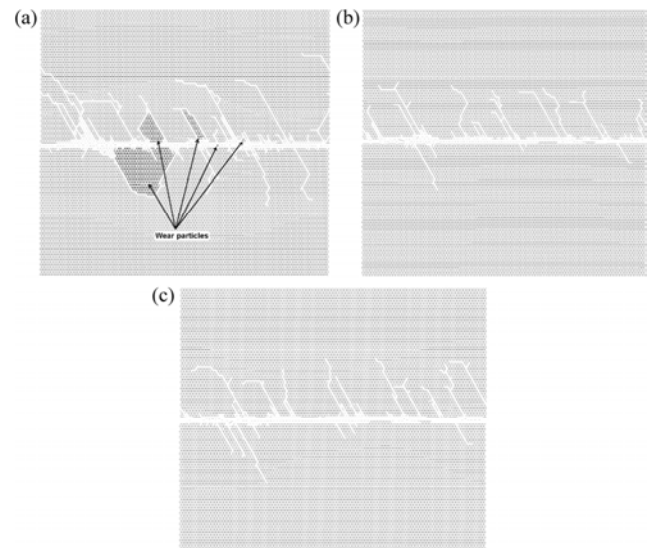


Fig. 14 Subsurface fracture in Y-TZP at dilatancy coefficient $\lambda = 0$ (a), $\lambda = 0.1$ (b), and $\lambda = 0.2$ (c).

Table 2 Parameters of $>0.05 \mu\text{m}$ length subsurface cracks in the model samples of Y-TZP.

Parameters	$\lambda = 0$	$\lambda = 0.1$	$\lambda = 0.2$
Mean value of crack length ¹⁾	0.26 μm	0.195 μm	0.18 μm
Mean in-depth penetration of cracks ²⁾	0.19 μm	0.15 μm	0.14 μm

Note: ¹⁾ Mean crack length has been determined as the total crack length-to-number ratio. ²⁾ Mean in-depth penetration of cracks has been determined as a total crack penetration depth into the bulk of the material along the y -axis over the total crack number. Only $>0.05 \mu\text{m}$ (5 automaton diameter) length cracks have been considered.

a tendency to a plateau behavior at $\lambda \sim 0.3$. Such a limitation of the submicron-crack-growth-suppressing mechanism by means of the phase-transformation-induced dilation is related to the opposing influence of the contact surface.

The column graph in Fig. 15(a) shows the wear particle size distributions generated by wear under conditions presented in Fig. 14. Each wear particle in the model contact zone was determined as an entity composed of only interlinked automata and isolated from the parent material by cracks (shown by arrows in Fig. 14(a)). The wear particle size in Fig. 15 is the so-called effective value, which is implied as a side length of a square wear particle composed of the same automaton number. The effective wear particle size was thus determined using the formula $D\sqrt{n}$, where D is the automaton diameter, and n is the number of automata belonging to the particle. Figure 15(a) shows that wear particles generated in the absence of the transformation-induced dilatancy $\lambda = 0$ (red columns) are at least one order of magnitude larger than those obtained with $\lambda = 0.1$ and $\lambda = 0.2$. The narrow and discrete wear particle size distributions in Fig. 15 were dictated by the limited model sample size as well as the finite size of the automaton, which is also the minimum wear particle size.

Even though the amount of large wear particles is two orders of magnitude less than that of fine ones composed of either one or few automata, their contribution to the volume/weight loss by wear is 50% higher. The results of modeling suggest that wear in the absence of dilatancy occurs by forming the wear particles of various size ranges with almost the same number of particles falling into each range. The dilatancy allows improving the fracture toughness by inducing the local compression stress within the geometrically constrained volumes, thus suppressing both the subsurface crack growth and generation of large wear particles.

Figure 15(a) shows that the increase in the dilatancy coefficient does reduce the wear particle size, which does not exceed the size of few automata at $\lambda = 0.2$ (see blue and magenta columns). These results suggest that the maximum size wear particles, as well as their contributions to total weight/volume losses, are in the reverse proportion to the local volume expansion degree that resulted from the phase transformation.

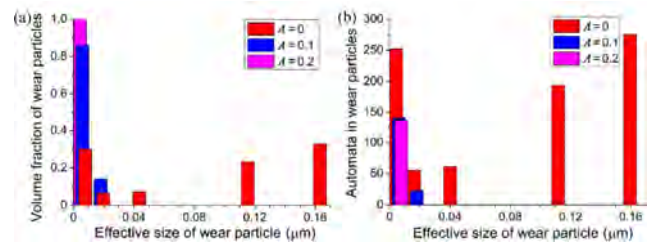


Fig. 15 Volume fractions (a) and mass contributions (b) of different size wear particles for three considered model ceramic materials with $\lambda = 0$ (red columns), $\lambda = 0.1$ (blue columns) and $\lambda = 0.2$ (magenta columns). Mass contributions are shown in arbitrary (automata amount) units.

When discussing the effect of this local volume expansion on wear, note that increasing the dilatancy coefficient results in manifold reduction of the wear particle total mass. The crossover from a classic “dilatancy-free” rheological model of the ceramics (von Mises plasticity) to the transformation-induced plasticity makes it possible to reduce the total wear losses by a factor of six (red and magenta columns in Fig. 15(b)).

Total mass losses by wear are assumed within this model framework as potential wear mass losses due to using the periodic boundary conditions, which do not imply any real mass losses.

The weight loss dependency on λ (Fig. 15(b)) shows a leveling upward tendency already at $\lambda = 0.2$. This may be explained by the above limitation of the crack growth suppression effect from the opposing influence of free wear particles of the contact surface. The results of modeling demonstrated the importance of transformation-induced dilatancy in modeling both the subsurface crack growth and wear.

Another result is that wear resistance improvement of Y-TZP ceramics is feasible by introducing alumina particles. A model Y-TZP-20% Al_2O_3 composite structure is given by Fig. 12(b). Alumina particles were homogeneously distributed in $1 \times 2.2 \mu\text{m}^2$ area. The results of modeling show that the subsurface damaged layer has much lower thickness compared with that on Y-TZP ceramics (Fig. 16 and Fig. 14(c)). Both the amount and length of the wear-generated subsurface cracks, as well as the total mass of the wear particles, are also several times lower. Crack propagation is retarded near alumina particles, so that they are redirected along the particle–matrix interface. This is especially the case in the constraint interparticle space

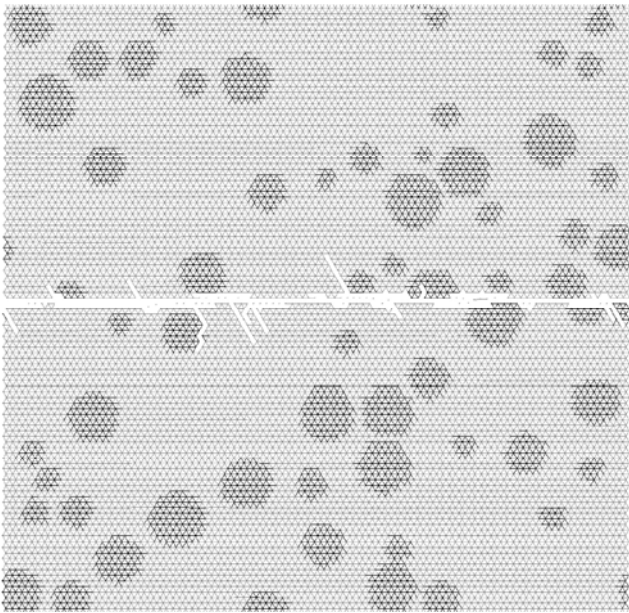


Fig. 16 Subsurface fracture on Y-TZP-20%Al₂O₃ at dilatancy coefficient $\lambda = 0.2$.

when two alumina particles are close to each other; therefore, the dilatancy exerts compression stress between the particles. When this interparticle distance is greater, the cracks may propagate deeper inside the ceramics long after less compression stress is generated.

When discussing the results of simulation, it necessary to mention that quantitative values of the parameters of subsurface cracks and wear particles were obtained using the particular (fixed) size of movable cellular automata. As shown in Ref. [37], when applying a local mesh-independent fracture criterion, for example, the fracture criterion (3)-the magnitudes of the “ultimate” local stresses at which asperities detach from the surface or subsurface cracks nucleate are automaton-size-dependent. Therefore, the automaton size determines the quantitative characteristics of the damage and wear of the surface layer. A promising way to eliminate this technical dependence is to apply the mesh-dependent (scaled) formulation of fracture criterion, which was first introduced and verified for adhesive contacts [38, 39] and described for the particular case of the discrete-element method [37]. Use of the mesh-dependent criterion should provide more-accurate estimates of the wear characteristics, while the above-discussed regularities of the influence of coefficient λ remain the same.

The results of numerical simulation using the MCA method and dilatant plasticity model support the conclusions made on the basis of experimental data. The dilatancy approach to modeling the wear behavior of transformation-induced plasticity ceramics therefore deserves attention and may be successfully applied.

5 Discussion

The LTD is inherent in almost all zirconia-based high-fracture-toughness ceramic materials that experience tetragonal-to-monoclinic transformation under mechanical loading, including sliding friction. It was shown earlier that wear in these ceramics is fully determined by a phase-transformation-dependent mechanism. These materials, however, are used in numerous sliding friction couples, including those working in high-humidity conditions where LTD is an especially fast-occurring process. The LTD may be inhibited by tetragonal grain refining or adding the reinforcement alumina grains, which exert internal residual stress in the composite because of thermal expansion. Therefore, there is interest in studying the LTD-aged samples’ behavior under sliding conditions.

In this work, the T-TZP-based LTD-aged samples were intentionally destabilized by storing them for 20 years in air under room temperatures, so that the amount of a monoclinic phase in Y-TZP was 60 vol.%. Despite that high monoclinic-phase content, the sliding-friction-induced tetragonal-to-monoclinic transformation occurred both in Y-TZP and Y-TZP-Al₂O₃ materials during wear. The transformation intensity depended, however, on a specific sliding speed and load combination, as well as the ceramics type.

The results of wear experiments show that a Y-TZP-Al₂O₃/steel couple had lower friction coefficients, lower AE energy, and higher median frequency values, as well as less damaged worn surfaces compared with those of Y-TZP/steel ones. On the basis of these results, as well as on the literature sources, these distinctions arise from differences in acting wear mechanisms, which are somehow connected with the transformation toughening.

5.1 Y-TZP

It was noted above that friction-generated heat has its

effect on the worn surface monoclinic phase so that inverse monoclinic-to-tetragonal transformation can occur almost simultaneously with the direct one. Also, mechanical fragmentation and grain subdivision of the ceramic grains during sliding will inevitably facilitate the inverse transformation. The result of these processes will be the formation of the XRD textures, which are detected by tetragonal and monoclinic peak I_{002}/I_{200} intensity inversions.

Increasing the sliding speed above 1 m/s results in heating the ceramic subsurface layer to temperatures that partially inhibit the direct stress-induced transformation and transformation-induced plasticity, thus causing catastrophic thermomechanical deterioration of the low-heat-conductivity zirconia ceramics.

The LTD-aged samples used in this work already had a 60 vol. % monoclinic phase in the subsurface layer; therefore, there were numerous defects.

Sliding at 0.5 m/s may easily peel this defect layer off the sample and, thus, form a wear debris layer, which is subjected to further deformation and heating. These particles may then partially experience inverse transformation and become tetragonal-phase ones. Simultaneously, tetragonal bulk grains experience strain-induced direct transformation and also form wear particles, which then may be heated at the real contact areas and become tetragonal ones again. Finally, we may have a tribological layer consisting of fine ceramic particles where both direct and inverse transformation dynamically occur during sliding and forming the XRD textures.

The vibration acceleration RMS changed in time in accordance with the friction coefficient, so that steady-mode friction with only background RMS values was observed for a long period until the formation of wide peaks. Such a steady-mode dynamics may be explained by the strain-induced for the material at low sliding speed. High-amplitude vibrations appeared closer to the end of the test and may be related to the loss of plasticity because of friction heating. For sliding at 0.5 m/s and 26 N, vibration acceleration RMS stays minimal only for a short period of time because of faster friction heating at that high load.

Sliding at 1 m/s and 13 N shifts the equilibrium to the inverse transformation region when there is no structural adaptability mechanism in the form of direct

transformation mechanisms. The result is catastrophic deterioration of the worn surface by cracking and detaching of large wear particles. Intense cracking definitely causes intense high-amplitude AE signals with low median frequency and high AE energy, whereas transformation-induced plasticity must give high median frequency and low AE energy because of the arresting of the subsurface crack propagation. The vibration acceleration RMS shows peaks from the beginning of the sliding, thus being in accordance with the friction coefficient and friction heat generated. The same could be true for sliding at 1 m/s and 26 N.

Numerical studies of wear in Y-TZP support the above-discussed experimental data, showing intense crack development in the material as a result of the transformation dilatancy effect.

5.2 Y-TZP-Al₂O₃

The specificity of wear and friction in the Y-TZP-Al₂O₃/steel couple may have several aspects. The first is that high-modulus reinforcement alumina particles are distributed among the zirconia ones, giving them high-thermomechanical stability and less sensitivity to high temperatures [40]. Such a reinforcement makes it possible to attain higher fracture toughness, even after full high-temperature loss of transformation toughening because of crack propagation deflection on the reinforcement particles.

The second aspect is that alumina particles create some constraint conditions to avoid excess strain-induced plasticity and microcracking, thus improving the effect of transformation toughening and arresting the subsurface crack propagation in sliding [40]. Relatively high heat conductivity of alumina particles, i.e., 40 W/(m·K) at 25°C as compared with 2 W/(m·K) of ZrO₂-Y₂O₃ in the temperature range 100–1,400 °C is the third aspect contributing to friction on Y-TZP-Al₂O₃. Therefore, Y-TZP-Al₂O₃ has better heat removal conditions in sliding and better thermodynamic conditions for strain-induced transformation toughening. These three aspects contribute to better wear resistance of Y-TZP-Al₂O₃ as compared to Y-TZP, and this is supported also by the fact that the Y-TZP-Al₂O₃ tetragonal $I_{(002)}/I_{(200)}$ and monoclinic $I_{(11-1)}/I_{(111)}$ ratios are higher than those of Y-TZP. The Y-TZP-Al₂O₃ may have experienced more-intense reversible

transformation.

That effective reversible transformation in Y-TZP- Al_2O_3 provides efficient stress relaxation on the worn surface and reduces surface deterioration. Relatively milder wear in the Y-TZP- Al_2O_3 /steel couple is accompanied by lower AE signal energy and higher median frequency.

Vertical and horizontal vibrations changed in time in accordance with friction coefficient except for those obtained in sliding at 1 m/s and 26 N. Also, there is steady stage of the vibration acceleration RMS dependence for 0.5 m/s and 13 N, which could be related to the above-discussed specificity of the wear and phase transformation in this metal. Also, high-RMS peaks might be caused by the indenting of the counter body by free alumina grains, which are harder than those of zirconia and do experience strain-induced transformation. Thus, wear debris should be composed of large alumina grains and smaller zirconia ones that still may be capable of strain-induced transformation for the reasons stated above.

Even though the MCA modeling could not reproduce any inverse transformation effects, it showed that the subsurface fracture zone thickness for Y-ZP- Al_2O_3 was less than that of Y-TZP.

6 Conclusion

Acoustic emission mean characteristics, such as median frequency and AE energy, were found to be a material response to sliding speed and load combinations, taking into account the cumulative effect of competing sliding process factors, such as strain and temperature, on the phase transformation in LTD-aged Y-TZP and Y-TZP- Al_2O_3 . Hybrid Y-TZP- Al_2O_3 /steel sliding showed better tribological characteristics than those of Y-TZP because of their structure. These results are supported by numerical-modeling ones that showed that Y-TZP strain-induced transformation dilatancy in a constraint shear condition within the contact spot retards the subsurface crack nucleation and crack arresting at a depth lower than that without taking account of the dilatancy. Similar results have been obtained for the Y-TZP- Al_2O_3 composite. Subsurface nucleates predominantly on the Y-TZP/ Al_2O_3 interfaces, which serve as stress concentrators and

then are arrested in the matrix by transformation-induced dilation constraint bulk stresses.

The worn surfaces of both materials showed the presence of inverse peak intensity ratios, i.e., the traces of reversible transformation. Inverse monoclinic-to-tetragonal transformation occurred in the case of higher friction heating, which also caused AE energy growth because of the loss of subsurface crack-arresting capability and inhibition of direct strain-induced transformation.

As shown, there is a strong correlation between AE signal parameters and XRD texturing of the monoclinic and tetragonal phases. Increasing the textured peak ratio leads to a decrease in AE signal energy and friction coefficient. The LTD-aged samples contained the same amount of monoclinic phase in their Y-TZP components. Nevertheless, the monoclinic phase I(11-1)/I(111) ratio increased after sliding with the AE signal median frequency and decreased with the AE signal energy and friction coefficient. Therefore, AE may be an effective method for *in-situ* monitoring of the subsurface wear of materials experiencing both direct and inverse transformation.

Acknowledgments

The work was financially supported by the Russian Federation via the Ministry of Education and Science of the Russian Federation (Agreement No. 14.607.21.0186, project identifier RFMEFI60717X0186).

Open Access: The articles published in this journal are distributed under the terms of the Creative Commons Attribution 4.0 International License (<http://creativecommons.org/licenses/by/4.0/>), which permits unrestricted use, distribution, and reproduction in any medium, provided you give appropriate credit to the original author(s) and the source, provide a link to the Creative Commons license, and indicate if changes were made.

References

- [1] Turon-Vinas M, Anglada M. Strength and fracture toughness of zirconia dental ceramics. *Dental Mater* 34(3): 365–375 (2018)

- [2] Deville S, Gremillard L, Chevalier J, Fantozzi G. A critical comparison of methods for the determination of the aging sensitivity in biomedical grade yttria-stabilized zirconia. *J Biomed Mater Res Part B Appl Biomater* **72B**(2): 239–245 (2005)
- [3] Reveron H, Fornabaio M, Palmero P, Fürderer T, Adolfsson E, Lughì V, Bonifacio A, Sergo V, Montanaro L, Chevalier J. Towards long lasting zirconia-based composites for dental implants: Transformation induced plasticity and its consequence on ceramic reliability. *Acta Biomater* **48**: 423–432 (2017)
- [4] Fischer T E, Anderson M P, Jahanmir S. Influence of fracture toughness on the wear resistance of yttria-doped zirconium oxide. *J Am Ceram Soc* **72**(2): 252–257 (1989)
- [5] Lee S W, Hsu S M, Shen M C. Ceramic wear maps: Zirconia. *J Am Ceram Soc* **76**(8): 1937–1947 (1993)
- [6] Swain M V, Hannink R H J. Metastability of the martensitic transformation in a 12 mol% ceria-zirconia alloy: II, grinding studies. *J Am Ceram Soc* **72**(8): 1358–1364 (1989)
- [7] Korolev P V, Savchenko N L, Kul'kov S N. Texture formation on the friction surface in transformation-toughened ceramics. *Tech Phys Lett* **30**(1): 12–14 (2004)
- [8] Becker P C, Libsch T A, Rhee S K. Wear mechanisms of toughened zirconias. In *Proceedings of the 9th Annual Conference on Composites and Advanced Ceramic Materials*. The American Ceramic Society, 1985: 1040–1058
- [9] Savchenko N L, Kul'kov S N. Friction and wear of Y-TZP and Y-TZP–Al₂O₃ ceramics in high-speed sliding on steel. *J Frict Wear* **30**(6): 444–448 (2009)
- [10] Wu K G, Choe C Y, Lee S M, Yoo J A, Hyun C Y, Hong D P, Byeon J W. Real-time monitoring of degradation of zirconia ceramic by acoustic emission. *Appl Mech Mater* **433–435**: 816–820 (2013)
- [11] Hua Z K, Fan Y W, Jin Z M. A biotribo-acoustic testing method for ceramic orthopaedic biomaterials. *Tribol Int* **71**: 1–6 (2014)
- [12] Taylor S, Manley M T, Sutton K. The role of stripe wear in causing acoustic emissions from alumina ceramic-on-ceramic bearings. *J Arthroplasty* **22**(S7): 47–51 (2007)
- [13] Wang L, Wood R J K. Acoustic emissions from lubricated hybrid contacts. *Tribol Int* **42**(11–12): 1629–1637 (2009)
- [14] Filippov A V, Rubtsov V E, Tarasov S Y. Acoustic emission study of surface deterioration in tribocontacting. *Appl Acoust* **117**: 106–112 (2017)
- [15] Filippov A V, Nikonov A Y, Rubtsov V E, Dmitriev A I, Tarasov S Y. Vibration and acoustic emission monitoring the stability of peakless tool turning: Experiment and modeling. *J Mater Process Technol* **246**: 224–234 (2017).
- [16] Filippov A V, Tarasov S Y, Fortuna S V, Podgornykh O A, Shamarin N N, Rubtsov V E. Microstructural, mechanical and acoustic emission-assisted wear characterization of equal channel angular pressed (ECAP) low stacking fault energy brass. *Tribol Int* **123**: 273–285 (2018)
- [17] Rubtsov V E, Kolubaev E A, Kolubaev A V, Popov V L. Using acoustic emission for the analysis of wear processes during sliding friction. *Tech Phys Lett* **39**(2): 223–225 (2013)
- [18] McBride S L, Boness R J, Sobczyk M, Viner M R. Acoustics emission from lubricated and rubbing surfaces. *J Acoust Emiss* **8**(1–2): 192–196 (1989)
- [19] Clarke D R, Arora A. Acoustic emission characterization of the tetragonal-monoclinic phase transformation in zirconia. In *Advances in Ceramics, Vol. 12, Science and Technology of Zirconia II*. Claussen N, Heuer A H, Ruhle M, Eds. Columbus, OH: American Ceramic Society, 1984.
- [20] Lankford J. Plastic deformation of partially stabilized zirconia. *J Am Ceram Soc* **66**(11): c212–c213 (1983)
- [21] Drozdov A V, Galenko V O, Gogotsi G A, Swain M V. Acoustic emission during micro- and macrocrack growth in Mg-PSZ. *J Am Ceram Soc* **74**(8): 1922–1927 (1991)
- [22] Chu L, Ren H, Ning J. Damage and Toughening Analysis of Ceramics by AE Location Method//G. Shen et al. (eds.), *Advances in Acoustic Emission Technology: Proceedings of the World Conference on Acoustic Emission-2013*, Springer Proceedings in Physics 158: 313–321
- [23] Jacobus K, Sehitoglu H, Balzer M. Effect of stress state on the stress-induced martensitic transformation in polycrystalline Ni-Ti Alloy. *Metall Mater Trans A* **27**(10): 3066–3073 (1996)
- [24] Stam G T M, Van Der Giessen E, Meijers P. Effect of transformation-induced shear strains on crack growth in zirconia-containing ceramics. *Int J Solids Struct* **31**(14): 1923–1948 (1994)
- [25] Sun Q P, Hwang K C. Micromechanics modelling for the constitutive behavior of polycrystalline shape memory alloys–I. Derivation of general relations. *J Mech Phys Solids* **41**(1): 1–17 (1993)
- [26] Patoor E, Lagoudas D C, Entchev P B, Brinson L C, Gao X J. Shape memory alloys, Part I: General properties and modeling of single crystals. *Mech Mater* **38**(5–6): 391–429 (2006)
- [27] Lagoudas D C, Entchev P B, Popov P, Patoor E, Brinson L C, Gao X J. Shape memory alloys, Part II: Modeling of polycrystals. *Mech Mater* **38**(5–6): 430–462 (2006)
- [28] Lankford J, Page R A, Rabenberg L. Deformation mechanisms in yttria-stabilized zirconia. *J Mater Sci* **23**(11): 4144–4156 (1988)
- [29] Nikolaevsky V N. *Geomechanics and Fluidodynamics: with Applications to Reservoir Engineering*. Dordrecht, Boston: Kluwer Academic, 1996

- [30] Stefanov Y P, Chertov M A, Aidagulov G R, Myasnikov A V. Dynamics of inelastic deformation of porous rocks and formation of localized compaction zones studied by numerical modeling. *J Mech Phys Solids* **59**(11): 2323–2340 (2011)
- [31] Eremin M O. Numerical simulation of fracture of ZrO_2 - Al_2O_3 ceramic composites. *Phys Mesomech* **19**(4): 452–458 (2016)
- [32] Psakhie S, Shilko E V, Smolin A, Astafurov S, Ovcharenko V E. Development of a formalism of movable cellular automaton method for numerical modeling of fracture of heterogeneous elastic-plastic materials. *Fract Struct Integr* **7**(24): 26–59 (2013)
- [33] Shilko E V, Psakhie S G, Schmauder S, Popov V L, Astafurov S V, Smolin A Y. Overcoming the limitations of distinct element method for multiscale modeling of materials with multimodal internal structure. *Comput Mater Sci* **102**: 267–285 (2015)
- [34] Psakhie S G, Shilko E V, Grigoriev A S, Astafurov S V, Dimaki A V, Smolin A Y. A mathematical model of particle–particle interaction for discrete element based modeling of deformation and fracture of heterogeneous elastic–plastic materials. *Eng Fract Mech* **130**: 96–115 (2014)
- [35] Dmitriev A I, Österle W, Wetzel B, Zhang G. Mesoscale modeling of the mechanical and tribological behavior of a polymer matrix composite based on epoxy and 6 vol.% silica nanoparticles. *Comput Mater Sci* **110**: 204–214 (2015)
- [36] Alejano L R, Bobet A. Drucker-prager criterion. *Rock Mech Rock Eng* **45**(6): 995–999 (2012)
- [37] Dimaki A, Shilko E V, Psakhie S, Popov V L. Simulation of fracture using a mesh-dependent fracture criterion in the discrete element method. *Facta Univ Ser Mech Eng* **16**(1): 41–50 (2018)
- [38] Pohrt R, Popov V L. Adhesive contact simulation of elastic solids using local mesh-dependent detachment criterion in Boundary Elements Method. *Facta Univ Ser Mech Eng* **13**(1): 3–10 (2015)
- [39] Popov V L, Pohrt R, Li Q. Strength of adhesive contacts: Influence of contact geometry and material gradients. *Friction* **5**(3): 308–325 (2017)
- [40] Kelly J R, Denry I. Stabilized zirconia as a structural ceramic: An overview. *Dent Mater* **24**(3): 289–298 (2008)



Nikolai L SAVCHENKO. He received his MS degree in metallurgical engineer at the Tomsk Polytechnic Institute (USSR) in 1987, PhD degree in physics in 1995 and Dr Sci degree in materials in 2015 at the Institute of Strength Physics and

Materials Science SB RAS in Tomsk (Russia). His current position is the leading researcher of Laboratory for Quality Control in Materials and Structures in the Institute of Strength Physics and Materials Science SB RAS. His research focuses on CMC and MMC tribology, interfacial phenomena, surface characterization, etc.



Andrey V FILIPPOV. He received his PhD degree at the Institute of Strength Physics and Materials Science SB RAS in 2015. He joined the Tomsk Polytechnic University (TPU), Department of at Materials Machining Technologies in 2011. His current positions are a researcher at

the Institute of Strength Physics and Materials Science SB RAS, Laboratory of Surface Hardening Physics, and an associate professor at Tomsk Polytechnic University. His research areas cover structural evolution of fine- and ultrafine-grained materials under severe subsurface deformation by friction and cutting with detailed analysis of vibration and acoustic emission phenomena.



Sergei Yu TARASOV. He received his PhD and Dr. Sci. degrees at the Institute of Strength Physics and Materials Science SB RAS in 1994 and 2009, respectively. His current position is a leading researcher at the Institute of Strength Physics

and Materials Science SB RAS. He joined the Tomsk Polytechnic University in 2013 as a professor. His research areas cover all aspects of material structural evolution materials under severe subsurface deformation by friction with special attention given to friction stir processing of iron- and aluminum-base materials.



Andrey I DMITRIEV. He received his PhD and Dr. Sci. degrees in condensed mater physics at the Institute of Strength Physics and Materials Science (ISPMS) SB RAS in 1997 and 2006, respectively. He joined the Tomsk State University (TSU), Department

of Metal Physics in 2005. His current positions are a principal researcher at ISPMS SB RAS, Laboratory of Computer-Aided Design of Materials, and a professor at Tomsk State University. His research areas cover computer modeling in tribology and nanotribology using numerical methods of various scales on the basis of discrete approach.



Evgeny V SHILKO. He received his MS degree in solid state physics in 1995 from Tomsk State University, Russia. After that he obtained his PhD and Dr Sci degrees in deformable solid mechanics at the Institute of Strength Physics and Materials Science SB RAS (ISPMS SB RAS), Tomsk,

Russia, in 1998 and 2007, respectively. He joined the Laboratory of Computer-Aided Design of Materials at ISPMS SB RAS from 1998. His current positions are a principal researcher of the laboratory and a professor at the Physical Faculty at Tomsk State University. His research areas cover computer modeling of fracture at different scales, mechanics of fluid-saturated solids and contact mechanics.



Aleksandr S GRIGORIEV. He received his MS degree in applied mechanics in 2012 from Tomsk State University, Russia. He joined the Laboratory of Computer-Aided Design of Materials at the Institute of Strength Physics and Materials

Science SB RAS (ISPMS SB RAS), Tomsk, Russia, from 2012. His current position is a junior researcher of the laboratory. His research interests include computer modeling in the fields of dynamic mechanical behavior of solids, rock mechanics and contact interaction of solids.

60 years of Rabinowicz' criterion for adhesive wear

Elena POPOVA^{1,*}, Valentin L. POPOV^{1,*}, Dae-Eun KIM^{2,3}

¹ Institute of Mechanics, Technische Universität Berlin, Berlin10623, Germany

² School of Mechanical Engineering, Yonsei University, Seoul 03722, Republic of Korea

³ Center for Nano-Wear, Yonsei University, Seoul 03722, Republic of Korea

Received: 21 June 2018 / Revised: 04 August 2018 / Accepted: 06 August 2018

© The author(s) 2018. This article is published with open access at Springerlink.com

Abstract: 60 years ago, in 1958, Ernest Rabinowicz published a 5 page paper titled “The effect of size on the looseness of wear fragments” where he suggested a criterion determining the minimum size of wear particles. The criterion of Rabinowicz is based on the consideration of the interplay of elastic energy stored in “asperities” and the work of separation needed for detaching a wear particle. He was probably the first researcher who explicitly emphasized the role of adhesion in friction and wear. In a recent paper in *Nature Communications*, Aghababaei, Warner and Molinari confirmed the criterion of Rabinowicz by means of quasi-molecular dynamics and illustrated the exact mechanism of the transition from plastic smoothing to formation of wear debris. This latter paper promoted the criterion of Rabinowicz to a new paradigm for current studies of adhesive wear. The size arguments of Rabinowicz can be applied in the same form also to many other problems, such as brittle-ductile transition during indentation, cutting of materials or ultimate strength of nano-composites.

Keywords: adhesion; plasticity; wear; Archard's law of wear; Rabinowicz criterion; surface topography; history of Tribology

1 Introduction

Ernest Rabinowicz is the author of one of the most influential books on friction and wear in the history of Tribology [1]. It appeared one year before the famous report of Peter Jost [2] and, together with it, marked the birth of Tribology. The mystery of the popularity and impact of the book of Rabinowicz—not only among tribologists but also in engineering design—lies in its simplicity and the robustness of the concepts developed and presented by Rabinowicz. A persistent problem of Tribology is its poor “availability”—in this field there are practically no simple methods and concepts having high predictive power [3]. Rabinowicz succeeded in finding a small number of key concepts, rough at the edges but robust, which allowed for qualitative understanding of tribological properties and setting rules for

tribological design. In the 1950s and 1960s, tribology was not yet mature enough for a detailed theoretical analysis or quantitative calculation of contact phenomena. Only a picture in the impressionist style could be drawn at the time—ignoring or distorting up close “details”, but still presenting a coherent whole.

The name of Rabinowicz is deservedly associated with the role of adhesion in tribological processes. This was a backbone concept of his research and his book. For him, adhesion was the key concept for considering both friction and wear [4]. In considering wear, Rabinowicz distinguished the processes of material transfer from one partner to the other and of wear debris formation. Indeed, one of his most influential papers, co-authored with Tabor, is devoted to the radioisotope tracer study of metal transfer [5]. In later work, Rabinowicz extended his adhesion concept by introducing the notion of “similar” and

* Corresponding authors: Elena POPOVA, E-mail: elena.popova@tu-berlin.de; Valentin L. POPOV, E-mail: v.popov@tu-berlin.de

“dissimilar” materials, which describes the tendency of material pairings to form alloys [6].

The main idea of how adhesion determines the process of wear was put forward by Rabinowicz in 1958 [7]. He assumed that the process of wear is governed by the interplay of elastic energy stored in a medium and the work of adhesion needed to separate two parts of a body—just as suggested by Griffith in his theory of crack propagation [8]. Griffith’s idea was specified by Rabinowicz by equating the critical stress of crack propagation to the plastic flow stress. This modification allowed applying Griffith’s idea to the problem of wear, but impeded any detailed analytical theory. Note that the general interest in adhesion in contact mechanics started only in the 1970s with the work of Johnson, Kendall and Roberts [9], so that in 1958 these ideas were ahead of time.

The lack of numerical possibilities at that time, Rabinowicz compensated with experimental work (Fig. 1), which he interpreted not by comparison with analytical or numerical solutions, but by carrying out correlation analysis, while the proper “coordinates” were determined using simple ideas and estimations.

The geometry of the problem of wear particle formation is much more involved compared to that of a crack, so that a simple analytical theory of particle



Fig. 1 Ernest Rabinowicz “hard at work”. On this photo taken in the late 1950s or early 1960s he is absorbed in work with a cylinder on cylinder rolling tester [10].

formation was not possible at that time and is not possible even now. It therefore remained “only an idea” for almost 60 years until Aghababaei, Warner and Molinari [11] carried out a numerical experiment very similar to the “thought experiment” of Rabinowicz of 1958.

While the basic idea of Rabinowicz from 1958 could only obtain the status of a verified paradigm 60 years after the fact, it was still developed during these years on a qualitative level. In the present paper, we try to follow the life of this idea in the years between 1958 and 2016.

2 Rabinowicz’ criterion for “looseness of wear particles”

The initial idea formulated by Rabinowicz is very vague [7]. Following his experimental findings, he never speaks directly about wear particle formation but about two related processes—the material transfer from one body to the other one and the subsequent process of formation of loose particles and illustrates it by a sketch reproduced in Fig. 2.

While the details of the processes described by Rabinowicz were left mostly unspecified, the central idea formulated by him does not depend on these details. He assumes that the wear fragment has a hemispherical shape and that it detaches *after* direct contact has been lost. The maximum elastic energy stored in the fragment during contact is of the order of $\frac{1}{2} \frac{\sigma_Y^2}{E} V$, where E is the Young modulus, σ_Y the yield stress of the fragment material, and V the volume of the hemisphere. Since, after the losing contact, only residual stresses remain in the fragment, Rabinowicz assumes that the elastic energy associated with these stresses is only around 0.1 (square of the Poisson-number) of the maximum energy, so that the fragments will detach from the surface if this energy is sufficient for creating new surfaces with the area A of the

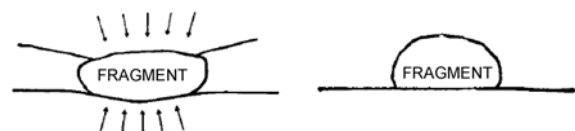


Fig. 2 Illustration of the formation of a “wear fragment” during contact and after losing contact [7].

hemisphere, which leads to the criterion

$$\frac{1}{10} \frac{\sigma_Y^2}{E} \frac{\pi D^3}{12} \geq W \frac{\pi D^2}{4} \quad (1)$$

where W is the specific work of adhesion. Thus, only particles with diameter larger than the critical one,

$$D > D_c \geq \frac{30EW}{\sigma_Y^2} \quad (2)$$

can detach spontaneously.

Thus initial idea of Rabinowicz was not about wear particle *formation* per se, but whether already formed particles will leave the surface after the immediate contact with the counter body is lost. In the same way he thought about the material *transfer* [12]. Note that from the point of view of the energetic criterion used, there is no difference between adhesion and *cohesion*. In other words, the Rabinowicz' criterion does not differentiate of whether the crack and detachment occurs along an interface between two different materials (adhesion) or inside a material (cohesion). In the latter case, only the specific work of adhesion, W , has to be replaced by the specific work of cohesion, W_c .

In a later work, Rabinowicz applied this criterion to a medium covered by a thin soft layer of a solid lubricant [13]. His theoretical arguments were very simple: Rabinowicz argued that there should be different wear mechanisms depending on whether the critical size of looseness of wear particles is larger or smaller than the thickness of the layer. Most interesting are his experimental results, which indeed show that there exists some critical thickness under which wear decreases drastically (Fig. 3).

In the paper [14], it was shown by direct application of a Rabinowicz-like energetic criterion to the problem of formation of a wear particle of a thin soft layer, that indeed there exists a *critical thickness*, below which the wear intensity decreases abruptly. Note that in Fig. 3 the vertical axis shows a quantity proportional to the life time (and thus inversely proportional to the wear intensity).

Rabinowicz always had a relatively complicated process of “wear fragment” formation in mind—due to both material transfer and detachment of particles. He was a practitioner and always proceeded from

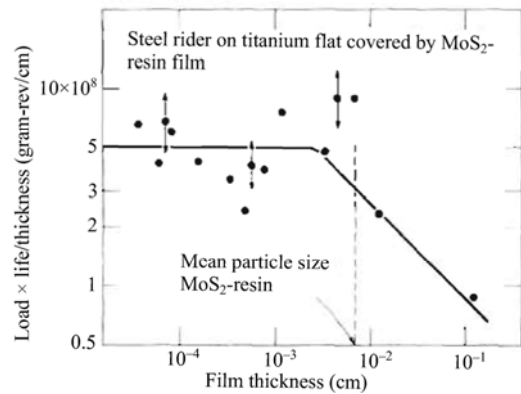


Fig. 3 The function load \times life time/thickness plotted as a function of thickness for titanium flat surfaces lubricated by MoS₂-resin (reproduced from Ref. [13]).

empirical observations and not from theoretical models. His work inspired many subsequent studies of this two-stage wear process, e.g., the experimental study [15], which appeared shortly after the paper [7] of Rabinowicz.

3 Failure modes in a contact of two asperities

The Rabinowicz criterion states that there are some conditions that must be fulfilled to make wear particle formation possible. But what happens when these conditions are not fulfilled (the junction size is smaller than the critical one)? Rabinowicz himself favored the idea of “atom-by-atom” removal, as opposed to wear debris formation. When speaking of such a process he uses the terms “burnishing” or “least wear” [16].

In the 60 years, there were many attempts to understand the mechanism of wear under conditions when free wear particles cannot be formed. For example, in Ref. [17], three types of failure modes of contact of two asperities are investigated using FEM analysis: shear, fracture and slip tongue.

Interestingly, a transition from plastic deformation to formation of wear particles also exists in the case of abrasive wear [18].

4 Other applications of Rabinowicz' criterion

The conclusion about the existence of a critical size

applies not only to wear, but also to the strength of materials. The initial idea of Rabinowicz was related to the process of spontaneous detachment of a prestressed fragment of a material. This idea can be applied not only to fragments on the surface, but also inside the volume. If material has been intensively deformed plastically, it will have internal stresses on the order of the yield stress of the material, σ_Y . If the characteristic size of “structural elements” of the material is D , the material will spontaneously crack if the Rabinowicz criterion (2) is fulfilled. For smaller structural elements, spontaneous cracking is impossible. This leads to existence of some critical size of phases in composites, under which they become “crack-resistant”, and in particular tolerant to material flaws as shown by Gao et al. [19].

Absolutely the same “Rabinowicz”-like criterion arises in the problem of crushing small particles, where there exists a critical size

$$d_{\text{crit}} = \frac{32EW}{3\sigma_Y^2} \quad (3)$$

which coincides with the Rabinowicz criterion up to a constant coefficient [20]. If particles are smaller than this critical value, further crushing or pulverization is not possible. In the paper [20], Kendall writes further: “These size arguments are relevant not only for crushing but also to other processes connected with the brittleness and ductility of materials. For example, brittle substances may be indented plastically with a sharp tool, providing the indentation is below a certain size, above which cracking takes place. For calcium carbonate this critical size is $3 \mu\text{m}$ [21], a value comparable with that calculated from Eq. (3). Another example is that of cutting, which can only occur if the depth of cut is sufficiently small to prevent cracking. Ductile machining swarf has been observed when glass was cut by very fine tungsten carbide tool [22]. The depth of cut when this became apparent was $0.5 \mu\text{m}$, as compared with figure of $0.9 \mu\text{m}$ from Eq. (3)”.

Kendall’s experiments with small particles reveal the “mechanism” of the brittle-ductile transition. The mechanism is obviously a competition between cracking and plasticity (Fig. 4). This transition does not automatically mean that very small particles are

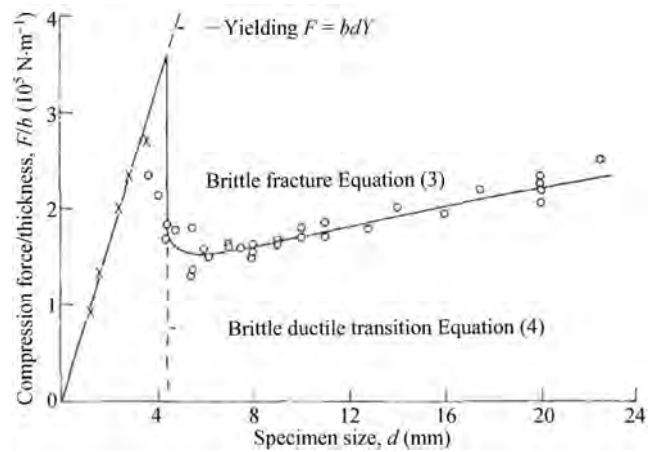


Fig. 4 Compression results obtained by K. Kendall for a range of specimen sizes illustrating cracking (°) for large samples and yielding (×) of small ones. Reproduced from Ref. [20].

especially strong. Figure 4 shows that decreasing of the particle size eventually leads to the decrease of the critical force of failure. Only the mechanism of failure changes from cracking to plastic deformation. This competition of plasticity and adhesion is discussed in detail in a “toy model” described in Ref. [23] showing that some plastic deformation generally occurs even in cases where cracking is the primary mechanism.

5 Rabinowicz’ criterion and Archard’s wear equation

The most popular law of adhesive wear states that the worn volume V is proportional to the normal force F_N and the sliding distance s and inversely proportional to the hardness σ_0 of the softer counterpart:

$$V = k \frac{F_N s}{\sigma_0} \quad (4)$$

The constant k is the so called adhesive wear coefficient. It is common to associate this wear law with the name of Archard. Even though similar formulations have been used before Archard’s seminal work [24, 25], the law of adhesive wear deservedly carries his name—due to his enormous contribution to understanding the mechanics and physics of rough surfaces in contact. Rabinowicz used Archard’s law and discussed adhesive wear in terms of the adhesive wear coefficient as the only reliable tool available.

However, already the fact that the adhesive wear coefficient can vary over seven orders of magnitude shows that Archard's law (4) can only be a very crude approximation. All not-well-understood details are just gathered in the empirical adhesive wear coefficient. Already several decades ago it was clear that neither of the dependencies of Archard's law is universal. Thus, Rhee [26] has shown in 1970 that the dependence of the wear volume on the normal force is non-linear in most cases and can be better described by power-law dependencies.

Many different adjustments and alternatives to Archard's law have been proposed over time. The review of Meng and Ludema of 1995 shows hundreds of different wear "laws", none of which became widely recognized.

Note that Archard's law of adhesive wear does not include the surface energy as a parameter at all. However, the Rabinowicz criterion clearly implies that such dependence should appear at least under some conditions (for example if the size of junctions in contact becomes smaller than the critical one). A recent investigation shows clearly that application of the Rabinowicz criterion to the analysis of wear intensity leads to non-linear dependencies of wear volume on the normal force [28]. Note that introducing the surface energy as a possible governing parameter of the wear equation necessarily also leads to non-linear dependence on the force and even the sliding distance. Experiments and dimensional analysis carried out in Ref. [29] suggest the following power law

$$V = k \frac{W^{1.775}}{E^{3.225}} F_N^{1.47} L^{1.25} \quad (5)$$

Equations of this type may be of much higher value than Archard's law of wear, as they implicitly contain a dependence on surface energy and thus provide an estimation for the adhesive wear coefficient.

6 Adhesion versus plowing model of friction

The adhesion theory of friction and wear advocated and developed by Rabinowicz did not prevail without a challenge. Another school of thought regarding the origin of friction stemmed from the view that, rather

than adhesion, mechanical interaction that occurs between two solids during sliding can be a more dominant factor in dictating the frictional behavior. This notion was ironically, or quite suitably, proposed by Nam P. Suh who was Rabinowicz's colleague at MIT. In the paper published by Suh on the topic of genesis of friction, friction was expressed as the sum of three components: asperity deformation, plowing and adhesion [30]. Of these three components, it was suggested that plowing was the most dominant factor in many metallic sliding systems. This reasoning was derived from the experimental data obtained from numerous friction tests conducted using identical and different metals. The fact that friction coefficient varied with sliding history was a key observation that led to the belief that adhesion alone could not be the dominating factor in dictating the frictional behavior of a sliding system. Furthermore, the typical increasing trend in the friction coefficient with increasing sliding distance suggested that as wear particles are created, surfaces get plowed by the strain hardened particles, which in turn contributes to the drastic increase in friction. Such experimental evidence disproved the fundamental concept behind Rabinowicz's compability chart that was constructed based on the thought that since friction is caused by adhesion, friction between identical or similar materials will be higher than that between dissimilar materials [1]. According to Suh, whether the materials in contact are identical or not, friction can be high due to wear particles that act to plow the contacting surfaces during sliding. As we know today, certainly both mechanisms play important roles on generating friction depending on the nature of the sliding system and conditions.

The contrasting views regarding the dominating friction mechanism between Rabinowicz and Suh instigated the tribology community on the topic of the origin of friction in a positive manner in the years to come. Such a debate on the dominant mechanism of friction prevailed not only in the professional community but also in the classrooms at MIT. Tribology was a graduate course offered at MIT Mechanical Engineering Department which was taught by both Rabinowicz and Suh. The students were excited by the opportunity to learn from these two great minds in the field who used their own books for the lectures: *Friction and Wear of Materials* by Rabinowicz [1] and

Tribophysics by Suh [31].

It was through a classical topic such as friction from which the students were exposed to conflicting views and arguments. For many, this served as a motivation to go into the field of tribology, which at that time, unlike many other disciplines in mechanical engineering, still seemed to offer the opportunity for new theoretical developments and challenges. Students who were honored by the presence of both Rabinowicz and Suh in their Ph.D. thesis committee examinations were often overwhelmed with the burden to satisfy both of them with different views on friction. Nevertheless, the professors seemed to derive satisfaction from providing such a harsh and challenging environment to the students, who ultimately benefited tremendously from such an experience.

Rabinowicz's philosophy towards student education may be further evidenced by his policy on accepting a consulting job. He once told the students that he only accepts consulting jobs if the problem is interesting enough and at the same time sufficiently challenging to be applied to Ph.D. qualifying exams. This indeed demonstrates Rabinowicz's deep passion for breeding future generation tribologists as well as to the field of tribology to which he contributed greatly.

7 Discussion and conclusion

Ernest Rabinowicz takes a very special place in Tribology. He was a practitioner, which determined his widely empirical approach to tribological phenomena. He successfully managed to find a small number of key concepts, which allowed a very rough but robust and useful interpretation of a large amount of empirical data. He often used correlation analysis presented in double logarithmic coordinates, as many interrelations in Tribology can only be seen if one disregards the details and looks at the very rough picture. A very typical example of analysis by Rabinowicz can be read in his famous book when discussing the role of hardness in wear ([1], 6.22 Materials to be used in adhesive wear). Rabinowicz writes: "In the use of hard materials, it should be pointed out the wear rate does not generally produce very drastic effects. Suppose that we have an alloy steel which half-hard has a Rockwell C value of 40 (~400 kg/mm²) and

when fully hard has a Rockwell C hardness of 80 (~800 kg/mm²). This difference by a factor of two in hardness will produce a difference by a factor of two in the adhesive wear rate, which is only just large to be measurable, since difference between repeat tests under identical conditions is likely to be a factor of 3!"

In part, it was this concentration on general dependencies (neglecting "fluctuations" by a factor of 3!) that allowed Rabinowicz to achieve such general understanding of tribological phenomena. His book is not only cited but it is actively used in practice—a very rare phenomenon in the tribological literature.

Now, 60 years after Rabinowicz formulated a basic model for adhesive wear, his concepts transform to paradigms for detailed model wear analysis based on new computational and experimental capabilities.

Acknowledgement

The authors thank Judith Raymond née Rabinowicz for providing a photo of Ernest Rabinowicz working in his lab.

Open Access: The articles published in this journal are distributed under the terms of the Creative Commons Attribution 4.0 International License (<http://creativecommons.org/licenses/by/4.0/>), which permits unrestricted use, distribution, and reproduction in any medium, provided you give appropriate credit to the original author(s) and the source, provide a link to the Creative Commons license, and indicate if changes were made.

References

- [1] Rabinowicz E. *Friction and Wear of Materials. Second Edition*. John Wiley & Sons, inc., 1995 (First Edition 1965).
- [2] Jost H P ed. *Lubrication (tribology)—A report on the present position and industry's needs*. Department of Education and Science, H. M. Stationary Office, London, UK, 1966.
- [3] Popov V L. Golden age of tribology? Grand challenges in tribological education and research. *Frontiers in Mechanical Engineering, Section Tribology*, 2018.
- [4] Rabinowicz E. Influence of surface energy on friction and wear phenomena. *Journal of Applied Physics* 32(8): 1440–1444 (1961)

- [5] Rabinowicz E, Tabor D. Metallic transfer between sliding metals: An autoradiographic study. *Proceedings of the Royal Society A: Mathematical, Physical and Engineering Sciences* **208**(1095): 455–475 (1951)
- [6] Rabinowicz E. Friction coefficients of noble metals over a range of loads. *Wear* **159**(1): 89–94, (1992)
- [7] Rabinowicz E. The effect of size on the looseness of wear fragments. *Wear* **2**: 4–8 (1958)
- [8] Griffith A A. The Phenomena of Rupture and Flow in Solids. *Philosophical Transactions of the Royal Society of London A* **221**: 163–198 (1921)
- [9] Johnson K L, Kendall K, Roberts A D. Surface energy and the contact of elastic solids. *Proc. R. Soc. London A* **324**: 301–313 (1971)
- [10] Photo provided by Judith Raymond née Rabinowicz from family archiv.
- [11] Aghababaei R, Warner D H, Molinari J-F. Critical length scale controls adhesive wear mechanisms. *Nature Communications* **7**: 11816 (2016)
- [12] Rabinowicz E. The Nature of the Static and Kinetic Coefficients of Friction. *Journal of Applied Physics* **22**(11): 1373–1379 (1951)
- [13] Rabinowicz E. Variation of Friction and Wear of Solid Lubricant Films with Film Thickness. *ASLE Transactions* **10**(1): 1–9 (1967)
- [14] Popov V L. Adhesive wear: Generalized Rabinowicz' criteria. *Facta Universitatis, Series: Mechanical Engineering* **16**(1): 29–39 (2018)
- [15] Cocks M. Interaction of Sliding Metal Surfaces. *Journal of Applied Physics* **33**(7): 2152–2161 (1962)
- [16] Rabinowicz E. The least wear. *Wear* **100**: 533–541 (1984).
- [17] Keer L M., Xu Y., Cheng H S., and Xuan, J L. Simulation of Wear Particle Creation in Asperity Contacts Using the Finite Element Method. *Tribology Transactions* **36**(4): 613–620 (1993)
- [18] Yin X., Komvopoulos K. A slip-line plasticity analysis of abrasive wear of a smooth and soft surface sliding against a rough (fractal) and hard surface. *International Journal of Solids and Structures* **49**(1): 121–131 (2012)
- [19] Gao H, Ji B, Jager I L, Arzt E, Fratzl P. Materials become insensitive to flaws at nanoscale: Lessons from nature. *Proceedings of the National Academy of Sciences* **100**(10): 5597–5600 (2003)
- [20] Kendall K. The impossibility of comminuting small particles by compression. *Nature* **272**(5655): 710–711 (1978)
- [21] Shaw M C. Plastic flow in the cutting and grinding of materials. *Proceedings of the National Academy of Sciences* **40**(6): 394–401 (1954)
- [22] McClintock F A, Argon A S. *Mechanical Behaviour of Materials*. Reading USA: Addison Wesley, 1966, 495 p.
- [23] Popov V L. Generalized Rabinowicz' criterion for adhesive wear for elliptic micro contacts. *AIP Conference Proceedings* **1909**: 020178 (2017)
- [24] Archard J F. Contact and rubbing of flat surfaces. *Journal of Applied Physics* **24**: 981–988 (1953)
- [25] Archard J F, Hirst W. The wear of metals under unlubricated conditions. *Proc R Soc London A* **236**: 397–410 (1956)
- [26] Rhee S K. Wear equation for polymers sliding against metal surfaces. *Wear* **16**(6):431–45 (1970)
- [27] Meng H C, Ludema K C. Wear models and predictive equations: their form and content. *Wear* **181**: 443–457 (1995)
- [28] Popov V L, Pohrt R. Adhesive wear and particle emission: Numerical approach based on asperity-free formulation of Rabinowicz criterion. *Friction* in press, DOI 10.1007/s40544-018-0236-4.
- [29] Kar M K, Bahadur S. The wear equation for unfilled and filled polyoxymethylene. *Wear* **30**(3): 337–348 (1974)
- [30] Suh N P, Sin H-S. The Genesis of Friction. *Wear* **69**: 91–114 (1981)
- [31] Suh N P. *Tribophysics*. Prentice-Hall, 1986.



Elena POPOVA. She studied Slavistics at the Tomsk State University, Russia (graduated 1987 with degree Dipl.-Phil.) and German literature studies and Philosophy at the University of Paderborn, Germany (graduated 2003 with

degree Magistra Artium). She worked at the Tomsk Pedagogical University, Russian Academy of Sciences and later at the University of Potsdam. Since 2007, she coordinated double degree programs in Engineering Science with Russia and China at the Berlin University of Technology and carried out research in the field of history of tribology.



Valentin L. POPOV. He is full professor at the Berlin University of Technology. He studied physics and obtained his doctorate in 1985 from the Moscow State Lomonosov University. 1985-1998 he worked at the Institute of Strength Physics and Materials Science of the Russian Academy of Sciences and was a guest professor in the field of theoretical physics at the University of Paderborn (Germany) from 1999 to 2002. Since 2002 he is the head of the Department of System Dynamics and the Physics of Friction at the Berlin University of Technology. He has published over 300 papers in leading international journals and is the author of the book “Contact Mechanics and Friction: Physical principles and applications” which appeared in three editions in German, English, Chinese, and

Russian. He is the member of editorial boards of many international journals and is organizer of more than 20 international conferences and workshops over diverse tribological themes. Prof. Popov is honorary professor of Tomsk Polytechnic University, of East China University of Science and Technology, and of Changchun University of Science and Technology and distinguished guest professor of Tsinghua University. His areas of interest include tribology, nanotribology, tribology at low temperatures, biotribology, the influence of friction through ultrasound, numerical simulation of contact and friction, research regarding earthquakes, as well as topics related to materials science such as the mechanics of elastoplastic media with microstructures, strength of metals and alloys, and shape memory alloys.



Dae-Eun KIM. He is currently a professor in the School of Mechanical Engineering and the Director of the Center for Nano-Wear (CNW) at Yonsei University. Prof. Kim received his B.S. degree from Tufts Univ., and M.S. and Ph.D. degrees from M.I.T. He was an assistant professor at the Ohio State University before joining Yonsei

University in 1993. He served as the Editor-in-Chief of IJPEM and Senior Editor of JMST. He is currently the President of the Korean Tribology Society and also serves as the Chair of the Technical Committee for Tribology of International Federation for the Promotion of Mechanism and Machine Science (IFTToMM). His research interests are micro/nano-tribology, functional coatings, and surface modification techniques.